Giza, Marcin (2026) *Post-processing in perovskite solar cells: challenging your assumptions*. PhD thesis.

https://theses.gla.ac.uk/85820/

Post-Processing in Perovskite Solar Cells: Challenging Your Assumptions

Marcin Giza

A thesis presented for the degree of
Doctor of Philosophy

School of Chemistry
College of Science and Engineering
University of Glasgow

March 2026

Abstract

Exploiting the vast source of energy provided by the sun is one of the most promising pathways towards reducing fossil fuel use and shifting to renewable energy sources. The development of novel solar cells is thus of high importance to maximise the benefits this approach can provide. In the field of cutting-edge photovoltaic technologies, perovskites have emerged as one of the best-performing candidates for the solar cells of the future. Much of the research into perovskites is now focused on tackling some of the issues they face limiting their potential for industry-level adoption. The implementation of a related class of materials, know as Layered Perovskites (LPKs) is an increasingly popular approach to achieve the requirements of longevity and high efficiencies.

Here, the unique combination of properties provided by the alternating organic and perovskite sheets results in a highly-tunable hybrid material that is stable and well-suited to improving performance across a range of perovskite solar cell compositions. Whilst the implementation of LPKs is a well-established avenue of research, questions still remain about some of their fundamental properties.

The work presented in this thesis seeks to challenge some of the assumptions that are universally applied to LPKs as a whole. The interplay between the organic components and the perovskite backbone is found to be highly complex, and it is difficult to draw clear relations between the chemistry of the A' cation, the material structure, and its optoelectronic properties. Many of the highly desirable properties such as improved stability are not strictly applicable to the extremely thin layers that are most widely utilised within solar cells, which readily degrade in ambient conditions. Indeed, the solar cell fabrication process can disrupt the LPK or even remove it entirely, highlighting that great care must be taken when exploring the mechanism behind their benefits to performance and stability.

Acknowledgments

Firstly, I would like to thank my supervisor, Prof. Pablo Docampo for inviting me to join his research group, and the many years of mentorship and guidance in the realm of 'perovskties'. I will forever aim to beautify every figure. I would like to also express my great appreciation to Prof. Graeme Cooke for his support and supervision during the final stages of my PhD.

A heartfelt thank you goes out to all of the members of the Docampo and Cooke groups, both past and present, for making my time at Glasgow such a fantastic experience. I have been very fortunate to share an office with many of the Docampos: Dr. Namrata Pant, Dr. Benjamin Vella, Dr. Ivan Shmarov, the recent Dr. Wai Kin Yiu, Fraser Angus and Madeleine McRoberts. The daily grind would not have been the same without the endless coffees, chess and heated whiteboard discussions on the nature of a lasagna. Thank you to all of the Cookies for their chemistry support - Dr. Michele Cariello, Dr. Dylan Wilkinson, Dr. Frances Tracey, Dr. Lewis Mackenzie, Gregor Macleod, Abdul-Wasir Shaka and Abarna Sekar. I appreciate every time you signed a COSHH form, ran an NMR or let me borrow your hotplates and glassware.

Throughout my PhD, I have had the pleasure to collaborate with a great number of fantastic scientists, both close to home and abroad. I would like to thank Dr. Paula Lalaguna for her support and patience in carrying out PL and AFM measurements on the numerous samples I prepared, and the Kadodwala group for assisting in my first publication. I truly appreciate the opportunity to work with and publish alongside the Draper group, Rubén Serrano and the team at IMDEA, and Prof. Aleksandra Djurišić and her group in HKU. Thank you to the fantastic team at the University of Warwick, lead by Dr. Rebecca Milot and Prof. James Lloyd-Hughes. The visits to Warwick and CLF were a great opportunity to learn some new science and work with Justas Deveikis, Dr. Jake Hutchinson, Dr. Folusho Balogun, Dr. Nathaniel Gallop, Dr. Edward Butler-Caddle and Yujie Wo. I hope any remaining samples live on for a few weeks more! I would like to thank everyone at the University of Newcastle I had the pleasure of collaborating with - Dr. Aleksey Kozikov, Vaibhav Verma, Dr. Leo Tsui and Prof. Noel Healy. Special thanks go to Dr. Elisabetta Arca, as without her expertise and mentorship there would be no XPS data anywhere in this work.

Much of my PhD work was carried out with the help of the Analytical Services staff, who have provided invaluable assistance, mentoring and support in accessing the facilities at the university. I would like to thank Dr. Claire Wilson for her support throughout all of my XRD measurements, James Gallagher for his generosity

in granting me long hours of access to the SEM instrument, and Dr. Christopher Kelly for his patience during repeated XPS measurement sessions.

On a more personal note, I would like to thank Lewis, Tess, Ben, Łucja, Tom, Ellie, Connor, Fraser, Madeleine, Marianna, James and everyone else who helped make so many great memories in Glasgow. I appreciate every time everyone played along with increasingly unlikely excuses for a costume party, and the many hours spent walking in remote, rainy parts of Scotland. I miss the beige banquets and rubicon crossings already.

Thank you to my family, Agnieszka, Piotr and Maciek, for their encouragement and their truly incredible patience as I moved to the end of the country and back. I hope the extra opportunities to visit Glencoe were worth it!

Finally, none of this would be possible without Jess, who has been a constant source of support throughout the last four years. You made a truly new place feel like home. Thank you for everything.

Author's Declaration

I declare that, except where explicit reference is made to the contribution of others, this thesis is the result of my own work and has not been submitted for any other degree at the University of Glasgow or any other institution. The research included in this thesis was conducted at the School of Chemistry within the University of Glasgow, with Prof. Pablo Docampo as my primary supervisor, and Prof. Graeme Cooke as my secondary supervisor, from October 2021 to May 2025.

Signed:
Marcin Giza
Date: 05/03/2026

Contents

List of Figures

List of Tables

List of Acronyms

ACN Acetonitrile

AFM Atomic Force Microscopy

BAV Bond Angle Variance

BCP Bathocuproine

BDI Bond Distortion Index

ButA Butylammonium

C.B. Conduction Band

CB Chlorobenzene

CCD Charge-Coupled Device

CTM Charge Transport Material

DE Diethyl Ether

DFT Density Functional Theory

DI Deionised

DJ Dion-Jacobson

DMF Dimethylformamide

DMSO Dimethyl sulfoxide

DoDecA 1,12-DoDecyldiammonium

ESD Estimated Standard Deviation

EtAc Ethyl Acetate

ETM Electron Transport Material

F-PEA 4-Fluoro phenylethylammonium

FA Formamidinium

FF Fill Factor

FK209 tris (2-(1H-pyrazol-1-yl)-4-tert-butylpyridine) cobalt(III) tri [bis(trifluoromethanesulfonyl)imide

FTO Fluorine-doped Tin Oxide

GBL γ-Butyrolactone

HexA Hexylammonium

HOMO Highest Occupied Molecular Orbital

HTM Hole Transport Material

IPA Isopropyl Alcohol

ITO Indium Tin Oxide

J_{SC} Short Circuit Current

LED Light Emitting Diode

LiTFSI Lithium bis(trifluoromethanesulfonyl)imide

LPK Layered Perovskite

LUMO Lowest Unoccupied Molecular Orbital

MA Methylammonium

MAPI methylammonium lead iodide

MPA Methyl pentanoate

MPP Maximum Power Point

N-I-P n-Type – Intrinsic – p-Type

NMR Nuclear Magnetic Resonance

OctA Octylammonium

P-I-N p-Type – Intrinsic – n-Type

PCBM [6,6]-Phenyl C_{61} butyric acid methyl ester

PCE Power Conversion Efficiency

PEA Phenylethylammonium

PentA Pentylammonium

PL Photoluminescence

PMA Phenylmethylammonium

PMMA Polymethylmethacrylate

PTAA Poly[bis(4-phenyl)(2,4,6-trimethylphenyl)amine

PTFE Polytetrafluoroethylene

RP Ruddlesden-Popper

SEM Scanning Electron Microscopy

Spiro-OMeTAD 2,2',7,7'-tetrakis [N,N-di(4-methoxyphenyl) amino]-9,9'-spirobifluorene

STEM Scanning Transmission Electron Microscopy

tBP *tert*-butyl pyridine

ThEA 2-Thiopheneethylammonium

ThMA 2-Thiophenemethylammonium

V.B. Valence Band

$\mathbf{V_{OC}}$ Open Circuit Voltage

XPS X-Ray Photoelectron Spectroscopy

XRD X-Ray Diffraction

Chapter 1

Introduction

1.1 Motivation - A Solar-Powered World

The importance of a greater adoption of renewable energies is now well-entrenched in the public consciousness. An international call to move away from coal and gas fuelled energy generation and a shift towards renewables has been cited as a key outcome of the recent COP28 climate change conference.[1] This is one of the most important changes aimed at helping slow global carbon dioxide emissions and minimising the rise in global temperatures to only 1.5 °C. Fossil fuels already see significant demand as precursors for the synthesis of chemicals and materials, so a reduction of its use for energy generation is crucial in the context of the growing world population.[2] This process is already in progress, with recent reports from the UK government highlighting that renewable energy sources provided 46.3% of UK power demand.[3] Breaking down the sources of this renewable energy as illustrated in Fig. 1.1, photovoltaics have been the fastest growing category in the UK over the last 15 years and are second in overall capacity, only outperformed by wind power. This is a direct reflection of the huge potential of photovoltaics for transforming energy generation. These technologies tap into the most direct and abundant energy source available on Earth - estimations of global energy consumption suggest that it only amounts to 0.0125% of the energy supplied by the sun.[4] This makes photovoltaic technologies uniquely positioned to have the potential to be scaled up until they can meet all of our energy demands, and help reach the goal of net-zero emissions by 2050 in the interim.[1,5]

Most of this photovoltaic capacity relies on established technologies based around crystalline silicon semiconductors, which make up around 90% of all solar panels installed.[6] With the first silicon cell reported in 1954, their maturity has helped to drive down costs and enabled their mass adoption.[7] On the other hand, further development is hampered by the limitations of silicon as a material, with many of its properties poorly suited for the role of light absorption and energy generation. Additionally, they require high quantities of expensive precursors and their manufacture leads to significant emissions which offsets some of the benefits they provide.[8,9] Alternative technologies based around materials which are intrinsically much more suited for light absorption such as copper indium gallium selenide or cadmium telluride have been used to fabricate 'second generation' solar cells. These are by and large far more efficient, but the elements they require are toxic and have

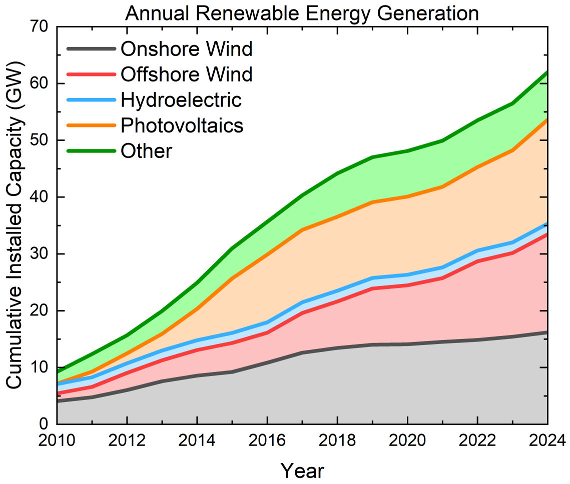

Figure 1.1: Cumulative UK renewable energy generation, by year. ‘Other’ technologies include biogas from various waste sources and liquid biofuels. Data taken from Ref. [3]. Contains public sector information licensed under the Open Government Licence v3.0.

a low natural abundance, limiting their large-scale implementation.[10] This means there is real demand for novel photovoltaic technologies which are efficient, easy to produce and can be adapted to a wide range of applications. The approach of modern ‘third generation’ photovoltaics is based around nanostructured thin films, which boast greater ease of fabrication than cells of the previous generations, and contain dedicated materials for the roles of light absorption and charge transport. Dye sensitised cells were the first of these third generation cells, and they demonstrated the potential of solution-processed materials for easy development of thin, flexible and lightweight solar panels.[11] Many candidate materials have been proposed for the light absorbing layers, from purely organic semiconductors to quantum-dots.[4] Amongst all of these, perovskites have emerged as the most promising and fastest-developing photovoltaic technology. This class of materials has a number of unique properties that both makes them particularly suitable as solar cell light absorbers, and brings a specific set of challenges that need to be tackled.

1.2 Principles of Solar Cells

Solar cells are able to directly convert incident light into electrical current, due to the mechanism of light absorption by semiconducting materials. A semiconductor is a material which has an electronic structure in-between that of a metal and an insulator. Within any material, the overlap of low lying occupied atomic energy levels and higher energy empty levels leads to the formation of electronic bands at different energies. In metals the highest occupied energy level, known as the Fermi level, is found within a band and thus there is a continuum of available energy levels directly above.[12] For insulators and semiconductors, the Fermi level instead is found between the occupied band, known as the Valence Band (V.B.), and the higher energy empty Conduction Band (C.B.). This difference is illustrated in Fig. 1.2. The distinction between a semiconductor and an insulator lies only in the degree of separation between the occupied V.B. and the empty C.B., also known as the bandgap. In the case of semiconductors, the bandgap is small enough to allow the promotion of electrons into the conduction band due to external excitation. For intrinsic semiconductors such as perovskites, the Fermi level lies in the centre of the bandgap.

1.2.1 Solar Cell Operation

The successful operation of a solar cell relies on capturing the solar spectrum as it appears on the surface of the earth, which covers energies from 0.5 - 4.4 eV, ranging from near infrared to low-energy UV radiation.[13] As such, materials with a bandgap that matches these photon energies can directly absorb the light, and convert it into electrical current. The fundamental principles of this process are shown in Fig. 1.3. The absorption of a photon results in an electron moving from the valence to the conduction band, creating an electron-hole pair also known as an exciton. Separating this electron-hole pair is required to harvest the energy absorbed. This is achieved by creating an energetic pathway for each of the charges to travel through. Excited electrons pass into materials with a lower energy conduction band, and holes into materials with a higher valence band. For traditional silicon solar cells the energetics of the material itself are varied by combining positively and negatively doped regions. In emerging technologies such as perovskites, this is done by dedicated Hole Transport Material (HTM) and Electron Transport Material (ETM) layers. This results in a spatial separation of the carriers, and creates an energetic barrier for travel 'back' into the absorber layer. Finally, conductive glass and metal contacts complete the energy level 'staircase' and allow the charges to flow through the circuit and eventually back into the material to start the process again.

To measure how well a solar cell operates, the current it outputs under illumination is measured whilst an applied voltage is varied. This generates a J / V curve, with the current (I) being converted to a current density (J) to eliminate the effect of the area of the solar cell. A representative example is shown in Fig. 1.4. Five key parameters are collected from this plot, known as the Short Circuit Current (J_{SC}), Open Circuit Voltage (V_{OC}), Fill Factor (FF), Power Conversion Efficiency (PCE) and Maximum Power Point (MPP). The J_{SC} value occurs at a condition where the Fermi levels of the semiconductor, Charge Transport Materials (CTMs) and elec-

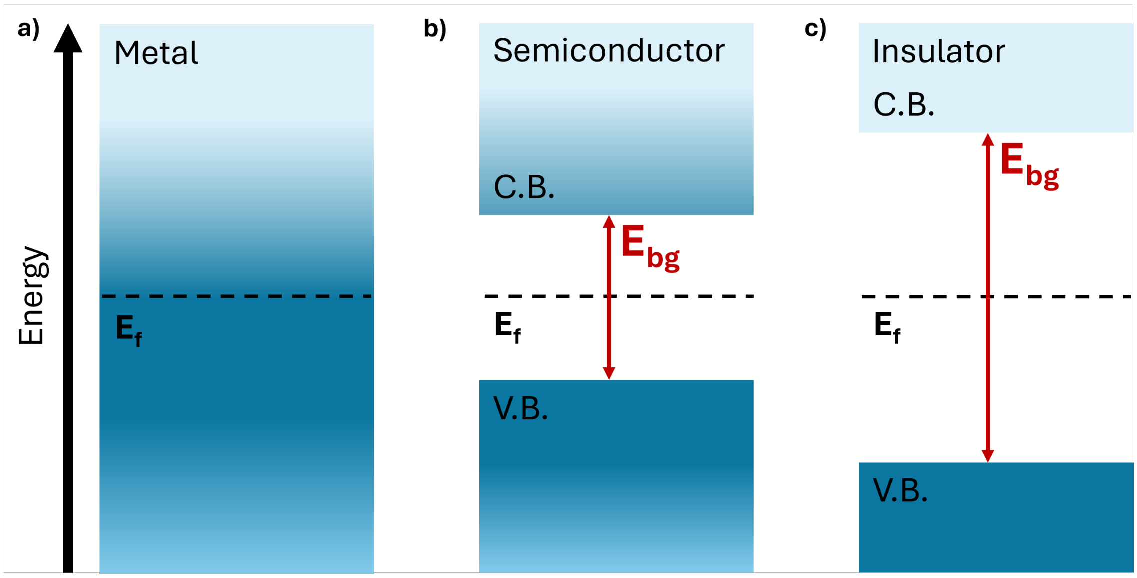

Figure 1.2: Comparison of the band structure of a) metals, b) semiconductors and c) insulators. E_{bg} and E_f denote the bandgap energy and the Fermi level respectively. V.B. and C.B. denote the valence and conduction bands respectively.

tronic contacts across the device are fully aligned. No power is generated at this condition as the potential difference is zero, but it indicates the maximum current flow through the cell. The J_{SC} is dependent on the generated photocurrent and the recombination current, which indicate how much light is absorbed to generate charge, and how much charge is lost before it is extracted. Generally, narrowing the bandgap increases J_{SC}, as more light can be absorbed to form charge carriers.[13]

The V_{OC} is the voltage value at the other, zero current limiting case. Here, the process of exciting electrons and the formation of holes under illumination means the relative distribution of the two charge carries within the conduction and valence bands varies. This creates two separate Fermi levels, with the electron level at a higher energy than the hole level, thus creating a potential difference between the two populations. This process is known as quasi-Fermi level splitting, and is influenced by how many charge carriers are generated in the cell, and how many are lost. This potential difference represents the maximum value of the V_{OC} in the cell.[14] The V_{OC} increases as the bandgap widens, until a point where not enough light is absorbed to generate sufficient charge carrier populations to cause significant quasi-Fermi level splitting. The V_{OC} value is always lower than the semiconductor bandgap, with a maximum ratio of 87% attainable at a bandgap of 3.6 eV.[13]

At voltage values in-between 0 V and the V_{OC}, the solar cell outputs power. The ratio of the power output versus the intensity of light incident on the cell is known as the PCE, and is the most common indicator of a solar cell's performance. The point where the power output of the cell is highest is known as the MPP. A comparison of the values of the current and voltage at the MPP to the product of the J_{SC} and the V_{OC} is known as the FF. This indicates how close the cell is operating to the idealised condition of maximum attainable current at the maximum possible voltage, with high values being evidence of a highly-optimised solar cell. Whilst

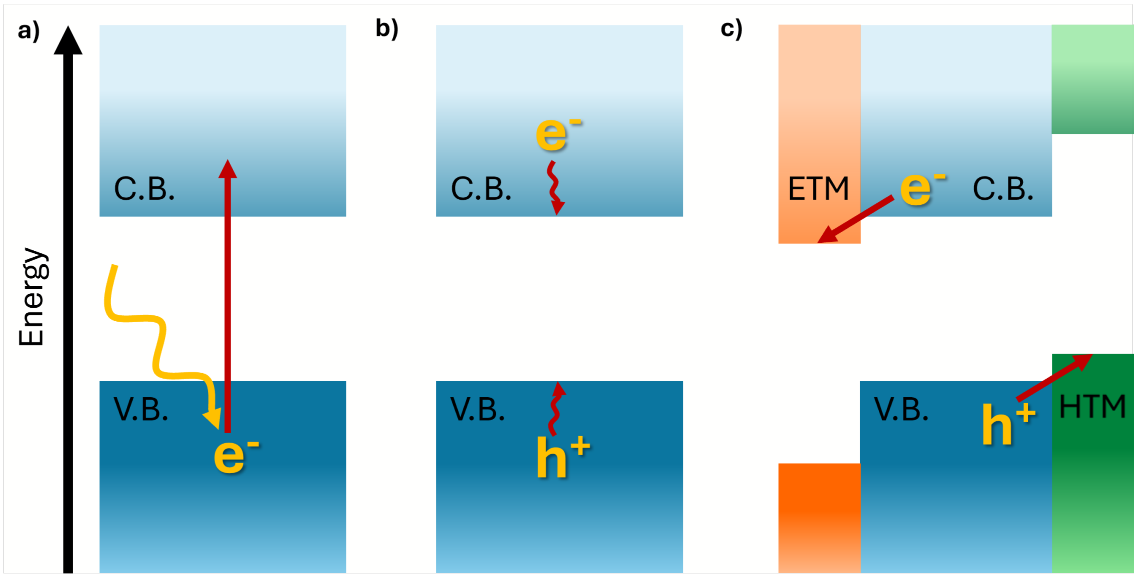

Figure 1.3: Schematic illustration of the process of converting light into electrical current in semiconductors. a) Light absorption by the semiconducting material to promote an electron from the V.B. to the C.B. and creating a hole in the V.B.. b) The relaxation of the excited carriers to the respective ground levels. c) The extraction of the charge carriers by dedicated Hole Transport Material (HTM) and Electron Transport Material (ETM) layers. Arrows indicate the movement of electrons between energy levels. Curly arrows indicate vibrational relaxation.

theoretical calculations for a perfect cell give potential FF values of over 90%, the best-performing perovskite cells in the literature can attain FFs of around 86%.[13,15]

1.2.2 Recombination and other limitations

The power solar cells supply is not without its limits, with several processes present which act to reduce their theoretical maximum operating efficiency. These can be broadly divided into unavoidable fundamental physical aspects, and limitations that arise as a consequence of the fabrication process.

When designing a solar cell, the first step is to choose a material with a suitable bandgap energy, which is well-matched to the light shining on it. Light with an energy smaller than the bandgap is not absorbed, and thus is effectively ‘lost’. Excess energy above the bandgap leads to the promotion of the electron into a vibrationally excited state, which is then also lost as heat as the photo-excited species relax back down to the conduction and valence band edges. Thus, the optimal bandgap energy represents a compromise between the current flow and the potential difference across the solar cell which maximises the power output.

Another limitation facing the efficiency of cells is how many of the incident photons are actually absorbed by the layer. This absorption coefficient is influenced by both the width of the bandgap, and whether it is direct or indirect. In indirect bandgap semiconductors such as silicon, a phonon is also required for successful absorption. This means that a photon is less likely to be absorbed than in direct

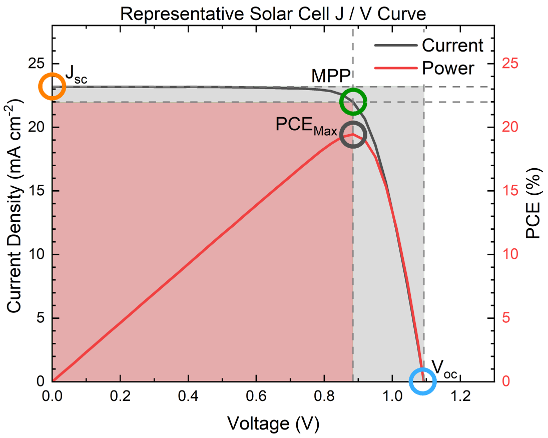

Figure 1.4: Plot of the characteristic current density / voltage response for a solar cell under illumination, with annotations of the positions of J_{SC}, V_{OC},the maximum PCE values, and the corresponding MPP. The FF is defined as the ratio of the current and voltage values at the MPP point versus the product of the J_{SC} and V_{OC}, indicated by the red and grey shaded areas respectively.

bandgap semiconductors, such as perovskites.[16,17] Perovskite solar cells can therefore be much thinner in comparison, without the need for complex surface structuring to trap light as in silicon cells.[5]

Once successfully absorbed, the excited charge carriers can always be lost via radiative band-to-band recombination.[18] Without any external interaction, the excited electron will eventually fall back down to its ground state, recombining with a hole and re-emitting a photon matching the bandgap energy. This is influenced by the dielectric constant of the material, with high values screening the electron-hole attraction, promoting separation and limiting recombination.[19] In perovskite cells, the separated charge carriers are long-lived with a high mobility, and thus have large calculated diffusion lengths of over 2 µm.[20,21] As this value is far larger than the typical thicknesses of the absorber layer, the losses via this pathway are relatively limited.

By taking all of these limitations into account, the maximum theoretical efficiency of a solar cell can be determined. This is known as the Shockley-Queisser limit, and it has recently been re-determined to be 33.16%, given an optimal bandgap of 1.34 eV and a temperature of 298.15 °K.[13,22] This value is calculated for the standardised ‘AM 1.5 G’ spectrum used as the basis for most laboratory solar simulators, which corresponds to a power intensity of 1000.4 W m^{-2}. There are several key assumptions within this calculation, with the solar cell absorbing all incident photons with matching energies to form one exciton, radiating light in all directions with no reflection, and experiencing no competing recombination processes.[13] It is also important to note that this maximum PCE is only applicable to a solar cell based around a single light absorbing layer. By combining different materials which have a range of bandgap values in tandem cells, more of the incoming light can be captured. Here, the absolute efficiency limit for an infinitely-layered solar cell is 68%, where the only losses occur due to radiative recombination.[23]

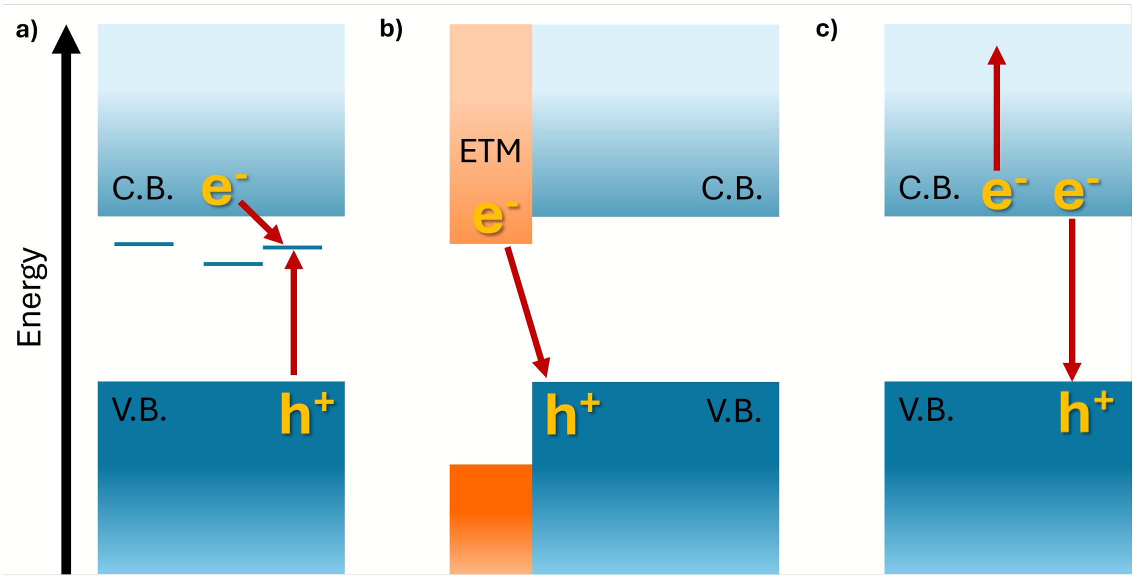

Figure 1.5: Schematic illustration of non-radiative solar cell recombination pathways. a) trap-assisted recombination. b) interfacial recombination. c) Auger recombination. Red arrows indicate the movement of electrons and holes to different energy levels which results in their recombination.

The 33.16% PCE value of the Shockley-Queisser limit detailed above represents an idealised case, with negligible impact from non-radiative recombination processes. These act as additional pathways which reduce the charge carrier density and thus the efficiency of a real working cell, and are illustrated in Fig. 1.5. The first of these is Trap-assisted recombination, also known as Shockley-Read-Hall recombination. Here, material defects or impurities lead to the presence of energy levels within the bandgap of the material. These offer a competing pathway for a free charge carrier to enter into, 'trapping' them within the absorber layer before they can be extracted. This attracts the corresponding charge carrier to also fall into the trap and recombine, either radiatively or non-radiatively.[24] This process is the primary recombination pathway for materials which have high populations of free electrons and holes, such as perovskites, as only one charge carrier is required to initiate it.[25] Furthermore, perovskites suffer from relatively easy trap formation via the presence of dangling bonds and crystal defects, which occur largely on the boundaries of perovskite grains.[26,27]

Another key recombination pathway present within solar cells occurs at the interfaces between two different layers. As illustrated in Fig. 1.5 (b), if charge carriers are not effectively injected from the perovskite into the CTMs, they can accumulate and recombine due to the Coulombic attraction between them.[18] This can greatly reduce the PCE of a material, as any interface present within the device can act as a potential recombination site. Minimising this recombination pathway requires a careful matching of the respective energy levels of the absorber, the CTMs, and any additional layers incorporated into the device, although recent reports have highlighted that the mobile ions within perovskites can screen and minimise the impact of poor energetic alignment.[28]

The final non-radiative recombination mechanism is Auger recombination, which is not localised at specific sites such as defects or interfaces. It is a three-body analogue to radiative recombination, where a hole and electron recombine. Instead of the excess energy being released as light, a third charge carrier is instead vibrationally excited.[29] Fig. 1.5 (c) illustrates this process. Whilst it is an ‘unavoidable’ physical process like radiative recombination, Auger recombination requires a high density of charge carriers. Thus, it is more prevalent when the solar cell is under intense illumination, and in materials where charges are not effectively extracted from the absorber layer.[25] As such, it has a relatively low impact on the efficiency of perovskite solar cells.

Finally, issues originating from the architecture of the solar cell as a whole can lead to additional losses. Here, each layer and interface within a solar cell circuit has an associated resistance value. The combined total of these resistances is known as the series resistance. In a poorly-matched system, a high series resistance leads to voltage losses outside of the solar cell absorber, reducing the gradient of the J-V curve around V_{OC}, and thus reducing the FF.[30] Shunt resistance losses occur when an alternative, low-resistance pathway is present within the cell. Usually, this is caused by poor coverage of the absorber layer, which allows a direct contact between the rest of the device. This leads to a leakage current which becomes more prominent at low voltage values, and which can also significantly reduce the fill factor of the solar cell.[30]

Limiting the impact of these recombination pathways and finding new ways to maximise solar cell performance is one of the constant targets of solar cell research. Whilst efficiency values as high as the 33.16% Shockley-Queisser limit are not attainable for real-world devices, the ‘gap’ to record breaking laboratory cells is continually growing smaller. Within the field of emerging solar cell technologies, perovskites have seen the fastest and largest rise in efficiency, which is largely due to their unique chemistry and structure, and the compositional flexibility this affords.

1.3 Metal Halide Perovskites

Perovskites are an exciting alternative to existing solar cell absorbers, overtaking all other third-generation competitors in terms of performance to directly compete with silicon cells.[31] They are an extremely broad class of compounds, comprised of ionic crystals with an ABX_3 stoichiometry of AB cations and X anions. In the context of photovoltaic technologies, however, this term is commonly used as a shorthand for metal halide perovskites specifically. Here, a divalent metal cation is surrounded by an octahedron of six halide anions, forming a lattice of 'BX_6' octahedra. The voids present in this structure are filled by an organic or inorganic 'A' cation such as Methylammonium (MA) or Cs completing the perovskite formula. This general structure is illustrated in Fig. 1.6 (a), and is referred to as a '3D' perovskite throughout the rest of this work. Due to their ionic nature, perovskites have a very high degree of chemical tunability, with the only real limitation on what species can form well-ordered structures imposed by the ratios of their ionic radii.[32,33] Small deviations from the 'optimal' value are accounted for by changes in the angles and shapes of the octahedra, without a loss of the overall structure. Perovskites templated by a wide range of metals such as tin, germanium, antimony or bismuth have been reported, but such compounds suffer from poor stability due to the ease of oxidation to B^{4+} states,[34,35] or the preferential formation of hexagonal perovskite-like structures which are intrinsically less conductive.[36,37] By far the most popular and successful class of perovskites are those based on lead as the central B cation. The stability of the Pb^{2+} state and the strong interactions with iodide and bromide ions make them a particularly well-suited framework for a wide range of applications.[38,39]

The popularity and widespread applicability of perovskites arises from how their chemical composition affects their properties. Metal-halide perovskites are intrinsic semiconductors, where the interactions between the metal s and p and halide p orbitals lead to the formation of a bandgap.[40,41] Here, the energetic separation between the occupied valence and empty conduction bands of the perovskite is directly related to the choice of metal and halide species, which gives it a unique degree of tunability. By changing the composition from $MAPbCl_3$ to $MASnI_3$, for example, the bandgap can be tweaked from 2.9 eV to 1.21 eV.[42,43] The A-site cation offers an additional degree of freedom, due to its secondary influence on the precise structure of the octahedra.[44] The size of the A-site cation and its interactions with the X halides drive the symmetry of the perovskite lattice and thus the orbital overlap that determines the material bandgap.[45] Typically, this results in the formation of direct or weakly-indirect bandgap semiconductors where the C.B. minimum and V.B. maximum are aligned, which is optimal for absorbing light without requiring interactions with phonons.[16,46] This means metal halide perovskites are highly suitable for photovoltaic applications, as straightforward compositional engineering approaches can be utilised to maximise their light absorption or tune their colour emission.[47,48] Fig. 1.6 (b) shows the structure of the widely-researched methylammonium lead iodide perovskite, which was the first to be successfully employed in solar cells.[49,50] In the years that have followed, perovskite compositions have been continually optimised, with mixed organic-inorganic approaches based around the incorporation of both Formamidinium (FA) and Cs A cations reaching efficiencies of over 26% for an individual solar cell.[15,51,52] Additionally, the compositional flexi-

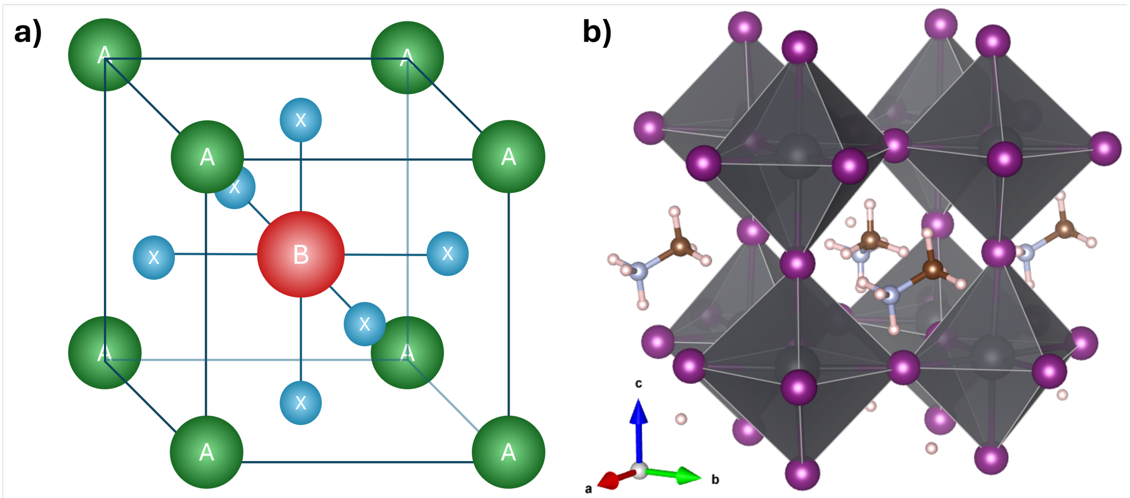

Figure 1.6: a) Schematic illustration of the ABX_3 perovskite structure, containing a single unit cell. b) Structure of Methylammonium Lead Iodide, obtained from Ref. [54]. Pb atoms are grey, I atoms are purple, C atoms are brown, N atoms are light blue and H atoms are white. Grey octahedra indicate PbI_6 units.

bility of perovskites allows them to be employed in synergy with existing materials such as silicon in tandem cells, improving their utility even further. This approach exploits wider bandgap Br-rich perovskites like $FA_{0.8}MA_{0.15}Cs_{0.05}Pb(I_{0.76}Br_{0.24})_3$ to create multi-absorber solar cells which are far more efficient than a single-layered equivalent.[53]

The above compositions all exist within the limitations imposed by matching ionic radii to form the perovskite lattice, but a key benefit of the ionic perovskite structure is the ability to form related classes of compounds which expand the obtainable material properties, and thus their potential applications. Here, the size tolerance factors that guide A cation selection apply only when considering the formation of the standard ABX_3 networks of perovskite octahedra. Increasing the size of the A cation so that it no longer fits in the voids present within the lattice can be exploited to create a whole range of perovskite-adjacent structures, known as Layered Perovskites (LPKs) and perovskitoids.

1.4 Layered Perovskites

LPKs are by far the most popular subset of the extended perovskite family, as they minimise many of limitations faced by traditional perovskite structures, such as poor ambient stability.[55] Here, the name refers to the change in the ordering of the perovskite octahedra. The typical A cations are replaced with much longer and bulkier organic counterparts, referred to as A' cations. Whilst their chemical structure can vary, the organic A' cations still contain a moiety which can interact with the perovskite lattice, typically via an ammonium end group. They sandwich a metal halide BX_6 octahedra from two sides in the C direction, stabilising a single quasi-two-dimensional sheet which extends in the *ab* plane. These then assemble into the characteristic layered perovskite structure, composed of alternating sheets of organic A' cations and BX_6 octahedra. The use of these materials as semiconducting channels in thin-film transistors predates the use of 3D perovskites in solar cells by over a decade.[56] Since that time, they have seen a surge in popularity, with a recent review by Li et. al. identifying no less than 88 large organic A' cations reported to template LPK films.[55]

LPKs are traditionally split into two sub-groups, know as Ruddlesden-Popper (RP) and Dion-Jacobson (DJ) phases. These refer to the details of how many A' cations split the perovskite octahedra, and consequently how this impacts the arrangement of the layers within the material. RP layers are templated by monoammonium A' cations, with a purely A' cation and metal halide BX structure having an A'_2BX_4 formula, as illustrated in Fig. 1.7 (a). This arrangement makes subsequent sheets display a lateral offset of half an octahedral unit.[57] The most commonly utilised RP-type A' cations are based on simple straight-chain aliphatic molecules, or ones containing an aromatic unit. Here, the intermolecular interactions between the organic A' molecules are what bind the structure together and control the ordering of the A' cations themselves. Linear A' cations form interdigitated arrangements held together by Van der Waals forces, whilst cations with aromatic rings often form more ordered π-π stacked structures. This means that generally, individual sheets of perovskite are only weakly held together.

The widened scope for chemical modification afforded by the relaxed limitation of the size of the A' cation means the strength of the intermolecular interactions both within and between the A' cation layers can be controlled to a great degree. Most commonly, this is achieved by additional hydrogen-bonding functionality via heteroatom substitution.[58–60] This also changes the balance of interactions between A' cation sheets and BX_6 perovskite octahedra, drawing the organic components closer together and reducing the distortions they induce throughout the perovskite backbone. Approaches based around A' cations which contain alkene or alkyne moieties have also been demonstrated. This allows cross-linking of the structure within and between the organic sheets, which can greatly increase the stability of the resulting material,[61] or incorporate a conductive organic polymer directly into the perovskite.[62]

The second class of LPKs, referred to as DJ structures (Fig. 1.7 (b)) are formed from double-ended di-cation A' molecules, with an $A'BX_4$ formula when only large

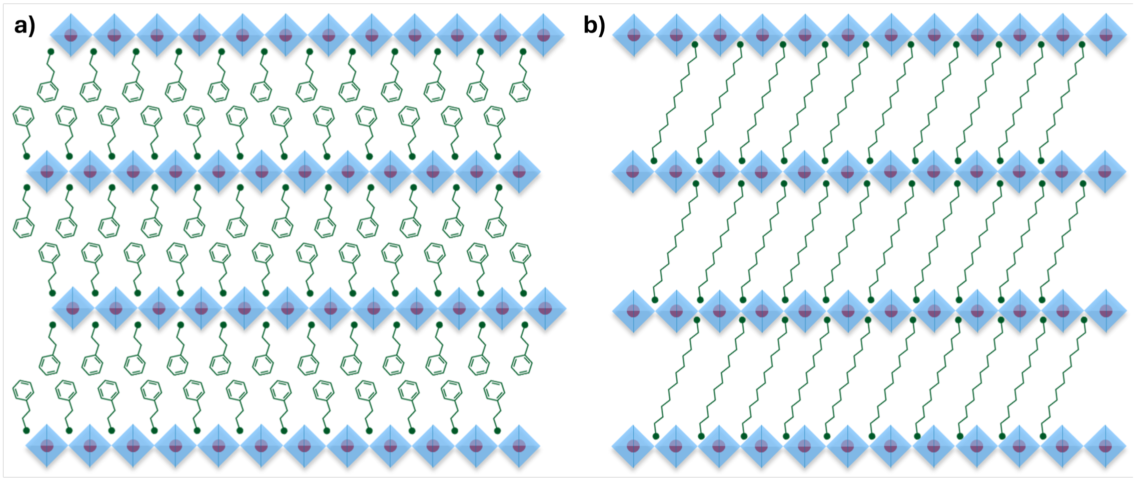

Figure 1.7: Schematic illustration of typical layered perovskite structures. a) A'$_2$BX$_4$ RP phase templated by monoammonium A' cations. b) A'BX$_4$ DJ phase templated by diammonium A' cations. B cations are represented by red circles, small organic / inorganic A cations are represented by large green circles, large organic A' cations are represented by the green aromatic or linear organic molecules, and the octahedral cage of six X halides is represented by the blue diamonds.

A' cations are utilised.[63,64] By joining the sheets with a single A' cation, the half-unit cell offset present within RP layers is eliminated, leading to a crystal structure which is far more similar to the typical 3D perovskite. They are generally less studied than the RP structures, due to the stricter structural limitations imposed by the need for two linked amine groups within the same compound. First described by Mao et.al. in 2018, DJ-type metal halide perovskite phases are reported to have many potential benefits over the RP structure, largely associated with the much stronger ionic interactions which now hold the lattice together.[64]

Both RP and DJ perovskite phases have far more relaxed A' cation size limitations when compared to the 3D perovskite structures, with the chief limitation being defined by the A' cation cross-sectional area.[65] Very thin and long A' cations have been successfully employed to template LPK structures, as demonstrated by Billing et al. Here, linear aliphatic chains of up to 18 carbons long were used, creating a perovskite with an Pb-Pb layer spacing of 32.2 Å, far longer than the 6.3 Å size of a typical PbI$_6$ octahedron.[54,66] Long chains of conjugated aromatic rings have also been used in both RP and DJ structures. For A' cations with a wider cross-sectional area, sufficient spacial separation between the 'body' and the ammonium 'head' is crucial for the formation of an ordered LPK. Large aromatic A' cations based around polycyclic pyrene and perylene rings have been successfully employed, largely due to the inclusion of long ethyl- or propyl-ether linkers. Similarly, rigid conjugated chains of thiophenes have all successfully been utilised to form RP and DJ structures thanks to the presence of an ethyl chain linking the ammonium.[67–69] This flexibility allows the A' cations to both interact with the perovskite lattice and pack in an optimised manner.

In contrast, comparably much smaller cycloheptyl or cyclooctyl structures which lack a connecting group are too bulky to be incorporated into a LPK structure, instead forming perovskitoids.[70] These are an even broader family of perovskite-related structures. Whilst they still contain octahedral units, the corner-sharing structure is lost. Edge- and face-sharing structures form instead, as the perovskite lattice 'collapses' into densely packed layers or 1D rods.[71] This creates larger spaces in between the octahedral elements for wider or less flexible A' cations to pack into. These structures can also form with the use of more typical A-type cations which are too large to template a 3D perovskite. Despite there being a far larger number of possible perovskitoid structures, they have generally less favourable optoelectronic properties, and as such they have seen far less implementation than their 'true' perovskite counterparts.

1.4.1 Properties of Layered Perovskites

The main consequence of the unique structure of LPKs is how their overall material properties are affected, and how they differ from the typical 3D perovskite case. Due to the splitting of the continuous 3D lattice into isolated sheets, LPKs have a very clearly defined orientation. Moving along the c axis of the lattice, the structure alternates between organic A' cation and inorganic perovskite. In contrast, in the ab plane, the continuous octahedral network has far more similarity to a traditional ABX_3 structure.

This structural anisotropy is most fundamentally manifested in how LPKs form and crystallise on substrates. They have an extremely strong preference to lie 'flat', with the ab plane of the layered perovskite oriented parallel to any underlying substrate.[72,73] This occurs in both highly-ordered single crystals and in thin polycrystalline films, and thus it is the out-of-plane properties measured along the c axis of LPK structures that are most relevant for any optoelectronic applications. Furthermore, the 'sandwich' structure of LPKs leads to very fast crystallisation, which allows the spontaneous formation of polycrystalline films without the need for antisolvent treatment or annealing steps as in traditional 3D perovskites.[74] Here, the presence of the bulky organic A' cations creates larger and more ordered intermediate structures in the solvent phase, which can directly assemble into crystalline perovskite.[75] This behaviour is not so pronounced in DJ perovskites, as the need for the A' cations to assemble in-between the perovskite sheets makes crystal formation more difficult. In general, this leads to structures with a higher degree of disorder, and means that DJ perovskites more commonly display a mixture of parallel and perpendicular orientations.[76,77]

The electronic structure of LPKs differs significantly from that of their 3D counterparts. The metal-halide interactions defining the band structure become discontinuous in one dimension due to the introduction of the organic A' cation component. This reduction in interaction widens the bandgap of the perovskite lattice to values above 2 eV for lead iodide-based structures, which makes them far less suitable for light absorption.[78,79] Furthermore, the A' cations usually have much larger energetic separations between their Highest Occupied Molecular Orbital (HOMO) and Lowest Unoccupied Molecular Orbital (LUMO) levels when compared to the perovskite valence and conduction bands.[79] This creates a quantum-well-like energetic structure within LPKs, which is illustrated in Fig. 1.8.

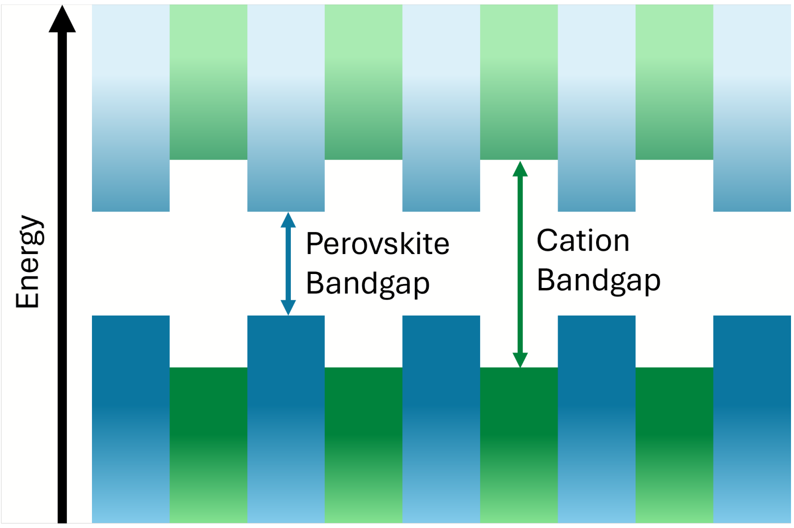

Figure 1.8: Illustration of the multiple quantum-well band structure of 2D perovskites. Figure adapted from Ref [80].

It is this unique electronic landscape that dominates the optoelectronic properties of layered perovskites. Excitons that are formed within the material are highly confined, with exciton binding energies in LPKs increasing to 230 meV from the 16 meV value determined for a typical methylammonium lead iodide (MAPI) perovskite.[81,82] The binding energy value describes the attraction within the exciton electron-hole pair that needs to be overcome to separate it into free electrons and holes, which is crucial for extracting charge carriers from the material. This high binding energy is due to both the quantum confinement of charges, which occurs due to the small size of the octahedral layer in one dimension, and the dielectric mismatch between the organic and perovskite components. Here, both holes and electrons face an energetic barrier of around 2 eV when moving from the perovskite to the organic layer, trapping them within the 'wells' of the flat BX_6 network.[83] In tandem, the alternating high dielectric perovskite and the low dielectric organic sheets do not screen electrostatic interactions effectively. Here, the electrical field of the charge carriers formed within the perovskite permeates through the organic layer, leading to a strong Coulombic attraction to one another.[79]. The spatial quantum confinement helps to maintain this attraction, increasing the likelihood that electrons and holes remain tightly bound as excitons instead of separating. Thus, any photogenerated excitons face a high likelihood of recombination before they can be successfully extracted, which further limits the suitability of LPKs as light absorbers.[84] Furthermore, this electronic structure forces charge transport through the layers to occur via a highly inefficient tunnelling mechanism.[85] This can be seen by very low carrier mobility values when compared to bulk 3D perovskite. Milot et.al reported a reduction in combined electron and hole mobility from 25 $cm^2\ V^{-1}\ s^{-1}$ for $MAPbI_3$ to 1 $cm^2\ V^{-1}\ s^{-1}$ for PEA_2PbI_4.

It is important to note that the quantum-well structure only limits the movement of charge between the separated sheets of perovskite. In-plane transport is much more efficient, as there are no energy barriers to overcome, much like in a typical 3D structure. This leads to a very high degree of anisotropy when measuring mobilities across the two different orientations of LPK structure, with values spanning up to three orders of magnitude.[86–88] As such, the potential applications of LPK structures can be widened by developing LPKs which show vertical orientation, with the *ab* plane perpendicular to the substrate, or materials which have a reduced degree of quantum confinement due to reduced mismatch between the energy levels of the organic A' and BX_6 sections.

1.4.2 Implementation of Layered Perovskites

The compositional flexibility of perovskite structures means that many of the drawbacks associated with LPKs which limit their potential applications can be mitigated by creating 'hybrid' LPK analogues. Indeed, the unique mix of LPK properties as detailed above is only strictly applicable to films of 'pure' LPK material which only contain bulky A' cations. Structures which maximise their benefits whilst minimising their limitations can be formed by creating LPKs with more '3D character', known as high-n perovskites, or by depositing small quantities of LPK on existing perovskite structures to form perovskite-LPK heterojunctions.

In the context of LPKs, the n-value refers to the number of BX_6 octahedra sheets present in-between the organic A' cation layer. Pure A'_2BX_4 LPKs have an n-value of 1. By introducing small A cations which can template a traditional 3D perovskite, an intermediate structure can be formed. For RP phase LPKs, these structures have a general formula of $A'_2A_{n-1}B_nX_{3n+1}$, where A' is the large organic cation, and A is a smaller organic or inorganic cation that can template a 3D perovskite. For DJ phase perovskites, the formula is instead $A'A_{n-1}B_nX_{3n+1}$. Fig. 1.9 shows examples of an $n = 2$ and an $n = 5$ RP phase LPK. As the n-value increases, the individual layers increase in size along the c axis, and the structure increasingly resembles an ABX_3 perovskite, which can be considered as an $n = \infty$ LPK analogue. The most widely reported mixed-n structures have n-values between 3 and 5, as reducing the ratio of large to small cations any further commonly results in a phase separation of the mixture into a 3D and low-n phase.[55]

Changing the LPK structure to have more '3D character' influences the material properties accordingly. The exciton binding energies of high-n materials are reduced,[89] their bandgaps are narrower,[64,83] and they see higher mobilities with a reduced anisotropy.[21,90] Indeed, the bandgap can be directly controlled by changing the n-value of the material.[91] They also have a weaker tendency to orient with the *ab* plane parallel to the substrate. High-n LPKs with *ab* planes perpendicular to the substrate have been reported via solvent engineering and slow crystallisation, which means the sheets of large A' organic cations no longer act as a barrier to charge transport across the LPK.[77,92] Thanks to these properties, high-n LPKs are far more suitable for use in optoelectronic devices. The chief limitation faced by high-n perovskites is the difficulty of forming well-ordered structures with a single n-value. Here, the fast crystallisation and intrinsic stability of both $n = 1$ and 3D perovskites means a phase separation into a 'graded' perovskite which has a highly varied n-number and dimensionality is a common occurrence.[93] This leads to disordered structures which lose any targeted bandgap values and energetic alignments.[94]

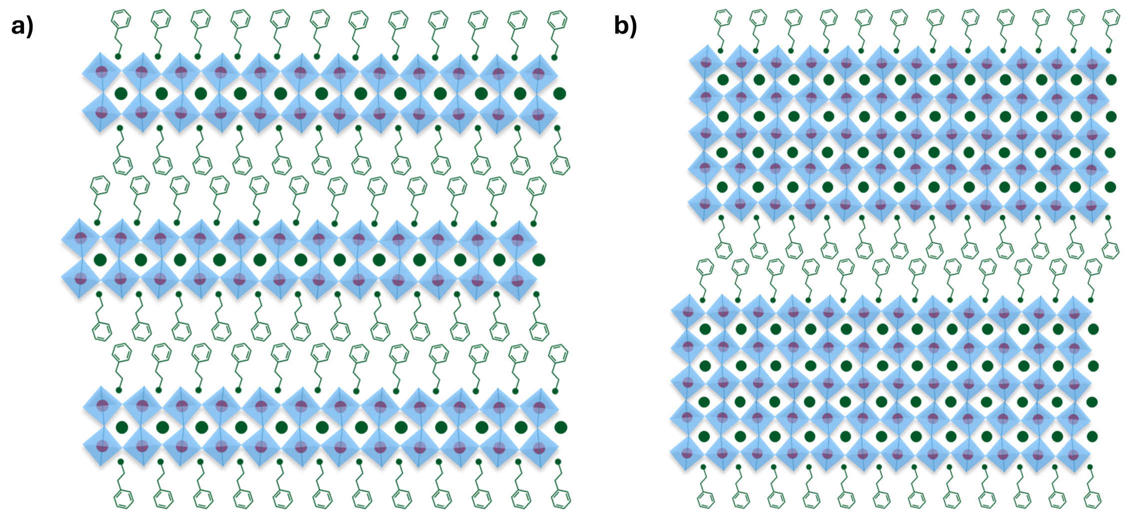

Figure 1.9: High-n LPKs. a) An $n = 2$ RP phase LPK, with the formula $A'_2AB_2X_7$. b) An $n = 5$ RP phase LPK, with the formula $A'_2A_4B_5X_{16}$. B cations are represented by red circles, small organic / inorganic A cations are represented by large green circles, large organic A' cations are represented by the green aromatic organic molecules, and the octahedral cage of six X halides is represented by the blue diamonds.

An alternative approach to utilise LPKs within optoelectronic devices relies on the formation of a perovskite-LPK heterojunction. Here, instead of forming a polycrystalline film of pure layered material, a 3D perovskite is used as a substrate to form a very thin LPK 'capping layer'. This templated approach has the benefit of forming uniform LPK layers as thin as 4 nm, which is far lower than what can be achieved via direct spincoating approaches.[95] Crucially, this occurs only on the surface of the sample. Localising the LPK on the top perovskite interface allows the fine-tuning of the energy level alignment between the perovskite C.B. and the HTM for more efficient charge extraction at their interface, whilst also minimising the issues associated with poor charge transport through the LPK due to its low thickness.[96,97]

This perovskite-LPK heterojunction can be formed by intercalating the large A' cations into an existing perovskite lattice.[95] Most commonly, this is achieved by dissolving the organic A' cations without any metal halide components in solvents such as Isopropyl Alcohol (IPA), and spincoating it on a 3D perovskite. This creates the necessary concentration gradient to drive the bulky A' cations into the perovskite lattice, which split the 3D grains until the top surface is converted into conformal LPK sheets. Both high and low n LPKs can be formed via this approach, by tweaking the contents of the casting solution and the underlying 3D perovskite. The formation of phase-pure $n = 1$ layers can be promoted by adding excess PbI_2 into the 3D perovskite.[98] Here, the PbI_2 forms distinct grains on the surface of the perovskite which are then dissolved during the LPK solution deposition and balance the stoichiometry of the newly-formed layer.[99] Alternatively, the formation of high-n LPKs can be promoted instead by adding smaller A-site cations into the bulky cation solution, without excess PbI_2 in the 3D perovskite.[96] Most of the reported perovskite-LPK heterojunctions utilise RP-type structures. Reports of the use of DJ cations are more limited, as they typically have poor solubility in IPA.[100]

Whilst the variety of perovskites and related compounds that can be formed is extremely broad, it is the implementation of these structures into optoelectronic devices that has made perovskites such a popular field of study. Much of the research behind perovskites and LPKs has been focused on the improvement of their performance as light absorbing materials within solar cells.

1.5 Perovskites in Solar Cells

The popularity of perovskites as a solar cell material cannot be only ascribed to their compositional flexibility. It is the ease of modifying the chemistry of perovskites that has helped drive their fast development and continually-improving performance. Fabrication of silicon, which is the most widely used solar cell absorber layer, requires temperatures of over 1100 °C and very pure precursors, whilst highly efficient copper indium gallium selenide cells need to be deposited by a high-temperature evaporation process.[8,101] In contrast, the ionic nature of the perovskite system means both the starting materials and the formed perovskite compounds are readily soluble in polar solvents. Starting from commercially available powder precursors, simple solution mixing is all that is required to prepare suitable perovskite inks. This means devices can be fabricated using spincoating techniques at the laboratory scale, with a typical approach illustrated in Fig. 1.10. After an initial deposition step, the thickness of the perovskite is controlled by the spin speed of the sample, and an antisolvent drip consisting of an apolar solvent in which perovskites are insoluble initialises the crystallisation process at room temperature. Finally, residual solvents are removed by annealing the sample to obtain the final crystalline solar cell absorber at comparatively low temperatures, ranging from 100 to 150 °C. This makes perovskite fabrication suitable for upscaling and full industrial adoption. Roll-to-roll printing techniques have now been successfully employed to quickly manufacture large-scale modules, indicating that perovskites are well on their way into transitioning to a commercial product.[102,103]

Thanks to this low ‘barrier of entry’, the perovskite formation process affords another opportunity for improving the performance of the material within a solar cell. Here, factors such as the solvent system, the time taken before the antisolvent step, and the antisolvent used all dictate the morphology and uniformity of the resulting film. The use of highly-coordinating solvents such as Dimethyl sulfoxide (DMSO) has now become widespread to control the crystallisation process, forming smooth and pinhole-free layers.[38,104–106] Here, the solvent acts to coordinate with PbI_6 units in solution, forming clusters which then slowly convert to the perovskite durnig the final annealing step. Indeed, extremely large, single crystal-like grains can be formed with the use of solvents which bind to the perovskite even more strongly.[107] Similarly, additives in the precursor solution containing Cl ions have become popular to form smooth and defect-free films, without being incorporated into the final perovskite.[108,109]

1.5.1 Device Architectures

For the successful operation of a perovskite solar cell, the architecture of the device as a whole must be carefully designed. Here, the perovskite layer carries out the main role of absorbing light and generating electrical current. The selection of materials used to extract the holes and electrons out of the central absorber layer is thus a key consideration during the fabrication process. These must be conductive materials which form a favourable energetic pathway for charge carriers to flow down, as determined by the energy level separations between their valence and conduction bands. This layered ‘sandwich’ structure forces at least one half

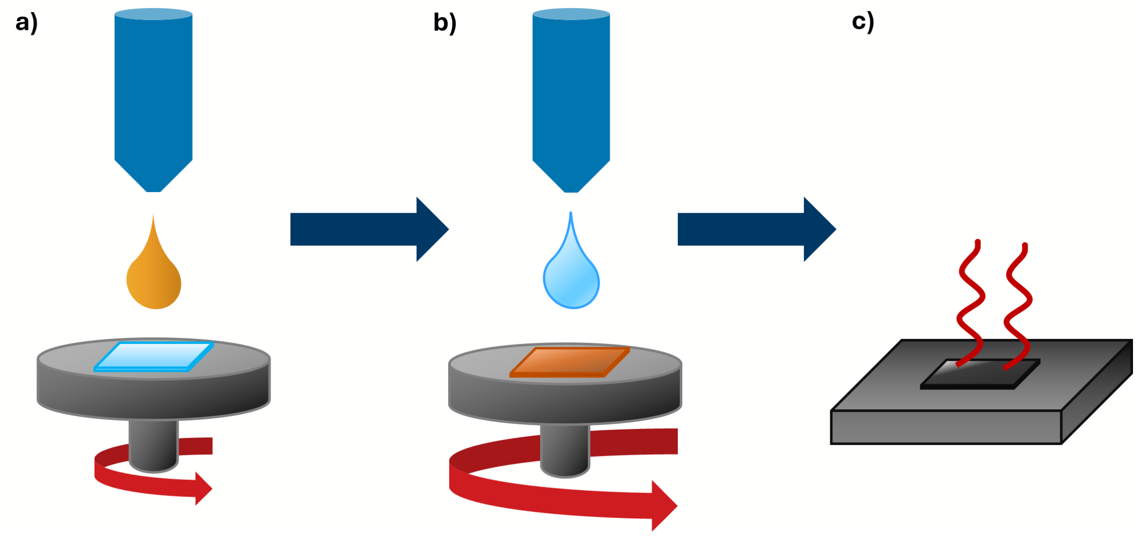

Figure 1.10: Schematic illustration of the formation of perovskite layers via solution processing. a) Deposition of precursor ink. b) Deposition of antisolvent. c) Annealing to obtain crystalline perovskite.

of the cell to be transparent to allow the central perovskite absorber to be illuminated, which places limitations on what materials are suitable. The most widely adopted approach is based around the use of transparent conductive oxides such as Indium Tin Oxide (ITO) or Fluorine-doped Tin Oxide (FTO) deposited on glass substrates. These act as the base of the cell, onto which the subsequent layers are deposited. This divides solar cells in to two categories - ones with a transparent ETM on the bottom surface, known as n-Type – Intrinsic – p-Type (N-I-P), and ones with a transparent HTM on the bottom, known as p-Type – Intrinsic – n-Type (P-I-N) cells. These two structures are illustrated in Fig. 1.11. Different materials are suitable for one of the two architectures, depending largely on the deposition method required to form them. For example, P-I-N cells commonly employ inorganic NiO_x or self-assembling layers of simple organic molecules as HTMs which can be deposited directly on the ITO substrate. In contrast, N-I-P cells rely on synthetically complex HTM molecules such as 2,2',7,7'-tetrakis [N,N-di(4-methoxyphenyl) amino]-9,9'-spirobifluorene (Spiro-OMeTAD), which require additional dopants to increase their conductivity.[110] The contrast in the top contact ETM materials is equally pronounced, with P-I-N cells using small organic molecules such as C_{60}, [6,6]-Phenyl C_{61} butyric acid methyl ester (PCBM) or Bathocuproine (BCP) which can be deposited from solution or directly evaporated, whilst N-I-P cells typically use SnO_x or TiO_2 metal oxides formed via chemical bath techniques or high-temperature deposition.[111–114] Balancing the costs, suitability and stability of the various non-perovskite components is of equal importance to optimising the perovskite absorber for solar cell development.

1.5.2 State-of-the-Art Devices

Due to the incredible variety of materials and deposition approaches that can be used, there is no true ‘best’ perovskite composition to obtain the most efficient device. Nonetheless, the state-of-the-art has moved away from the initially incredibly

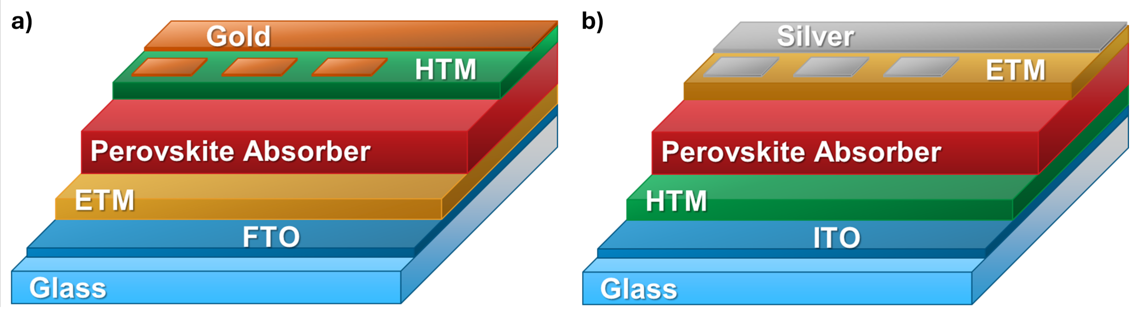

Figure 1.11: Schematic illustration of the arrangements of layers that make up perovskite solar cells. Note that the layer thicknesses are not representative of actual or relative thickness values. a) Example of an N-I-P cell architecture. b) Example of an P-I-N cell architecture.

successful MAPI perovskite, instead focusing on recipes based around FA molecules. Pure $FAPbI_3$ perovskite has a bandgap of 1.48 eV, which is much closer to the ‘ideal’ value of 1.34 eV predicted by the Shockley-Queisser when compared to the 1.55 eV of $MAPbI_3$.[115] This means $FAPbI_3$ absorbers boast a naturally higher efficiency. The FA molecule is too large to fit within the voids of the PbI_6 lattice, however, and the structure is thermodynamically unstable at room temperature. Without careful control, $FAPbI_3$ degrades to a photo-inactive perovskitoid δ phase. Due to this, most recipies for high-efficiency devices utilise a mixed-cation formulation to stabilise a predominantly FA perovskite. Here, smaller cations such as MA or Cs are used to reduce the internal strain within the perovskite lattice, resulting in so-called ‘Double Cation’ and ‘Triple Cation’ compositions.[116,117] The precise ratio of cations, and the presence of any bromide ions, needs to be carefully balanced to match the bandgap of the absorber with the energy levels of the CTMs. Most commonly, the additive cations are present in quantities of 2-5%, with some Triple Cation compositions favouring 10% of the MA component. To maximise performance, the crystal size and morphology also needs to be carefully controlled, and it is this process of tweaking and optimising the overall recipe that has been the focus of much of perovskite solar cell research. Overall, whilst N-I-P cells have historically seen better performance, both approaches have now successfully been employed to form cells utilising multi-cation FA-based absorber layers with efficiencies above 26%.[15,52]

1.6 The Perovskite Stability Challenge

Whilst the ionic structure of perovskites leads to many of their desirable properties that make them such excellent materials for solar cells, it also leads to issues with their stability. The lack of covalent bonding means the component ions of the perovskite lattice are free to move around, which means that perovskites with mixed compositions can phase-segregate when they absorb light.[118] Here, the formation of excited charge carriers favours the creation of domains with narrower bandgaps. This process is also driven by strain present within the films. This can be caused by the mismatch between thermal expansion coefficients of the perovskite and substrate, incompatible ionic radii or external bias.[119,120] This reduces the activation energy barrier for ions to migrate through the film to rearrange into less-strained structural analogues. In the case of highly efficient formamidinium lead iodide perovskites, for example, this leads to the formation of photo-inactive perovskitoids.[121]

Furthermore, metal halide perovskites are soluble in water. This makes them highly susceptible to degradation when exposed to humid conditions. They readily adsorb water molecules, which travel along individual crystal grains and penetrate deep into the perovskite structure.[122,123] This process is very fast, occurring within seconds of exposure.[124] Studies into the prototypical MAPI structure have found it can absorb as much as 10 vol % of water after being exposed to atmospheres with only 41% relative humidity.[125] Whilst the initial water absorption is reversible, continued exposure to moisture leads to the formation of mono- and di-hydrated perovskite analogues, with the ultimate loss of the perovskite structure. The small organic A cations are deprotonated, which allows the halide anion to reform into HI.[126] These components are more volatile and escape the film, leaving behind PbI_2 as a final degradation product.[127] This degradation process is illustrated in Fig. 1.12 (a).

Alongside water-mediated degradation, perovskites react with oxygen when illuminated, forming O_2^- superoxide species.[128] This superoxide can also deprotonate the organic cations, breaking apart the lattice into its constituent components. Once again, the polycrystalline structure of perovskites means oxygen can infiltrate deep into the film and steadily degrade the bulk structure. This process is mediated by the presence of iodide defect sites within the lattice, which catalyse the superoxide formation. Exposure to both light, humidity and oxygen in tandem leads to an even faster degradation, as water molecules act to stabilise the superoxide and catalyse its reaction with the A cations.[129]

Whilst these degradation mechanisms are quite a fundamental property of metal halide perovskites, there are methods to improve their stability. When perovskites are used within solar cells, many of the issues are mitigated with the use of glass or polymer encapsulation, which limits environmental exposure and can lead to negligible efficiency losses after of over 2000 hours of operation.[130] Naturally, external encapsulation does not prevent any degradation that may occur during the fabrication process itself, or degradation pathways which do not require interaction with outside environmental stressors. As such, the development of more intrinsically stable perovskites is of high importance to maximise their potential applicability. Solvent engineering approaches to form larger grains can slow the ingress of reac-

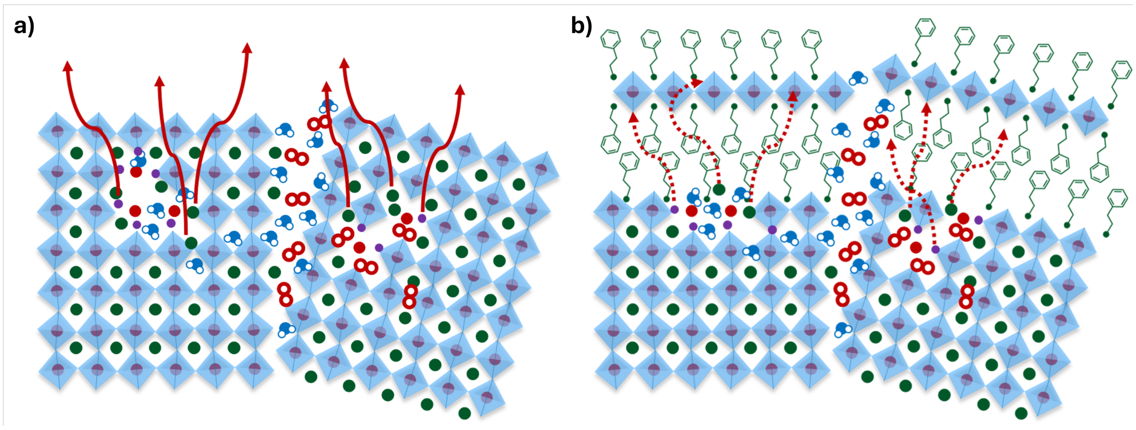

Figure 1.12: a) Characteristic perovskite degradation via the incorporation of moisture and / or oxygen into the lattice, and the resulting loss of volatile A cation and halide components. b) Stabilisation of the perovskite with LPK layers by preventing the escape of the degradation products out of the film. B cations are represented by red circles, small organic / inorganic A cations are represented by large green circles, large organic A' cations are represented by the green aromatic organic molecules, and the octahedral cage of six X halides is represented by the blue diamonds. Free halides are represented by small purple circles, oxygen molecules are represented by a pair of red rings, and water molecules are represented by the blue circles with two blue rings.

tive species,[131] and mixing different A-site cations can help reduce the internal film strain and slow the degradation reactions.[132] One of the most popular approaches for forming more intrinsically stable perovskite structures, however, relies on the use of LPK capping layers.

1.6.1 Layered Perovskites for Stable Devices

When compared to typical 3D perovskites, both RP and DJ layered perovskites have far better stability in ambient conditions, which is a key factor behind their increasing popularity as a component of perovskite solar cells. Inclusion of the larger A' cation sheets leads to reduced water uptake into the film and higher longevity under illumination.[133,134] Here, the layered structure greatly hinders ionic motion through the lattice by interrupting the hopping pathway of ions across vacancy sites between octahedra due to the presence of the A' cation sheets, which greatly slows the perovskite degradation processes.[135–137] This process is illustrated in Fig. Ionic migration and resulting changes to the layered perovskite structure do occur to some extent, however, and higher-n single crystals have been reported to rearrange into $n = 1$ perovskite layers after prolonged exposure to moisture.[138]

When employed within devices, pure $n = 1$ LPK semiconducting layers see very good longevity, but suffer from negligible performance.[72,139] Most of the focus on LPK-based devices has thus shifted to the use of high-n structures.[140] These have been employed with greater success, reaching efficiencies comparable to typical 3D perovskite compositions.[77,141,142] This approach does face some key limitations, however. The increase in '3D character' and resulting higher efficiency occurs in tandem with a reduction of their stability.[143] The layered phases must also be carefully grown to ensure vertical orientation of the perovskite *ab* plane relative to the device substrate. Horizontally oriented LPK sheets lead to significant performance limitations due to the need for charges to cross the layers of organic A' cations.[92] Finally, ensuring phase-pure tailored n-number films is difficult, and regions with varying lower n-values act as shallow traps within the material, leading to increased recombination.[93]

The most popular approach is to instead use perovskite-LPK heterojunctions, which combine the optimised performance of well-tuned 3D perovskites with the superior stability of the LPK layer.[96,98] Here, the LPK is able to increase device longevity and efficiency via multiple mechanisms. Whilst the thin sheets of LPK do not prevent water uptake into the film, the loss of mobile ions is hindered as for pure layered systems, preventing the irreversible moisture-induced degradation pathway.[127] This process is shown in Fig. 1.12 (b). The direct formation of the LPK on top of the 3D absorber layer also helps to passivate surface trap states. This has the dual effect of limiting their role in catalysing degradation, and reducing the losses associated with monomolecular recombination.[144–146] They also create a greater physical separation between the absorber and any CTM layers, reducing the likelihood of interfacial recombination.[147] Thanks to these widespread benefits, the use of LPK passivation has become a standard procedure for the formation of the best performing solar cells. Crucially, they see successes in both P-I-N and N-I-P cells, conferring their benefits with a large degree of tolerance to the make-up of the solar cell used.[15,148,149]

1.7 Thesis Outline - Studying Layered Perovskite Properties

Layered perovskites are well on their way to becoming an integral component of perovskite solar cells, and thus are becoming an increasingly important class of materials for research in the perovskite field. Their wide scope for improving the stability and performance of devices makes them one of the best and most flexible candidates for tackling some of the most fundamental challenges perovskite face for more widespread adoption. This motivates further developments of LPK-based approaches to maximise their potential, which will be driven by deepening our understanding of their fundamental properties and behaviours.

Chapter 3 of this thesis tackles the question of how the chemistry of the large organic A' cation influences the structure of the LPK as a whole, and how these structural changes manifest in the optoelectronic properties of the material. Contrary to expectations, even minor changes to A' cation chemistry such as extending the cation's length by a single carbon atom can have pronounced impact on the packing of the organic layer, and the distortions of the perovskite backbone. Attempts to link these structural changes to optoelectronic properties find that many of the commonly described relations between perovskite structure, bandgap and conductivity are only weakly applicable, and often do not hold across a set of aromatic and aliphatic A' cations. This complicates efforts to engineer A' cations which can template perovskites with specific bandgaps or charge transport properties. A mixed A' cation approach is proposed as a potential alternative. Here, mixing existing, well-studied A' cations leads to structures with spacing and distortion values which show a more complex behaviour than simple averages of the respective unmixed compounds, and which show intermediate bandgaps and improved conductivities.

Chapter 4 of this thesis focuses on the question of LPK stability. Investigations of extremely thin flakes of pure PEA_2PbI_4 perovskite find that they readily degrade under exposure to ambient conditions, but crucially, this process is self-limiting. The build-up of degradation products acts to quickly passivate the surface, which prevents large scale material loss and thus gives thicker layers of material the appearance of being highly stable. Transferring these insights into the very thin LPK layers used within the typical perovskite-LPK structures, it is found that their low thickness severely impacts their stability. Here, both RP and DJ layers deposited on MAPI were exposed to high humidity, intense light, and atmospheres containing typical fabrication solvents. Whilst they can confer some benefits to the stability of the underlying heterojunction, in many cases the LPK passivation is lost, the LPK undergoes a structural rearrangement, or the LPK is unable to limit the degradation process. This highlights the difficulties of exploiting high-n LPKs as passivation, as they readily undergo rearrangement into low-n analogues.

Finally, Chapter 5 explores how the reduced stability of the thin LPK capping layers influences its behaviour during the fabrication of a full solar cell. Here, the deposition of charge transport layers acts to severely disrupt the initially formed perovskite-LPK heterojunction. This occurs in both P-I-N and N-I-P solar cells, via a dual mechanism. Firstly, spincoating of small organic molecules leads to physical damage of the material surface, and a reduction in the crystallinity of the LPK. In the case of N-I-P cells which use HTM solutions with additional polar solvents, the additives act also to dissolve the LPK. Depending on the initial layer thickness, this either strips away the LPK entirely, or leads to the formation of disconnected 'platelets' on the perovskite surface. Crucially, optimal device performance correlates with no crystalline LPK present on the surface. Indeed, the variation in deposition approaches between P-I-N and N-I-P architecture is proposed to be a direct consequence of the different degree of LPK disruption cause by the CTM deposition step. This observation highlights that isolated heterojunctions which do not account for post-processing steps are not representative of the perovskite-LPK system as it appears in a completed solar cell.

Chapter 2

Methods

2.1 A' Cation Iodide Salt Synthesis

All A' cation preparation reactions followed the same general method of an acid-base neutralisation to yield the desired iodide salt. All reagents were used as received without further purification. Hexylammonium (HexA) iodide (>99%), Octylammonium (OctA) iodide (>99%) and 4-Fluoro phenylethylammonium (F-PEA) iodide (>99%) were obtained from Greatcell Solar. ^{1}H Nuclear Magnetic Resonance (NMR) spectra were obtained using a Bruker AVIII 400 MHz spectrometer, and are included in the appendix, section A.1. Acetone (>99%), ethanol (99%), and Ethyl Acetate (EtAc) (>99%) were obtained from VWR. Diethyl Ether (DE) (99%) and IPA (99%) was obtained from SLS. Hydroiodic acid (55%, without stabilisers) was obtained from Fisher Scientific. *Butylammonium (ButA) iodide was synthesised by Michele Cariello. NMR spectra were obtained by Gregor Macleod.*

Phenylmethylammonium (PMA) Iodide

Benzylamine (99%, Sigma-Aldrich) (2.32 mL, 21.27 mmol) was added to a round bottom flask containing 20 mL of ethanol and set to stir. 55% hydroiodic acid (3.2 mL, 23.4 mmol) was added dropwise, and the mixture was left to stir overnight at room temperature. The ethanol and water were removed under vacuum, the solids were collected and washed with DE. The solid was purified by recrystallising three times in hot IPA. The collected crystals were washed with DE after each step. 4.112 g (17.49 mmol) of off-white crystals were collected after drying. ^{1}H NMR (400 MHz, DMSO-d6): 8.11 (s, 3H), 7.47 – 7.36 (m, 5H), 4.05 (s, 2H).

Phenylethylammonium (PEA) Iodide

Phenethylamine (99%, Sigma-Aldrich) (4.94 mL, 40.15 mmol) was added to a round bottom flask containing 40 mL of ethanol and set to stir. 55% hydroiodic acid (6.04 mL, 44.16 mmol) was added dropwise, and the mixture was left to stir overnight at room temperature. The ethanol and water were removed under vacuum, the solids were collected and washed with DE. The solid was purified by recrystallising three times in hot IPA. The collected crystals were washed with DE after each step. 7.492 g (30.1 mmol) of white crystals were collected after drying. ^{1}H NMR (400 MHz, DMSO-d6): 7.76 (s, 3H), 7.36 – 7.23 (m, 5H), 3.07 – 3.03 (m, 2H), 2.86 (dd, J = 9.4, 6.5 Hz, 2H).

2-Thiophenemethylammonium (ThMA) Iodide

2-Thiophenemethylamine (96%, Sigma-Aldrich) (2.2 mL, 21.44 mmol) was added to a round bottom flask containing 27 mL of ethanol and set to stir. 55% hydroiodic acid (3.4 mL, 24.85 mmol) was added dropwise, and the mixture was left to stir overnight at room temperature. The ethanol and water were removed under vacuum, the solids were collected and washed with DE. The solid was purified by recrystallising three times, in hot ethanol, EtAc and hot ethanol. The collected crystals were washed with DE after each step. 3.2779 g (13.6 mmol) of off-white crystals were collected after drying. ^{1}H NMR (400 MHz, DMSO-d6): 8.17 (s, 3H), 7.60 (dd, J = 5.1, 1.3 Hz, 1H), 7.23 (ddt, J = 3.5, 3.4, 0.8 Hz, 1H), 7.09 (dd, J = 5.1, 3.5 Hz, 1H), 4.27 (d, J = 0.8 Hz, 2H).

2-Thiopheneethylammonium (ThEA) Iodide

2-Thiopheneethylamine (96%, Sigma-Aldrich) (2.35 mL, 20.08 mmol) was added to a round bottom flask containing 26 mL of ethanol and set to stir. 55% hydroiodic acid (3.4 mL, 24.85 mmol) was added dropwise, and the mixture was left to stir overnight at room temperature. The ethanol and water were removed under vacuum, the solids were collected and washed with DE. The solid was purified by recrystallising twice in hot ethanol and once in hot IPA. The collected crystals were washed with DE after each step. 4.509 g (17.67 mmol) of white powder was collected after drying. ^{1}H NMR (400 MHz, DMSO-d6): 7.79 (s, 3H) 7.42 – 7.4 (m, 1H), 7.01 – 6.97 (m, 2H), 3.07 (s, 4H).

Pentylammonium (PentA) Iodide

n-Pentylamine (99%, Sigma-Aldrich) (2.7 mL, 23.25 mmol) was added to a round bottom flask containing 25 mL of ethanol and set to stir. 55% hydroiodic acid (3.5 mL, 25.58 mmol) was added dropwise, and the mixture was left to stir overnight at room temperature. The ethanol and water were removed under vacuum, the solids were collected and washed with DE. The solid was purified by dissolving in hot ethanol and precipitating with DE as the antisolvent. The collected crystals were washed with DE after each step. 0.703 g (3.27 mmol) of yellow crystals were collected after drying. ^{1}H NMR (400 MHz, DMSO-d6): 7.60 (s, 3H), 2.77 (t, J= 7.6 Hz, 2H), 1.55 - 1.48 (m, 2H), 1.32 - 1.23 (m, 4H), 0.89 - 0.83 (m, 3H).

1,12-DoDecyldiammonium (DoDecA) Diiodide

1-12 Diaminododecane (98%, Sigma-Aldrich) (2.2 g, 10.9 mmol) was added to a round bottom flask containing 20 mL of ethanol and set to stir until it fully dissolved. 55% hydroiodic acid (3.2 mL, 23.39 mmol) was added dropwise, and the mixture was left to stir overnight at room temperature. The solid product was collected via vacuum filtration and washed with DE. The compound was purified by recrystallising three succesive times in hot EtAc with a small quantity of ethanol. The collected crystals were washed with DE after each step. 4.061 g (8.9 mmol) of off-white crystals were collected after drying. ^{1}H NMR (400 MHz, DMSO-d6): 7.59 (s, 6H), 2.78-2.75 (m, 4H), 1.5 (p, J = 7.3 Hz, 4H), 1.30-1.24 (m, 16 H).

2.2 Solution Preparation

2.2.1 Perovskite Solutions

Preparation of all perovskite solutions used for thin film fabrication and single crystal growth was carried out within a nitrogen-filled glovebox. H_2O and O_2 concentrations were maintained at 1 ppm or below during operation. Tables 2.1 and 2.2 list details of the makeup of solutions used throughout this work. 'Triple Cat' refers to perovskite solutions containing three A cations (FA^+, Cs^+ and MA^+). 'Double Cat' refers to perovskite solutions containing two A cations (FA^+ and Cs^+). After mixing, solutions were dissolved at 70 °C overnight. Before use, all solutions were allowed to cool to room temperature, and were filtered using a 0.45 µm Polytetrafluoroethylene (PTFE) filter. PbI_2 (>99.9%) and FAI (99.99%) were obtained from TCI. CsI (99.999%) and MACl (>99%) were obtained from Sigma-Aldrich. Dimethylformamide (DMF) (99.8% Extra Dry) and DMSO (99.7+% Extra Dry) were obtained from Fisher Scientific. *Methylammonium iodide was synthesised by Benjamin Vella, following the procedure outlined in Ref. [150]. For the formation of Double Cat solutions (prepared by Wai Kin Yiu), the suppliers are instead as follows. CsI (>99%), PbI_2 (>99.9%) and $PbBr_2$ (>99.9%) were obtained from TCI. FAI (>99%) and PEAI (>99%) were obtained from Greatcell solar. DMF (99.8%) and DMSO (99.7+%) were obtained from Alfa Aesar.*

Table 2.1: Representative LPK solution compositions dissolved in 1 mL of 9 : 1 DMF : DMSO, as used in Chapter 2.

Solution	PbI_2	A' Cation Iodide	Solution	PbI_2	A' Cation Iodide
PMA	368.8 mg	376.2 mg	ButA	368.8 mg	321.7 mg
PEA	368.8 mg	398.5 mg	PentA	368.8 mg	344.2 mg
ThMA	368.8 mg	385.8 mg	HexA	368.8 mg	366.5 mg
ThEA	368.8 mg	408.2 mg	OctA	368.8 mg	411.5 mg

Table 2.2: Representative perovskite solution compositions dissolved in 1 mL of 4 : 1 DMF : DMSO, as used in Chapters 3 and 4.

Solution	PbI_2	$PbBr_2$	FAI	MAI	CsI	MACl
MAPI	750 mg			160 mg		
MAPI (for $n = 1$ LPKs)	825 mg			160 mg		
Triple Cat	710 mg		227 mg	12.7 mg	18.2 mg	33.8 mg
Double Cat	630 mg	33.6 mg	217 mg		36.4 mg	

2.2.2 LPK (Heterojunction) Solutions

In Chapter 4, A' cation iodide salt solutions for $n = 1$ LPK heterojunction formation were prepared by dissolving 40 mM of the respective A' cation salt in IPA (99.8%, Fisher Scientific) to form a stock solution. The stock was dissolved at 70 °C overnight, and filtered using a 0.45 µm PTFE filter after cooling to room temperature. Additional solutions were then formed by diluting the 40 mM stock solution with IPA to achieve the target concentration. For the formation of $n = 5$ PEA heterojunctions, an 80 mM solution of MAI salt in IPA was prepared and combined with the 40 mM PEA solution to yield a 1:2 PEA : MA precursor.

In Chapter 5, A' cation iodide salt solutions for LPK heterojunction formation were prepared by dissolving 50 mM of the respective A' cation salt in IPA (99.8%, Fisher Scientific) to form a stock solution. The stock was dissolved at 70 °C overnight, and filtered using a 0.45 µm PTFE filter after cooling to room temperature. Additional solutions were then formed by diluting the 50 mM stock solution with IPA to achieve the target concentration.

2.2.3 CTM Solutions

ETM - P-I-N

PCBM (>99.8%, Lumtec), C_{60} (99.9%, Sigma-Aldrich) and Methyl pentanoate (MPA) (99%, Sigma-Aldrich) solutions were prepared by dissolving 20 mg of PCBM, C_{60} and MPA respectively in 1 mL of Chlorobenzene (CB) (99.8% Extra Dry, Fisher Scientific) at 60 °C overnight.
BCP (>99.5%, Lumtec) solutions were prepared by dissolving 1 mg in 1 ml of IPA at 60 °C overnight. All solutions were filtered using a 0.45 µm PTFE filter after cooling to room temperature.

ETM - N-I-P

The TiO_2 precursor solution was prepared by diluting 370 µL of titanium isopropoxide (99.999%, Sigma Aldrich) in 2.5 mL of IPA (99.8%, Fisher Scientific). Then 2.5 mL of IPA mixed with 35 µL of 2 M HCl (50% v/v, Alfa Aesar) was added dropwise whilst stirring within a fumehood.
The SnO_x precursor solution used for chemical bath deposition was prepared by mixing 412.5 mg $SnCl_2{\cdot}2H_2O$ (>99.99%, Sigma-Aldrich), 1.875 g urea(>99.99%, Sigma-Aldrich), 1.875 mL HCl (37%, Sigma-Aldrich), and 37.5 µL thioglycolic acid (>99%, Sigma-Aldrich) in 150 mL Deionised (DI) water (in-house supplier) within a fumehood.

HTM - P-I-N

NiOx fabrication was carried out by Jingbo Wang at the University of Hong Kong, Optoelectronics and Nanomaterials Lab.
In a fumehood, 6 g of $Ni(NO_3)_2{\cdot}6H_2O$ (Duksan) was dissolved in 80 mL of DI water (in-house supplier) under vigorous stirring until a clear solution was obtained. Subsequently, 80 mL of 1 M NaOH (97%, Alfa Aesar) solution (1 mol L^{-1} in DI water) was added dropwise at a controlled rate. The mixture was stirred continuously for 5 minutes. The resulting light green precipitate was collected via centrifugation at 10,000 rpm and washed several times with DI water. The purified product was then freeze-dried for at least 48 hours before being annealed at 270 °C for 2 hours, yielding black NiO_x nanoparticles. For deposition, 20 mg of the nanoparticles were

dissolved in 1 mL of DI water.
The Me-4PACz solution was prepared by dissolving 0.5 mg of Me-4PACz (99%, TCI) in 1 mL of IPA (99.8%, Alfa Aesar) .

HTM - N-I-P

The Spiro-OMeTAD HTM solution was prepared by dissolving 80 mg of Spiro-OMeTAD (99%, Sigma-Aldrich) in 1 mL of CB (99.8% Extra Dry, Fisher Scientific) at room temperature overnight. One hour before deposition, the HTM solution was doped via the addition of 23 µL of Lithium bis(trifluoromethanesulfonyl)imide (LiTFSI) (>99.9% anhydrous, Sigma-Aldrich) stock solution (520 mg in 1 mL Acetonitrile (ACN) (>99.9%, Sigma-Aldrich)), 14 µL of tris (2-(1H-pyrazol-1-yl)-4-tert-butylpyridine) cobalt(III) tri [bis(trifluoromethanesulfonyl)imide] (FK209) (>98%, Sigma-Aldrich) stock solution (375 mg in 1 mL ACN) and 32 µL of *tert*-butyl pyridine (tBP) (98%, Sigma-Aldrich) per 1 mL of CB. Finally, the HTM solution was filtered immediately before use through a 0.45 µm PTFE filter. For the preparation of the 'HTM Wash' model solution as used in Chapter 5, the dopants were added directly to 1 mL of CB as above.

2.3 Single Crystal Growth

Single crystals of layered perovskites were grown within a home-built setup, shown in Fig. 2.1. The apparatus consists of a set of aluminium 'ovens', lined with heating pads and insulated with mineral wool. Temperature control was achieved by varying the power supplied to the pads via a programmable power supply (Tenma). The ovens were turned on at least 24 hours before use to allow them to reach an equilibrium temperature. Super-saturated solutions of perovskite were prepared within the glovebox and dissolved at 120 °C. Details of the compositions used are included in Table 2.3. Each solution was quickly deposited between a pair of glass slides which were pre-heated to the maximum oven temperature (approximately 110 °C). Once placed in the oven, the samples were left to slowly cool to room temperature following the programme detailed in section 2.3.1, resulting in the formation of large flakes of perovskite crystal. γ-Butyrolactone (GBL) was obtained from Sigma-Aldrich (>99%).

Table 2.3: Representative perovskite solution compositions used for single crystal growth, dissolved in GBL.

Solution	PbI_2	PEAI	PMAI	ButAI	GBL
PEA_2PbI_4	97.9 mg	106.1 mg			109.4 mg
PMA_2PbI_4	97.7 mg		99.7 mg		115.5 mg
$PMA_1ButA_1PbI_4$	73.8 mg		37.6 mg	32.3 mg	56.4 mg

2.3.1 Oven programming

A slow, continuous cooling of the ovens was achieved with the use of a LabVIEW script. Maximum (35 V) and minimum (0 V) voltage values for the power supply

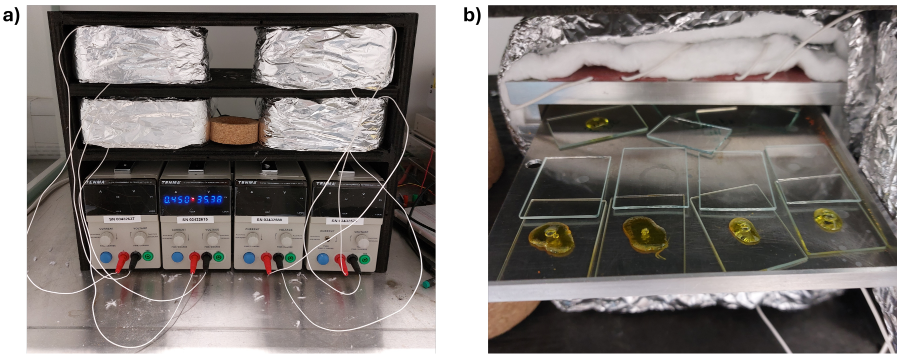

[h]

Figure 2.1: a) Programmable setup used for growth of single crystals. b) Samples of supersaturated solution placed within the oven before the slow cooling procedure.

were set, corresponding to approximately 110 °C and room temperature respectively. Next, the voltage was steadily reduced at a rate of 0.01 V min^{-1} , corresponding to a 2.4 day cooling time. This time was sufficient to grow large flakes suitable for further analysis, and ensured a smooth cooling gradient, as illustrated in Fig. 2.2.

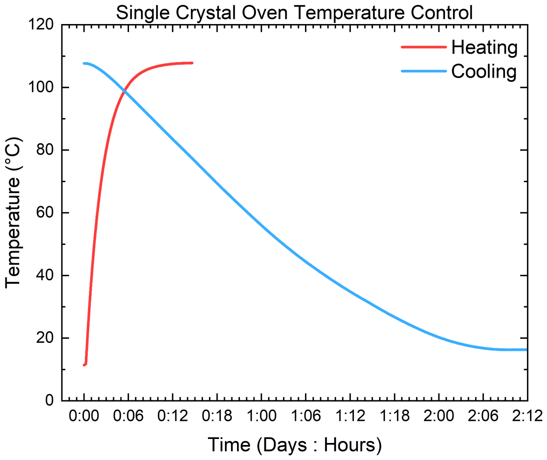

Figure 2.2: Example heating and cooling curves for the home-built single crystal oven.

2.4 Perovskite Thin Film Formation

For characterisation samples, all substrates (Glass / FTO / ITO) were cleaned sequentially using a 2% solution of Hellmanex III (Sigma-Aldrich), DI water (in-house supplier), acetone (>99%, VWR), ethanol (99%, VWR) and DI water again, and dried using compressed air. All substrates were then treated with UV-Ozone (Ossila) for 20 minutes before being immediately transferred into the glovebox. All perovskite compositions listed in Tables 2.1 and 2.2 were spincoated by dynamically depositing filtered solutions of perovskite onto the substrate. Table 2.4 lists the spin speeds, and antisolvent timings (if used) for each of the perovskite compositions used within this work. After spincoating, samples were annealed as detailed in Table 2.5. The CB for MAPI was obtained from Fisher Scientific (99.8% Extra Dry), the CB for Double Cat was obtained from Aladdin, (>99.5%) and EtAc for Triple Cat was obtained from Fisher Scientific (99.9% Extra Dry).

2.4.1 Perovskite Heterojunction fabrication

In Chapter 4, LPK heterojunctions were formed by depositing 50 µL of the cation iodide salt solutions onto annealed perovskite layers. A dynamic deposition method was adopted, where the solution was deposited immediately after the start of a one step 6000 rpm / 45 s spincoating procedure. The samples were then annealed at 70 °C for 10 min.

In Chapter 5, LPK heterojunctions were formed by depositing 50 µL of the cation iodide salt solutions onto annealed perovskite layers. Here, a static deposition method was adopted, where the solution was spread with a pipette tip to ensure it covers the whole slide. After 5 seconds, a one step 5000 rpm / 30 s spincoating procedure was used to complete the heterojunction formation. An optional annealing step was carried out at 70 °C for 10 min.

Table 2.4: Conditions used for spincoating perovskite solutions. The timing of the antisolvent addition is given in seconds before the end of the second spinning step.

Solution	Spinning Step 1	Spinning Step 2	Antisolvent
LPK (Film)	1000 RPM / 10 s	5000 rpm / 30 s	None
MAPI	1000 RPM / 10 s	5000 rpm / 30 s	150 µL CB @ 23 s
Triple Cat	1000 RPM / 10 s	4000 rpm / 40 s	300 µL EtAc @ 5 s
Double Cat	1000 RPM / 10 s	4000 rpm / 40 s	250 µL CB @ 20 s
LPK (Capping)	None	5000 rpm / 30 s	None

Table 2.5: Conditions used for annealing perovskite films.

Solution	Pre-Annealing	Annealing
LPK (Film)	RT / 20 min	100 °C / 20 min
MAPI	RT / 20 min	100 °C / 20 min
Triple Cat	None	100 °C / 60 min + 150 °C / 10 min
Double Cat	None	100 °C / 30 min
LPK (Capping)	None	70 °C / 10 min

2.5 Solar Cell Fabrication

2.5.1 P-I-N Solar Cells

The P-I-N cell fabrication detailed below was carried out by Wai Kin Yiu at the University of Hong Kong, Optoelectronics and Nanomaterials Lab.

Pre-patterned ITO substrates were sequentially cleaned by using a 1% Decon 90 solution in DI water (in-house supplier), followed by DI water, acetone (in-house supplier) and ethanol (in-house supplier) by sonication for 15 minutes in each solvent. The cleaned substrates were then dried with nitrogen gas and treated with oxygen plasma at 10 V for 10 s (Spectrolinker XL 15000). For the hole transport layer, a NiOx nanoparticle ink was spin-coated on to the ITO surface at 4000 rpm for 30 s inside a fumehood. The coated substrates were then annealed at 110 °C for 10 min, followed by UV-ozone treatment for 20 min being transferred to a nitrogen-filled glovebox. The Me-4PACz solution was spin-coated next at 4000 rpm for 30 s and annealed at 100 °C for 10 min. The Double Cation perovskite solution and the LPK capping layer was formed and deposited as detailed in Section 2.4. For the electron transport layer, the PCBM solution was spin-coated at 1200 rpm for 30 s, followed by an annealing at 100 °C for 10 min. ETM analogues as used in Chapter 5 were deposited in the same manner. The BCP layer was deposited by spin coating at 4000 rpm for 30 s. A 90 nm thick silver (99.99%, Kurt J. Lesker) electrode was thermally evaporated through a shadow mask, defining an electrode area of 0.09 cm^2. The completed devices were encapsulated using microscope glass and polyisobutylene tape, with edges sealed using UV-cured epoxy.

2.5.2 N-I-P Solar Cells

FTO glass substrates were chemically patterned using a mixture of Zn powder (>99.99%, Sigma-Aldrich) and 3 M hydrochloric acid (50% v/v, Alfa Aesar), then cleaned sequentially using a 2% solution of Hellmanex III (Sigma-Aldrich), DI water, (in-house supplier) acetone (>99%, VWR), ethanol (99%, VWR) and DI water. The ETM was prepared via a chemical bath deposition procedure. Substrates were placed vertically in a beaker containing the SnO_x precursor solution, and the beaker was placed in a water bath heated to 90 °C for 4.5 h inside a fumehood. After deposition, the substrates were sonicated in deionised water and isopropyl alcohol for 5 min each and dried at 100 °C for 1 h. The substrates were then annealed at 190 °C for 1 h and treated with UV-ozone (Ossila) for 30 min. Substrates were then transferred to a nitrogen-filled glovebox before perovskite deposition. The Triple Cation perovskite solution and the LPK capping layer was formed and deposited as detailed in Section 2.4. For the hole transport layer, 50 µL of the HTM solution was spin-coated on the perovskite at 3000 rpm for 30 s. The HTM components as used in Chapter 4 were deposited in the same manner. Samples were then moved to a desiccator and allowed to oxidise for 24 h. Finally, a 50 nm thick gold (99.99%, Tesbourne) electrode was thermally deposited through a shadow mask, defining an electrode area of 0.16 cm^2 (unannealed devices) or 0.0625 cm^2 (annealed devices). The variations in electrode area are due to optimisation of the device architecture throughout the timeframe of the experiments. The unannealed device set was then sealed using sealing tape (Helioseal PVS 101).

LPK Devices

FTO substrates were cleaned and etched according to the protocol detailed above. The ETM was formed by spincoating the TiO_2 solution at 2000 rpm for 45 s, which was dried at 150 °C for 30 min. The substrates were then annealed at 500 °C for 45 min, and transferred to a nitrogen-filled glovebox before perovskite deposition. The perovskite precursor solutions used are listed in Table 2.1, and deposited as detailed in Section 2.4. For the hole transport layer, a 75 mg mL^{-1} Spiro-OMeTAD solution in CB was doped with 30 µL of LiTFSI stock solution (170 mg in 1 mL ACN) and 10 µL of tBP prior to spin coating. 50 µL of the HTM solution was then spin-coated on the perovskite at 3000 rpm for 30 s. Samples were then moved to a desiccator and allowed to oxidise for 24 h. Finally, a 50 nm thick gold electrode was thermally deposited through a shadow mask, defining an electrode area of 0.0625 cm^2.

2.6 Characterisation

2.6.1 X-Ray Diffraction

X-Ray Diffraction (XRD) diffractograms were taken on a Rigaku Miniflex benchtop diffractometer, which used unfiltered Cu Kα radiation. Thin-film perovskite samples were deposited on FTO or ITO slides and loaded into the instrument on custom-made magnetic sample holders. The scans were carried out at 40 kV and 15 mA, with a 2θ range of 2 - 45°, step size of 0.01° and speed of 12° min^{-1}. Analysis was carried out by plotting the data in Origin software, after processing to remove sample offset errors as detailed below.

Correcting Sample Offset

Due to the use of non-standard, 3D printed sample holders and the use of plasticine as space-filling material, it was necessary to account for the small variation in sample height when placed in the instrument. To correct for the shift in peak angle due to sample displacement, the following equation was used, taken from Ref. [151]:

$$\Delta 2\theta = \frac{-(2s\cos\theta)}{R}$$

Here, s is the vertical displacement for a flat plate sample, and R is the radius of the goniometer circle. This correction was implemented via a Python script, as shown in Fig. 2.3. The position of the most prominent FTO or ITO substrate peaks was determined by a Pseudo-Voigt fit, and the offset from the reference values of 26.5° (FTO) or 30.4° (ITO) was calculated.[152,153] Finally, this correction was applied to the dataset to shift all of the 2θ values to eliminate the displacement error.

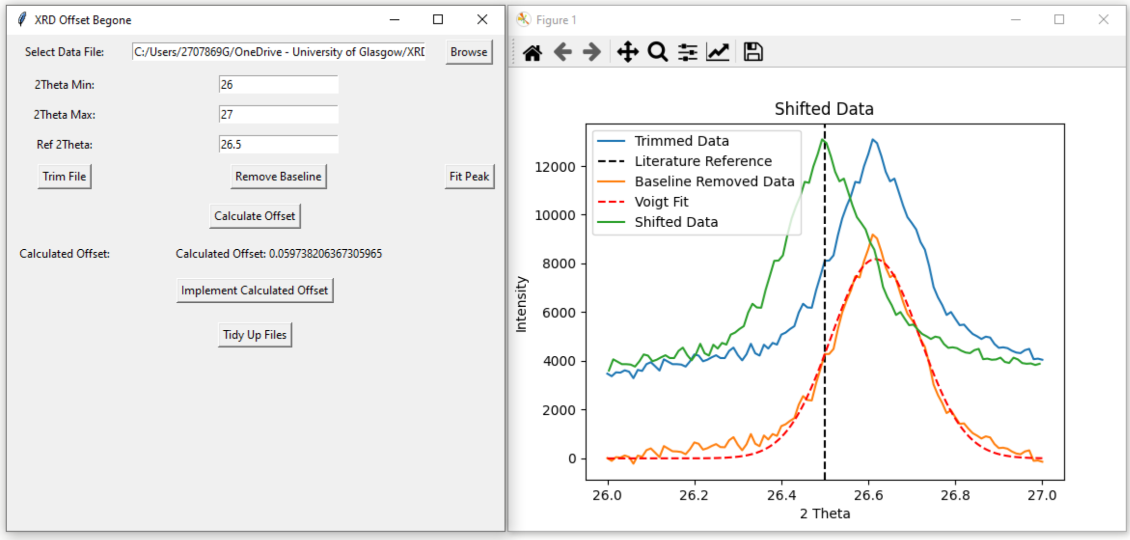

Select Data File: C:/Users/2707869G/OneDrive - University of Glasgow/XRI

2Theta Min: 26

2Theta Max: 27

Ref 2Theta: 26.5

Calculated Offset: Calculated Offset: 0.059738206367305965

Figure 2.3: Offset fixing script user interface and example file showing the offset correction process in progress.

2.6.2 Uv-Vis Spectroscopy

UV-Vis spectra were collected on a Shimadzu UV-3600 UV-Vis Spectrophotometer. Thin film samples were affixed to the outside of the cuvette holder for measurement.

2.6.3 Photoluminescence

All Photoluminescence (PL) measurements were carried out by Paula L. Lalaguna at the University of Glasgow School of Chemistry, Kadodwala group laboratory.
A schematic of the home-built PL setup is included in Fig. 2.4. A 404 nm laser diode was used as the excitation source. The laser beam is collimated, and two polarizers are used to control the excitation power. The beam is directed towards the sample using a 50:50 beam splitter and a 60x objective (numerical aperture = 0.9, beam spot size 4 µW). Photoluminescence is collected in a reflection geometry and a 10:90 beam splitter is used to direct 10% of the light towards a scientific camera, where the sample can be visualized, and 90% of the signal towards an optical fibre which carries the photoluminescence signal to the Charge-Coupled Device (CCD)/camera (Newton CCD, Andor Technology).

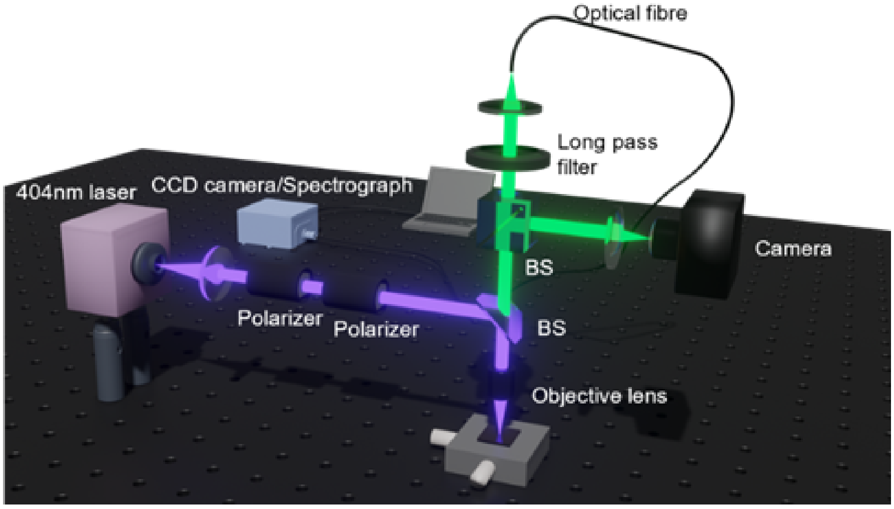

Figure 2.4: Schematic of thePL set up used to perform PL spectroscopy of perovskite thin films. *Figure reproduced with permission from Ref. [154] under the terms of the CC BY 4.0 license.*

2.6.4 Conductivity - In Plane

ITO glass substrates were cleaned sequentially using a 2% solution of Hellmanex III (Sigma-Aldrich), DI water, (in-house supplier) acetone (>99%, VWR), ethanol (99%, VWR) and DI water. An interdigitated electrode pattern was etched onto the glass using a Rofin Easy Mark IV F20 laser etcher. This formed a 37.2 cm long and 70 µm wide channel within each 2 cm x 2 cm substrate, with the quality of the etch being assessed with an optical microscope. After the etch, the substrates were once again cleaned following the procedure above. Conductivity measurements were obtained by measuring the current-voltage characteristics of the samples using a Keithely 2611b source meter unit. I/V characteristics were obtained by setting a voltage range of -1.3 to 1.3 V for data acquisition, and measuring current at randomly determined voltage values within the range to reconstruct a linear I/V sweep from a scatter plot. This avoided hysteresis in the measurement due to ionic motion within the samples. Before material deposition, each substrate was measured to check for shorts and issues with the patterning process. This was done by measuring the I/V characteristics of a patterned substrate after the cleaning procedure, with no deposited material present. Only substrates with initial conductivity values below 1×10^{-9} S cm^{-1} were used. Deposition of perovskite thin films was carried out as detailed in section 2.4 above. Additional silver pads were added onto the samples using conductive silver paint to ensure good electrical contact between the substrate and the instrument. For details of how conductivity values were calculated see section 2.8.3.

2.6.5 Thickness Measurements

Microscope slide glass substrates were cleaned sequentially using Hellmanex III (Sigma-Aldrich), DI water, (in-house supplier) acetone (>99%, VWR), ethanol (99%, VWR) and DI water. The deposition of perovskite thin films was carried out as detailed in Section 2.4 above. Four different LPK compositions were used to obtain representative thickness values, formed with PEA, ThMA, HexA and OctA cations. For each film, the solution concentration was varied from 0.8 M to 0.1 M. After deposition, a razor blade was used to etch a step across the centre of the slide. The step height was measured using a Bruker Dektak XT Stylus Profiler, or a Bruker Innova Atomic Force Microscopy (AFM) and analysed using Gwyddion software.[155] Fig. 2.5 shows the dominant factor controlling the thickness of the perovskite is the concentration of the LPK solution.

AFM thickness measurements were carried out by Gregor Macleod at the University of Glasgow, School of Chemistry.

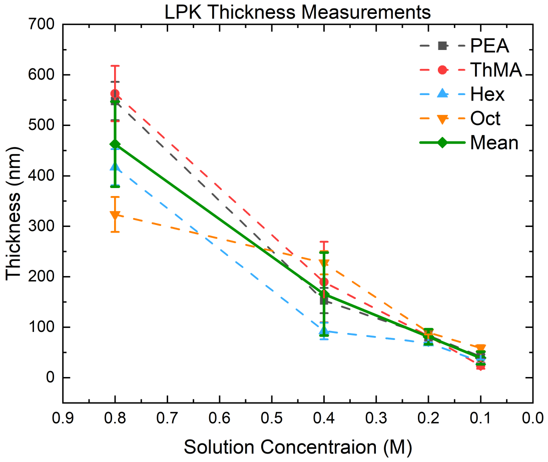

Figure 2.5: Thickness measurements of a range of LPK thin films deposited from varying solution concentrations.

2.6.6 Optical Images

Optical images and associated analysis was carried out by Aleksey Kozikov at the University of Newcastle, School of Mathematics, Statistics and Physics, Kozikov group laboratory.

Fresh crystal samples were mechanically exfoliated in air in the vicinity of an optical microscope. The exfoliated flakes were left uncovered, and immediately transferred into the microscope to find a suitable area for time dependence measurements. The inspection of the surface of substrates to find suitable areas was done using a low-magnification objective (5x and 10x), red optical filter and low light intensity to prevent premature degradation. All optical images were taken using a 100x objective, with degradation time measurements started when samples were exposed to unflitered room light. The optical contrast values n were calculated using the expression:

$$n = \frac{I_p - I_s}{I_p + I_s}$$

where I_p and I_s is the intensity of the reflected light from the perovskite flake and the silica substrate, respectively. The intensities were extracted from the optical images using ImageJ software, using the red channel for thin flakes and the green channel for thick flakes.

2.6.7 X-Ray Photoelectron Spectroscopy

X-Ray Photoelectron Spectroscopy (XPS) spectra were collected on a Kratos Analytical AXIS Supra+ instrument, using an Al Kα (1486.6 eV) excitation source. For thin film samples included in Chapter 4, a charge neutraliser beam set to 0.45 A, 1 V bias and 4 V balance was utilised. In Chapter 5, no charge neutraliser was used for thin film samples. For reference A' cation powder samples, the charge neutraliser beam was set to 0.45 A, 1 V filament bias and 4 V charge balance. Samples were affixed to the mounting bar using adhesive carbon tabs. Good electrical contact between the thin film samples, mounting bar and the instrument was obtained by evaporating gold contacts on top of the sample surface (40 nm) and using adhesive copper tape. If sample charging was present, binding energy values were referenced to the C-C adventitious carbon peak at 284.8 eV. Samples were kept in a nitrogen atmosphere during preparation and transferred into the instrument to minimise air exposure. The chamber pressure was between 8.3×10^{-8} to 1.3×10^{-7} Torr during measurement.

2.6.8 Pump-Probe Measurements

Pump-probe measurements were carried out by Jake Hutchinson at the University of Warwick, Department of Physics, Milot group laboratory.

Samples analogous to those used in the XRD measurements were prepared on quartz substrates following the protocol described in section 2.4. The source for the custom-built transient absorption spectroscopy system was a Ti:sapphire amplifier (Spectra Physics, Spitfire Ace) with a 800 nm centre wavelength, 1 kHz repetition rate, and 35 fs pulse duration. The white-light probe was generated by focusing a portion of the beam onto a CaF_2 window. The 410 nm pump beam was generated using an optical para-metric amplifier (TOPAS Prime from Light Conversion) and passed through an optical chopper operating at 500 Hz. The pump and probe beams were overlapped onto the sample at a slight angle to facilitate filtering before the detector. The transmitted probe beam was coupled into an optical fibre and detected with a spectrometer (Advantes) that samples at the 1 kHz repetition rate of the laser. The change in transmission and optical density were then calculated from the difference between probe spectra taken with the pump on and off.

2.6.9 Scanning Electron Microscopy

Scanning Electron Microscopy (SEM) images of perovskite film surfaces at magnifications from 1×10^{-5} x to 8×10^{-5} x were taken on a TESCAN Clara S8152 instrument, operated at an acceleration voltage of 15 keV, with a 300 pA beam current, set to dark field secondary electron detection (ANALYTICAL mode). Samples were affixed to Al mounting stubs with the use of adhesive carbon tabs. Silver paint was used to ensure good electrical connection between the sample and the mounting stubs, with no sputtered metal surface coating used.

2.6.10 Solar cell performance

P-I-N Cells

Measurements of P-I-N cells were carried out by Wai Kin Yiu at the University of Hong Kong, Optoelectronics and Nanomaterials Lab.

J-V measurements were carried out using a Keithley 2400 source measure unit under 1 sun illumination (100 mW cm^{-2}) with AM 1.5 G spectrum. An ABET Sun 2000 solar simulator was calibrated with an Enli PVM silicon standard reference cell. The measurements were conducted in ambient conditions (room temperature, relative humidity of 50-60%) using an aperture mask of 0.04 cm^2. The reverse scan was performed from 1.2 V to -0.2 V with a step of 0.03 V and a delay of 10 ms, and the forward scan was conducted from -0.2 V to 1.2 V.

N-I-P Cells

J-V measurements were carried out using an Ossila source meter unit and a Wavelabs Sinus-70 AAA solar simulator with 1 sun (AM 1.5 G) illumination, calibrated using a Fraunhofer ISE calibration diode, and referenced to an AMS Osram BPW 34 silicon diode to monitor drift. The measurements were conducted in ambient conditions (room temperature, relative humidity of 30-40 %). The illuminated cell area was defined using an aperture mask of 0.125 cm^2 (unannealed devices) or 0.049 cm^2 (annealed devices). The variations in mask area are due to optimisation of the device architecture throughout the timeframe of the experiments. The cells were pre-biased at 1 sun and 1.2 V for 10 seconds before the measurement. The reverse scan was performed from 1.3 V to -0.1 V at a rate of 0.2 V s^{-1} and a delay of 10 µs, and the forward scan was conducted from -0.1 V to 1.3 V.

2.7 Degradation of LPK-MAPI Heterojunctions

Degradation of the LPK perovskite heterojunction samples described in Chapter 3 was carried out by placing samples within one of three gas tight glass cylinders. These are schematically illustrated in Fig. 2.6. For light-induced degradation, samples were sealed in the vessel within a glovebox to ensure a pure nitrogen atmosphere. The vessel was then placed in a fixed position underneath a white-light Light Emitting Diode (LED). The light intensity at each sample position was adjusted to 0.7 sun via a programmable power supply, as measured by a Fraunhofer ISE calibration diode referenced to a Wavelabs Sinus-70 AAA solar simulator. For humidity exposure, the vessel was fitted with a pair of hose adapters and connected to a nitrogen cylinder. A slow stream of humid nitrogen was obtained by connecting the line to a bubbler. The humidity level was controlled by the gas flow and the water level within the bubbler, and monitored by a hygrometer placed at the outlet end of the vessel. The apparatus would be turned on for an hour before samples were placed inside to allow the system to equilibrate at the appropriate humidity value. The vessel was wrapped in foil to minimise light exposure. For degradation within solvent-containing atmospheres, a 1 mL glass vial was placed within the centre of the vessel. 50 µL of the 4:1 DMF: DMSO solvent system used for perovskite fabrication was added to the vial. The vessel was then immediately sealed with samples inside and was wrapped in foil to minimise light exposure.

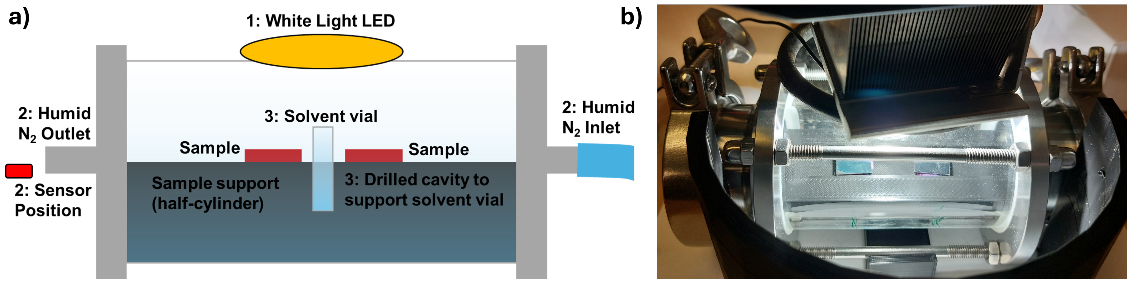

Figure 2.6: a) Illustration outlining the degradation vessels used for controlled exposure to light, humidity or solvents. One of three configurations would be utilised: 1) A white-light LED placed outside the vessel. 2) A pair of hose adapters replacing the solid end caps connected to gas supply. 3) A 1 mL vial of solvent placed within the central sample support. For configurations 2 and 3, the vessel was wrapped in foil to exclude light. b) Photo showing the degradation vessel in configuration 1.

2.8 Data Analysis

2.8.1 LPK Pb-Pb Layer Distance Calculation

Pb-Pb layer spacing values were obtained from thin-film diffractograms of layered perovskites as follows. After correcting for sample offset, the 2θ positions of the (00n) peaks were collected. These are the most prominent peaks in the diffractogram due to the preferential orientation of the sample parallel to the substrate. The corresponding crystal plane spacing d was calculated using Bragg's Law:[156]

$$n\lambda = 2d\,sin\theta$$

The d spacing can then be related to each of the unit cell lengths of the perovskite lattice, assuming an orthorhombic symmetry with the following equation:[157]

$$\frac{1}{d^2} = \frac{h^2}{a^2} + \frac{k^2}{b^2} + \frac{l^2}{c^2}$$

Here, the h, k, l values indicate the Miller indices of the peak, and the a, b, c values give the corresponding distance of the unit cell. In the case of the (00n) reflections, the h, k, a and b parameters do not affect the peak position, thus allowing for a straightforward calculation of the distance c, which was taken to be double the vertical Pb-Pb layer spacing.

For determining the Pb-Pb layer spacing values from single-crystal structure data, the parameter was obtained via a direct measurement of the c distance for cells with orthorhombic symmetries, or calculated by determining the vertical component of the c spacing after taking into account the α and β angles (which here is equivalent to the d spacing of the (002) peak) using the following equation:[157]

$$d_{002} = \frac{c\sqrt{1 - \cos^2\alpha - \cos^2\beta - \cos^2\gamma + 2\cos\alpha\cos\beta\cos\gamma}}{2\sin\gamma}$$

2.8.2 LPK Distortion Value Determination

All measurements of bond lengths and angles were carried out by analysing .cif files using VESTA software.[158] The nitrogen penetration depth was calculated by subtracting the average z-axis position of the N atom from the average position of the top I atoms of the octahedra. Bond Distortion Index (BDI) values were calculated using the equation proposed by Baur:

$$BDI = \frac{1}{6}\sum_{i=1}^{6}\frac{|d_i - d_{av}|}{d_{av}}$$

Where d_i and d_{av} are the individual and average Pb-I bond lengths respectively. Bond Angle Variance (BAV) values were calculated using the equation first reported by Robinson et.al.:

$$BAV = \frac{1}{11}\sum_{i=1}^{12}(\theta - 90)^2$$

Where θ is one of the I-Pb-I angles present within the octahedron.

2.8.3 Conductivity Calculation

In-plane conductivity values σ were calculated from current-voltage plots by modelling the perovskite thin film deposited within the etched channel as a wire, using the following equation:

$$\sigma = \frac{1}{\rho} = \frac{l}{AR}$$

Here, ρ is the resistivity of the sample, l is the length of the thin film, determined by the width of the etched channel, A is the cross-sectional area determined by film thickness and channel length, and R is the resistance, determined by calculating the gradient of the current-voltage data. For pure A' cation-based samples, four measurements were obtained from two different substrates. For mixed A' cation-based samples, two measurements were obtained form two different samples. The error in the final conductivity value was obtained by propagating the standard deviations of averaged thickness and length values.

2.8.4 Out-of-Plane Conductance Calculation

Out-of-plane conductance values were obtained from performing a linear fit around the V_{OC} region of pure LPK N-I-P cells, after converting the current density into a current value. For each sample, four values were obtained from four different substrates. This method assumes the series resistance within the solar cell is dominated by the LPK component.

2.8.5 LPK *n*-value Calculation

The assignment of low-angle diffractogram peaks to the correct n-valued layered perovskites was carried out following a methodology developed by Hu. et. al.[96] Here, the 2θ values for any given layered perovskite are estimated by assuming that a sheet of lead iodide octahedra is approximately 6.1 Å thick in the (00n) plane of the layered perovskite. By adding multiples of this value to the known Pb-Pb layer spacing for an $n = 1$ LPK from a single crystal structure, the expected separation of (00n) planes of $n = (1 + \mathrm{x})$ LPKs can be calculated. This can then be used to determine the corresponding 2θ value by using the approach described in section 2.8.1 in reverse, using Bragg's Law to calculate the angle values. These angles were then compared to diffractogram data to find the corresponding LPK n-number. An example table showing calculated peak positions for PEA-based LPKs is shown in Table 2.6. It is important to note that some of the calculated peaks are very low in intensity. For example, for $n = 5$ PEA LPKs, only the (006) reflection is readily detectable by the bench-top diffractometer utilised, which has been observed in the literature previously.[127]

2.8.6 XPS Peak Fitting

XPS data analysis was carried out using Igor Pro software with the XPST extension. The baseline for the fitting was varied between a linear and Shirley step function, depending on the region analysed. Each peak was fitted with a Pseudo-Voigt function, with the Gaussian-Lorentzian ratio varied from 0.3 to 0.5 to obtain a satisfactory fitting of the data.[159,160] For peaks with multiple components, the minimum amount

Table 2.6: Calculated peak positions for PEA-templated LPKs of varying n-values.

n	Est Thickness	(002)	(004)	(006)	(008)	(0010)	(0012)
1	16.36 Å	5.40°	10.81°	16.24°	21.71°	27.23°	32.82°
2	22.46 Å	3.93°	7.87°	11.81°	15.77°	19.75°	23.75°
3	28.56 Å	3.09°	6.18°	9.28°	12.39°	15.50°	18.63°
4	34.66 Å	2.55°	5.10°	7.65°	10.20°	12.76°	15.33°
5	40.76 Å	2.17°	4.33°	6.50°	8.67°	10.84°	13.02°
6	46.86 Å	1.88°	3.77°	5.65°	7.54°	9.43°	11.32°
7	52.96 Å	1.67°	3.33°	5.00°	6.67°	8.34°	10.01°
8	59.06 Å	1.49°	2.99°	4.48°	5.98°	7.48°	8.98°

of peaks required to obtain a satisfactory fit of the data was utilised, with each individual component assigned to a corresponding chemical state. For the Pb 4f peaks, spin-orbit splitting was reproduced with the use of a doublet peak which had a defined binding energy separation of 4.88 eV and a ratio of 3:4.[161]

2.8.7 LPK Thickness limit estimation

The estimation of what thickness of LPK is below the limit of detection within the XRD instrument was carried out by the use of the integral breadth method.[162] This calculates the peak broadening of a sample with respect to its volume average thickness in a given direction according to the following equation:

$$\beta_{hkl} = \frac{\lambda V}{\cos\theta \int T_{hkl}\, dV}$$

Here, β_{hkl} is the peak broadening in the hkl direction, V is the crystal volume, T_{hkl} is the crystal thickness in the hkl direction, λ is the X-Ray wavelength, and θ is the peak angle. As outlined in Ref. [162], the volume integral of a flat platelet in the (00n) direction is exactly 1. Thus, by taking the average thickness of a single sheet of PEA_2PbI_4 to be 1.64 nm, the peak broadening of a sample can be correlated with the number of layers present. This calculation assumes that all of the individual LPK layers are perfectly aligned parallel to the substrate, with well-ordered single crystallites. This is the typical behaviour seen for LPK thin films on glass substrates, which have a very high intensity of (00n) reflections and negligible intensities of peaks corresponding to any other orientations, as seen in the appendix, section A.3. In the case of LPK capping layers deposited on 3D perovskite this preferred orientation may be less pronounced, which would result in underestimating the quantity of material for a given intensity of broadening. Nonetheless, the calculation offers a meaningful lower bound for the amount of LPK in the sample. As shown in Fig. 2.7, the sample contribution to the XRD peak broadening reduces sharply as the number of LPK layers increases.

For samples of three layers or fewer, the peak broadening is high enough for the signal to be lost in the background noise of the XRD measurement. To demonstrate this, an LPK peak from a thick heterojunction deposited from a 15 mM solution was fitted with a Voigt function to act as a ‘base’ peak. The instrumental broadening contribution at this angle was estimated via a Voigt fit of the first (002) peak

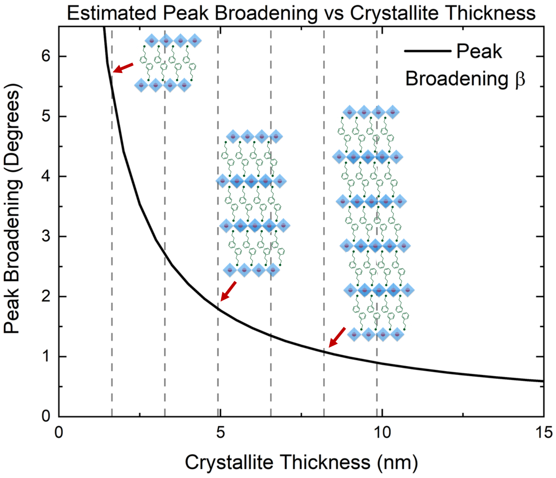

Figure 2.7: Calculated changes in the peak broadening within thin film XRD measurements due to increasing crystallite thickness, assuming an ideal parallel alignment of the crystallites to the sample.

of a pure PEA_2PbI_4 thin film sample. This component was then separated from the 'base' peak by removing the Gaussian and Lorentzian components separately according to the following equations:[163,164]

$$\beta_G = \sqrt{{\beta_{G,t}}^2 - {\beta_{G,i}}^2} \quad \text{and} \quad \beta_L = \beta_{L,t} - \beta_{L,i}$$

Here, β_G, $\beta_{G,t}$ and $\beta_{G,i}$ indicate the Gaussian width parameters of the sample, the fitted data, and the instrumental contribution while β_L, $\beta_{L,t}$ and $\beta_{L,i}$ indicate the corresponding Lorentzian parameters. Once the instrumental contribution to the data is removed, the two broadening values can be combined again to obtain the full width half maximum of the Voigt fit associated with the sample as follows:[165]

$$\beta_V = \frac{\beta_L}{2} + \sqrt{\left(\frac{{\beta_L}^2}{4} + {\beta_G}^2\right)}$$

Using this approach, the 15 mM sample peak has a broadening of 0.47°, which indicates a thickness in the range of 11 to 12 sheets of perovskite. The parameters of this fit were then altered to match the broadening values as calculated for a sample with only three LPK sheets, as calculated in Fig. 2.7. This new peak was then superimposed over a reference sample which had no LPK deposited, which offered the appropriate level of background noise. Fig. 2.8 (a) shows the effect of the artificial broadening of the LPK signal. Given that a thinner LPK also contains a smaller quantity of material, the peak area was additionally reduced by a factor of four. Plotted in Fig. 2.8 (b), it is clear once both effects are accounted for, the LPK signal is very difficult to distinguish from a sample with no LPK present.

2.8.8 Device Statistics

The numerical breakdown of fabricated devices is as follows. For N-I-P cells, each group of samples prepared with the same fabrication protocol contained two separate substrates containing four solar cells each. For the annealed and LPK devices, two substrates with eight solar cells each were prepared instead. For P-I-N cells,

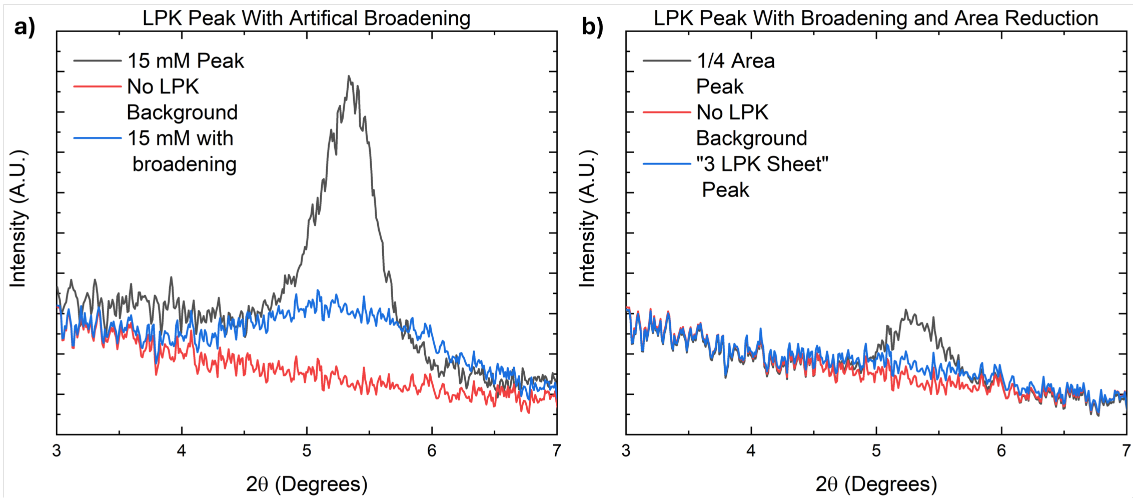

Figure 2.8: a) Superimposed LPK diffractogram peaks with added artificial broadening to simulate a sample containing only three sheets of LPK. b) Superimposed LPK diffractogram peaks with added artificial broadening and a corresponding reduction in peak area to account for the lower quantity of material in a sample containing only three sheets of LPK.

two substrates containing six cells each were prepared. The variations in device groupings per substrate are due to optimisation of the device architecture throughout the timeframe of the experiments in the case of N-I-P cells, and lab-to-lab variations in the case of the P-I-N cells. For the plots of device statistics, devices with FF values greater than 0.89 or less than 0, and J_{SC} values below 3 mA cm^{-2} were excluded to eliminate shorted or disconnected devices.

Chapter 3

The Relationship Between A' Cation and Perovskite Structures

Perovskites incorporating large organic A' cations, known as LPKs, have been seeing increasing implementation thanks to their potential to tackle the issues of stability faced by conventional perovskite structures. Maximising the benefits they can provide to solar cells requires an in-depth understanding of their electronic structure, band alignment and charge transport properties, in order to facilitate the optimisation of existing materials and the synthesis of novel A' cations. Here, many of the unique properties of LPKs are tied directly to their structure, which is defined by the choice of the organic A' cation. This means the relationship between the A' cation chemistry and the resulting perovskite is highly complex, requiring a methodical investigation of the structure-property relationships between the A' cation and LPK. In this chapter, studies of the single crystal structures and thin films of a related family of perovskites are used to explore how elements of the molecular structure impact the spacing and optoelectronics of the resulting perovskite layer. Contrary to expectations, it is found that the response of the perovskite is highly varied, and even a detailed analysis of how A' cations influence the structure of the lattice is insufficient to draw meaningful links with parameters such as photoluminescence peak position or conductivity. This complicates efforts to engineer A' cations which template perovskites with targeted properties. The sensitivity of the perovskite lattice to even minor changes in A' cation chemistry can be exploited, however, with LPKs based around mixed A' cations being identified as an alternative method of fine-tuning the resulting perovskite structure.

Declaration of Authorship

Data collected or analysed by my co-workers are detailed at the appropriate points. This includes: single crystal structure refinements carried out by Claire Wilson at the University of Glasgow, School of Chemistry; PL measurements carried out by Paula L. Lalaguna at the University of Glasgow, School of Chemistry, Kadodwala group laboratory; supporting thickness measurements for conductivity calculations carried out by Gregor Macleod at the University of Glasgow, School of Chemistry.

3.1 Introduction

Much of the success and popularity of perovskites as a class of optoelectronic materials can be attributed to their wide chemical tunability. In the case of layered perovskites, this has resulted in reports of dozens of chemically distinct spacer A' cations reported in the literature for a variety of applications.[55,65] This can largely be attributed to a less restrictive requirement of the balance of sizes and charges of the component ions when compared to the conventional 3D perovskite A cations, given the additional 'dimension' granted by the presence of the organic cation interlayer.[33,65]

With an increase in the chemical diversity of the perovskite components comes a greater degree of complexity, and in turn, a higher number of physical parameters that can be changed to influence the material properties. For the 'traditional' 3D metal-halide perovskites, the bandgap is largely dependent on the p-orbital overlap between the core metal B cation and the X halides that form the octahedral structure.[40,41] In LPKs, these interactions are now partially broken up by the A' cation sheets, leading to a quantum-well like electronic landscape.[83] Here, factors such as the length of the organic A' cation, the interactions between the A' cations and perovskite octahedra, and the underlying energetics of the A' cation itself will influence the positions of the V.B. and C.B. of the resulting perovskite.[166–168]

Crucially, the influence of the A' cation on the 'main' metal-halide interactions that determine the bandgap is secondary, tweaking the structure and overlap but not the p-orbital energy levels themselves, as would be the case with halide or metal substitution. The complexity of these interactions makes it difficult to predict how a given perovskite material may respond, as any chemical modification inevitably will change both the molecular structure and the molecular orbital energies of the A' cation. This can have a number of possible knock-on effects on the measurable properties of the perovskite that were not intended due to the resulting changes in the band structure of the LPK. Conversely, this offers opportunities to tune structural and optoelectronic parameters to a far greater degree than what is possible within the more limited scope of metal and halide substitutions.[169] Indeed, variation of the A' cation component in LPKs has been used to control the relative band alignment between the A' cation and material by matching perovskite V.B. and C.B. levels to the A' cation HOMO and LUMO energies to minimise the quantum well confinement,[68,166] form non-centrosymmetric compounds for piezoelectric applications,[170] or alter the bonding perovskite backbone to achieve white-light emitting LEDs.[171]

The work presented in this chapter investigates the links between the chemistry of the A' cations used to form RP phase $n = 1$ LPKs, and the structures and optoelectronic properties of the resulting material. Two families of aromatic and aliphatic A' cations were selected to explore the variation that is observed due to basic chemical modifications, attained by varying the length of the carbon-carbon chains present in the molecules, or by changing the nature of the aromatic moiety present. In-depth analysis of the single crystal structures of the LPKs reveals that even these simple changes lead to significant variation in how the A' cations arrange in the lattice, and the structure of the perovskite lattice itself. Studies of the UV-

Vis absorption, PL emission and charge transport through these materials reveal that drawing clear links to underlying structural parameters is difficult. Parameters derived from structural studies do not sufficiently describe the soft perovskite lattice and the complex combination of factors which ultimately determine properties such as the perovskite bandgap. This means that simple structural parameters and arguments based solely around variations in A' cation chemistry are not sufficient to make predictions regarding how optoelectronic properties will vary. For such predictions, more in-depth approaches such as determining the band structure via computational techniques appear to be required.

LPKs templated from a mix of large organic A' cations are instead proposed as a promising method of expanding the range of parameters that are obtainable for $n = 1$ RP phase LPKs from the same synthetic cation space. Depending on the precise combination of A' cations, highly ordered structures with intermediate layer spacing and optical bandgaps can be prepared via a simple solution mixing process. These mixed structures appear to have a lower degree of disorder within the perovskite octahedra themselves and demonstrate remarkably high conductivities when compared to the single-cation materials. This highlights the potential this approach has for compositional engineering of novel LPK materials.

3.2 Determining the influence of the A' cation on the perovskite backbone

The very broad range of compounds which can template LPKs highlights the value of obtaining clear structure-property relations between the organic A' cation and resulting perovskite. The most widely used compounds in the perovskite field can be grouped into small aromatic and aliphatic molecules which template RP-phase materials, and which see a similar degree of performance when utilised as interlayers within solar cells.[98,145,146,172] As such, exploring the properties of a representative subset of these A' cations offers the opportunity to gain relevant insights for the current state of the perovskite solar cell field.

In this chapter eight different compounds were chosen, with iodide salts prepared for each as detailed in the methods section 2.1. The molecular structures of the A' cation sections are shown in Fig. 3.1 (a). They represent sets of chemically-similar A' cations which template structures with similar spacings. This allows for the exploration of the influence of both the overall lattice parameters and the A' cation chemistry on the optoelectronic properties of the perovskite, as there is a significant degree of overlap between the size and chemistry of the chosen A' cations. The selection includes four aromatic A' cations, namely PMA, PEA, ThMA and ThEA, as well as four linear A' cations, namely ButA, PentA, HexA and OctA. All of the above A' cations template well-ordered $n = 1$ RP-phase lead iodide structures, as demonstrated by the XRD diffractograms in Fig. 3.1(b). The individual diffraction patterns are included in the appendix, Figs A.7 and A.8. In each case, the diffractogram only shows peaks indexed to $(00n)$ crystal orientations corresponding to horizontal sheets of LPK forming on top of the substrate, with no evidence of side phases or other orientations. The LPK structures also have closely comparable spacings between the planes of the Pb-Pb atoms - i.e. the centres of two sheets of octahedra. They are listed in Table 3.1, with details of how they were calculated included in methods section 2.8.1.

The addition of a carbon atom into the 'linker' element of each A' cation results in a similar widening of the Pb-Pb layer spacing, usually by a little over 1 Å. This motivated a more in depth study to explore whether other trends in the properties of the perovskite can be identified. By varying the Pb-Pb layer spacing within a limited range, the overall structure of the perovskite is kept as similar as possible. Thus, any optoelectronic properties defined chiefly by the vertical separation of the sheets of perovskite octahedra can be easily determined. Additionally, by using chemically distinct A' cations with matching spacing, the influence of changing the perovskite lattice is minimised, and changes can be more readily assigned to the impact of the changed A' cation chemistry.

From a chemical perspective, the selected A' cations can be categorised into linear aliphatic carbon chain cations and aromatic cations, with a further subdivision into phenyl- and thiophene-containing systems. Within each of these groups, the A' cations only differ by the number of carbon atoms linking the ammonium head to the rest of the molecule. This choice was based around the following hypothesis. The inclusion of specific elements such as aromatic rings or heteroatoms will have

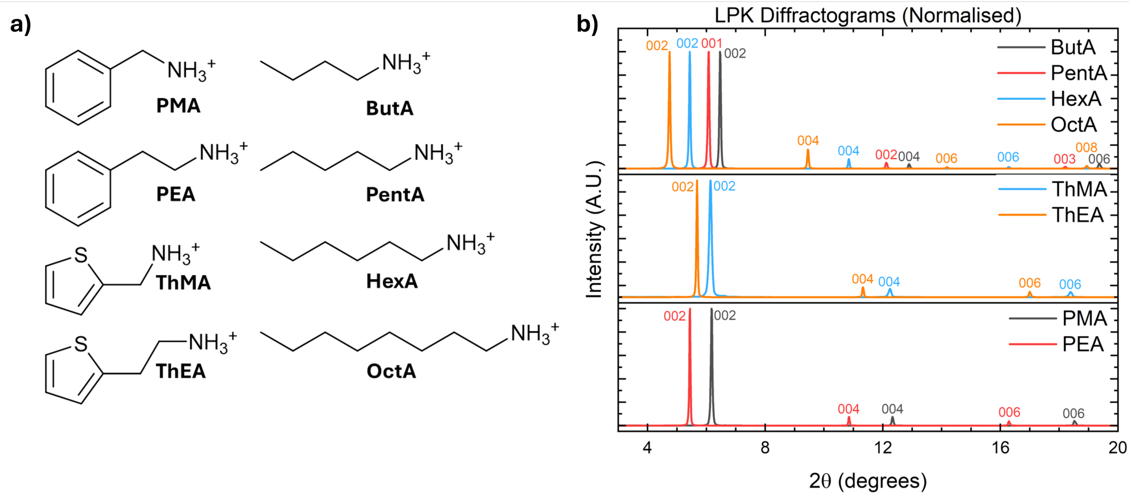

Figure 3.1: a) Molecular structures of the organic A' cations included in this study. b) Diffractograms of $(A')_2PbI_4$ thin films, where A' is the cation studied. The annotations indicate the hkl value of each respective peak in the diffractograms.

Table 3.1: Calculated Pb-Pb layer spacing values for LPK thin films, obtained from powder XRD data.

A' Cation	Pb-Pb Layer Spacing	A' Cation	Pb-Pb Layer Spacing
PMA	14.35 ± 0.01 Å	ButA	13.72 ± 0.02 Å
PEA	16.29 ± 0.02 Å	PentA	14.59 ± 0.02 Å
ThMA	14.44 ± 0.02 Å	HexA	16.31 ± 0.01 Å
ThEA	15.61 ± 0.02 Å	OctA	18.69 ± 0.03 Å

a pronounced and systematic impact on the structure and distortion of the lattice, which themselves strongly influence factors such as the conductivity of the sample. As such, measurements of a set of known A' cations can be used to determine how the A' cation chemistry will change the properties of the LPK as a whole. Utilising groups of A' cations that cover a similar 'synthetic space' allows for greater confidence in linking any given chemical unit to the observed parameters. From this baseline, the set of properties of a perovskite that are most sensitive to changing the chemical composition of the A' cation can be obtained. Ultimately, by studying existing structures, novel A' cations with tailored chain lengths, aromatic elements, heteroatoms or similar could be used to template perovskites with fine tuned optoelectronic properties.

Room-temperature single crystal structures of each of the compounds were analysed to determine a wide range of structural parameters, with a set of [100] and [010] projections shown in Figs. 3.2, 3.3, 3.4 and 3.5. These were obtained from the Cambridge Crystallographic Data Centre, except for the PMA and ThMA structures, which were determined for this work.[170,173,174] As the ThEA crystal structure has a unit cell defined at a 45° angle with respect to the other structures, [110] and [-110] projections have been shown instead to match the orientation of the octahedra with the other structures.

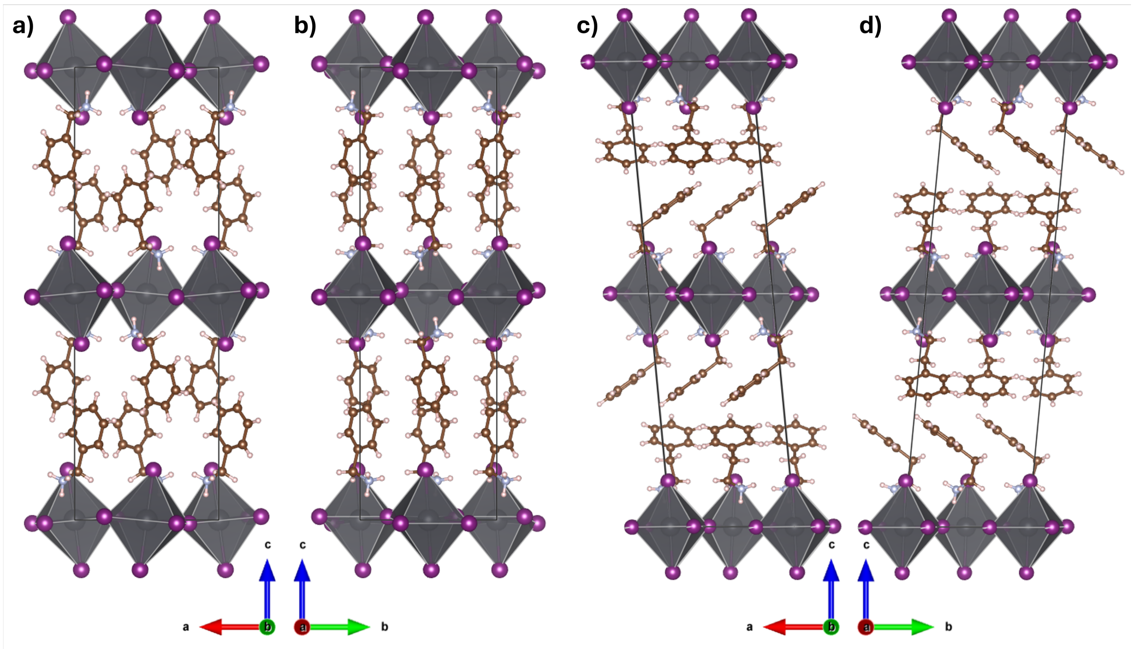

Figure 3.2: Single-crystal structures of the aromatic A' cation templated LPKs featured in this work. a) [100] projection and b) [010] projection of the PMA-templated structure. c) [100] projection and d) [010] projection of the PEA-templated structure (CCDC 1542461). Pb atoms are grey, I atoms are purple, C atoms are brown, N atoms are light blue and H atoms are white. Grey octahedra indicate PbI_6 units. *Single crystal structure refinement for PMA was carried out by Claire Wilson.*

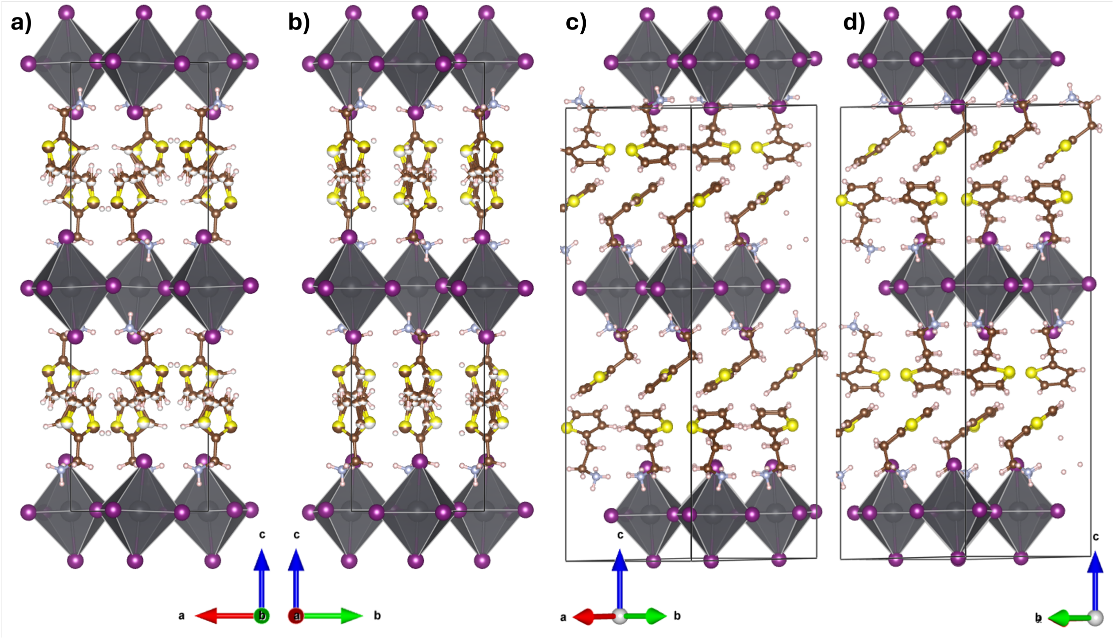

Figure 3.3: Single-crystal structures of the aromatic A' cation templated LPKs featured in this work. a) [100] projection and b) [010] projection of the ThMA-templated structure. c) [110] projection and d) [-110] projection of the ThEA-templated structure (CCDC 1043214). Pb atoms are grey, I atoms are purple, S atoms are yellow, C atoms are brown, N atoms are light blue and H atoms are white. Grey octahedra indicate PbI_6 units. *Single crystal structure refinement for ThMA was carried out by Claire Wilson.*

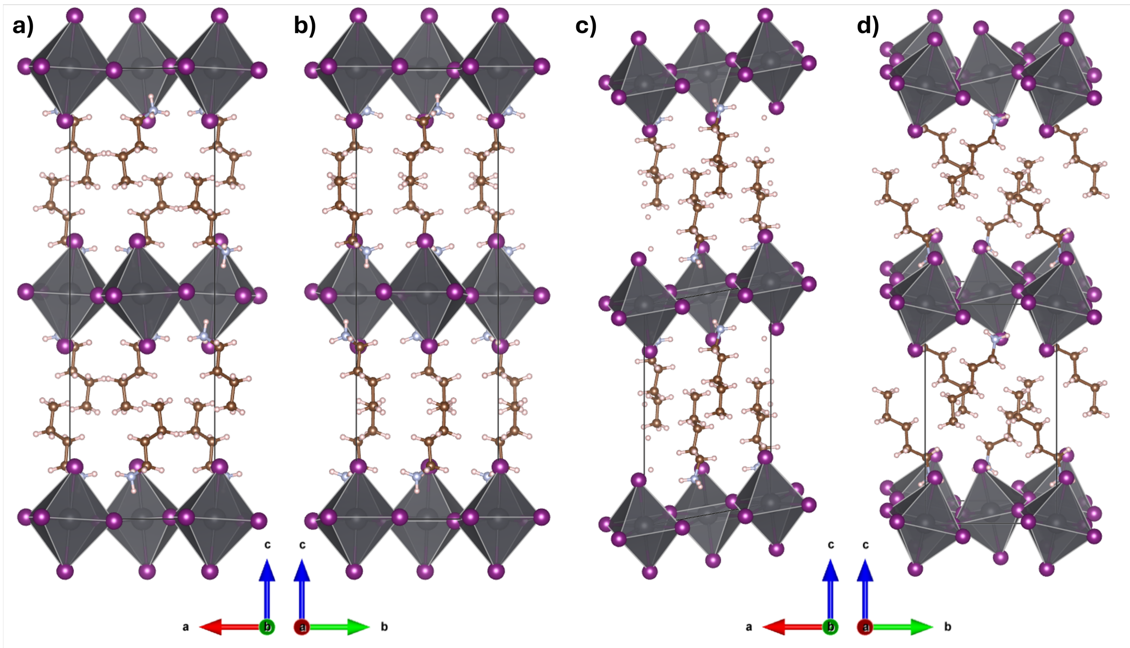

Figure 3.4: Single-crystal structures of the linear A' cation templated LPKs featured in this work. a) [100] projection and b) [010] projection of the ButA-templated structure (CCDC 665690). c) [100] projection and d) [010] projection of the PentA-templated structure (CCDC 665692). Note that two unit cells are displayed for the PentA structure for ease of comparison. Pb atoms are grey, I atoms are purple, C atoms are brown, N atoms are light blue and H atoms are white. Grey octahedra indicate PbI_6 units.

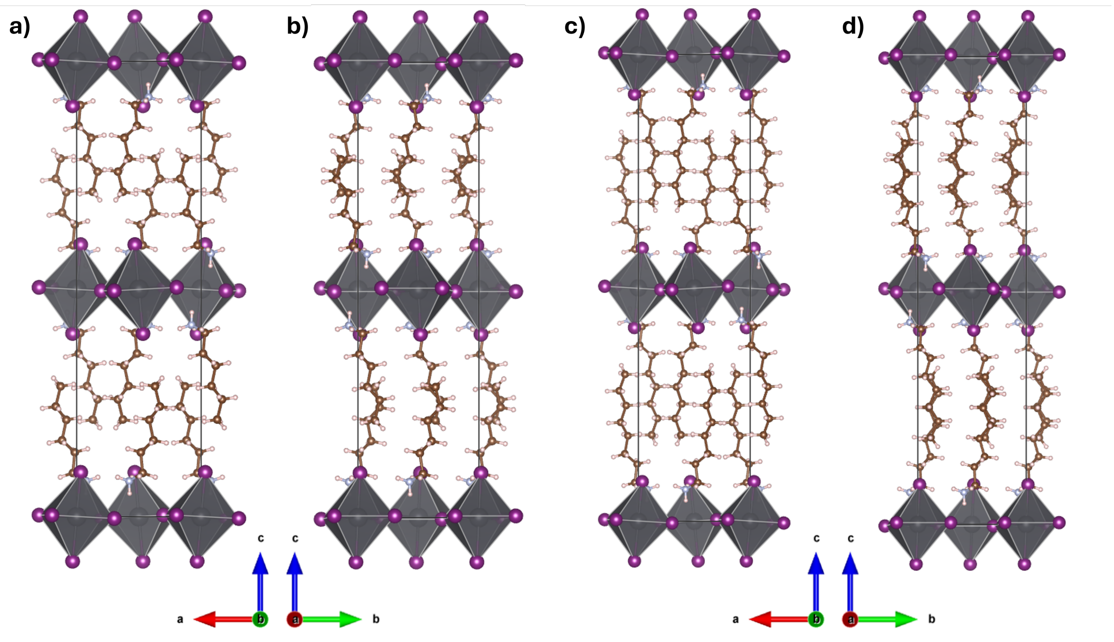

Figure 3.5: Single-crystal structures of the linear A' cation templated LPKs featured in this work. a) [100] projection and b) [010] projection of the HexA-templated structure (CCDC 665695). c) [100] projection and d) [010] projection of the OctA-templated structure (CCDC 805431). Pb atoms are grey, I atoms are purple, C atoms are brown, N atoms are light blue and H atoms are white. Grey octahedra indicate PbI_6 units.

Within the aromatic A' cation templated subset in Figs. 3.2 and 3.3, there is a distinct difference between the shorter chain methyl-linked A' cations, and the longer ethyl-linked A' cations. Here, the length of the linker determines the type of $\pi - \pi$ stacking. If the chain is only one carbon long, as in the PMA and ThMA structures, the A' cations show face-to-edge $\pi - \pi$ stacking interactions with the aromatic rings pointed along the *c* axis within the lattice, whilst being oriented perpendicular to one another in the *ab* plane. For A' cations with a two carbon linker chain, as in the PEA and ThEA structures, displaced parallel $\pi - \pi$ stacking is seen instead. The aromatic rings adopt a much more pronounced tilt within the layer, angling away from the *c* axis direction, whilst remaining parallel to one another in the *ab* plane. Fig. 3.6 illustrates this difference clearly, with [001] and [100] projections of the layers of PMA and PEA cations within their respective crystal structures. These two sets of $\pi - \pi$ stacking arrangements are also present within the ThMA and ThEA counterparts, indicating that it is the flexibility of the A' cation as a whole that directs how they will stack within the LPK structure, and that the presence of the thiophene unit does not affect the optimal packing to a significant degree. Crucially, the presence of $\pi - \pi$ stacking has been widely reported as a valuable interaction within the perovskite layer, as it has been identified with an increase in material stability.[67,167,175] These reports have largely focused on structures which display displaced parallel $\pi - \pi$ stacking. As such, studies into the impact of $\pi - \pi$ stacking interactions on the stability of LPKs should take into account and explore the impact of the different possible stacking arrangements. Equally, novel A' cations seeking to exploit these interactions must be carefully designed with the overall flexibility of the molecule in mind, so that the 'intended' type of $\pi - \pi$ stacking is present.

Furthermore, only the ethyl-linked LPK structures which have displaced parallel interactions contain a Van der Waals gap between the A' cation layers. This is often reported to be a general property of RP LPKs, and has been linked to poor out-of-plane conductivity and a reduced stability of the structure as a whole.[80,176,177] Other reports highlight the benefits of a Van der Waals gap and it's capacity to accommodate small molecular dopants into the LPK layer.[178] Regardless of its role, it is important to note that the appearance of this feature within the perovskite structure is highly dependent on the length of the linker between the amine and the rest of the A' cation. This suggests it can be controlled via chemical modifications of the A' cation which influence its flexibility, rather than solely being dependent on the presence of $\pi - \pi$ stacked aromatic moieties.

The set of linear A' cation templated perovskites in Figs. 3.4 and 3.5, shows far less variation in the A' cation packing. In all cases, the chains interdigitate to a large degree, with no Van der Waals gap and a high degree of uniformity. Instead, far greater variation is seen in the influence the A' cation has on the arrangements of the perovskite octahedra. Here, every A' cation with an even number of carbon atoms within the chain has an orthorhombic symmetry, with a flat and well-ordered perovskite backbone. The PentA-templated structure is notably different, with a smaller unit cell consisting of just one A' cation layer. It also has a lower symmetry, adopting a monoclinic structure despite having a Pb-Pb layer spacing in between the ButA and HexA structures as expected. Previous studies have identified these straight-chain based perovskites have a rich landscape of structural transitions across

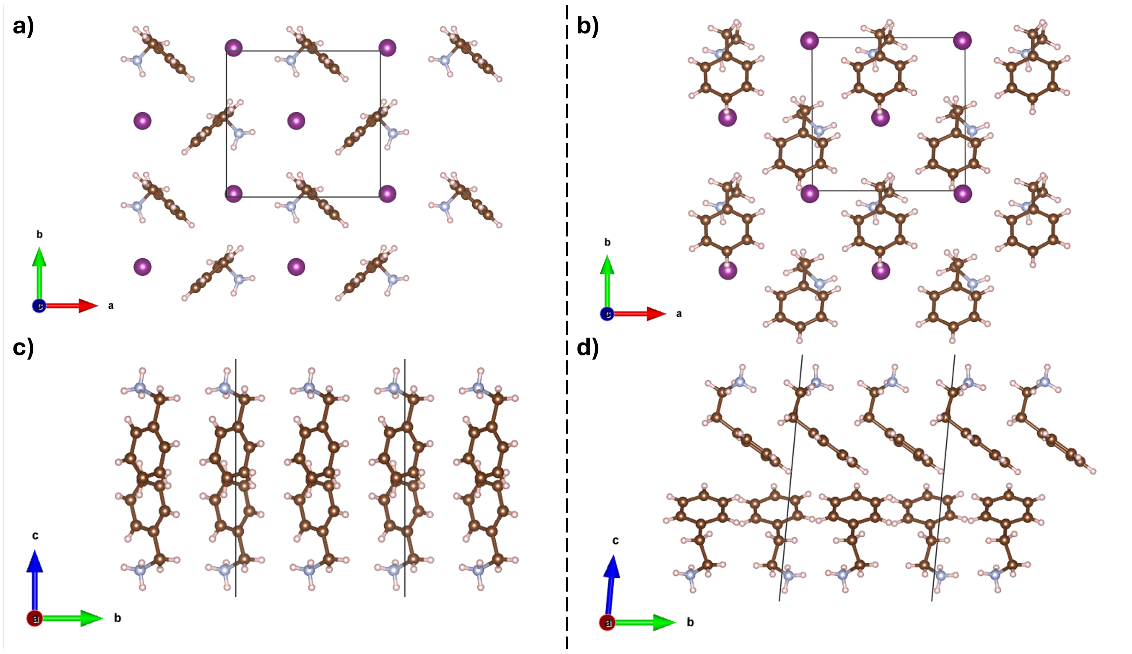

Figure 3.6: a) [001] projection and c) [100] projection of a sheet of PMA_2PbI_4, with A' cations showing face-to-edge $\pi - \pi$ stacking. b) [001] projection and d) [100] projection of a sheet of PEA_2PbI_4, with A' cations showing displaced parallel $\pi - \pi$ stacking. I atoms are purple, C atoms are brown, N atoms are light blue and H atoms are white.

a wide temperature range, with the PentA system adopting an orthorhombic structure similar to its even-numbered counterparts between 293 K and 333 K.[173] This suggests that an odd number of carbon atoms induces a higher energetic requirement for the structure to rearrange and adopt a symmetry closer to the even carbon systems. Indeed, literature reports have identified odd-numbered linear aliphatic chain A' cations to template structures with more distortion than their even-numbered counterparts.[179] Here, Density Functional Theory (DFT) calculations were used to identify the variation in chain packing, with odd numbers of carbons showing a far lower packing efficiency than chains with even numbers of carbons due to the orientation of the terminal C-C bond. For A' cations with an odd number of carbons, this poor packing effect leads to crystal structures with a lower symmetry and increased structural disorder.

The observed variations in perovskite sheets motivated further in-depth studies of how the cations influence the structure of the perovskite lattice. Here, a set of key parameters was determined for each structure with the use of VESTA software by measuring the Pb-I bond lengths and I-N distances, the Pb-I-Pb angles between two octahedral centres across the bridging iodine, the I-Pb-I angles within an octahedral unit, and by determining the nitrogen penetration depth parameter.[158] From these values, two additional indicators of octahedral distortion were derived, namely the Bond Distortion Index (BDI) and the Bond Angle Variance (BAV).[180,181] These quantify how much the Pb-I lengths and I-Pb-I angles vary from the average or optimal values within the octahedra, and are a good indicator of how much the perovskite structure has been distorted by the A' cations present within.[44] Sets of these values for the aromatic and linear structures are listed in Table 3.2 and plotted

Table 3.2: Parameters used as indicators of structural distortion, obtained from single crystal data. Values in brackets indicate the ESD for each parameter.

A' Cation	Pb-Pb Dist.	Pb-I-Pb Angle	Av. Pb-I Dist.	Av. I-N Dist.
PMA	14.380(1) Å	158.40(1)°	3.2068(2) Å	4.552(3) Å
PEA	16.355(2) Å	153.31(3)°	3.1890(3) Å	4.459(7) Å
ThMA	14.39(4) Å	153.57(3)°	3.164(2) Å	4.411(7) Å
ThEA	15.688(2) Å	152.83(3)°	3.1829(3) Å	4.433(4) Å
ButA	13.801(1) Å	155.08(3)°	3.1882(3) Å	4.476(5) Å
PentA	14.645(3) Å	153.68(3)°	3.1878(3) Å	4.471(7) Å
HexA	16.351(1) Å	155.65(5)°	3.1943(6) Å	4.499(9) Å
OctA	18.741(2) Å	156.05(4)°	3.1963(4) Å	4.508(8) Å
A' Cation	N Pen. Depth	BAV	BDI	
PMA	0.661(5) Å	11.96(3)	0.0030(1)	
PEA	0.571(13) Å	3.64(3)	0.0056(1)	
ThMA	0.525(14) Å	7.68(7)	0.0057(5)	
ThEA	0.546(9) Å	3.93(3)	0.0076(1)	
ButA	0.589(10) Å	5.63(3)	0.0031(1)	
PentA	0.592(16) Å	5.68(2)	0.0033(1)	
HexA	0.621(19) Å	6.67(6)	0.0025(2)	
OctA	0.623(15) Å	6.88(6)	0.0017(1)	

in Figs. 3.7, 3.8 and 3.9. Further details on how the nitrogen penetration depth, BAV and BDI were calculated are given in the methods, section 2.8.2. Numbers in brackets in the table indicate the Estimated Standard Deviation (ESD) for each parameter.

Comparisons of the collected parameters show that it is difficult to draw clear links between the detailed structure of the perovskite and the A' cation chemistry that hold across the full set of samples studied. The variation in Pb-Pb layer spacing, shown in Fig. 3.7 (a), black curve, follows the expected trends, increasing with additional carbon atoms in the structure. The Pb-I-Pb angle (red curve) shows the distortion of the perovskite lattice, with smaller angles indicating a more distorted arrangement of octahedra.[41] In the case of the aromatic A' cations, an increase in Pb-Pb layer spacing correlates with greater distortion of the perovskite backbone, as indicated by the reduction of the inter-octahedral Pb-I-Pb angle. For the aliphatic A' cations the opposite trend is broadly true, with the even-numbered series showing an increase in spacing and Pb-I-Pb angle. The odd-numbered PentA cation is again an outlier from its even-numbered counterparts, with a significantly more pronounced lattice distortion as indicated by the small Pb-I-Pb angle. This suggests the nature of the A' cation packing drives the configuration of the perovskite sheet. Here, parallel $\pi - \pi$ stacked A' cations which lie in isolated sheets force the perovskite lattice to compress and distort with small Pb-I-Pb angles, whilst the face-to-edge $\pi - \pi$ stacked or aliphatic A' cations interdigitate instead, thus being more able to accommodate a perovskite backbone with inter-octahedral angles closer to 180°. It is important to note that even within this small sample size, exceptions to

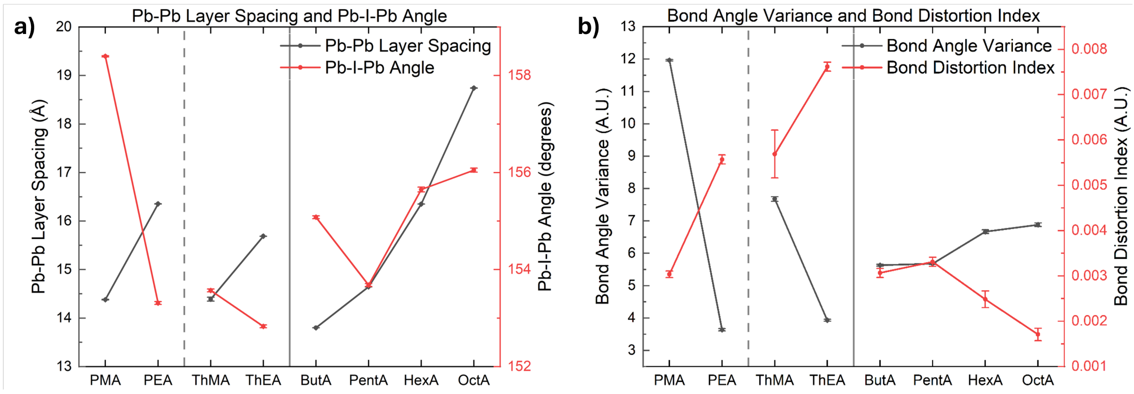

Figure 3.7: Comparisons of how changing A' cation chemistry and increasing carbon chain length influences: a) Pb-Pb layer spacing and Pb-I-Pb angles, b) Bond Angle Variance (BAV) and Bond Distortion Index (BDI). Trend lines join sets of A' cations which only vary by the length of the carbon chain, to illustrate the corresponding impact on structural parameters. *Error bars have been included in the figure, but may be obscured by the data range and marker size.*

this broad observation appear. The thiophene-based A' cations show this behaviour to a much smaller extent, and the PentA templated structure shows small Pb-I-Pb angles despite a good degree of interdigitation.

The two indicators of octahedral distortion - BAV and BDI, shown in Fig. 3.7 (b) - appear to occur in opposition to one another. As the A' cation length is changed within each subset, as one parameter increases, the other decreases. Here, large BAV values which indicate octahedra with angles away from the expected 90° occur in samples with low lattice distortion, as indicated by Pb-I-Pb angles closer to 180°. As the lattice distortion is increased, the octahedral angles move closer to 90°, and the Pb-I bond lengths begin to vary instead leading to a high BDI value. The small size of the error bars, derived from the ESD values, shows that the two parameters are indeed heavily influenced by the A' cation in the lattice. This suggests that when the lattice as a whole distorts, the octahedra can adopt a more optimal shape, and compensate for this by varying the metal-halide bond lengths.

The strength of the A' cation-halide interaction has been previously linked to the average I-N distance, with smaller values indicating a stronger bond, which are plotted in Fig. 3.8 (a), black curve.[67] The pronounced difference in I-N distances within the set of four aromatic A' cations is unexpected, given that the chemistry of the cation 'body' would be expected to have a minimal impact on the hydrogen bonding interactions. Counter-intuitively, the presence of a thiophene moiety leads to the shortest I-N distances, despite the fact that the electron-rich S atom is a potential site for intramolecular hydrogen bonds, which should lead to a weaker A' cation-halide bonding interaction. It is unclear why the opposite behaviour is observed, and why the two ethyl linked aromatic cations - PEA and ThEA - show opposing changes in I-N bond length when compared to PMA and ThMA. The behaviour of the linear aliphatic A' cation set shows much less variation, with the differences between I-N distances not significantly larger than the errors due to the estimated standard deviations. This could indicate that the I-N distance variation seen is rel-

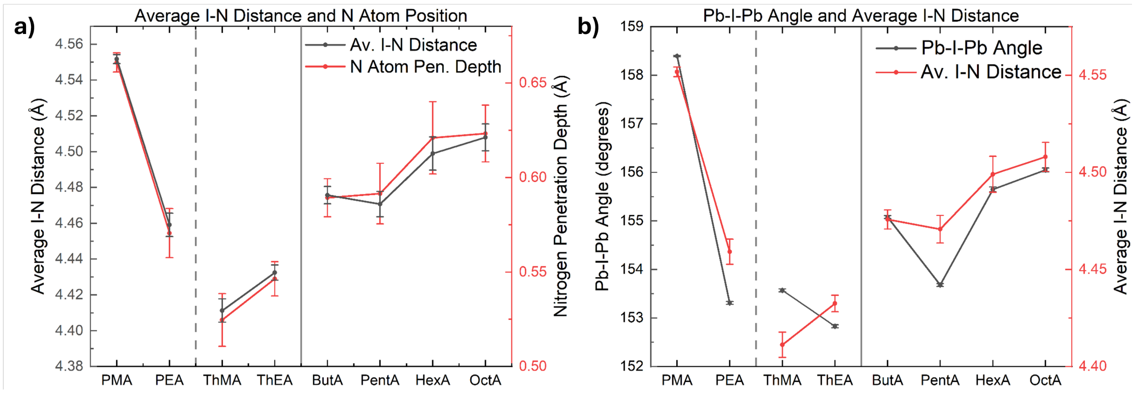

Figure 3.8: Comparisons of how changing A' cation chemistry and increasing carbon chain length influences: a) Average I-N distance and nitrogen penetration depth. b) Average I-N distance and Pb-I-Pb angle. Trend lines join sets of A' cations which only vary by the length of the carbon chain, to illustrate the corresponding impact on structural parameters. *Error bars have been included in the figure, but may be obscured by the data range and marker size.*

atively low, and an A' cation which has a significant impact on the I-H-N hydrogen bonding would need to be studied to observe a meaningful difference in the interaction. It is also important to note that the average I-N distance correlates perfectly with a shallower nitrogen penetration depth, indicating that strong A' cation-halide interactions pull the cation out of the void between the perovskite octahedra and more in-line with the terminal iodine atoms. Fig. 3.8 (b) shows that the I-N distance also correlates very strongly with the reduction of Pb-I-Pb angles away from 180°. Here, stronger A' cation-halide bonding acts to tilt the lattice, reducing the Pb-I-Pb angles as the A' cations and terminal iodine atoms move closer together, which has been previously observed in the literature.[170]

Finally, looking at the distortion of the octahedra themselves, A' cations which sit deeper in the perovskite lattice correlate with a greater degree of BAV, as shown in Fig. 3.9 (a). This suggests that an A' cation which has weaker bonding interactions with the halide ions and greater I-N distances sits deeper in the lattice and ultimately distorts the shape of the octahedra themselves. When the A' cation-halide interactions are strong and I-N distances are small, the BDI increases instead as the balance of the Pb-I bonding interactions is changed within the structure and the iodide atoms are drawn away from the lead centre. An alternative explanation can be proposed if we look at the average bond length and the nitrogen penetration depth, shown in Fig. 3.9 (b). Here, the structures which show the deepest nitrogen penetration have the longest average Pb-I bond distances. As such, the position of the nitrogen in the lattice closer to the plane of Pb atoms may simply be a consequence of the octahedra themselves expanding. For the aliphatic A' cation set, greater nitrogen penetration depth follows the trend of increasing A' cation length and Pb-Pb layer spacing, suggesting that the structure as a whole simply expands. The phenyl-based aromatic A' cations display a contrary behaviour, however, suggesting the link between the octahedral size and the overall Pb-Pb layer spacing is more complex.

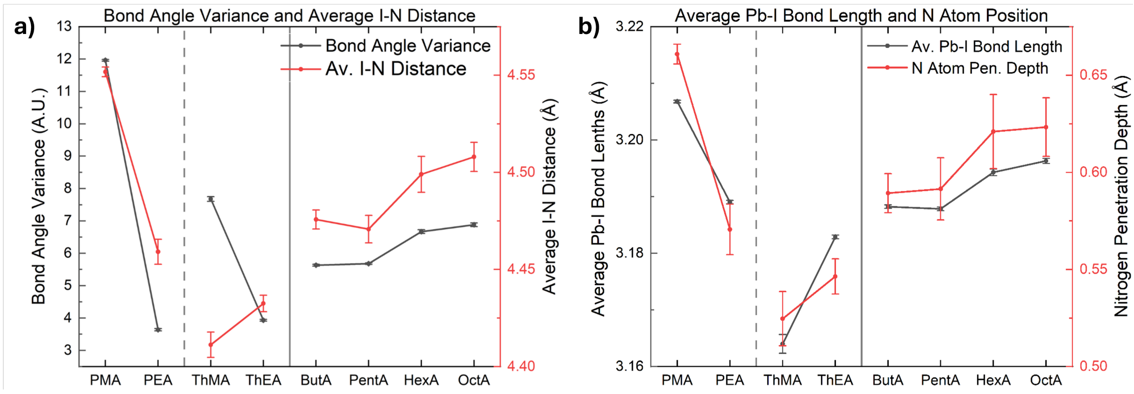

Figure 3.9: Comparisons of how changing A’ cation chemistry and increasing carbon chain length influences: a) BAV and average I-N distance, b) Average Pb-I bond lengths and nitrogen penetration depth. Trend lines join sets of A’ cations which only vary by the length of the carbon chain, to illustrate the corresponding impact on structural parameters. *Error bars have been included in the figure, but may be obscured by the data range and marker size.*

Overall, the study of links between A’ cations and the crystal structures shows that perovskite structures are highly varied, and it is difficult to predict how a given chemical modification can change the A’ cation arrangement, perovskite lattice bonding, or the distortion of the octahedra themselves. For example, the presence of $\pi - \pi$ stacking interactions can increase or decrease the strength of the A’ cation-halide bond, depending on the precise nature of the aromatic system present. Additionally, it is difficult to determine which of the observed correlations is the ‘driving force’ behind the observed trends in related parameters. This is contrary to the hypothesis developed when the work in this chapter began, which proposed strong correlation between the A’ cation chemistry and the perovskite structure. Furthermore, other chemical modifications outside the scope of the compounds studied can introduce additional elements of complexity. For example, changes to the cross-sectional area of the A’ cation will impact the efficiency with which it can pack in-between the octahedral layers. The inclusion of heteroatoms in different positions can be used to tweak the bonding between A’ cation sheets, or the A’ cations and the halides of the perovskite lattice. This highlights the need for expanding such structural analysis to include additional A’ cations which fall within the broad chemical families studied here, but expand the synthetic parameter space in a systematic way. Without the development of a more robust dataset which can identify which LPK parameters are most sensitive to A’ cation chemistry, gaining insights into how a novel A’ cation may impact a perovskite lattice can only be carried out by direct analysis of crystal structures.

3.3 Correlating LPK structural parameters with optoelectronic properties

Tailoring energetic alignments and maximising conductivities is key for practical applications of LPKs, such as solar cells. The optoelectronic properties of the LPK are largely dictated by the underlying perovskite lattice, which is indirectly influenced by the A' cation as discussed in detail above. It is therefore highly beneficial to explore how varying the A' cation chemistry impacts the properties of the resulting material. Here, UV-Vis absorption and PL emission spectra were collected for each A' cation, and the in-plane and out-of-plane charge transport properties were determined. In each case, polycrystalline thin-film samples were used, with the details of the deposition included in methods section 2.4. This allowed for an overview of the most relevant properties for the applications of LPKs within devices, which were hypothesised to be determined by a combination of the A' cation chemistry, and the distortions of the perovskite lattice.

The complexity of the structure-property landscape of layered perovskites can be seen in the plot of their absorption and emission profiles, shown in Fig. 3.10. Whilst they broadly cover a similar range of wavelengths and feature a similar Stokes shift of around 40 meV (9 nm), the case-to-case variation as carbon atoms are added to the A' cations is unintuitive. For the aromatic A' cations, an extra carbon atom shifts the PL peak of the PEA structure 14 meV higher (- 3.1 nm) than the PMA structure, whilst the ThEA peak is 6 meV lower (+ 1.4 nm) than the ThMA peak. For the linear chains, the even-numbered materials emit within 7 meV of one another, but the odd-numbered PentA-templated structure emits an an energy around 60 meV higher. To rationalise these behaviours, the PL peak energy was plotted as a function of a pair of structural parameters. Numerous reports have linked a higher degree of lattice distortion and smaller Pb-I-Pb angles to a wider bandgap and higher PL peak energy.[64,67,168,182,183] Fig. 3.11 (a) shows that whilst the general trend is indeed that a smaller, more distorted Pb-I-Pb angle leads to a higher energy PL peak, there is little overlap between the two sets of A' cations studied, with the linear A' cations showing a far greater sensitivity than aromatic ones to changes in the bond angle. Quantifying this trend with linear fits gives poor results, with the linear A' cations having an R^2 value of 0.78, and the aromatic A' cations only 0.58. Indeed, if the PMA and PentA samples were excluded and the remaining A' cations were treated as one dataset, the trend appears to reverse with bigger Pb-I-Pb angles correlating to a wider bandgap. There is also little correlation between the PL peak energies and the BAV parameters indicating the distortion of the octahedra themselves (Fig. 3.11 (b)). This is unexpected, given that the bandgap of a perovskite is determined by the overlap of Pb 6s / 6p and I 5p orbitals.[40,41] As such, any distortion of the octahedra should directly impact the relative geometry of the atoms, the degree of their orbital overlap and thus the band structure of the material. It is important to note that the Pb-I-Pb angle or BAV individually do not fully capture how the atomic orbital overlap changes between structures, as it will be influenced by variations in all of the interatomic angles and Pb-I distances simultaneously. Instead of looking at one of the structural parameters in isolation, a compound function may need to be developed which can fully characterise how the distortion of the perovskite network is changing the bandgap of the material.

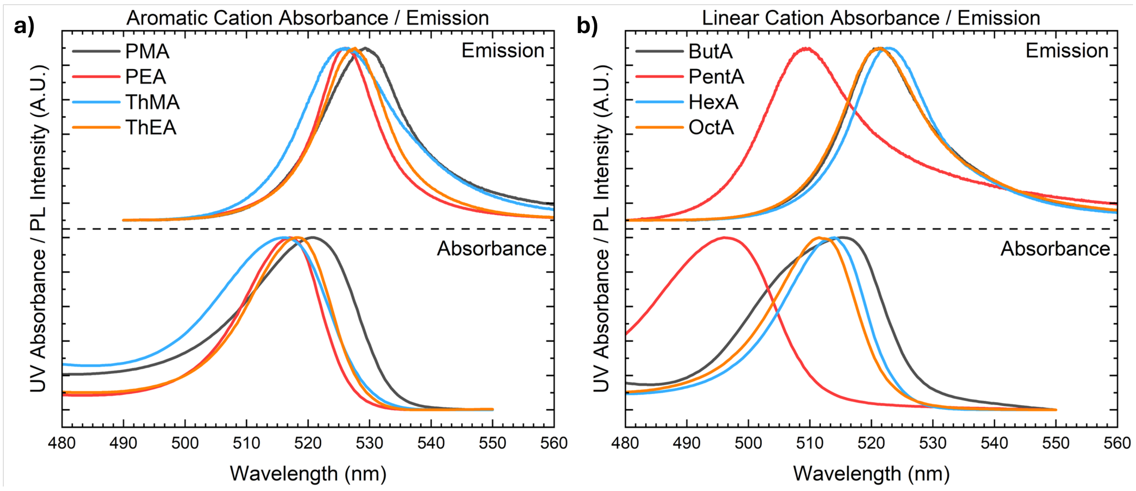

Figure 3.10: Normalised UV-Vis/PL spectra of a) aromatic and b) linear A' cation templated thin films of $(A')_2PbI_4$ perovskite. *All PL measurements were carried out by Paula Lalaguna.*

A further potential explanation for this poor correlation stems from the 'soft' nature of the perovskite structure.[184,185] The time-averaged structure obtained during single crystal measurements may not accurately reflect the actual shape of the perovskite lattice, which distorts under illumination.[186–188] This process occurs due to lattice-phonon interactions and is influenced by the stiffness of the A' cation backbone, suggesting more in-depth studies of the interactions within the layer are needed to be able to predict how PL emission will change. An alternative explanation to this disconnect has been proposed by Sichert. et. al., who identified that smaller A' cations do not sufficiently screen interactions between the separate perovskite layers.[182] This leads to the formation of 'minibands' within the quantum-well energetic landscape of the perovskite. Instead of discrete energy levels, 'minibands' create a continuum of allowed energy states for charge carriers to occupy within the conduction and valence bands, which extend into the energetic 'wells'. This effectively narrows the band gap and decouples it from the structure of the octahedra. As such, great care must be taken when correlating changes in the bandgap of a sample to structural variations, as numerous other effects may be at play which cannot be captured by time-averaged structural characterisation such as single crystal measurements.

As well as the bandgap energy, charge transport is a key metric for the implementation of perovskite materials. Here, the presence of the organic A' cation layers splits the network of conductive octahedra of the perovskite and thus greatly influences the movement of charge through and across the LPK layers. The in-plane conductivities of the LPKs were measured by depositing a thin film of perovskite within a channel etched in ITO-coated glass as detailed in methods sections 2.6.4 and 2.8.3. Due to the preferential orientation of the perovskite sheets parallel to the substrate surface, the conductivity across the etched channel corresponds to the conductivity of the material in the plane perovskite layer. The obtained values are plotted against the Pb-I-Pb angle and the BAV, shown in Fig. 3.12 a) and b). These were chosen to represent the distortion of the overall lattice and of the individual

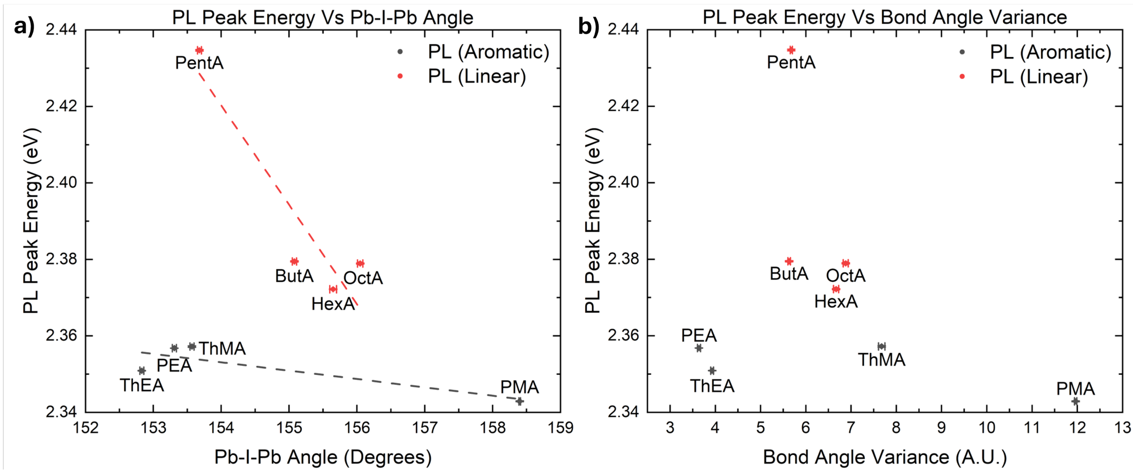

Figure 3.11: PL peak energies of of $(A')_2PbI_4$ perovskite plotted vs a) the Pb-I-Pb angle, and b) the BAV. Dashed lines indicate linear fits of the aromatic or aliphatic cation groups. *Error bars have been included in the figure, but may be obscured by the data range and marker size.*

octahedra respectively. Here, smaller Pb-I-Pb angles correlate with an increased conductivity of the layered perovskite material, whilst the BAV shows the opposite behaviour. The results show that the most conductive samples have uniform internal Pb-I angles close to 90° within a relatively distorted, closely packed octahedral lattice with small Pb-I-Pb bridging angles. This shows that instead of a requirement of an undistorted octahedral sheet, where Pb-I-Pb angles close to 180° lead to uninterrupted pathways for the movement of charge and the best performance, the in-plane conductivity of the perovskite depends far more on the orbital overlap within a single octahedral unit. Unexpectedly, this also suggests that both axial and equatorial Pb-I interactions influence the conductivity across the perovskite sheet. This balance of intra-octahedral BAV distortion versus inter-octahedral Pb-I-Pb angle distortion is in turn sensitive to the packing of the A' cations themselves. The rigid, $\pi - \pi$ stacked A' cation networks of PEA and ThEA which contain a Van der Waals gap help to template perovskite sheets with the highest conductivity, whilst the interdigitated aromatic PMA and ThMA cations and the linear A' cations show much lower conductivity values. The higher conductivity values of PEA and ThEA are not a consequence of the inclusion of an aromatic unit, as changing the type of π-stacking from displaced parallel to head-to-tail arrangements of the PMA and ThMA films leads to a sharp reduction in conductivity. This difference occurs despite the fact that such chemically similar pairs of A' cations should have minimal differences in properties such as dielectric constant. Thus, these results show that it is the interplay between A' cation packing and the resulting impact they have on the distortion within the perovskite octahedral sheet that is of greatest importance. In order to determine the impact of changing the chemistry of the cation on the conductivity of the sample, the change in structural parameters must be identified first.

The preferential planar orientation of LPKs means that the out-of-plane conductivity, across the alternating sheets of A' cation and perovskite, is what influences its performance within a device. The conductivity of LPKs has been widely reported to have a strong degree of anisotropy, with out-of plane values being much

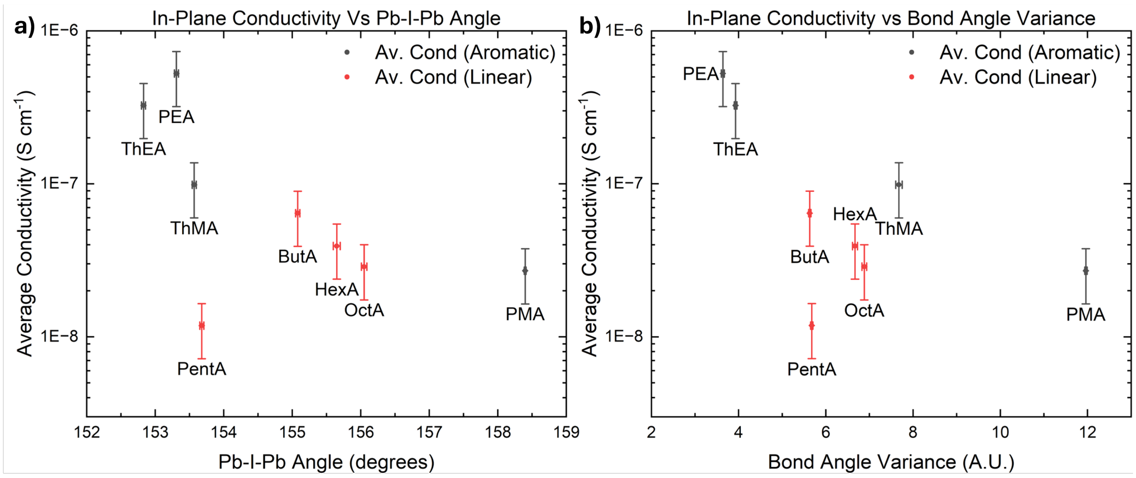

Figure 3.12: In-plane conductivity values of thin films of $(A')_2PbI_4$ perovskite, plotted against a) the Pb-I-Pb angle, and b) the BAV.

lower than the in-plane counterparts.[87,88] This makes a direct determination of this value difficult, due to the limitations of film thickness and the low currents involved. By preparing LPKs in a solar cell configuration and measuring their performance, their out-of-plane conductance can be determined instead. In a full device, the n = 1 perovskite layer acts as the main source of series resistance, due to the multiple quantum well-like structure of the layered material, and their perfect alignment parallel to the substrate. Thus, the conductance of the material can be extracted from the gradient around the V_{OC} of the device. It is important to note this method only applies to the pure $n = 1$ perovskite. The presence of vertically oriented phases, or more conductive perovskite phases, renders this approach invalid. Devices were successfully fabricated for five of the A' cations studied following the method detailed in section 2.5.2, with the PentA, HexA and OctA-based devices showing extremely poor wetting of the hole transport layer required to complete a functioning solar cell.

The values of the out-of-plane conductance plotted vs the Pb-Pb layer spacing and Pb-I-Pb angle are shown in Fig. 3.13. Here, for the two aromatic A' cation groups a reduction in the layer spacing between the perovskite sheets leads to a reduction in the resistance within the material. Given the commonly reported tunnelling mechanism behind charge transport across the octahedra / A' cation stack, it follows that a reduction in the 'quantum well width' results in easier movement of charges.[67,83,84] Equally, samples with a larger Pb-I-Pb angle have higher conductance values. It is important to note that in the case of the out-of-plane measurement, the highest values are seen for the methyl-linked aromatic A' cations, which is the opposite trend to what was seen in the in-plane measurements. This suggests that highly ordered, uniform A' cation sheets and the presence of the Van Der Waals gap ultimately hinders charge transport through the stacked layers of material.

The studies into LPK structure-property relations revealed that, somewhat unexpectedly, it is very difficult to draw meaningful links between how a given A' cation family may influence the perovskite lattice and thus its optoelectronics. By and large, the structures and behaviours of linear systems differed greatly from the aromatic counterparts. Even when clear patterns in the structure variation are ob-

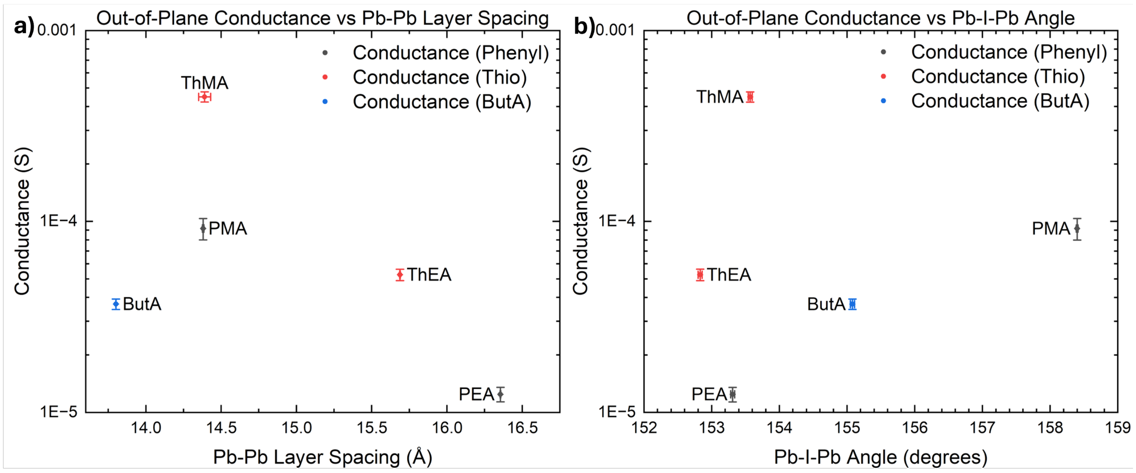

Figure 3.13: Out-of-Plane conductance values for solar cell stacks based on $(A')_2PbI_4$ thin films, plotted vs a) the Pb-Pb layer spacing, and b) the Pb-I-Pb angle. *Error bars have been included in the figure, but may be obscured by the data range and marker size.*

served, such as in the case of the phenyl- and thiophene-based aromatic A' cations, this does not extend to the variation in PL energies. This lack of correlation indicates that the properties of a perovskite have a more complex relationship with the component A' cations than initially hypothesised. The structural parameters commonly used to rationalise variations between two different perovskites, such as BAV, BDI or nitrogen penetration depth do not reliably correlate to measurable values such as PL or conductivity. This could be due to the fact that the time-averaged single crystal structures do not reflect the 'actual' state of the perovskite when measured under illumination or bias, and thus are not sufficiently representative of the samples they are compared with. Another explanation for the lack of clear trends is that the chosen family of closely chemically related A' cations is too alike in terms of both structure and optoelectronic properties, and expanding the chemical variation of the A' cation will lead to perovskites with significantly different structures which will allow clearer trends to be obtained. Alternatively, the key structural parameters that govern the properties of the perovskite have not been identified and analysed to find more reliable correlations. Thorough characterisation of both known and novel LPK compounds to develop a reliable and representative dataset will be needed to identify the complex interplay between the A' cation and the perovskite as a whole.

3.4 Investigation of mixed A' cation systems

The aim of understanding structure-property relations between A' cations and perovskite optoelectronics was to help guide novel A' cation design, and to allow the fine tuning of material parameters such as Pb-Pb layer spacing or PL peak energy. Unfortunately, the fundamental properties of LPKs make drawing clear conclusions regarding the link between the two very difficult. This complexity can be exploited, however, by adopting a mixed-cation approach. By simply combining two known and widely used A' cations within the same LPK, the A' cation-cation and A' cation-halide interactions influencing the structure of the material will be changed, potentially unlocking a way of subtly tweaking the optoelectronic properties. This approach has been widely used in mixed-halide systems to tune the perovskite bandgap to a great degree.[47,48] Varying the RP A' cation component instead has the key additional benefit of the much lower ionic mobilities of the bulky organic A' cations, which will limit issues associated with phase segregation of such mixed systems.[119,189]

To explore this hypothesis, a set of perovskite films formed from a 50-50 combination of two A' cations were prepared, and characterised according to the techniques used in the section above. The corresponding XRD diffractograms are shown in Figs. 3.14 and 3.15, shown alongside diffractograms of thin films made from just one of the component cations. These focus on just one of the LPK peaks, to more clearly show the subtle changes in the lattice parameters. The full diffraction patterns included in the appendix, Figs. A.9 - A.11. Here, three behaviours are observed, referred to as Type 1 - 3. For samples showing Type 1 mixing, shown in Fig. 3.14 (a), two distinct peaks are visible in the diffractogram. Here, the A' cations only partially mix together, and phase-separated perovskites occur alongside a phase which contains a disordered mix of the two component A' cations. The disordered mixed A' cation phase corresponds to the larger of the two peak seen in the diffractogram, which has a lattice spacing approximately matching an average of the two A' cations. Additionally, distinct peaks corresponding to domains of pure PEA or ThEA-templated perovskite are still clearly visible as shoulders in the diffractograms. This Type 1 mixing only occurs for combinations of the ethyl-linked aromatic spacers with the linear chains, indicating that the highly uniform displaced parallel π-π stacking interactions create an energetic barrier to an effective mixing of the A' cations, and a uniformly disordered phase is kinetically unfavourable.

Type 2 mixing, shown in Figs. 3.14 (b) and 3.15 (a), is indicated by a single averaged peak in the sample diffractogram. It occurs when a single phase containing a disordered mix of the two component A' cations throughout the structure is formed. Here, the sample displays an overall lattice spacing that lies in between the two constituent A' cations, as in the PEA + ThEA mix, or is dominated by the component with the wider spacing, as in the case of the PMA + ThMA mix. This type two behaviour occurs whenever structurally analogous A' cations are mixed. It follows that A' cations which have similar packing will mix well to form an intermediate-spaced structure, without any large regions of one phase pure A' cation. It is noteworthy that the ButA cation mixes very well with the other A' cations forming the fully disordered Type 2 structures, with the ThEA + ButA mix being the only outlier.

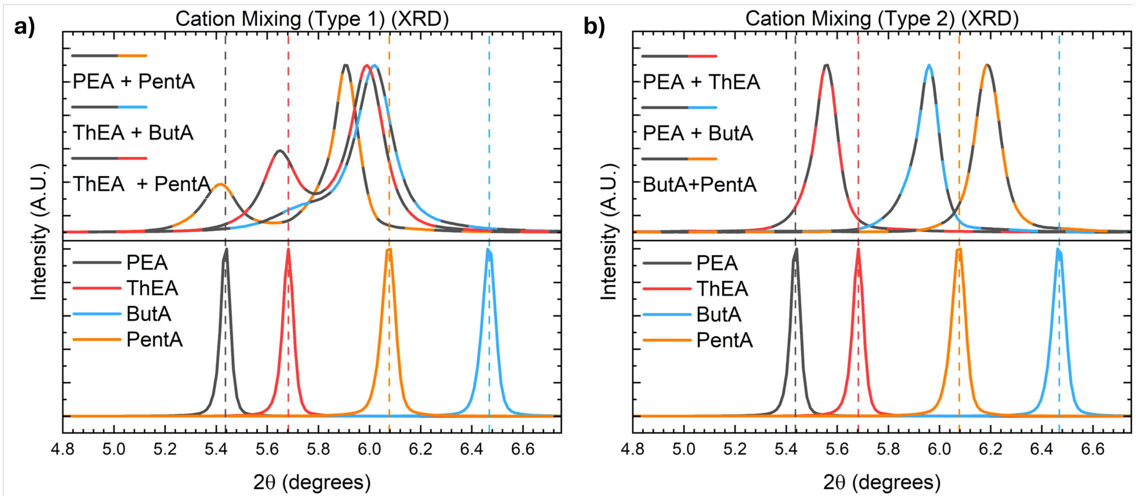

Figure 3.14: XRD diffractograms showing the first (002) peak of mixed A’ cation films, compared with mono-cation counterparts. a) Type 1 mixing, showing an intense disordered phase with an averaged lattice spacing of the two component cations and a shoulder corresponding to an aromatic cation phase. b) Type 2 mixing, showing a single disordered phase with an averaged lattice spacing of the two component cations.

This suggests that the shorter chain with less potential for intermolecular Van der Waals interactions is highly suited to act as a soft ‘packing cation’, where it can fit in-between various other A’ cation packing arrangements.

The most interesting mixing behaviour is Type 3, which is shown in Fig. 3.15 (b). When the shorter-chained PMA and ThMA A’ cations are mixed with the linear aliphatic A’ cations, they template structures which have a spacing greater than the two individual components. This indicates the mixed A’ cation interaction can be more complex than a simple averaging of the two components within the lattice, especially when face-to-edge $\pi - \pi$ stacked and straight chain aliphatic A’ cations with matching interdigitated packing are combined. The PMA + PentA structure is particularly noteworthy, as there are three distinct phases visible in the diffractogram which closely matched lattice spacing. These become easier to distinguish at higher 2θ values, as seen in Fig. A.11 (d). All of these phases have a spacing that is significantly larger than the constituent single-cation LPKs, suggesting that three distinct, fully disordered arrangements of cations are present within the material.

The compositions leading to Type 3 structures were chosen for more in-depth analysis, with single crystals of the PMA + ButA mixed system successfully obtained. The structure of the resulting $PMA_1ButA_1PbI_4$ perovskite is shown in Fig. 3.16 (a) and (b). Note that the as the single crystal structure is defined with the a axis as the longest, the projection axes are different to the mono-cation samples seen previously. The observed orientation of the sample remains the same, however. The two A’ cations overlap within the structure, giving the appearance of a high degree of disorder. However, isolating the two components allows their orientation and packing structure to be resolved. As shown in Fig. 3.16 (c-f), the cation packing remains highly ordered, despite the presence of two compounds within the organic A’ cation sheet. The PMA cations maintain the face-to-edge $\pi - \pi$ stacking, and both cations remain interdigitated. Indeed, the configurations differ very little from the packing

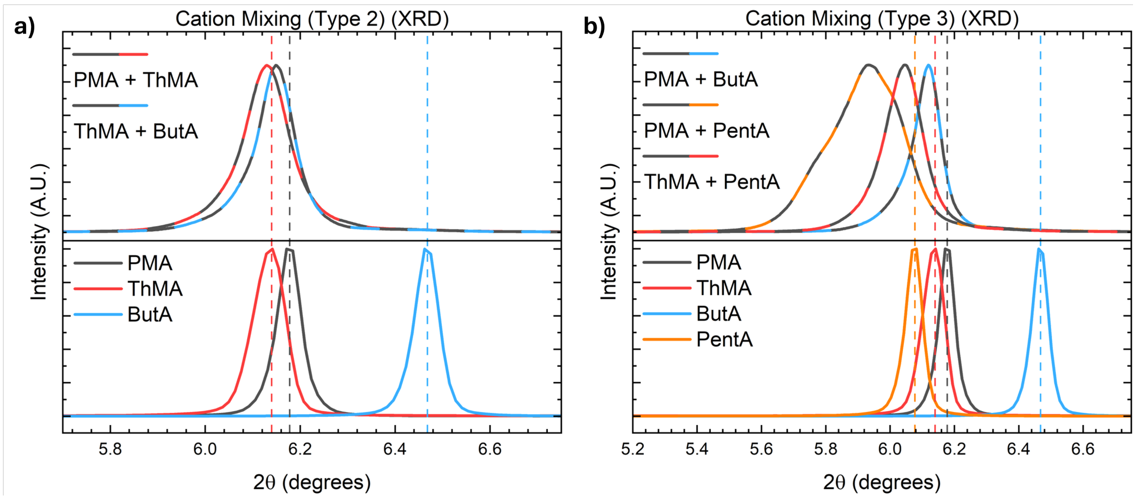

Figure 3.15: XRD diffractograms showing the first (002) peak of mixed A' cation films, compared with mono-cation counterparts. a) Type 2 mixing, showing a single disordered phase with an averaged lattice spacing of the two component cations. b) Type 3 mixing, showing a single disordered phase with a new, larger Pb-Pb layer spacing that does not match to the two component cations.

seen in the matching single-cation PMA_2PbI_4 and $ButA_2PbI_4$ compounds, as highlighted in Fig. 3.17. Here, only minor differences in the angles the cations adopt within the lattice are distinguishable. This clearly shows that even though the A' cations mix to a sufficient degree to avoid forming domains which can be detected in the single crystal structure, their local, short-range ordering is relatively unchanged. Whilst the A' cation sheets show a minimal difference upon mixing, measurements of the structural distortion parameters show that the perovskite sheet differs significantly from the pure-cation cases, as listed in Table 3.3. The overall lattice is more distorted, with a smaller Pb-I-Pb angle and a smaller average I-N distance. Crucially, both indicators of octahedral distortion - BAV and BDI - are greatly reduced within the mixed crystal. This occurs despite the nitrogen atom sitting far deeper within the lattice, which previously was found to correlate with greater distortion of the octahedra. Here, it is likely that mixing the two different A' cations leads to less-favourable cation-cation interactions where the respective $\pi - \pi$ and Van der Waals interactions are interrupted, forming a less 'rigid' A' cation layer. This allows the lattice as a whole to adopt the most favourable structure, whilst minimising the distortions within the Pb-I bonds present in the octahedra.

3.4.1 Mixed A' Cation Optoelectronic Properties

PL data collected for mixed A' cation thin film samples are shown in Figs. 3.18 and 3.19. Here, a complex landscape of behaviours emerges, that does not strictly follow the different types of mixing as indicated by the XRD study. For the PEA + PentA, ThEA + ButA and ThEA + PentA samples (Fig. 3.18 (a)), the PL has clear shoulders in the 500 nm region, suggesting the formation of wide-bandgap regions of perovskite. Here, combining the highly uniform π-stacked aromatic A' cations with aliphatic chains acts to increase the overall disorder in the structure and widen the bandgap, even if the A' cations do not fully mix. Indeed, the PEA + ButA structure which forms a uniformly disordered Type 2 LPK shows the most

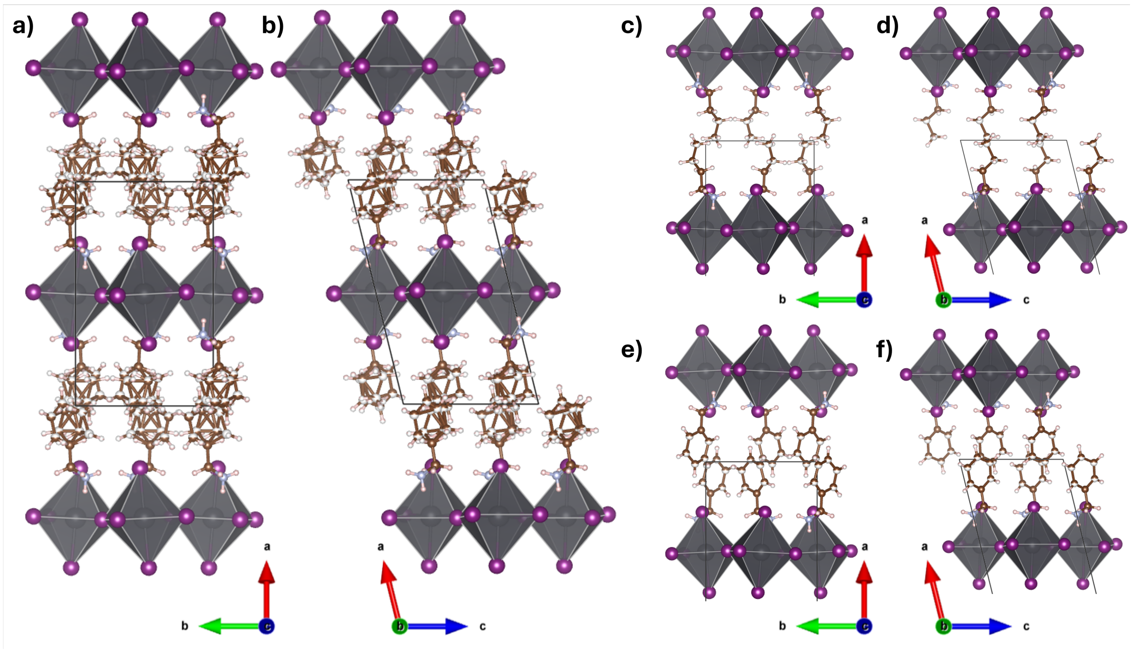

Figure 3.16: Single-crystal structure of the mixed PMA + ButA LPK. a) [001] projection and b) [010] projection of the $PMA_1ButA_1PbI_4$ single crystal structure. c) [001] projection and d) [010] projection only showing the ButA cations within the structure. e) [001] projection and f) [010] projection only showing the PMA cations within the structure. Pb atoms are grey, I atoms are purple, C atoms are brown, N atoms are light blue and H atoms are white. Grey octahedra indicate PbI_6 units. *Single crystal structure refinements were carried out by Claire Wilson.*

Table 3.3: Comparison of distortion parameters for pure and mixed A' cation based structures. Values in brackets indicate the ESD for each parameter.

A' Cation	Pb-Pb Dist.	Pb-I-Pb Angle	Av. Pb-I Dist.	Av. I-N Dist.
PMA	14.380(1) Å	158.40(1)°	3.2068(2) Å	4.552(3) Å
Mix	14.43(1) Å	154.61(2)°	3.1897(3) Å	4.470(5) Å
ButA	13.801(1) Å	155.08(3)°	3.1882(3) Å	4.476(5) Å
A' Cation	**N Pen. Depth**	**BAV**	**BDI**	
PMA	0.661(5) Å	11.96(3)	0.0030(1)	
Mix	0.849(9) Å	2.95(2)	0.0025(1)	
ButA	0.589(10) Å	5.63(3)	0.0031(1)	

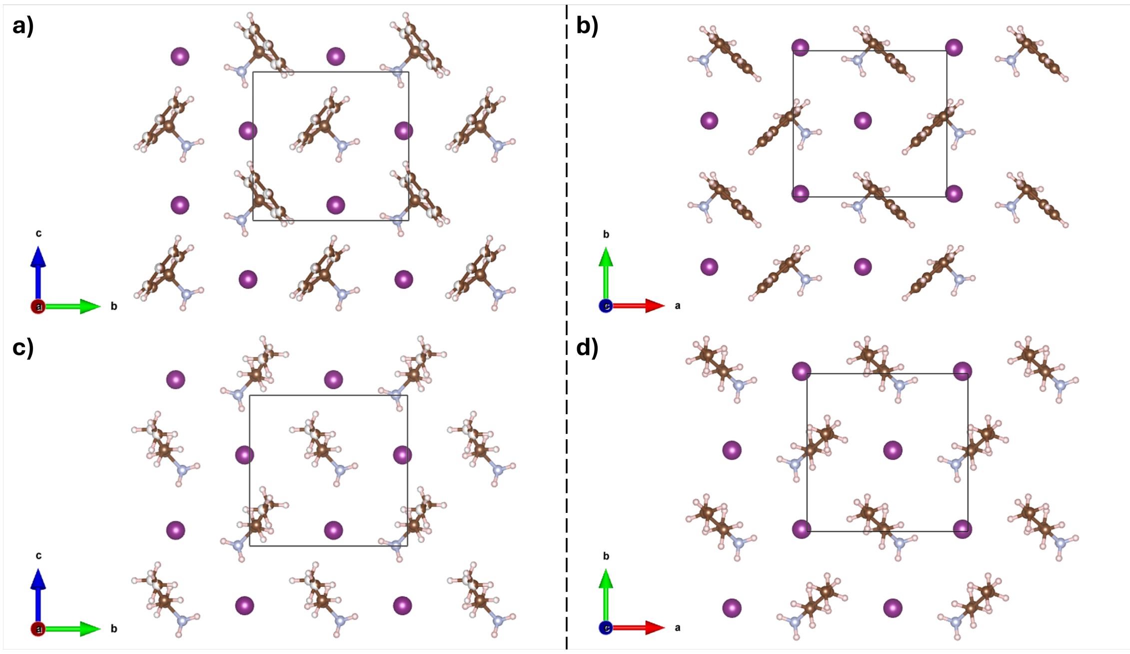

Figure 3.17: Projections of the A' cation layers within the mixed PMA + ButA single crystal structure and the mono-cation counterparts. The projection axes have been chosen to offer the same view for all the crystal structures. a) [100] projection of PMA cations within the $PMA_1ButA_1PbI_4$ structure. b) [001] projection of cations within PMA_2PbI_4. c) [100] projection of ButA cations within the $PMA_1ButA_1PbI_4$ structure. d) [001] projection of cations within $ButA_2PbI_4$. I atoms are purple, C atoms are brown, N atoms are light blue and H atoms are white. *Single crystal structure refinements were carried out by Claire Wilson*

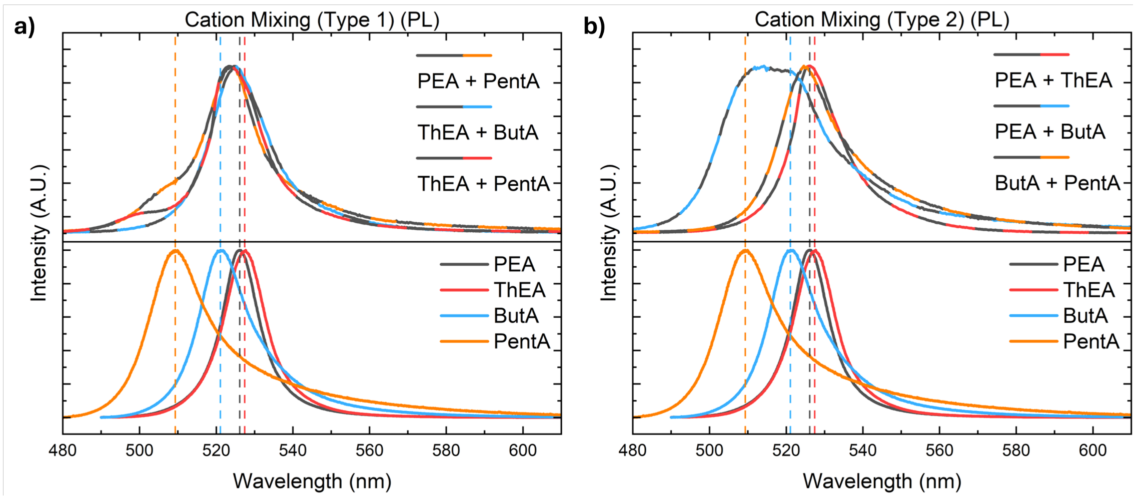

Figure 3.18: Photoluminescence spectra of mixed A' cation films, compared with mono-cation counterparts. a) Poorly mixed Type 1 ethyl-linked aromatic and aliphatic A' cations. b) Well mixed Type 2 ethyl-linked aromatic and aliphatic A' cations.

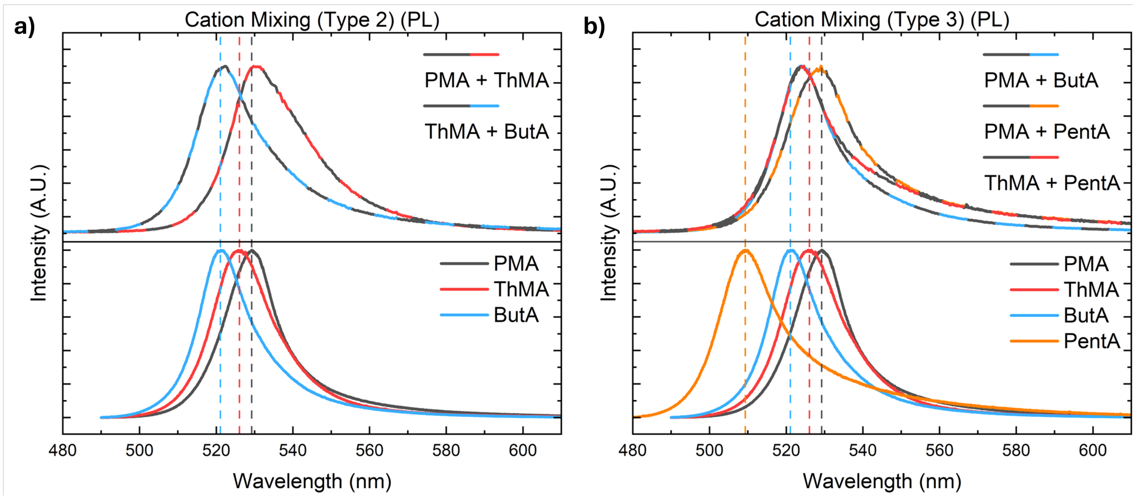

Figure 3.19: Photoluminescence spectra of mixed A' cation films, compared with mono-cation counterparts. a) Well mixed Type 2 methyl-linked aromatic and aliphatic A' cations. b) Wide-spaced Type 3 mixed methyl-linked aromatic and aliphatic A' cations.

intense high-energy peak component, suggesting that domains of perovskite with a wider bandgap that are not visible in the diffractogram are present. For most of the other Type 2 mixes, the peak position matches closely to one of the original components, with an increased low-energy 'tail'. Usually, the peak position corresponds to whichever component has the lowest energy emission, with the exception of the ThMA + ButA sample. The Type 3 structures (Fig 3.19 (b)) generally show a different behaviour, with the peak positioned in-between the two constituent A' cation peaks. This suggests the presence of an 'intermediate' bandgap. There are exceptions to this trend, with the Type 3 PMA + PentA mix peak matching the pure PMA case, and with the poorly mixed ThEA + ButA showing an averaged emission peak.

To demonstrate this variability more clearly, Fig 3.20 shows the energy values of the most prominent PL peak for the mixed A' cation films, compared to their respective mono-cation samples. Note that the cohort has been split into two subsets for ease of comparison, without grouping the samples into the three subgroups found in the XRD study. The plot again highlights how some films match the energy of one of the constituent cations, some are an average of the two, and some display an entirely distinct bandgap from the corresponding individual films. For example the case of ThEA + PEA (Fig 3.20 (b)) energy matches the PEA value, whilst the ButA + PentA sample (Fig 3.20 (a)) has an energy lower than either of the two components.

In general, mixing A' cations has a pronounced and rather uncontrolled impact on the perovskite bandgap. This is further evidenced by the reduction of peak symmetry within all of the emission spectra. This may be an intrinsic property of the multi-cation samples which contain domains of narrower- or wider-bandgap perovskites which have poor crystallinity and are not readily detectable within the diffractograms. This leads to a complex band structure, which in turn leads to numerous peaks in the PL spectra. Alternatively, the observed PL emission is a

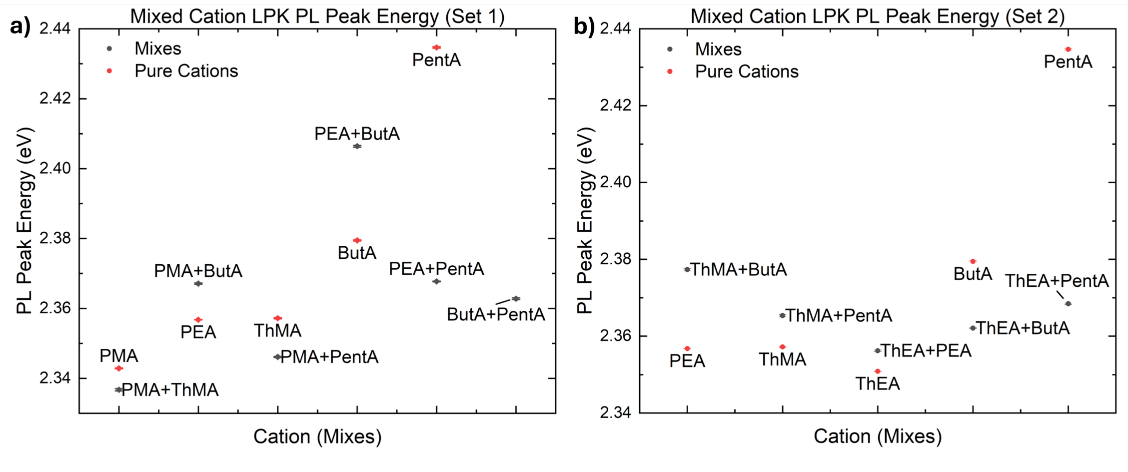

Figure 3.20: PL peak energies of mixed A' cation films, compared with mono-cation counterparts. a) Mixed films which do not contain the ThEA cation as a component. b) Mixed films which do not contain the PMA cation as a component. *Error bars have been included in the figure, but may be obscured by the data range and marker size.*

consequence of an unoptimised deposition protocol, which induces some degree of phase segregation due to a kinetic barrier for efficient mixing of the two component A' cations. Some parallels can be drawn between the trends in the structural parameters as observed in the XRD. However, nearly every trend features some sort of exception, making direct comparisons between the mixing behaviour and the resulting bandgap difficult. Nevertheless, this approach shows promise as a straightforward way of obtaining intermediate bandgap energies without the need for synthesising novel candidate A' cations.

Finally, the in-plane conductivity of mixed A' cation samples was explored. The values are plotted in Fig. 3.21, where they are compared to the values for the single A' cation templated samples. Rather unexpectedly, the mixed A' cation samples display a much higher conductivity, with an average increase of an order of magnitude versus single A' cation films. Only two samples are not meaningfully different, with the ButA + PentA cation mix matching the conductivity of the ButA cation, and the PMA + PentA mix lying within the error of the pure PMA film.This pattern of behaviour again shows that the chemical properties of the A' cation, such as their dielectric constant, have a relatively minor impact on the in-plane conductivity of the sample. Instead, the A' cation sheets influence the charge transport by the way they distort the perovskite backbone, and thus change the orbital interactions between the Pb-I atoms. The most conductive single-cation samples were PEA and ThEA, which had the smallest octahedral distortion, as indicated by the low BAV values. It follows that upon A' cation mixing, the octahedral distortion reduces, driven by the reduction in A' cation interactions creating a 'softer' cation backbone. This allows the structure to adopt a more optimal arrangement for charge transport through the PbI_6 sheets. Indeed, this reduced BAV is directly observed in the mixed $PMA_1ButA_1PbI_4$ single crystal structure. It is also important to note that these samples all showed good Type 2 or Type 3 mixing, suggesting that a fully disordered mix of the two A' cations is also beneficial to maximising in-plane conductivity.

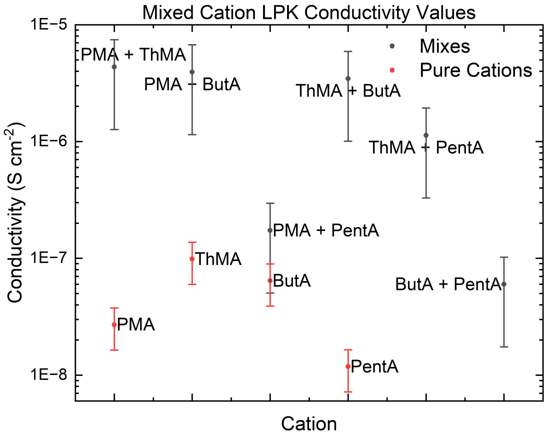

Figure 3.21: In-plane conductivity values of mixed A’ cation films, compared with mono-cation counterparts. Note that combinations of only four component cations were studied.

The above findings further highlight the highly complex relationship between A’ cations and the optoelectronic properties of the resulting perovskite layer. Well-ordered crystalline structures can be obtained with many A’ cation combinations, which template structures with intermediate or larger Pb-Pb layer spacings than the pure-cation counterparts. These mixed LPKs display complex PL emission behaviour, with the potential for more subtle adjustment of the bandgap energy than what can be achieved with metal or halide substitutions alone. They also boast very high conductivity values, suggesting they are a worthwhile avenue of research for varying the optoelectronics of perovskites formed from existing, widely-utilised A’ cation families.

3.5 Conclusions

This chapter presents a collection of studies into the structure and optoelectronic properties of a series of $n = 1$ RP perovskite materials. The set of eight A' cations studied - two containing aromatic rings with phenyl moieties, two aromatic thiophene counterparts, and four linear aliphatic chains from four to eight carbon atoms long - was selected on the basis of maximising the similarities between all of the molecules, whilst introducing systemic chemical variation. Whilst the Pb-Pb layer spacing of the perovskites they templated followed expected trends, in-depth analysis of the single crystal structures of these materials shows that even very basic chemical modifications can have profound effects on the packing of the A' cation and the underlying perovskite lattice. For the aromatic molecules, the addition of an atom into the chain attached to the ammonium moiety greatly influenced the flexibility of the A' cation as a whole, dictating the type form of π - π stacking present, and determining whether they would interdigitate or form a structure with a Van der Waals gap. For the linear aliphatic A' cations, the even-numbered molecules all had broadly similar structures, whilst the odd-numbered chain templated a structure with a much higher degree of distortion. This difference occurs despite similar interdigitated arrangements of the chains within the perovskite, suggesting that one additional carbon atom can change the optimal packing of the A' cations and lead to pronounced differences in the overall lattice. This variation in response complicates efforts to identify conclusive links between how the A' cation impacts the perovskite sheet across different families of materials. Whilst the set of A' cations studied was chosen to maximise the set of related structures, it appears it needs to be expanded even further before reliable links can be found. Carrying out the same structural analysis on more varied aromatic molecules, or longer odd and even linear chains, would make the dataset more reflective of the variety of A' cations used in the literature, and give further support to the initial trends observed.

Investigations into the PL emission and conductivity of these LPKs give further support to this observation, with highly varied behaviour seen across the A' cation families. Commonly reported links such as reduced Pb-I-Pb angles between octahedra leading to wider bandgaps are found to only be partially applicable to the dataset studied. Equally, in-plane and out-of-plane charge transport through the perovskites appears to have an opposite response to the degree and type of distortion present. Here, a pair of structurally similar aromatic A' cations see diverging changes in bandgap but very similar shifts in conductivities. Uniform A' cation sheets which contain a Van Der Waals gap see very efficient in-plane but very poor out-of-plane charge transport, indicating two competing mechanisms depending on the direction of charge transport. These results again show that the energetic landscape of perovskites is highly complex. The lack of clear trends across the chosen dataset studied suggests that simple structural studies are insufficient to accurately identify the relations between A' cation chemistry and their influence on resulting perovskite properties.

Whilst it is difficult to link specific chemical or structural parameters to target desired material properties, mixing sets of A' cations is identified as a promising method of forming compounds with intermediate properties. A subset of aromatic and linear A’ cations were successfully mixed to create perovskite sheets with varied interlaying spacing, intermediate bandgaps, and much higher conductivities. Here, mixing the A’ cations as a disordered phase between the perovskite octahedra allows each sheet to adopt a more ‘optimal’ arrangement whilst minimising the distortion of the perovskite octahedra. Crucially, as they utilise existing, widely-used A’ cations, they avoid the requirement of synthesising novel compounds. This highlights the potential of this very broad new family of LPK compounds for materials where in-plane lateral transport is key, or where emission wavelengths need to be tuned to a finer degree than what is possible with typical metal or halide substitutions.

Chapter 4

Degradation of Layered Perovskites

One of the most widely-adopted solutions to the intrinsic instability of perovskite light absorbing layers is the use of LPK capping layers. Alongside conferring numerous benefits to device performance, the formation of these perovskite-LPK heterojunctions results in significant improvements to device lifetimes. Nonetheless, questions remain about how LPKs behave when exposed to external environmental stressors, with literature reports demonstrating they are not fully stable when exposed to moisture and light. This highlights the need for studies of LPK stability both as an isolated material, and as a surface passivation layer. In this chapter, the intrinsic instability of defect-free PEA_2PbI_4 is demonstrated. Optical microscopy, AFM, PL and XPS measurements conclusively identify a pinhole-mediated mechanism which affects extremely thin layers of the perovskite. This degradation is found to be self-limiting, giving LPK materials the appearance of long-term stability. Furthermore, studies into a set of LPK capping layers on top of MAPI show they are highly susceptible to degradation or rearrangements when exposed to intense light, humidity or solvent-containing atmospheres. They offer limited protection to the underlying perovskite, which highlights the care that needs to be taken when referring to these materials as ‘passivation layers’.

Declaration of Authorship

The experimental results included in this chapter has been published in the journal *Small Structures*, titled ‘Illuminating the Devolution of Perovskite Passivation Layers’.[154] Data collected or analysed by my co-workers are detailed at the appropriate points. This includes: flake exfoliation and corresponding optical and AFM studies by Aleksey Kozikov at the University of Newcastle, School of Mathematics, Statistics and Physics, Kozikov group laboratory; PL measurements carried out by Paula L. Lalaguna at the University of Glasgow, School of Chemistry, Kadodwala group laboratory; pump-probe measurements carried out by Jake Hutchinson at the University of Warwick, Department of Physics, Milot group laboratory.

4.1 Introduction

One of the main limitations for widespread implementation of perovskite solar cells are issues with their intrinsic stability. Whilst this can be mitigated via the use of external encapsulation methods, development of more durable perovskite materials is key. Layered perovskites - structures that contain large organic A' cations which break up the perovskite lattice into distinct sheets - are one of the most promising candidates for stabilising perovskite solar cells. As a standalone layer, they have been reported to have excellent stability in ambient conditions as a solar cell absorber, but they typically suffer from poor performance with low PCE values.[72,140]

The development of a perovskite-LPK heterojunction could provide an optimal solution, combining the solar cell efficiency of 3D perovskite materials with the stability of LPK structures.[96] Here, the LPK interlayer limits ion transport through the perovskite.[98,136,190] This helps prevent the onset of many of the degradation mechanisms present in perovskite solar cells when they are exposed to high humidity or intense light.[26,127,191] This approach is widely utilised within state-of-the-art solar cells which now boast power conversion efficiencies of over 25% and lifetimes of over 2000 hours.[148,192]

Despite their popularity, questions remain about the behaviour of these layers once they are placed within a solar cell. Studies have shown that these materials are not fully stable when exposed to high humidity, with water uptake resulting in recrystallisation of the LPK layers.[127,193] A deeper understanding of such recrystallisation is crucial, especially when high n-value perovskites are employed.[96,112,194] These offer superior control over the band alignment and charge transport within the solar cell, but remain vulnerable to unwanted rearrangements to other n-valued layers.[83,91,138,195] The reports of LPK instability highlight the need for further studies into how LPK materials are affected by environmental stressors which may be present throughout the fabrication process. A combined approach, which looks into both phase-pure 2D LPK materials and the more device-relevant perovskite-LPK heterojunctions allows the development of mechanistic insights into the evolution of these layers.

The work in this chapter follows the methodology proposed above, combining insights from studies into both pure LPKs and ones in a perovskite-LPK heterojunction configuration. Here, The self-limiting degradation of single crystals of PEA_2PbI_4 is demonstrated via the use of optical imaging, AFM, PL and XPS. Extremely thin flakes are, in fact, highly susceptible to degradation under ambient conditions, but the build-up of PbI_2 acts to passivate the material below. Optical images show that this degradation is initiated at pinhole sites within defect-free exfoliated surfaces, which eventually spreads across the entire sample surface. This is corroborated by AFM and PL measurements which show an increased roughness and sub-bandgap emission in degraded samples. XPS measurements are then used to conclusively identify this surface degradation material as PbI_2, which remains after the loss of the more volatile cations. These findings lead to the proposal of a pinhole-mediated degradation mechanism, which removes whole sheets of perovskite, but does not degrade the LPK fully. Instead of a total degradation of the perovskite material into PbI_2 residue, significant quantities of pristine LPK remain underneath the accumulated degradation components. Thus, thicker perovskite sheets have the appearance of long-term stability, as the degraded surface is a relatively small fraction of the overall material.

The identification of this spontaneous degradation mechanism is of particular importance when considering the impact it may have on the extremely thin sheets used as a part of a perovskite-LPK heterojunction. Thus, the evolution of LPK heterojunctions is studied after exposure to high humidity, intense light and fabrication solvents. XRD measurements demonstrate that in many cases, the LPK capping layer is significantly impacted by the exposure to environmental stressors, undergoing rearrangements or failing to protect the underlying material from degradation. These results are corroborated by in-situ XRD and transient absorption studies which again show that the LPK layers evolve or vanish over a prolonged exposure to ambient atmospheres. These findings highlight the care that needs to be taken when discussing the LPK interlayers as ‘environmental passivation’ when employed within solar cells.

4.2 Devolution of Exfoliated Flakes

One of the issues facing studies of perovskite degradation is the need to minimise any defects that may form during the fabrication process. Single crystals are ideal samples for this purpose, as the slow-growth mechanism naturally leads to samples with a minimal amount of instrinsic defects. Thus, exfoliated flakes of PEA_2PbI_4 single crystals were used to study the degradation behaviour of layered perovskites in ambient atmospheres. Here, large and flat single crystals of perovskite were grown via a slow cooling method, as detailed in the methods, section 2.3. These single crystals were then broken down into smaller flakes via an exfoliation process, which splits the LPK sheets along the interface between layers of organic A' cations. This creates micrometer-sized flakes with very smooth surfaces and a minimal population of defect sites.[196] Work on the degradation of 3D perovskites has found that degradation is fastest at defect sites within the film and grain boundaries within polycrystalline films.[123,131] Thus, the presence of both 'exposed' flake edges and pristine flake surfaces allows the study of defect-mediated and spontaneous degradation under the same environmental conditions within one sample.

A cluster of exfoliated flakes on a silicon substrate is shown in Fig. 4.1, repeatedly imaged over a period of 41 minutes whilst exposed to ambient atmosphere at 20 - 22 °C and 45% - 55% humidity. Here, the colour of the flake corresponds to its thickness, due to interference effects of the incident light by the thin layers of material on the smooth silica substrate.[197] As the thickness of the flake increases, the colours change from translucent to green to yellow to orange. Initially (Fig. 4.1 (a)), the thinnest translucent flakes visible are around 10 nm or 6 sheets thick, with the thickest orange flake is around 200 nm, or 120 sheets. Almost immediately after imaging begins, dark pinholes start appearing in the surface of the flakes (Fig 4.1 (b-e)), with an example area highlighted by the dashed red circles. These pinholes grow, until they cover the whole flake surface and the initially visible layer is gone (Fig 4.1 (f-h)). For the thinner flakes in the centre of the images, this results in a significant reduction in thickness, until they are near translucent. For the thicker flakes visible on the edges of the imaged area, the loss manifests as a change towards a yellow colour. This loss is more pronounced at the flake edges, which are thinner than the centre of each respective flake. Fig. 4.1 (k) shows the evolution of the contrast values for two flakes in the sample. The optical contrast is an indication of the strength of the interference effects due to the presence of a flake, determined by the difference in how light of a given wavelength is reflected from the sample and substrate.[197] Details of how the values were determined are included in the methods, section 2.6.6. The thin flake (blue outline, blue data points) has a negative red-channel contrast against the substrate, whilst the thick flake (orange outline, orange data points) has a positive green-channel contrast against the substrate. Crucially, the magnitude of both contrast values steadily reduces upon exposure of the flakes to ambient atmospheres, indicating that both of the flakes are reducing in thickness after the measurements began.

These images offer compelling evidence that even brief exposure to ambient conditions causes spontaneous degradation of the layered perovskite. Defects can accelerate the degradation leading to greater material loss at the flake edges, but the

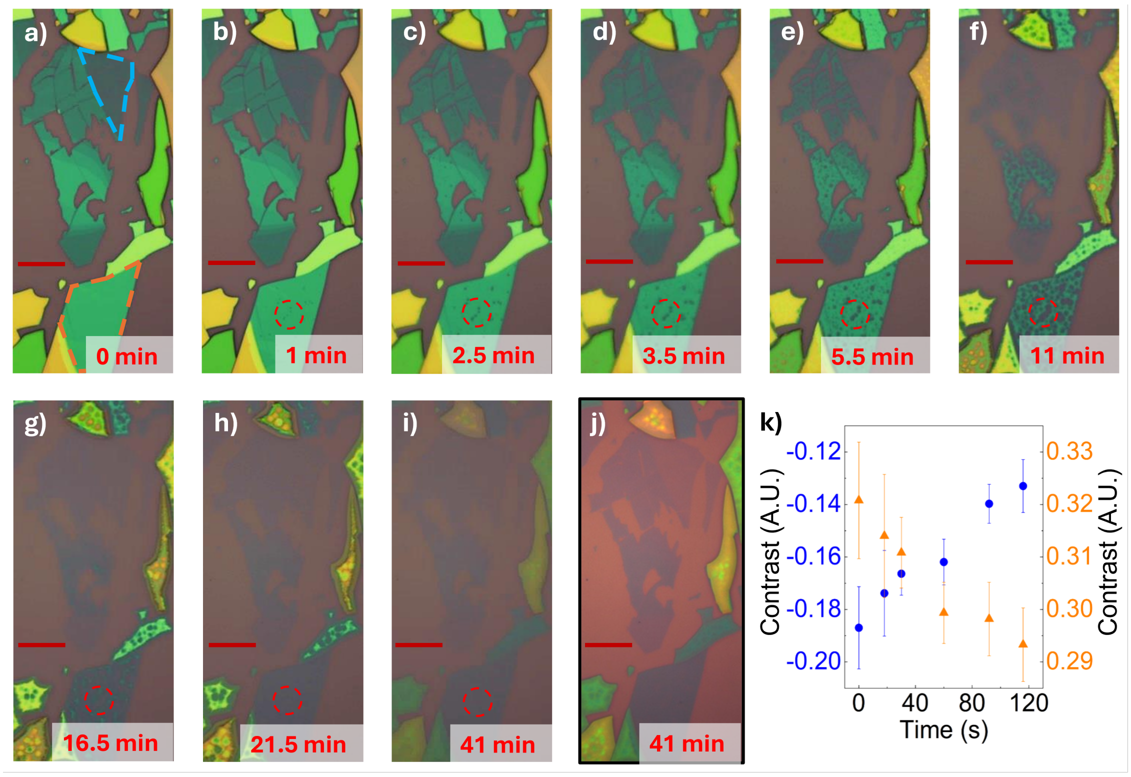

Figure 4.1: a) - i) Optical images of perovskites of different thickness with time in minutes. j) Contrast-enhanced Lookup Table image of (i) to help distinguish flakes of different sizes and make pinholes look clearer. k) Optical contrast of perovskites flakes delineated by dashed blue and orange lines in (a) in the first two minutes, indicating changes in perovskite thickness. The scale bar (red line in optical images) is 10 µm. The dashed red circle indicates a growing area of pinholes on the flake surface. *Exfoliation of flakes and image collection was carried out by Aleksey Kozikov. Figure reproduced with permission from Ref. [154] under the terms of the CC BY 4.0 license.*

process also spontaneously begins within an initially pristine surface. Once formed, these sites appear to function as a defect themselves, seeding further degradation and forming an expanding pinhole. Crucially, the temperature and light intensity required to triggered this process is far below the 50% humidity, 85 °C and AM 1.5 G solar spectrum standards of the ISOS-L3 laboratory degradation testing protocol.[198] Despite the continuing growth of pinholes and pronounced edge degradation, the thickest flakes persist throughout the study. The uniform colour of the residual flakes suggests that a well-ordered layered material is still present underneath the accumulated degradation material on the surface. Furthermore, despite the reduced thickness, further pinholes do not appear to form. This could indicate that the observed defects on the perovskite surface eventually act to passivate the material underneath once a sufficient quantity has accumulated. However, a limitation of the use of optical imagery to track degradation is that it is difficult to confirm the composition of the observed flakes. Equally, it is hard to determine whether the thinnest translucent flakes visible are perovskite, or simply residual degradation products left on the substrate once the reaction with ambient air has gone to completion. As such, additional studies were carried out to determine the composition of the degradation products, and their impact on the long-term LPK stability.

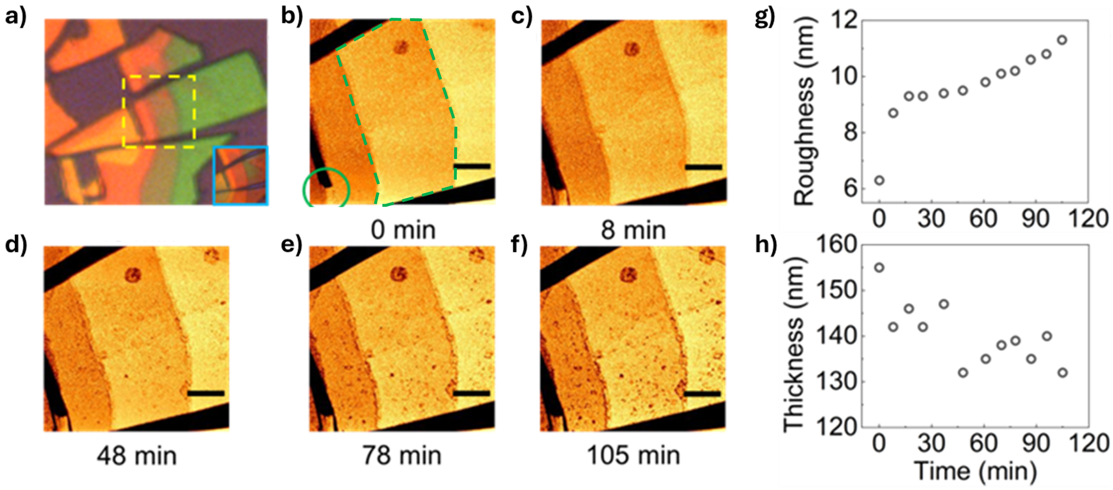

Figure 4.2: Evolution of the perovskite surface. a) Optical image of the region of interest taken in the AFM. The yellow dashed square marks the area for AFM measurements. The inset indicated by the blue solid square shows the area of interest after 5.5 hours. b) - f) AFM topography of the area delineated by the yellow square in (a) as a function of time. The green circle in (b) marks cracks in the flake to track its evolution with time. The scale bar (black solid line) is 4 µm. g) Root mean square roughness, and h) thickness of the middle perovskite terrace extracted from the AFM measurements in (b-f), marked by the dashed green outline in (b). *AFM measurements were carried out by Aleksey Kozikov. Figure modified with permission from Ref. [154] under the terms of the CC BY 4.0 license.*

Firstly, the evolution of the flake surface was further studied via AFM topography measurements, shown in Fig. 4.2. Here, a flake with multiple distinct terraces is shown. Each terrace represents a ‘step down’ to a lower number of perovskite sheets, which allows us to observe a pristine ‘bulk’ perovskite, and the exposed edge of a perovskite sheet. Once again, pinhole defects appear both at the flake edges and on the initially smooth ‘bulk’ surface as it is exposed to ambient atmospheres. This results in a sharp increase in the roughness of the sample, and a corresponding reduction in the material thickness, as detailed in Fig 4.2 (g-h). This process again occurs at a very short timescale, with the most significant increase in roughness occurring within the first 20 minutes, which aligns with the process of pinhole growth observed in the optical images. These observations gave unequivocal evidence that even a pristine layer of PEA_2PbI_4 will undergo a spontaneous degradation process.

Next, PL spectroscopy was used to study both freshly exfoliated PEA_2PbI_4 flakes, and ones which were left exposed to ambient air for several hours to accumulate surface degradation products. Due to the delay between exfoliation and the PL measurements, the flakes were covered in a thick layer of Polymethylmethacrylate (PMMA). Shown in Fig. 4.3, extended exposure to ambient atmospheres again causes the flake to look rougher and covered in pinholes. The PL emission spectra, shown in Figure 4.3 (c-d), show an intense peak at 2.35 eV, which matches well to values reported in the literature for a PEA_2PbI_4 perovskite.[199] This is the only component visible in the PL spectrum of the centre of the freshly-exfoliated flake (Figure 4.3, black line). However, an additional component is present at the grain boundaries, and in the bulk of the air-exposed flake. This lower-energy PL peak lies at around 2.27 eV, indicating emission from sub-bandgap states. This feature

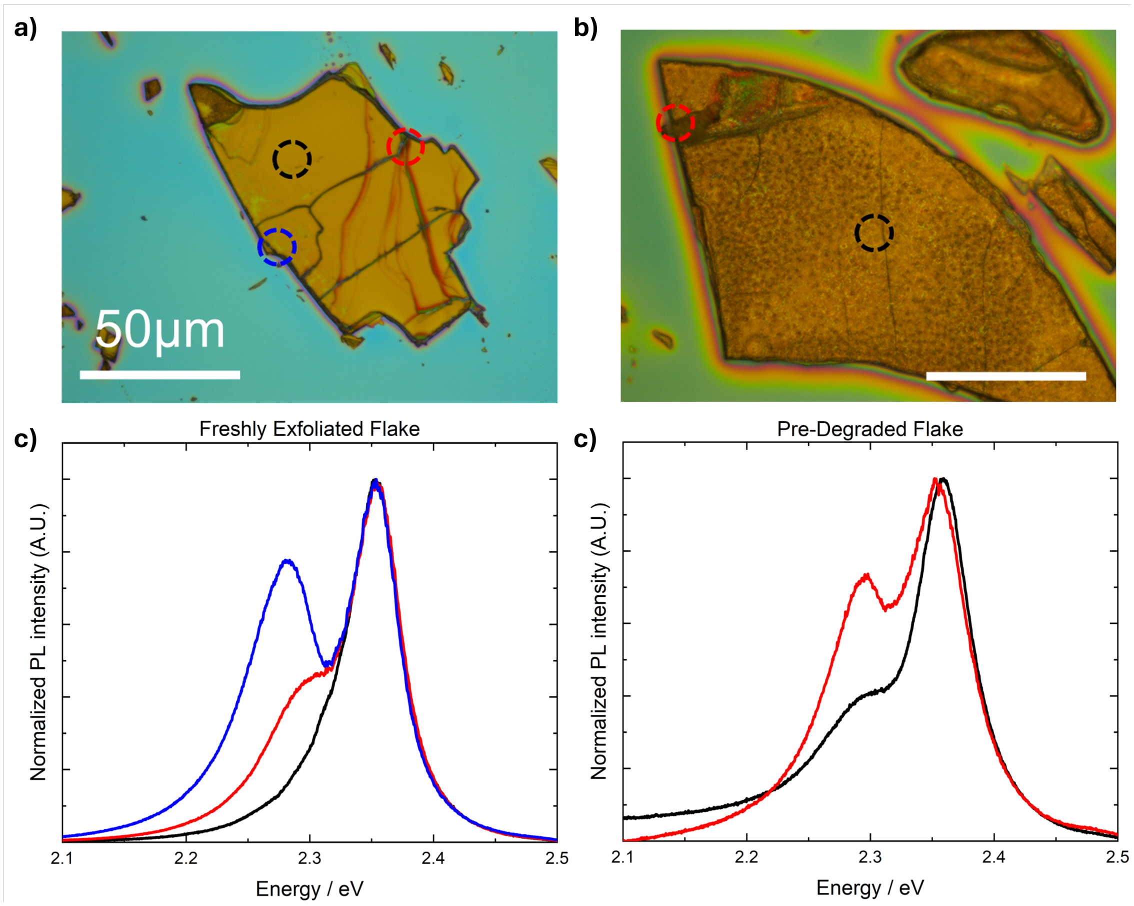

Figure 4.3: a) Optical microscopy image of freshly exfoliated PEA_2PbI_4 flakes covered in PMMA. b) Optical microscopy image of a PEA_2PbI_4 flake after several hours of ambient air exposure, covered in PMMA. c) PL emission from the colour-coded regions on the fresh flake shown in (a). d) PL emission from the colour-coded regions on the degraded flake shown in (b). *PL measurements were carried out by Paula Lalaguna. Figure modified with permission from Ref. [154] under the terms of the CC BY 4.0 license.*

has been previously reported in the literature, where it was also found to be more prominent at the edges of flake sheets.[200] Studies by Levine et.al. have linked such low-energy components to surface degradation of layered perovskite flakes. They demonstrated the emission was localised on the material surface, and showed that exfoliating the top layer removes the second low-energy peak.[201] This may explain why ambient-condition degradation of layered perovskites is rarely commented upon. Unless dealing with an extremely thin exfoliated flake, where emission from thin surface states is readily visible against the 'background' LPK emission, the quick formation and accumulation of degradation products does not damage enough of the material to be readily noticeable.

To identify the chemical nature of the defects forming on the perovskite surface, XPS measurements were carried out on thin films of the material. XPS is particularly appropriate for studying the surface chemistry of a sample given its very low penetration depth. Here, larger area polycrystalline films of PEA_2PbI_4 were either prepared just before measurement, or left exposed to ambient air for over 1 month to allow a complete build-up of degradation products. Fig. 4.4 shows the data for the

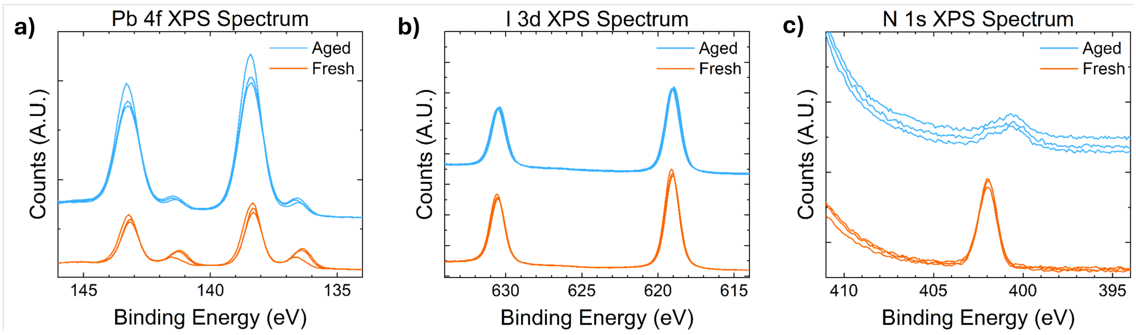

Figure 4.4: XPS spectra collected for thin films of PEA_2PbI_4, showing the a) Pb 4f region, b) I 3d region, and c) N 1s region. Each sample contains overlaid signals from three different spots. *Figure reproduced with permission from Ref. [154] under the terms of the CC BY 4.0 license.*

lead, iodine and nitrogen regions, collected at three sites for each sample. Both samples show two distinct peaks in the Pb 4f spectrum at 143.2/138.3 and 141.4/136.5 eV, respectively, which is evidence of the presence of both Pb^{2+} and Pb^0 on the film surface. The formation of Pb^0 is a known consequence of exposure of perovskite materials to the ultra-high vacuum and X-Ray beam of the XPS instrument.[202] The ratio of the Pb^{2+} to Pb^0 peaks is much higher in the aged sample, indicating that allowing the build-up of degradation product helps to protect the surface of the sample to some degree against vacuum-induced degradation. This also shows that the degradation products formed during exposure to ambient air consist of Pb^{2+} phases, and are not made up of metallic Pb^0. Furthermore, given the lack of any significant binding energy shifts between the two samples, the chemical environment of the Pb atoms within the degraded material appears to be similar to that found within a ‘pristine’ perovskite.

The chemical composition of these surface degradation products was determined by a quantitative analysis of their peak areas. This allows the calculation of the ratio of iodine to lead, which is shown in Fig. 4.5. Here, two values are provided for each of the samples. One is calculated by comparing the intensity ratio of the I peak to the Pb^{2+} peak component only (solid markers), which is attributed to Pb-I bonding environments. For the second value, the intensity of the I peak is compared to both the Pb^{2+} and Pb^0 peaks (hollow markers). This approach accounts for the fact that the Pb^0 is formed within the vacuum of the instrument from the Pb^{2+} species that were initially present in the sample. The results clearly show that whilst the pristine sample has a high I-Pb ratio of 4 or greater, as expected from the chemical composition of PEA_2PbI_4, the surface of the aged sample is almost purely PbI_2. This result agrees very closely with previous literature reports, which found PbI_2 to be the chief degradation product for layered perovskites exposed to intense laser illumination.[203] In the study, the organic PEA^+ cation reacts with the iodide ions to form hydrogen iodide and phenylethylamine, and both species eventually escape the film as gas as the sample is illuminated. The N 1s spectra offer further support that this process is occurring here, as shown in Fig. 4.6. The intensity of the N 1s peak is greatly reduced for the aged sample, indicating a loss of the organic A’ cation. The reduction in intensity at 402.2 eV occurs alongside the appearance of a peak at 400.2 eV, which is evidence of the formation of the neutral NH_2 amine

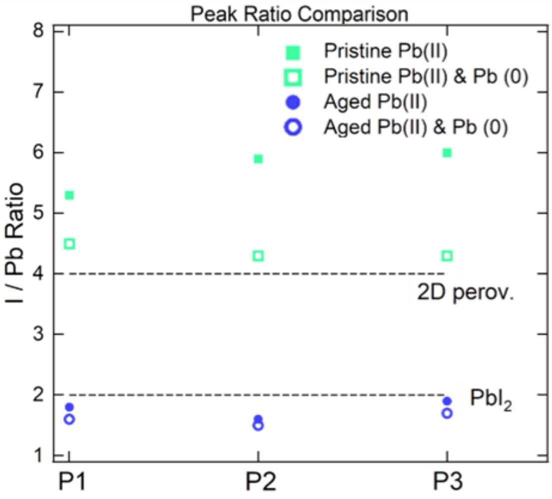

Figure 4.5: Quantitative analysis of the relative intensities of I 3d and Pb 4f peaks, calculated for three different regions of the samples. Solid markers indicate ratios determined using only the Pb^{2+} components, whilst hollow markers incorporate both the Pb^{2+} and Pb^0 components. *Quantitative analysis of XPS peak area was carried out by Elisabetta Arca. Figure modified with permission from Ref. [154] under the terms of the CC BY 4.0 license.*

species.[204] The evidence presented by the XPS studies thus points to an effective loss of a hydrogen iodide equivalent within the LPK material, with the remaining phenylethylamine and lead iodide persisting on the surface.

Given the evidence from the XPS, PL, AFM and optical microscopy studies, the following mechanism is proposed for the pinhole mediated degradation of layered perovskites, shown in Fig. 4.7. Initially, light and ambient air induce local defects in the film, creating strain within the layer which has been reported to catalyse the degradation of perovskites.[205] This localised strain catalyses light- and oxygen-mediated disproportionation of the layered perovskite into the neutral amine, hydrogen iodide, iodine and lead iodide. Both hydrogen iodide and iodine are proposed as potential degradation products as these have been found to be the dominant iodine species for light and oxygen-induced degradation respectively.[131,203] The disproportionation can occur at the edges of a crystal grain, or in the bulk as a pinhole. As shown in the optical images and AFM data, these defect sites continue to spread across the surface. XPS data show that this degraded surface layer is made up largely of PbI_2 with small quantities of the organic amine remaining - this corroborates literature reports of neutral amine species combining with lead iodide to form PbI_2 perovskitoid sheets.[172] Thus, it is the accumulation of these PbI_2 species that acts to eventually limit the degradation to only the top surface of a perovskite flake or film. PbI_2 has indeed been reported to passivate perovskites, especially when it is formed on top of a well-ordered structure.[206,207] This hypothesis is further supported by PL data showing sub-bandgap emission in degraded samples. Whilst PbI_2 has a very weak PL emission,[138,172] edge- and face-sharing '1D' perovskitoid structures, which are a likely intermediate product of this degradation process, have bandgaps narrower than that of a pure 2D perovskite.[208]

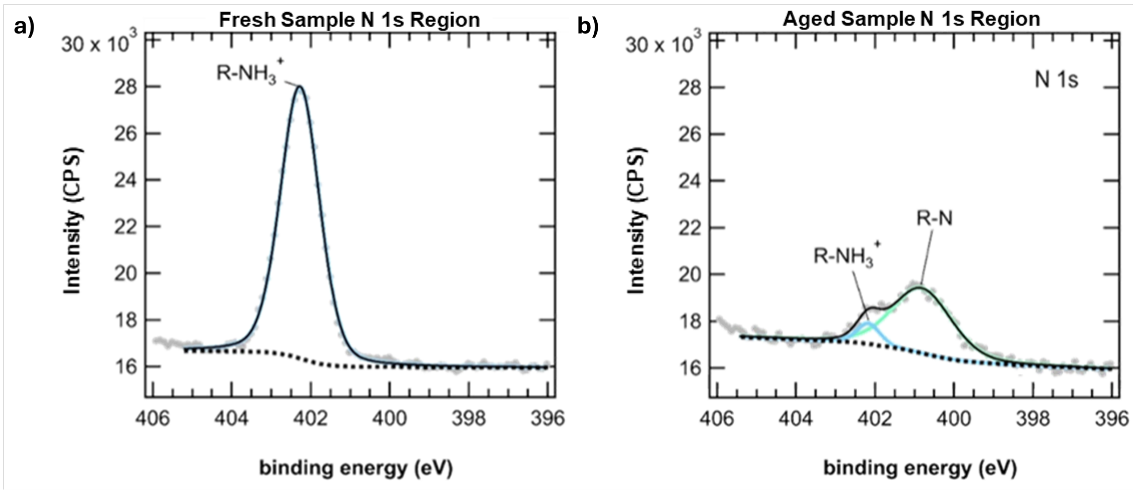

Figure 4.6: XPS spectra showing fitted peak data of a) the N 1s region of a fresh sample and b) a degraded sample. *Peak fitting of XPS data was carried out by Elisabetta Arca. Figure modified with permission from Ref. [154] under the terms of the CC BY 4.0 license.*

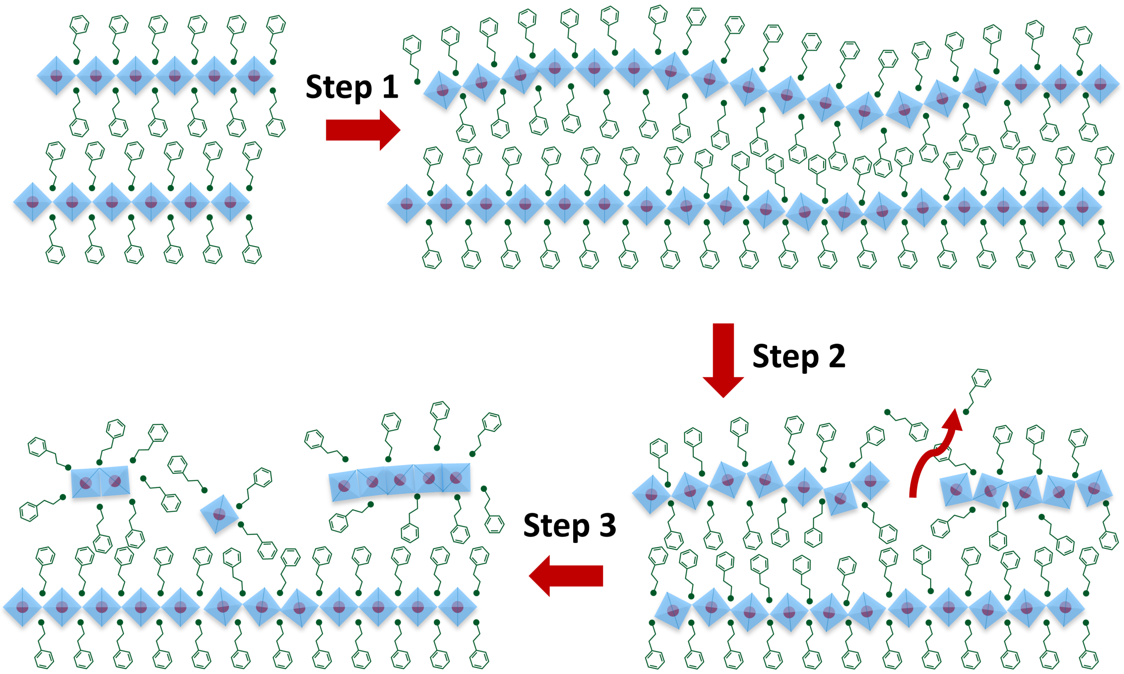

Figure 4.7: Proposed mechanism of pinhole-mediated layered perovskite degradation. Step 1: Structural distortion leading to increased surface roughness. Step 2: Loss of organic A' cations and iodide anions as amines and HI or I_2, leading to the formation of pinholes in the perovskite lattice. Step 3: Formation of PbI_2 sheets to act as a final passivating layer. B cations are represented by red circles, small organic / inorganic A cations are represented by large green circles, large organic A' cations are represented by the green aromatic organic molecules, and the octahedral cage of six X halides is represented by the blue diamonds. *Figure reproduced with permission from Ref. [154] under the terms of the CC BY 4.0 license.*

The determination of a self-limiting passivation mechanism is of crucial importance for the application of layered perovskite materials in solar cells. A pure, thick crystal or film of PEA_2PbI_4 will undergo only a small degree of surface degradation, which can be difficult to observe. However, the passivation layers used within devices are extremely thin, and often are formed via conformal growth on the relatively disordered polycrystalline surface of a '3D' perovskite. As such, systems more representative of those found in devices must be studied, which is the focus of the following section.

4.3 Devolution of LPK Capping Layers

Whilst single-crystal samples are excellent for studies of material properties, they differ significantly from the ‘real’ LPKs as utilised within solar cells. Here, the layers instead are used in a heterojunction configuration, consisting of a very small quantity of layered material formed directly on top of the light absorbing 3D perovskite structure via solution processing. Thus, a range of LPKs formed from different A’ cations and utilising different deposition approaches were prepared on top of a MAPI thin film to gain a more representative understanding of the degradation behaviours that may occur in devices. These are schematically illustrated in Fig. 4.8. The formation of LPK capping layers was achieved by depositing solutions of cation iodide salts in IPA on top of annealed MAPI films, as detailed in the methods, sections 2.2.2 and 2.4.1.

For the study of PEA-templated layered perovskites, both $n = 1$ and $n = 5$ LPK capping layers were found to readily form on the MAPI surface. The XRD diffractogram in Fig. 4.9 (a) (red curve) shows the effect of depositing a 40 mM PEAI salt solution in IPA on a MAPI surface. Three principal peaks are visible in the low angle regions. These correspond to the direct crystallisation of PEAI salt at 4.6° as marked by a # symbol, the (002) reflection of $n = 1$ PEA layers at 5.3°, and the (002) reflection of $n = 5$ layers at 6.5°. Due to the low quantity of LPK material formed on the surface, often only the most intense (002) peaks are detectable above the background signal for any given phase. For details of how the n-number assignments were carried out throughout the rest of this section, see methods section 2.8.5. The two types of LPK film form due to complimentary formation mechanisms. In both cases, initially high-n layers form via a quick intercalation of the A’ cation into the surface of the perovskite. This process can either further split the sheets until only an $n = 1$ layer remains, or stabilise at a higher n-value.[95,96] The stoichiometry of the MAPI substrate or the LPK casting solution can be tweaked to help direct the formation of phase-pure LPK films. By adding a small excess of PbI_2 to MAPI, the quantity of PbI_2 on the surface is increased, which promotes the formation of $n = 1$ films by allowing a direct PEA-PbI_2 reaction pathway.[98] Alternatively, $n = 5$ films can be selectively formed by adding MAI to the cation-iodide precursor solution, which compensates for the changes in film stoichiometry and suppresses the continued A’ cation intercalation. Diffractograms of phase-pure $n = 1$ and $n = 5$ layers are shown in Fig. 4.9 (a) (blue and orange curves), with peaks corresponding to just one of the LPK phases visible in the low-angle regions with no evidence of excess cation salt, alongside the peaks associated with the underlying MAPI, residual PbI_2 and FTO substrate. In the case of the pure $n = 1$ layer, the PEA solution concentration had to be halved to 20 mM, to avoid the direct crystallisation of PEA on the sample surface as in the unoptimised case. As well as the widely-utilised PEA cation, a family of straight-chain aliphatic A’ cations were also used to form LPK capping layers. These were chosen due to the closely-matched Pb-Pb layer spacing of the $n = 1$ layered perovskites they form - PEA with 16.50 Å, HexA with 16.35 Å and DoDecA with 16.04 Å. This allowed the comparison of the passivation and degradation behaviours of aromatic and aliphatic straight-chain RP capping layers as well as aliphatic straight-chain DJ capping layers. A comparison of their respective diffractograms is included in Fig. 4.9 (b). The peaks showing

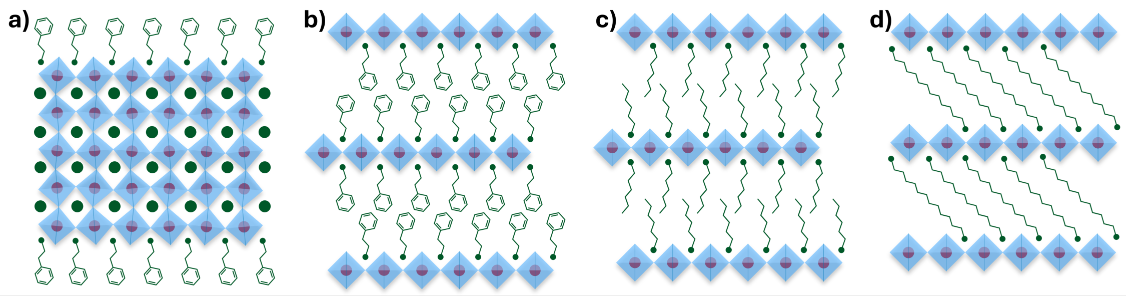

Figure 4.8: Schematic illustration of the structures of the layered perovskites used to cap 3D MAPI substrates. a) $n = 5$ PEAI-based LPK. b) $n = 1$ PEAI-based LPK. c) $n = 1$ HexAI-based LPK. d) $n = 1$ DoDecAI-based LPK. B cations are represented by red circles, small organic / inorganic A cations are represented by large green circles, large organic A' cations are represented by the green aromatic or linear organic molecules, and the octahedral cage of six X halides is represented by the blue diamonds.

the formation of the $n = 1$ layers all lie at similar angle values, as expected from the closely-matched Pb-Pb layer spacing. In all cases, any excess PbI_2 added to the MAPI film is consumed during the LPK formation process. The broad peak for the DoDecA LPK suggests a low degree of crystallinity of the surface capping layer. This is likely due to the two linked ammonium groups in the molecule inhibiting the formation of well-ordered perovskite sheets. Here, the typical mechanism of cation interaction with solvated PbI_2 and subsequent self-assembly into perovskite is slowed due to the need for a single A' cation molecule to interact with two separate PbI_2 units.[94,105,209] As such, the capping LPK crystallites that form are smaller and have a less intense diffractogram peak. Indeed, when monoammonium A' cations are used instead, the LPK peak is very narrow and intense, as the A' cations can more easily react with the excess PbI_2 on the sample surface to form the desired perovskite phase. The DoDecA peak is also shifted to slightly lower angles than those seen in a pure 2D layer - this has been previously reported for DJ capping layers, and attributed to a change in the LPK growth mechanism on top of a perovskite substrate.[100] A notable feature of the HexA-LPK coated MAPI sample is the presence of additional peaks immediately adjacent to the principal (110) orientation. These peaks correspond to (002) oriented MAPI, which appears as a preferred orientation for all HexA samples. This perovskite orientation has been previously reported to preferentially form during room-temperature deposition of MAPI films, and is usually lost after annealing.[210] Here, the deposition of the HexA LPK capping layer largely reverts this process. It is likely that the presence of significant quantities of LPK on the sample surface promotes a rearrangement of the crystal structure to the (002) orientation, which must be better able to accommodate the capping layer.

Next, the stability of these model LPK layers was tested in a range of degradation conditions. The samples were selectively exposed to one of three environmental stressors - high humidity (85% RH), intense light (0.7 sun) and a mixed DMF/DMSO-solvent containing atmosphere. Details of how each condition was achieved can be found in the methods, section 2.7. In brief, samples were placed within a gas-tight vessel and were left to degrade over a period of 2-8 hours, depending on the condition. Initial measurements were carried out on uncapped MAPI layers to establish the baseline response of the underlying material. XRD measurements of the sam-

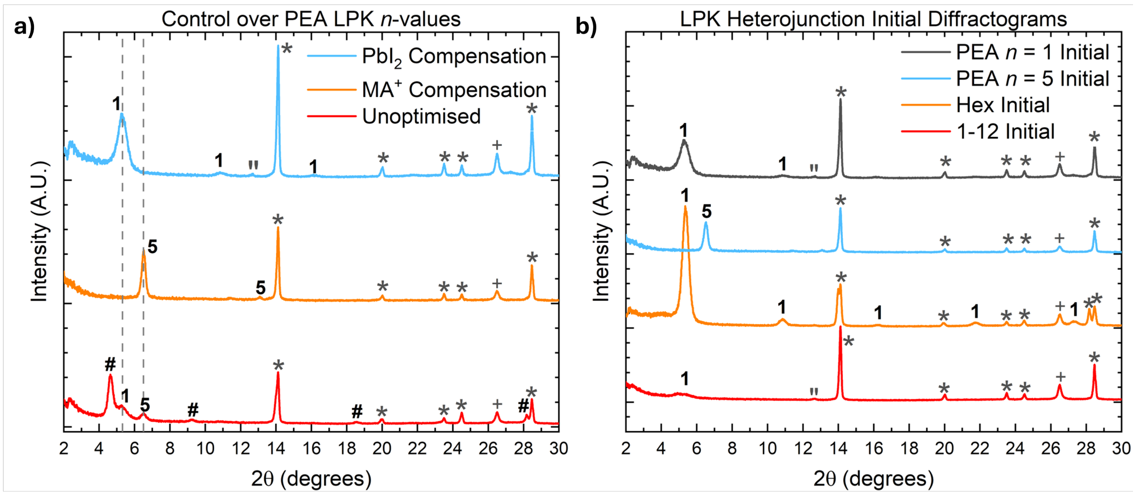

Figure 4.9: a) Diffractograms of the formation of different LPKs after depositing PEAI solutions on top of MAPI. Different compensation approaches can lead forming $n = 1$ or $n = 5$ layers. b) As-deposited diffractograms of the LPK materials used within the stability studies. Numbers indicate the n-value of the LPK material present. The symbols correspond to peaks attributed to different materials as follows: * indicates MAPI, " indicates PbI_2, # indicates PEAI, and + indicates the FTO substrate. The vertical dashed lines are guides to show the position of LPK peaks across the samples. *Figure modified with permission from Ref. [154] under the terms of the CC BY 4.0 license.*

ples were taken immediately before and after degradation started. The results for a control uncoated MAPI thin film can be seen in Fig. 4.10. Initially, the characteristic peaks corresponding to the (110)-oriented crystallites at 14.2° and 28.3°, the FTO glass substrate at 26.5° (marked with a + symbol) and less prominent MAPI orientations (marked with * symbols) are visible.[152,211]

After exposure to the environmental stressors, there is clear evidence of the onset of degradation of the MAPI film. Exposure to intense light has the most significant impact on film integrity, with a dramatic loss of the crystalline perovskite and the formation of PbI_2 as evidenced by the new peak at 12.6°. Light absorption and subsequent charge accumulation have previously been reported to induce significant strain into the MAPI film, and locally disorder the octahedral structure by disrupting existing bonding interactions.[188,212] This leads to large-scale ion migration and subsequent loss of the organic material from the perovskite lattice to form PbI_2, which has been previously identified as the principal MAPI degradation mechanism.[213,214] Exposure to high humidity leads to a less-obvious degradation of the film. A closer analysis of the low-angle region, shown in Fig. 4.11 (a), reveals the appearance of extra peaks at 8.5° and 10.5° (marked by an @ symbol). These are direct evidence of the formation of MAPI monohydrate, which is formed due to the incorporation of moisture into the perovskite crystal structure.[215] The appearance of a PbI_2 peak at 12.6° could also potentially indicate the formation of dihydrate phases. Studies in the literature have found the dihydrate degradation product to be quite unstable, decomposing to PbI_2 during exposure to ambient atmospheres, which was necessary for the XRD measurements.[125] Finally, exposure of MAPI films to an atmosphere containing DMF and DMSO solvent results in a significant uptake of the solvent into the crystal lattice, and the appearance of numerous additional

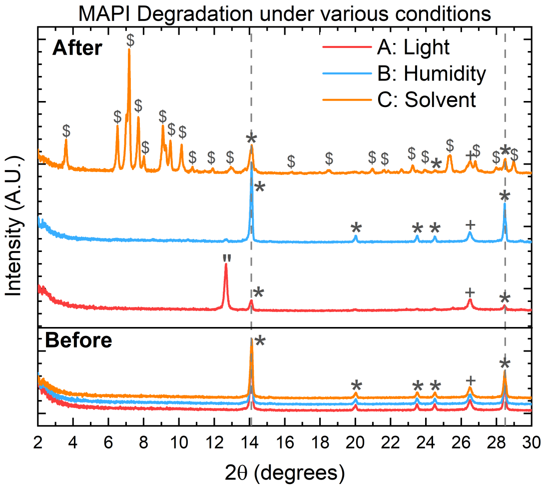

Figure 4.10: Diffractograms showing the degradation of MAPI layers after exposure to different environmental stressors: 0.7 Sun equivalent light (8 hours), 85% humidity nitrogen (8 hours), DMF+DMSO solvent rich atmosphere (4 hours). The symbols correspond to peaks attributed to different materials as follows: * indicates MAPI, " indicates PbI_2, $ indicates MAI-PbI-DMSO phases, and + indicates the FTO substrate. The vertical dashed lines are guides to show the presence of matching MAPI peaks in all diffractograms. *Figure modified with permission from Ref. [154] under the terms of the CC BY 4.0 license.*

peaks in the diffractogram, seen in Fig. 4.11 (b) and marked by $ symbols. This process essentially reverts the film into the pre-annealed state - the plot of an unannealed, as-spincoated film in Fig. 4.11 (b) almost exclusively contains these new low-angle peaks. They are clear evidence of the presence co-crystallised MAI-PbI_2-DMSO perovskitoids and PbI_2DMSO_2, matching closely to literature reports.[38]

Having identified the expected degradation behaviours of an uncoated MAPI substrate, LPK-passivated MAPI samples were exposed to the same degradation conditions to see if they can effectively passivate the underlying perovskite. The diffractograms of the samples after degradation are included in Figs. 4.12, 4.13 and 4.14. All films show very poor stability upon exposure to intense light, with a significant loss of the perovskite phases and formation of PbI_2, shown in Fig. 4.12. Here, the self-passivating effect which limits degradation observed for the single flakes of PEA_2PbI_4 does not occur. The uniformly-ordered and highly smooth layers of the remaining, undegraded LPK were able to act as a suitable substrate for the formation of a blocking layer of PbI_2. In the case of the polycrystalline MAPI film, as the thin surface LPK degrades to PbI_2 as before, it is unable to form a uniform layer of degradation product on top of the small MAPI crystallites. Sites such as grain boundaries remain exposed, and thus the light-induced lattice distortion, pinhole formation and A or A' cation loss are not stopped. The DoDecA-capped layer is a notable exception with the MAPI and LPK peaks still visible, suggesting that despite forming a relatively disordered structure, the DJ templating A' cation is superior at limiting the ion migration out of the perovskite.

Exposing the films to high humidity environments leads to a far more varied behaviour, as illustrated in Fig. 4.13. The $n = 1$ PEA film shows the greatest resilience, with minimal changes to both the layered perovskite and the underlying

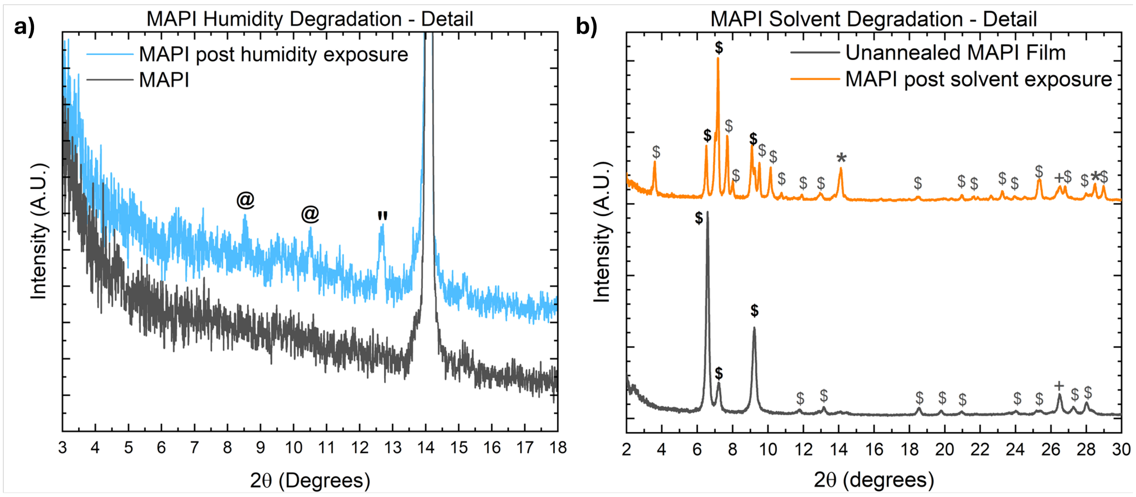

Figure 4.11: a) Detailed section of a MAPI film exposed to high humidity over 8 hours. b) Comparison of MAPI films exposed to DMF+DMSO-containing atmospheres to unnanealed MAPI films. The symbols correspond to peaks attributed to different materials as follows: * indicates MAPI, " indicates PbI_2, @ indicates MAPI hydrate, $ indicates MAI-PbI-DMSO phases, and + indicates the FTO substrate. Bold symbols highlight the most prominent peaks present in both degraded and unannealed samples.

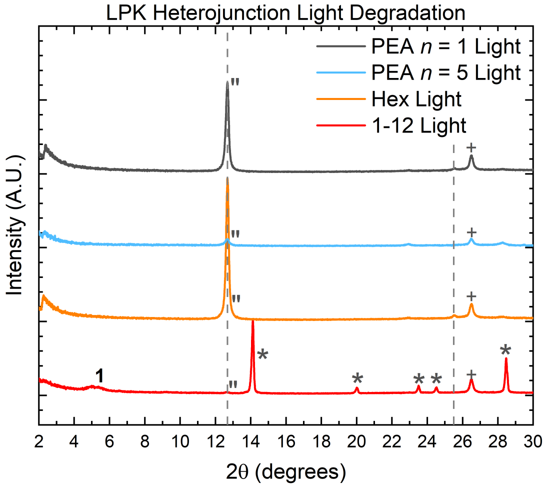

Figure 4.12: Diffractograms of LPK-capped MAPI after exposure to intense light (0.7 sun) for 8 hours. The symbols correspond to peaks attributed to different materials as follows: * indicates MAPI, " indicates PbI_2, and + indicates the FTO substrate. The vertical dashed lines are guides to show the presence of matching PbI_2 peaks in all diffractograms.

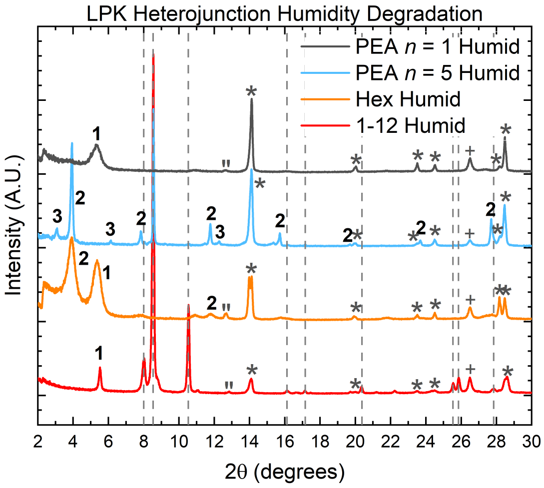

Figure 4.13: Diffractograms of LPK-capped MAPI after exposure to 85% relative-humidity nitrogen for 2 hours. Numbers indicate the n-value of the LPK material present. The symbols correspond to peaks attributed to different materials as follows: * indicates MAPI, " indicates PbI_2, and + indicates the FTO substrate. The vertical dashed lines indicate the position of MAPI hydrate phase peaks in the diffractograms. Unmarked peaks correspond to unknown crystal phases.

MAPI, and no evidence of monohydrate formation. The other films all show evidence of recrystallisation of the top LPK surface. In the case of the HexA-capped perovskite, two peaks are now visible in the diffractogram, corresponding to $n = 1$ and $n = 2$ phases. Similarly, the initially $n = 5$ PEA film undergoes a rearrangement to $n = 2$ and $n = 3$ LPK phases, alongside clear evidence of PbI_2 monohydrate formation with the appearance of the peak at 8.5°. For the DoDecA-capped sample (red curve), the (002) $n = 1$ LPK peak at 5.5° uniquely increases in intensity after the humidity degradation treatment. The layer does not offer any protection from hydrate formation, with clear evidence of the hydrate phases. Counter-intuitively, this process also seems to allow the A' cation-templated LPK to restructure and form a far more ordered phase within the film.

Finally, solvent exposure, as shown in Fig 4.14, has similar impact to humidity - there is evidence of the incorporation of solvent into the perovskite structure to create the MAI-PbI_2-DMSO adducts observed previously. This also dissolves the LPK material on top, which is either lost, as in the case of $n = 1$ PEA, or recrystallised into an intermediate n-valued LPK as indicated in the HexA and $n = 5$ PEA diffractograms. The (002) peak of the $n = 1$ DoDecA capping layer again shows an increase in crystallinity, suggesting the mechanisms behind humidity- and solvent-catalysed degradations follow similar intermediate phases which allow the DJ LPK phase to reform.

The above results offer compelling evidence that even with LPK passivation, the perovskite surface is subject to a mixture of competing processes upon exposure to environmental stressors. The various degradation pathways of the capping LPK phases observed are illustrated in Fig. 4.15. These have been found to occur in tandem with the more 'typical' degradation of 3D perovskites, which result in the formation of new water- or solvent-containing crystalline intermediates. The degree

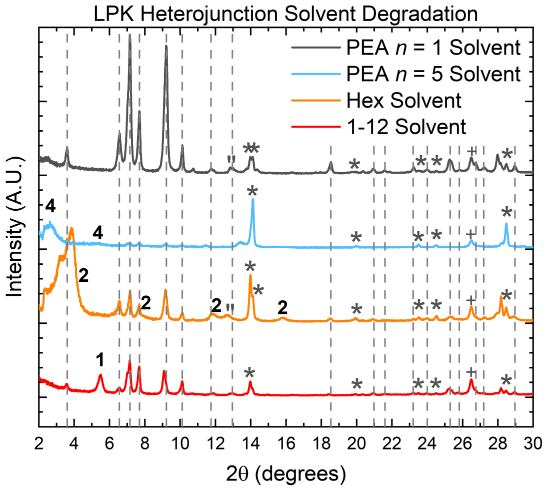

Figure 4.14: XRD diffractograms of LPK-capped MAPI after exposure to DMF+DMSO-containing atmospheres for 4 hours. Numbers indicate the n-value of the LPK material present. The symbols correspond to peaks attributed to different materials as follows: * indicates MAPI, " indicates PbI_2, and + indicates the FTO substrate. The vertical dashed lines indicate the position of MAI-PbI-DMSO phase peaks in the diffractograms.

of disruption varies from material to material, but overall all samples are sensitive to water and solvent-mediated recrystallisation, and see a complete degradation upon intense light exposure. In some cases, however, the chemistry of the A' cation can hinder the formation of unwanted side-phases. For example the presence of n = 1 PEA capping layers minimises material loss and inhibits PbI_2 formation upon exposure to moisture. This is likely due to the large, well ordered aromatic rings of the molecule limiting uptake of water into the MAPI layer and the subsequent migration of MAI out of the film.[127]

Further studies were carried out on the n = 5 PEA capping layer, to explore how it 'devolves' into lower n-valued analogues. Figs. 4.16 and 4.17 show two studies carried out on samples tracked over time using XRD or transient absorption respectively. In the XRD study, the sample was repeatedly measured every 15 minutes with a fast 2 minute scan in a 3-16°angle range over a period of 14 hours, whilst kept within the dark ambient atmosphere environment of the diffractogram chamber. After an initial 6 hour period of stability, the n = 5 peak steadily reduces in intensity. At the same time, a new peak corresponding to the n = 1 phase appears, and grows as the measurement continues. Throughout this time, there is no detectable variation in the intensity of the underlying MAPI peak. This measurement once again demonstrates the surprising instability of the deposited LPK, even in conditions where the environmental stressors such as moisture are present in insufficient quantities to form the intermediate crystalline phases observed in the prior set of degradation experiments. The steady transformation between the two initially favourable PEA-based LPK phases suggests a significant degree of ion migration occurs, with a steady phase separation of the large A' cations onto the sample surface, and a corresponding movement of the smaller A cations into the sample bulk. The lack of evidence for intermediate n-valued phases suggests that if they form, they are present in very small quantities, below the detection threshold of the instrument. This process is most likely initiated by the incident X-rays on the sample, which

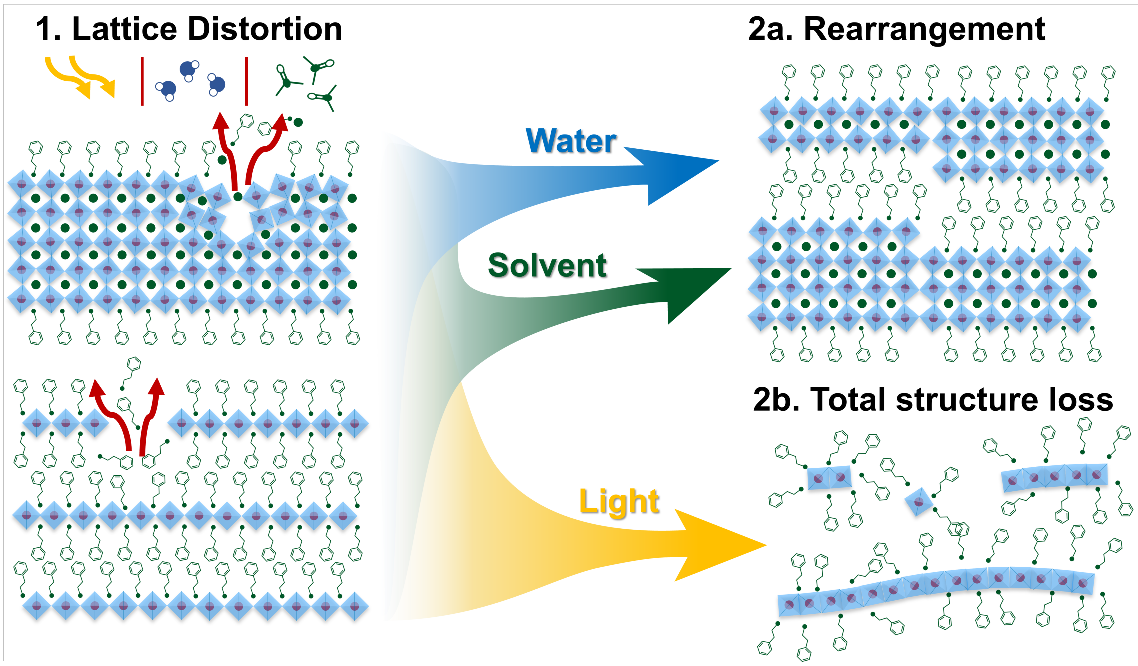

Figure 4.15: Proposed degradation pathways of perovskite-LPK heterojunction capping layers. 1: Upon exposure to environmental stressors such as light, water or solvents, the perovskite lattice is distorted. Pinholes or solvent adducts form within the film. 2a: The LPK recrystallises to account for any changes to stoichiometry or to form a more stable phase, alongside the formation of water or solvent adducts (not pictured). 2b: The structure degrades completely to PbI_2. B cations are represented by red circles, small organic / inorganic A cations are represented by large green circles, large organic A' cations are represented by the green aromatic organic molecules, and the octahedral cage of six X halides is represented by the blue diamonds.

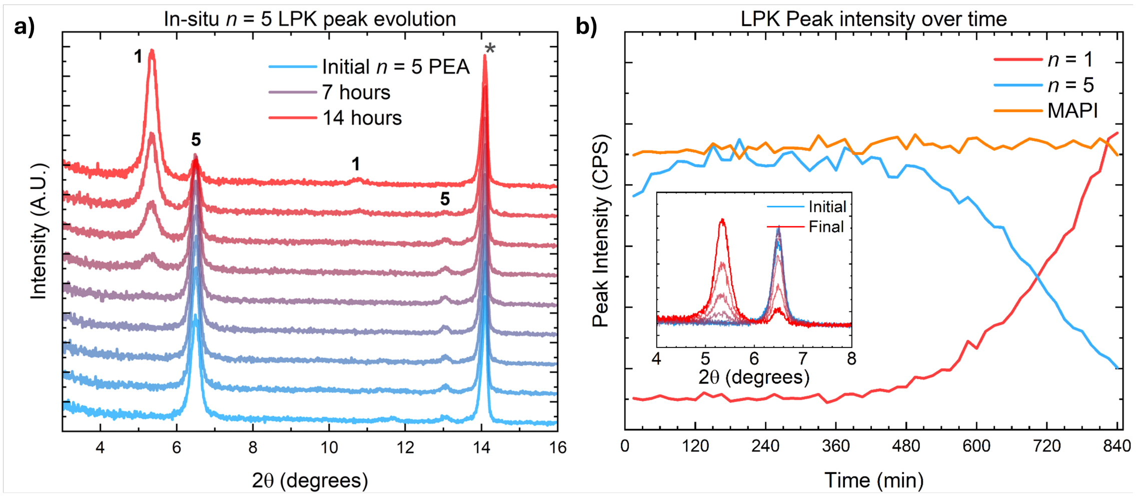

Figure 4.16: a) Short-duration 2 minute diffractograms of the same $n = 5$ PEA-capped MAPI film over a period of 14 hours, shown here at 105 minute intervals. b) Intensity values for peaks corresponding to $n = 1$ PEA LPK, $n = 5$ PEA LPK and MAPI, plotted over the duration of the experiment. Inset: Comparison of the two peaks shown in (a), without offsetting the data. Numbers indicate the n-value of the LPK material present. *Figure modified with permission from Ref. [154] under the terms of the CC BY 4.0 license.*

combined with the partial dissolution of the lattice due to the absorption of any water in the atmosphere provide enough energy for the structure to rearrange into the ultimately most stable $n = 1$ phase. This mimics the competing $n = 1$ formation pathway during spincoating, where A' cations can continuously intercalate into the formed $n = 5$ LPK.

Transient absorption measurements were employed next, as they allow the study of non-crystalline phases which will not appear in XRD measurements. Here, the change in UV-Vis absorption is probed after the sample is excited with a 'pump' pulse. This pump depopulates the ground state of the sample, leading to a bleaching effect which can be used to identify small, disordered domains of layered perovskite.[216] The resulting differential absorption profiles are shown in Fig. 4.17. Initially, the expected main bleach feature is observable at 758 nm corresponding to the MAPI absorber, as well as less prominent bleaches at 670, 640 and 610 nm, corresponding to $n = 5$, 4 and 3 PEAI phases respectively.[194] This suggests the LPK capping layer underwent a rearrangement process during transport to the measurement laboratory, despite being stored in a dark, nitrogen-filled container. During the initial phase of the measurements, the samples were kept under nitrogen. There were no changes to the differential absorption profile during this time, suggesting that the measurement itself had minimal impact on the sample. Once the sample was exposed to ambient atmosphere with a humidity of 45%, the most prominent $n = 4$ bleach feature at 640 nm rapidly reduced in intensity, being completely lost after around 8 hours. Alongside the loss of the LPK, the MAPI bleach similarly reduced in intensity, ultimately stabilising at around 50 % of the initial value. The initial period of stability suggests that the combined presence of oxygen and light is required for the onset of degradation. Here, no further rearrangement or restructuring of the layered perovskite occurs. Indeed, all of the LPK bleach signals are lost at a very similar time, with no LPK showing improved stability as in the previous XRD studies. The loss of both perovskite materials within the heterojunction likely follows the pinhole-mediated degradation observed for pure 2D flakes, which results in the eventual self-stabilisation of the MAPI layer.

The behaviour seen in the two studies above suggests that the higher-n LPKs are not the thermodynamically most stable LPK phase, and that they will readily rearrange into lower-n analogues. This process can be triggered by the action of external stressors such as oxygen, light or humidity. It follows that the mechanisms which drive ion migration through the perovskite leading to the eventual loss of cation or halide equivalents can drive the rearrangement of a kinetically-trapped $n = 5$ layer. Crucially, it appears that both rearrangement and degradation of the layer can occur in tandem. It is difficult to determine the exact mechanism by which these transformations occur. There is little evidence in the measurements collected for the formation of hydrated phases in Fig. 4.16, or the shifting of diffraction peaks which would indicate internal strain due to the expansion of the perovskite lattice.[205] Notably, the high-n LPK is not simply dissolved and lost into the 'bulk' MAPI underlayer, as evidence of a remaining LPK layer is present within all of the degradation studies except light degradation. Given that different phases were observed to form preferentially across the experiments carried out ($n = 1$ in Fig. 4.16, $n = 2$ in Fig. 4.13 and $n = 4$ in Figs. 4.14 and 4.17), the rearrangement behaviour is clearly highly complex and sensitive to minor changes in the driving factor, where multiple potential products exist in kinetic competition with one another. As such, the processes which drive the evolution of high-n capping layers must be studied further to accommodate their implementation within devices.

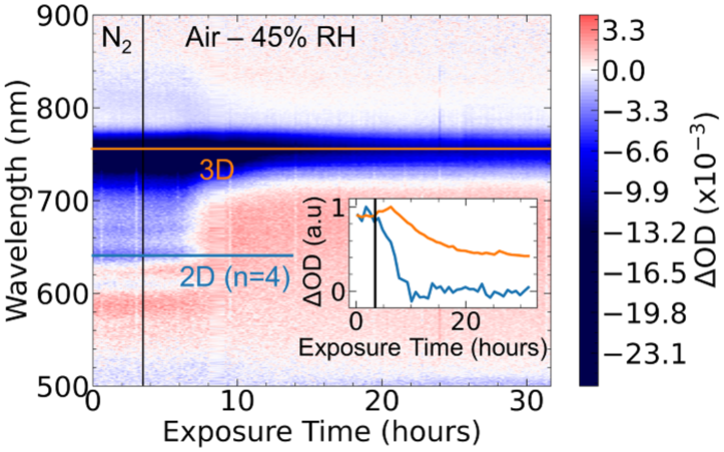

Figure 4.17: The change in absorption induced by a 410 nm excitation pulse with a fluence of 93 µJ cm-2, and a pump-probe delay time of 1 ps, tracked over 32 hours, initially in a nitrogen environment. (inset) Evolution of the bleaching signals at 640 nm (associated with the $n = 4$ layered structures) and at 758 nm (associated with MAPI). *Pump-probe measurements were carried out by Jake Hutchinson. Figure reproduced with permission from Ref. [154] under the terms of the CC BY 4.0 license.*

4.4 Conclusions

In conclusion, this chapter demonstrates that layered perovskites are susceptible to degradation in ambient conditions, both as a single crystal and when employed as a perovskite heterojunction passivating layer. Studies of thin flakes of PEA_2PbI_4 via optical imaging and AFM identify the formation of pinholes as a driving force for the build-up of very thin layers of PbI_2, as confirmed by PL and XPS measurements. This layer of degradation material serves to protect the remaining perovskite, stopping the degradation of exfoliated flakes and helping to stabilise thin films of perovskite against exposure to high vacuum. As the 'bulk' of the perovskite remains unaffected, thick samples of pure layered material have the appearance of long-term stability.

Crucially, this process is found to not occur in the very thin LPK capping layers commonly employed in devices. Studies of a range of different LPK compounds show they are susceptible to recrystallisation when exposed to moisture and solvents, and do not act to protect against degradation under intense light. The lower uniformity and thickness of the perovskite-LPK heterojunction prevents the build-up of degradation material which can limit further degradation. Some LPK layers do, however, display an increased stability, with the DoDecA A' cation in particular showing good potential for minimising ion migration out of the perovskite film.

The results presented in this chapter highlight the potential limitations of using LPK passivation. In many cases, they remain a relatively 'soft' ionic lattice, and thus are vulnerable to changes after deposition. This complicates approaches which rely on energetically-tailored heterojunctions, and motivates further studies into how LPKs behave within a solar cell. Furthermore, these findings are of importance to large-scale manufacture of perovskite solar cells, where exposure to fabrication solvents will be far more likely.

Chapter 5

Layered Perovskites in Devices

The addition of LPK surface passivation to perovskite absorber layers in solar cells has seen widespread adoption in the best-performing, state-of-the-art devices. Numerous studies have demonstrated the beneficial impact they have on various device characteristics. However, questions remain about how the LPK changes throughout the rest of the fabrication process. In addition, LPK passivation can improve the performance of both regular (N-I-P) and inverted (P-I-N) devices, despite significant differences in the recipes used to deposit it.

Here, subsequent fabrication steps after the deposition of the LPK are found to thin down, remove and recrystallise the layer that is initially formed. XRD, SEM and XPS studies unambiguously demonstrate both ETM and HTM solutions can act to disrupt the LPK. The variation in the deposition approaches between N-I-P and P-I-N devices is proposed to be a direct response to the precise disruption mechanism at play, which depends on the CTM solution components. Furthermore, combined device and XRD studies are used to demonstrate that optimal solar cell performance occurs with minimal quantities of crystalline LPK present in the film. In fact, significant quantities of LPK passivation hinder performance instead by limiting the short-circuit current.

The key finding of this chapter is that measurements of isolated perovskite-LPK heterojunctions do not accurately represent the layer as it appears in a completed device, highlighting the importance of in-depth studies which take into account subsequent fabrication steps.

5.0.1 Declaration of Authorship

The experimental work included in this chapter has been published in the journal *Cell Reports Physical Science*, titled ‘The Case of the Vanishing Perovskite layer’.[217] The text of the manuscript has been rewritten, and the contents of the supplementary information have been included in the body of the chapter. Data collected or analysed by my co-authors is detailed at the appropriate points. This includes: supporting XRD measurements taken by Madeleine McRoberts at the University of Glasgow, School of Chemistry; N-I-P devices fabricated and measured by Wai Kin Yiu with contributions from Jingbo Wang at the University of Hong Kong, Optoelectronics and Nanomaterials Lab.

5.1 Introduction

Perovskite solar cells have seen an unprecedented rate of development amongst emerging solar cell technologies. A significant contribution to the ever-increasing efficiencies of these devices is the implementation of LPK passivation layers. Formed directly on top of the perovskite absorber, small quantities of LPK have been reported to bring numerous benefits to the device. They lead to greatly improved stability,[112,148,218] improved charge carrier extraction,[219] reduced recombination losses,[146] improved band alignment[220] and help to passivate surface defects.[117,221] A large part of their success is owed to the fact that LPK passivation displays a large degree of 'process flexibility', offering improved performance to a wide range of solar cell architectures. Furthermore, LPKs are able to provide these widespread benefits despite reports of their intrinsic instability when exposed to environmental stressors such as intense light, moisture or fabrication solvents.[138,154,203]

Despite this widespread implementation, the recipes used for forming LPK passivation layers show some of the largest variation when compared to other device layers. In a field where the best-performing P-I-N and N-I-P mixed perovskite compositions differ by as little as 5%, optimised LPK solution concentrations cover a full order of magnitude. Table 5.1 contains a representative selection of the LPK solution concentrations found to lead to optimal performance for both N-I-P and P-I-N architectures. In the case of N-I-P cells, the LPK is formed directly underneath the HTM layer, deposited from a relatively high solution concentration which leads to the formation of highly crystalline layers. P-I-N cells employ an opposite approach, with a low concentration of LPK solution used to form a layer between the perovskite and ETM. Fig. 5.1 illustrates this difference, showing the position of the LPK relative to the typical solar cell layers in both architectures.

Table 5.1: Selection of N-I-P and P-I-N Solar Cell compositions reported in the literature. 'Conc.' values are A' cation salt solution concentrations used in devices with the highest PCE using that cation in the work.

Device	Perovskite Composition	A' Cation	Conc.	Ref.
N-I-P	$FA_{0.93}Cs_{0.07}PbI_3$	$DecA^+$	15 mM	[148]
	$FA_{0.85}MA_{0.1}Cs_{0.05}PbI_3$	$MeO\text{-}PEA^+$	16 mM	[149]
	$FA_{0.85}MA_{0.1}Cs_{0.05}PbI_3$	PEA^+	20 mM	[192]
	$FA_{0.95}MA_{0.05}PbI_{0.95}Br_{0.05}$	PEA^+	20 mM	[194]
	$FA_{0.92}MA_{0.08}PbI_3$	PEA^+	20 mM	[221]
	$(FA_{0.83}MA_{0.17})_{0.9}Cs_{0.1}Pb(I_{0.83}Br_{0.17})_3$	PEA^+	16 mM	[222]
		$F\text{-}PEA^+$	7.5 mM	
P-I-N	$(FA_{0.98}MA_{0.02})_{0.95}Cs_{0.05}Pb(I_{0.98}Br_{0.02})_3$	OLA^+	2.5 mM	[51]
	$(FA_{0.9}MA_{0.1})_{0.97}Cs_{0.03}PbI_3$	OLA^+	1.25 mM	[112]
	$FA_{0.85}MA_{0.1}Cs_{0.05}PbI_3$	PEA^+	4 mM	[194]
	$(FA_{0.95}MA_{0.05})_{0.95}Cs_{0.05}Pb(I_{0.95}Br_{0.05})_3$	PEA^+	4 mM	[219]
	$FA_{0.98}Cs_{0.02}PbI_3$	PEA^+	4 mM	[117]
		$F\text{-}PEA^+$	3.7 mM	
	$FA_{0.93}MA_{0.02}Cs_{0.05}PbI_{2.94}Br_{0.06}$	PEA^+	4 mM	[223]

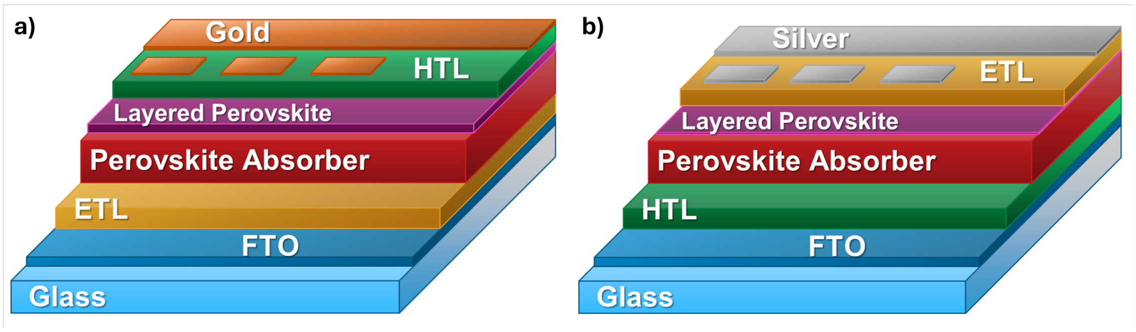

Figure 5.1: Schematic illustration of the individual component layers contained in a typical perovskite solar cell with an LPK interlayer, showing the general structure for: a) N-I-P cells and b) P-I-N cells. Note that layer thicknesses are not representative of actual or relative thickness values.

Crucially, the same LPK interlayer can offer benefits to very varied perovskite compositions, which have different energetic alignments of their respective conduction and valence bands and the CTM HOMO and LUMO levels. This adds a layer of complexity when attempting to identify what is the chief benefit a given LPK confers to the solar cell. This is compounded by the fact that most studies into the behaviour of LPK passivation are carried out on an isolated perovskite-LPK heterojunction, which is missing the CTM layers and metal contacts present within a full device. Thus, the system that is investigated is not fully representative of the LPK as it would appear in an 'actual' solar cell.

The aim of the following chapter is to address this disconnect, by combining measurements carried out throughout the full solar cell fabrication process alongside bilayer measurements which account for subsequent processing steps. Herein, XRD, SEM and XPS studies are used to demonstrate that CTM deposition severely disrupts the underlying LPK passivation layers. Spincoating of the small molecule CTMs and the presence of polar dopants within the solution act to thin down the LPK, either removing it entirely or causing it to be recrystallised into small, disconnected plates. Furthermore, studies into device performance find that maximum efficiency is obtained in systems where there is no evidence of crystalline LPK after all fabrication steps are completed. This occurs for both N-I-P and P-I-N architectures, despite the difference in approaches in LPK deposition. A 'convergent optimisation' process is proposed to explain this finding, where optimised recipes have been developed to compensate for a greater degree of LPK disruption by initially depositing higher quantities of material. When a more 'gentle' processing condition is used, only a very small quantity of LPK is formed. As a consequence of this compensation, a variety of perovskite compositions ultimately contain a very similar quantity of LPK.

5.2 Impact of fabrication on LPK heterojunctions

Research into LPK passivation is most commonly carried out on pure LPK samples or isolated bilayers. This forms a disconnect between the understanding of how the material behaves in isolation, and the actual application of LPKs within solar cells, where they are sandwiched between the perovskite and CTM layers. Thus, XRD measurements were carried out throughout the full fabrication procedure of a set of N-I-P and P-I-N solar cells to explore its impact on perovskite-LPK heterojunctions. These cells utilised complex multi-cation, multi-halide compositions found in state-of-the-art recipes, as detailed in the methods section 2.5. In brief, the N-I-P cells use a triple cation $FA_{0.85}MA_{0.1}Cs_{0.05}PbI_3$ composition, abbreviated to 'Triple Cat'. P-I-N cells use a double cation $FA_{0.9}Cs_{0.1}PbI_{2.87}Br_{0.13}$ composition, abbreviated to 'Double Cat'. The sequentially deposited layers that make up the full solar cell are schematically illustrated in Fig. 5.2 (a, c) for N-I-P and P-I-N cells respectively, with the corresponding XRD diffractograms shown in Fig. 5.2 (b, d).

Here, the initial growth of the 3D perovskite absorber layers is clearly observable, as indicated by the characteristic peaks at 14.1°(red curves in Fig. 5.2 (a, c)). The subsequent deposition of 15 mM PEAI solution leads to the expected appearance of an $n = 1$ LPK peak at 5.4°, as seen in the pink curve. Data for measurements of cells fabricated with a full range of PEAI solution concentrations varying from pure IPA to 50 mM are shown in Figs. 5.3 and 5.4. Once the solution concentration is above 5 mM, the LPK peak can be resolved in the diffractogram data. Additionally, at the highest 50 mM concentration the direct crystallisation of PEAI salt occurs on the sample surface, as evidenced by the appearance of a peak at 4.6° which is marked by a # symbol. The key change in the diffractograms occurs at the next step in the solar cell fabrication process, with the deposition of the CTM as detailed in Figs. 5.3 (b) and 5.4 (b). For the 5 and 15 mM samples, the LPK peak is all but gone, with significantly reduced intensities and increased broadening. For the high concentration 50 mM samples, the co-crystallised non-perovskite PEAI salt peak is affected instead, either being lost entirely in the N-I-P case, or reducing in intensity in the P-I-N case. This occurs alongside the appearance of a new peak at 4.0°, which has been previously identified with an $n = 2$ LPK phase.[127]

Not only is this behaviour direct evidence of the loss of crystalline LPK layers after CTM deposition, the underling perovskite absorber remains unaffected. The peaks associated with PbI_2 and the 3D perovskite show no changes to their intensity or broadening. This indicates that the observed changes are not caused by an attenuation of the X-Ray signal by the CTM deposited on top, proving the changes occur directly at the LPK-CTM interface. As can be seen in Fig. 5.2, further processing of the solar cell layers has minimal additional impact on the observed diffractograms, even when another solution processed layer of BCP ETM is deposited for the P-I-N cells. Only the evaporation of metal contacts acts to reduce and broaden the peaks in some samples - here, this behaviour is due to signal attenuation by the surface Au or Ag coating, as would be expected. Thus, the CTM deposition step was further explored as a driving force behind the LPK disruption.

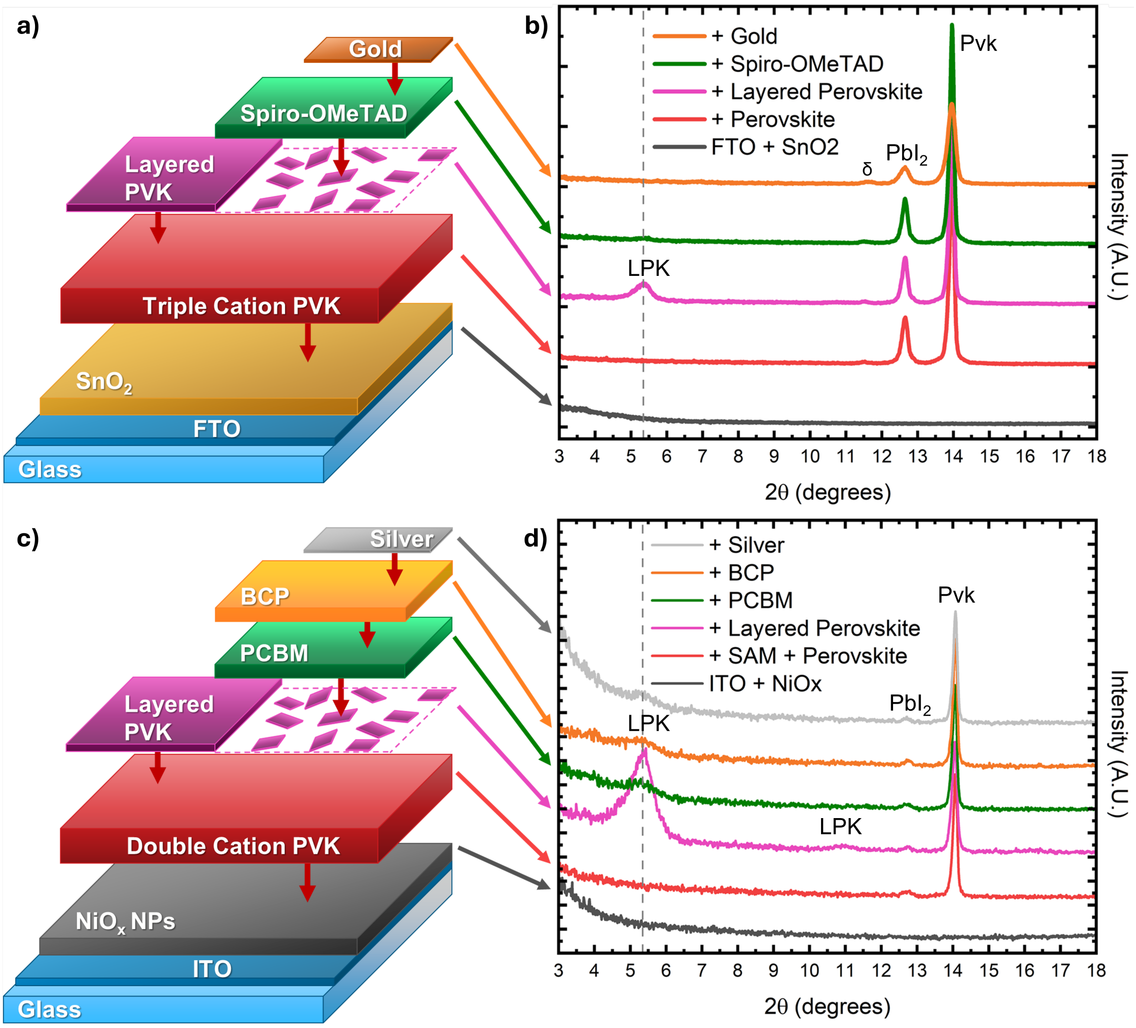

Figure 5.2: a), c) Illustration of the sequential deposition of the layers making up an N-I-P (a) and P-I-N (c) solar cell. b), d) The corresponding XRD Diffractograms of N-I-P (b) and P-I-N (d) perovskite solar cells after the deposition of each layer during fabrication. Peak labels identify the corresponding crystalline phase, with the position of the (002) $n = 1$ layered perovskite peak indicated by the dashed line. The δ symbol indicates the presence of δ-phase FAPI. *Data collection carried out by Madeleine McRoberts. Figure reproduced with permission from Ref. [217] under the terms of the CC BY 4.0 license.*

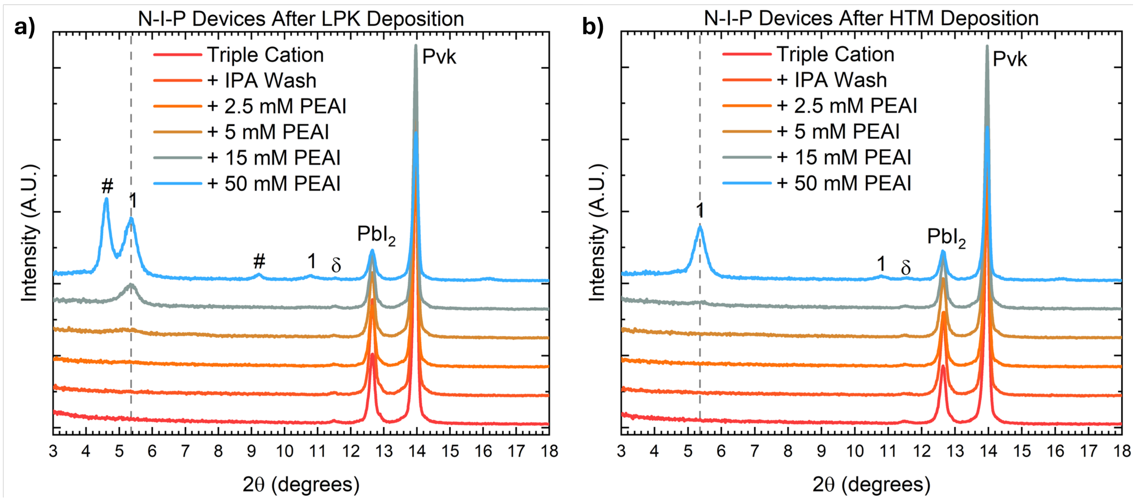

Figure 5.3: XRD diffractograms taken throughout the fabrication of N-I-P perovskite solar cells, after a) the LPK deposition step, and b) after the HTM deposition step. The location of the $n = 1$ layered perovskite (002) peak is indicated by the dashed line. The δ symbol indicates the presence of δ-phase FAPI. The peak marked by the # symbol indicates unreacted PEAI salt, with the numbers identifying the n-value of the LPK present. The vertical dashed line shows the position of the (002) LPK peak. *Data collection carried out by Madeleine McRoberts.*

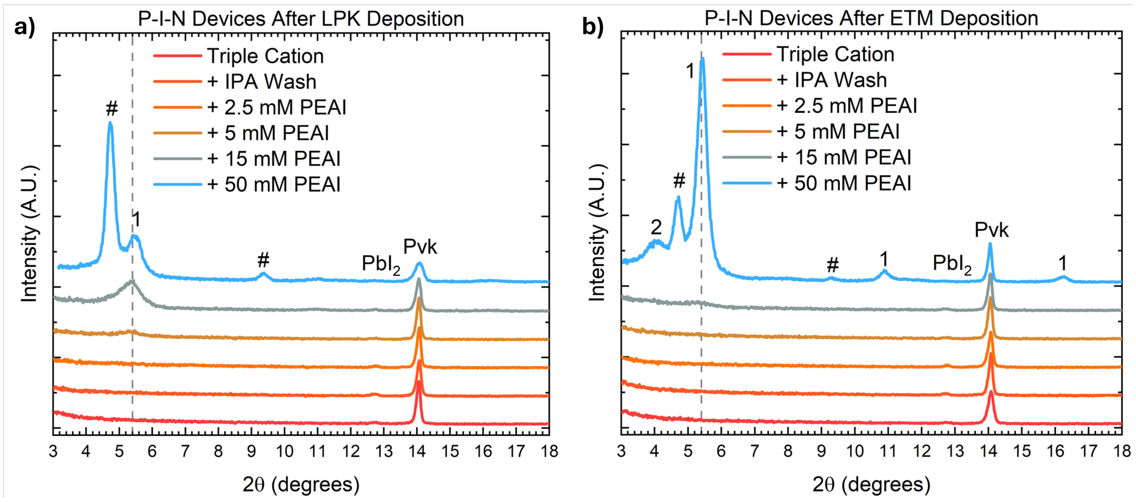

Figure 5.4: XRD diffractograms taken throughout the fabrication of P-I-N perovskite solar cells, after a) the LPK deposition step, and b) after the ETM deposition step. The location of the $n = 1$ layered perovskite (002) peak is indicated by the dashed line. The peak marked by the # symbol indicates unreacted PEAI salt, with the numbers identifying the n-value of the LPK present. The vertical dashed line shows the position of the (002) LPK peak. *Data collection carried out by Madeleine McRoberts.*

5.2.1 Identifying the Mechanism of LPK distruption

The magnitude of changes to the LPK peak during a standard solar cell fabrication procedure motivated an in-depth study of the root causes of this process. The loss of the initially deposited crystalline films of material has significant implications on how the LPK is able to interact with and passivate the underlying perovskite. Most research into the behaviour of the LPK is carried out without considering any subsequent fabrication steps, potentially limiting their applicability to the 'real' state of the LPK. Thus, an investigation of the mechanism behind the loss LPK material upon the deposition of CTMs was carried out via XRD and SEM measurements. Here, a series of perovskite-LPK heterojunctions were prepared, formed with 15 mM solutions of PEAI. This provided a set of samples with well-resolved and clearly identifiable LPK diffractogram peaks, without any unwanted side phases. The underlying 3D perovskite was also matched to the two architectures studied, with Triple Cat films deposited for model N-I-P bilayers and Double Cat films used for P-I-N. Next, the two CTMs utilised in P-I-N and N-I-P cells were 'split' into the base components present in the solution, as detailed in methods section 2.2.3. In brief, for N-I-P devices three CB solutions were prepared containing Spiro-OMeTAD doped with LiTFSI and FK209 dissolved in ACN with tBP as is standard in a device, one with undoped Spiro-OMeTAD, and one containing the dopants only, referred to as an 'HTM Wash'. For P-I-N devices, which use PCBM which does not require doping, two 'sections' of the molecule were instead modelled with the use of C_{60} and MPA solutions in CB to represent the fullerene and ester components respectively.

The impact of depositing the HTM solution components on the model N-I-P bilayers is shown in Fig. 5.5. The diffractogram in Fig. 5.5 (a) shows the behaviour observed in the direct device study is accurately reflected, with the complete loss of the LPK peak after depositing doped Spiro-OMeTAD on top. In the case of undoped Spiro, the peak reduces in intensity, but remains clearly visible. A similar reduction in intensity occurs when the LPK is washed with just the dopant salts and tBP, with the additional appearance of the $n = 2$ LPK peak at 4.0°, showing the surface material has undergone a recrystallisation process.

The corresponding SEM images are shown in Fig. 5.5 (b-f). Without any LPK coating (b), the large-grained structure of the triple cation perovskite is clearly visible. After depositing 15 mM of PEAI solution (c), the conformally grown LPK appears as a series of 'waves' which now cover the initially much smoother grain surfaces. Imaging the impact of the deposition of Spiro-OMeTAD HTM solutions was carried out after washing the film off with pure CB after the initial spincoating procedures to reveal the underlying perovskite surface. Shown in Fig. 5.5 (d), using doped Spiro-OMeTAD removes the LPK layer entirely. The grain surface once again appears smooth, with only small specks of material indicating any previously-deposited material. This could either be evidence of small quantities of residual LPK or the washed-off HTM. In contrast, undoped Spiro-OMeTAD (e) does not significantly affect the LPK, and the surface remains relatively unchanged, with the wave-like conformally grown LPK still clearly distinguishable as in Fig. 5.5 (c). Finally, rinsing the sample surface with the 'HTM Wash' leads to a clear and distinct recrystallisation of the surface LPK coating. The large Triple Cat perovskite is relatively unaffected, with a visible 'roughening' of the grains but no changes

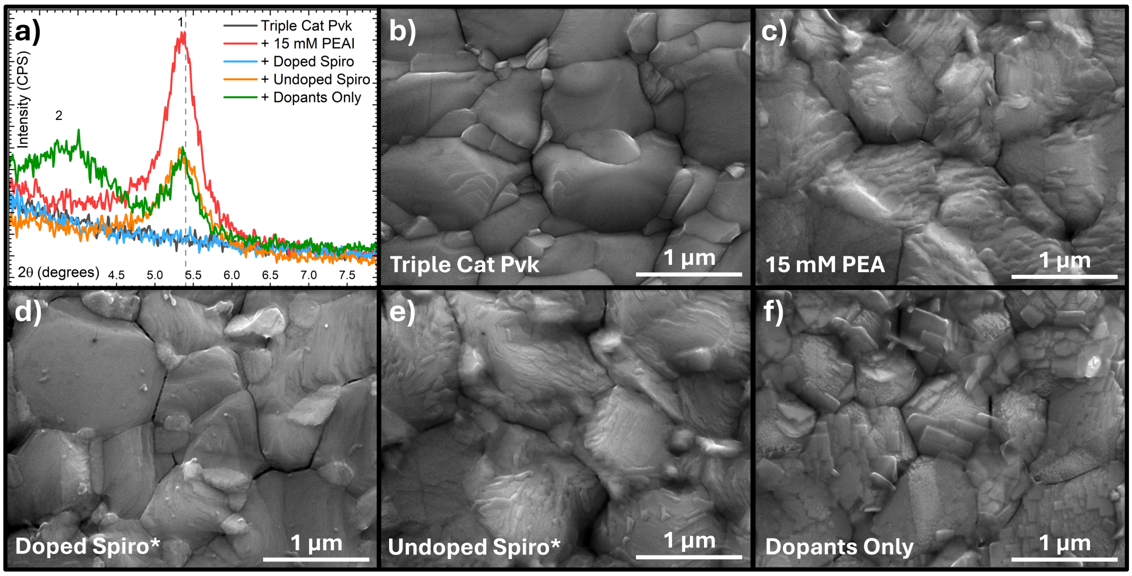

Figure 5.5: a) XRD diffractograms of the (002) LPK peaks and SEM images (b-f) after deposition of various HTM components. b) A reference Triple Cat perovskite film. c) A Triple Cat film coated with 15 mM of PEAI solution. d) A 15 mM film after depositing Spiro-OMeTAD, following a CB rinse. e) A 15 mM film after depositing undoped Spiro-OMeTAD, following a CB rinse. f) A 15 mM film after a dopant-only 'HTM Wash'. The vertical dashed line in (a) shows the position of the (002) LPK peak. *Figure reproduced with permission from Ref. [217] under the terms of the CC BY 4.0 license.*

to their morphology. The LPK, however, now appears as much larger rectangular 'platelets'. These appear disconnected from the underlying perovskite, and span grain boundaries in numerous locations. A more detailed image of an HTM-dopant washed sample surface is included in Fig. 5.6, with a selection of platelet edges outlined in red.

In the case of the model P-I-N system, shown in Fig. 5.7, the diffractograms (a) again reflect the behaviour seen in full devices, with PCBM deposition resulting in a significant reduction of the LPK peak intensity. Both of the model components - C_{60} and MPA - also reduce the intensity of the LPK peak, but to a lesser degree. The SEM images (Fig. 5.7 b-f) initially show a similar smooth grained perovskite with a smaller grain size, and the formation of a conformally-grown wavy surface layer after LPK deposition. Deposition of the ETM components has a far less pronounced effect on the appearance of the LPK, with the material still clearly present in its original form in the images. The sample surface after washing off the deposited PCBM and C_{60} shows minimal differences from the intact heterojunction shown in Fig. 5.7 (c). Spincoating a solution of MPA results in a slight roughening of the underlying perovskite grains as observed in the HTM additive wash above, but no recrystallisation of the LPK can be observed.

The impact of rinsing the samples with a plain CB solutions was also tested, shown in Fig. 5.8. In both N-I-P (a-c) and P-I-N (d-f) samples, the wash results in a slight reduction of the XRD peak intensity, albeit to a much smaller degree than in the cases of the model CTM solutions investigated above. There are essentially no changes to the appearance of the sample surface before and after the CB wash, so

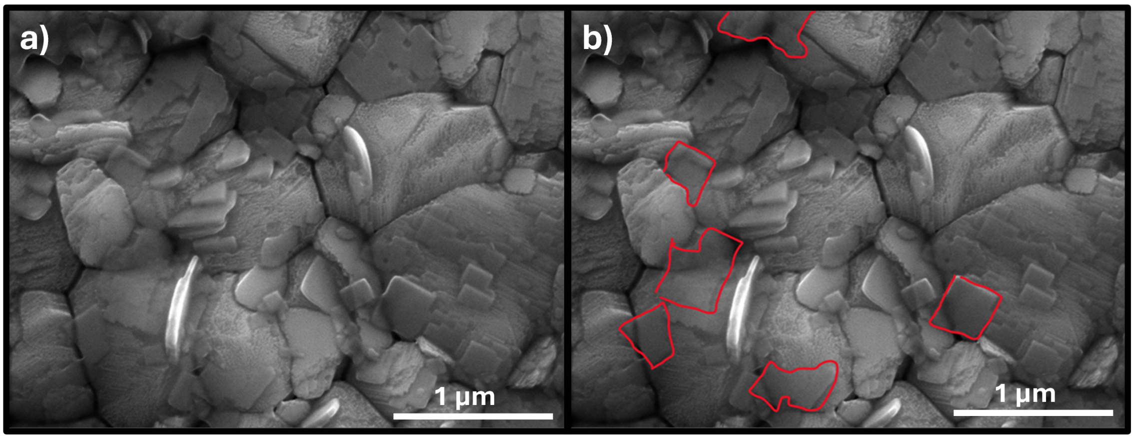

Figure 5.6: SEM Images of a triple cation perovskite film coated with 15 mM of PEAI solution, after a 'HTM Wash'. Original image in a), outlines highlight disconnected, recrystallized platelets in b). *Figure reproduced with permission from Ref. [217] under the terms of the CC BY 4.0 license.*

the impact of the CTM solvent was taken to be minimal in this case. To further confirm the CB rinse utilised in removing deposited CTM material is not impacting the data collected, a set of diffractograms of samples with and without the washing step is included in Fig. 5.9. Here, washing the CTM off results in the LPK peak increasing in intensity, which is either an effect of sample-to-sample variation, or a reduced attenuation of the XRD signal.

The evidence presented by the XRD and SEM results indicates the presence of two distinct mechanisms by which LPKs are damaged by CTM deposition. Firstly, the spincoating of small molecule CTMs results in a physical ablation of the surface material, as illustrated in Fig. 5.10 (a). This leads to a thinning of the LPK with minimal changes to the surface structure, and it is the primary mechanism of loss in P-I-N cells. The second mechanism present is the dissolution of the LPK surface by the CTM solvent system, illustrated in Fig. 5.10 (b). Here, polar solvent additives or elements of the CTM itself act to dissolve the thin LPK layer. This either removes the material entirely, or leads to a recrystallisation into non-conformal platelets. Overall, it is the action of these two mechanisms of LPK disruption in tandem that causes the pronounced reduction in the crystallinity of the LPK. This carries serious implications for the understanding of the role of LPK passivation within solar cells. Disruption of the layers occurs to some degree in a wide variety of solvent compositions, even with the use of orthogonal solvents and molecules which do not undergo chemical reactions with the perovskites.

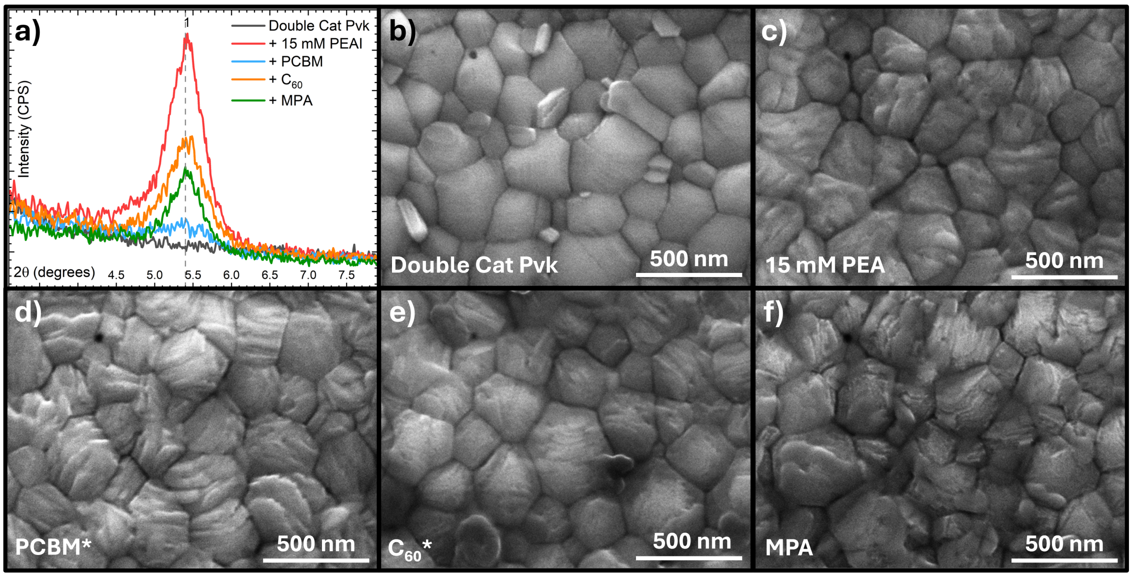

Figure 5.7: a) XRD diffractograms of the (002) LPK peaks and SEM images (b-f) after deposition of various ETM components. b) A reference Double Cat perovskite film. c) A Double Cat film coated with 15 mM of PEAI solution. d) A 15 mM film after depositing PCBM, following a CB rinse. e) A 15 mM film after depositing C_{60}, following a CB rinse. f) A 15 mM film after washing with MPA in CB. The vertical dashed line in (a) shows the position of the (002) LPK peak. *Figure reproduced with permission from Ref. [217] under the terms of the CC BY 4.0 license.*

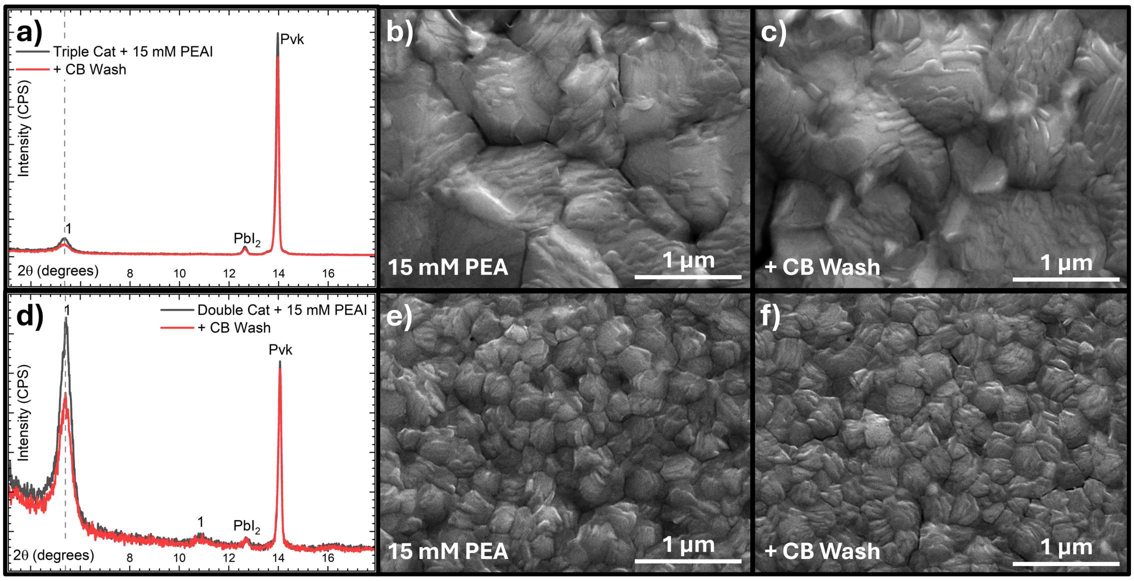

Figure 5.8: a), d) Diffractograms of a perovskite-LPK heterojunctions before and after a CB wash. Despite the change in peak intensity, there are minimal changes in the peak broadening, indicating a similar quantity of material. The numbers identify the n-value of the LPK present. b), e) SEM images of the perovskite-LPK heterojunctions before washing with CB. c), f) SEM images of the heterojunction after washing with CB. No change to the morphology of the LPK on the surface is visible. The vertical dashed line in (a) and (d) shows the position of the (002) LPK peak. *Figure modified with permission from Ref. [217] under the terms of the CC BY 4.0 license.*

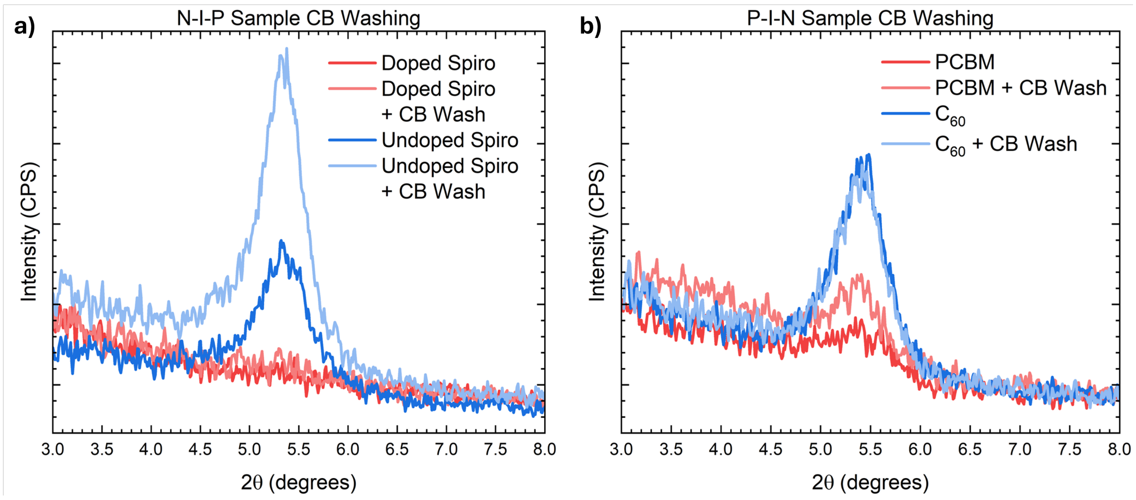

Figure 5.9: Diffractograms of a) N-I-P, and b) P-I-N perovskite-LPK heterojunction samples after the deposition of HTM / ETM respectively, before and after washing off the deposited material with CB. The increase in the intensity of the LPK peak is due to sample-to-sample variation and less signal attenuation from the surface material. *Figure reproduced with permission from Ref. [217] under the terms of the CC BY 4.0 license.*

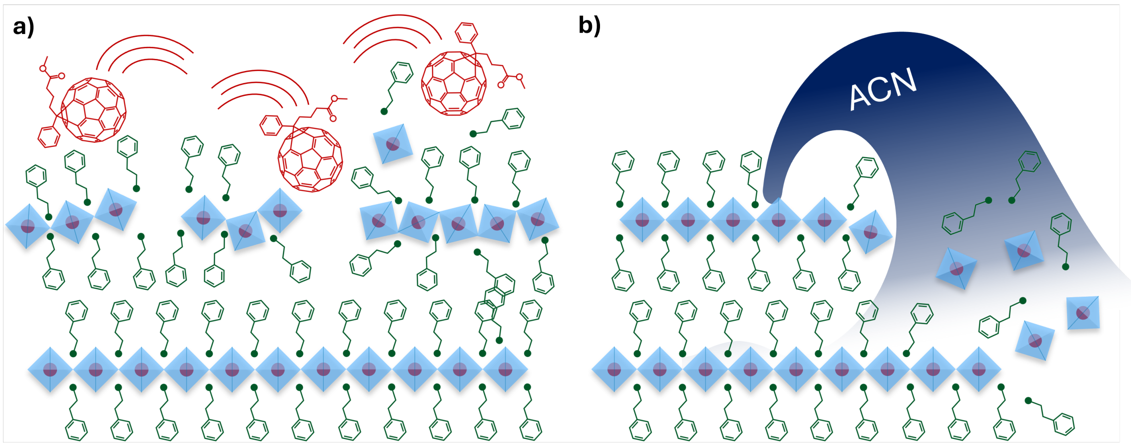

Figure 5.10: Proposed mechanisms for the loss of LPK after CTM deposition. a) Physical ablation of the surface during the deposition of small molecule ETMs in non-polar solvents. b) Washing of the surface during the deposition of HTMs which require the addition of polar solvents. B cations are represented by red circles, small organic / inorganic A cations are represented by large green circles, large organic A' cations are represented by the green aromatic organic molecules, the octahedral cage of six X halides is represented by the blue diamonds, and small-molecule ETMs are represented by the red PCBM molecules. *Figure reproduced with permission from Ref. [217] under the terms of the CC BY 4.0 license.*

5.2.2 Dependence on LPK Processing Conditions

Having identified that a wide variety of CTMs can disrupt the perovskite-LPK heterojunction, the impact of varying post-processing conditions and compositions of the LPK layer was explored next. Low concentrations of annealed LPK are most widely employed in P-I-N cells, whilst N-I-P architectures deposit a higher concentration of LPK without annealing. As such, it is crucial to explore how this processing variation impacts the LPK response to subsequent CTM deposition. Here, XRD and SEM studies were carried out on PEA LPK layers deposited at a wide range of concentrations, with and without an annealing step after spincoating. The 'HTM Wash' method was used for these samples, as it allows a direct study of the LPK surface without the use of additional CB rinse steps.

The XRD data taken before and after the 'HTM Wash' is shown in Figs. 5.11 and 5.12. Initially, the intensity of the LPK peak increases with the concentration of the casting solution, and is more pronounced for annealed samples. Without annealing, (Fig. 5.12) a peak corresponding to co-crystallised PEA salt occurs at lower concentrations, indicating that the conversion of salt into the LPK is driven by the annealing step. The diffractograms after the wash step offer strong evidence of pronounced recrystallisation of the sample surface. The initial LPK peaks are significantly reduced in intensity and additional peaks corresponding to $n = 2$ phases appear, as observed in the mechanism study above. These $n = 2$ peaks are broad and have low intensity, indicating a comparatively low crystallinity and order when compared to the initial $n = 1$ phase. Samples made from 50 mM solution again show a slightly different behaviour, with the LPK peak instead growing in intensity. Here, the unreacted PEA cation reacts with residual PbI_2 during the 'HTM Wash', forming new regions of perovskite as evidenced by the loss in intensity of their respective PEAI salt and PbI_2 XRD peaks at 4.6° and 12.7°. Overall, annealed samples are more robust, with residual LPK still visible in samples formed with lower PEA concentrations.

The SEM images corresponding to the XRD study, included in Figs. 5.13 and 5.14 offer additional evidence of LPK recrystallisation. For the lowest 5 mM PEA concentration, no LPK is visible, and the 'HTM Wash' has a minimal effect, with only the perovskite grain boundaries appearing more pronounced. The wave-like features of conformally grown LPK appear in 15 mM samples, increasing to a mass of material spread over the surface for the 50 mM concentration. After the 'HTM Wash', the surface LPK is recrystallised into rectangular platelets. The quantity of material observable on the surface is largely directed by the annealing treatment of the perovskite. For the 15 and 50 mM annealed samples, approximately 76% to 99% respectively of the perovskite surface is covered in platelets. Without annealing, these values reduce to 0% and 49%. Fig. 5.15 shows how the values for the annealed 15 mM and unannealed 50 mM samples were determined. The fact that platelets only appear in samples where an LPK peak is visible in the XRD diffractograms, and increase in quantity as the deposited solution concentration increases, is strong evidence that they are indeed the recrystallised layered perovskite.

The impact of changing the A' cation chemistry was explored next, with F-PEA cations selected as they are reported to be a more robust and stable alternative to

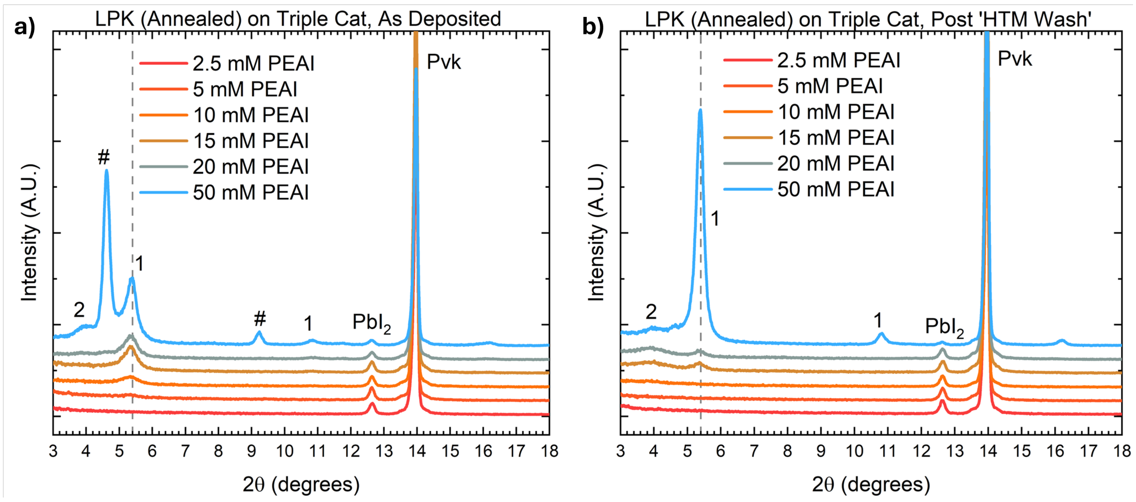

Figure 5.11: XRD Diffractograms of triple-cation perovskite films with increasing concentrations of layered perovskite deposited with annealing. a) films after deposition, with no further processing. b) Films after the 'HTM Wash'. Peaks have been labelled with the n-value of the layered perovskite they correspond to. The # symbol indicates unreacted PEAI salt. The vertical dashed line shows the position of the (002) LPK peak. *Figure modified with permission from Ref. [217] under the terms of the CC BY 4.0 license.*

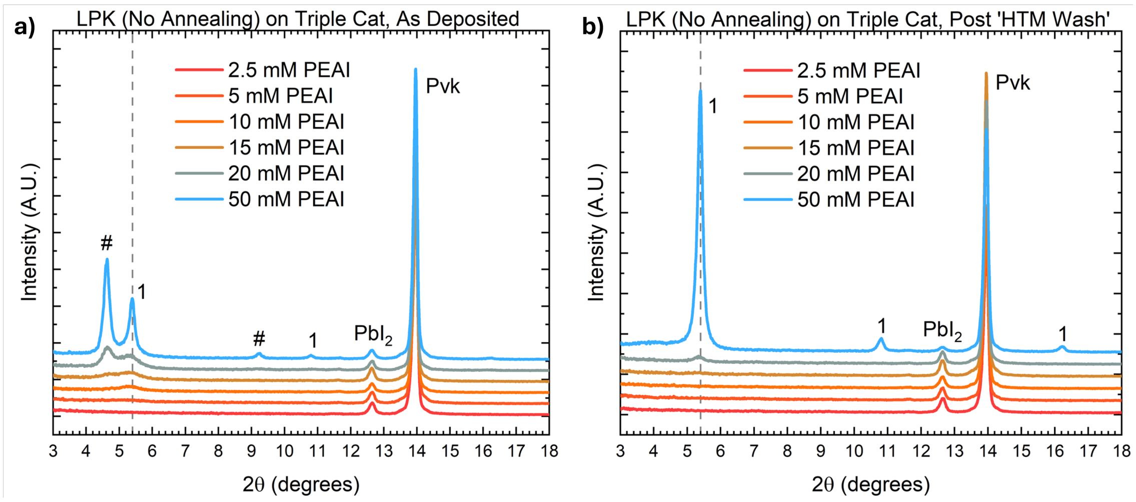

Figure 5.12: XRD Diffractograms of triple-cation perovskite films with increasing concentrations of layered perovskite deposited without annealing. a) films after deposition, with no further processing. b) Films after the 'HTM Wash'. Unreacted PEAI cation salt, labelled with the # symbol, occurs at a far lower concentrations than in annealed films. The numbers identify the n-value of the LPK present. The vertical dashed line shows the position of the (002) LPK peak. *Figure modified with permission from Ref. [217] under the terms of the CC BY 4.0 license.*

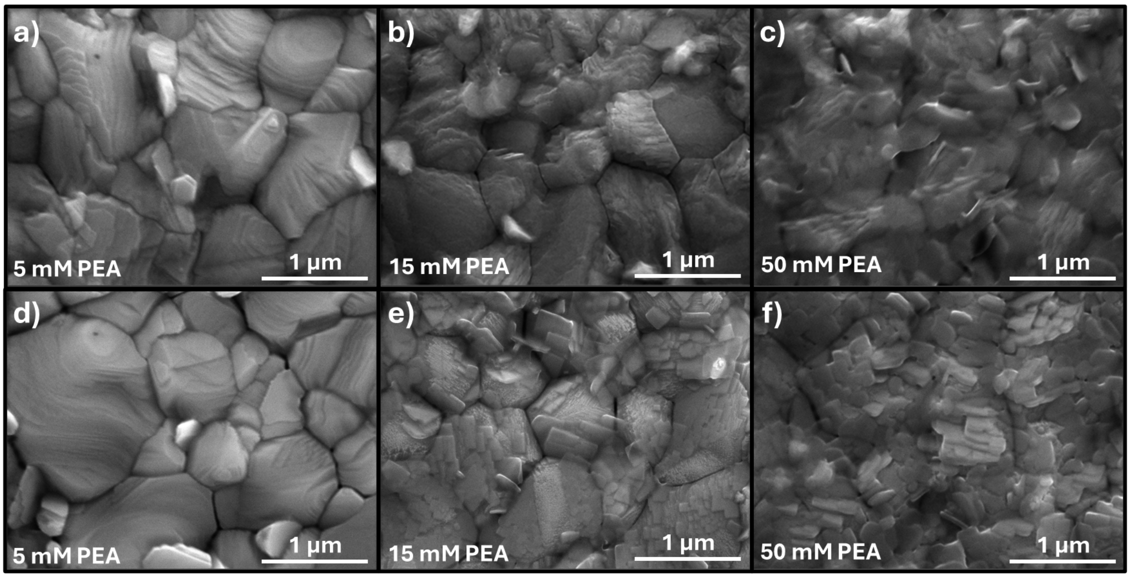

Figure 5.13: SEM images of annealed perovskite-LPK heterojunctions before (a-c) and after (d-f) a 'HTM wash', as in Fig. 5.11. a), d) A triple cation perovskite film coated with 5 mM of PEAI solution. b), e) A triple cation perovskite film coated with 15 mM of PEAI solution. c), f) A triple cation perovskite film coated with 50mM of PEAI solution. *Figure reproduced with permission from Ref. [217] under the terms of the CC BY 4.0 license.*

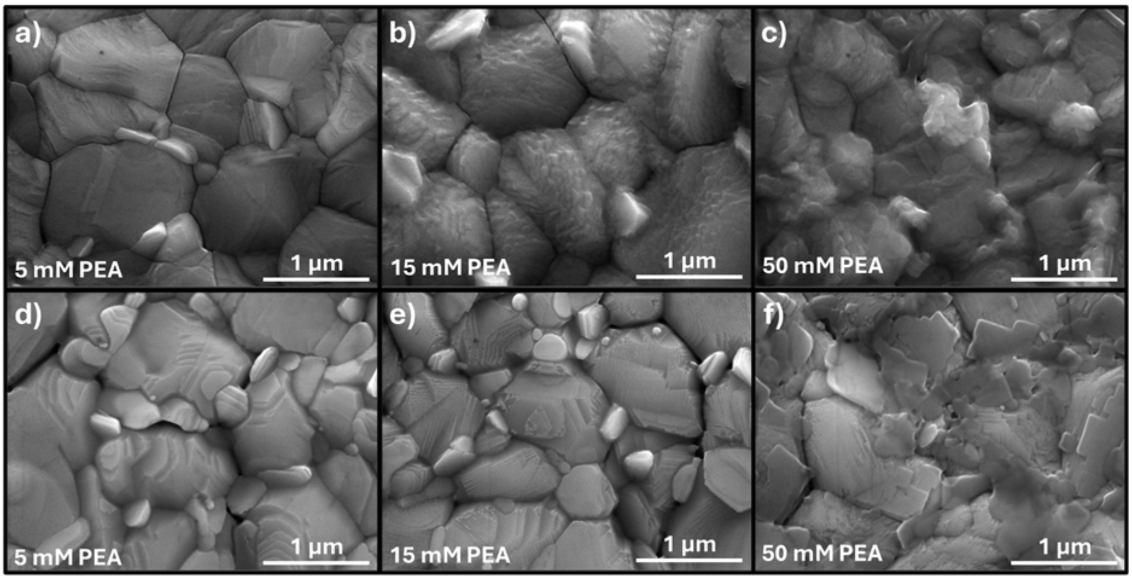

Figure 5.14: SEM images of unannealed perovskite-LPK heterojunctions before (a-c) and after (d-f) a 'HTM wash', as in Fig. 5.12. a), d) A triple cation perovskite film coated with 5 mM of PEAI solution. b), e) A triple cation perovskite film coated with 15 mM of PEAI solution. c), f) A triple cation perovskite film coated with 50mM of PEAI solution. *Figure reproduced with permission from Ref. [217] under the terms of the CC BY 4.0 license.*

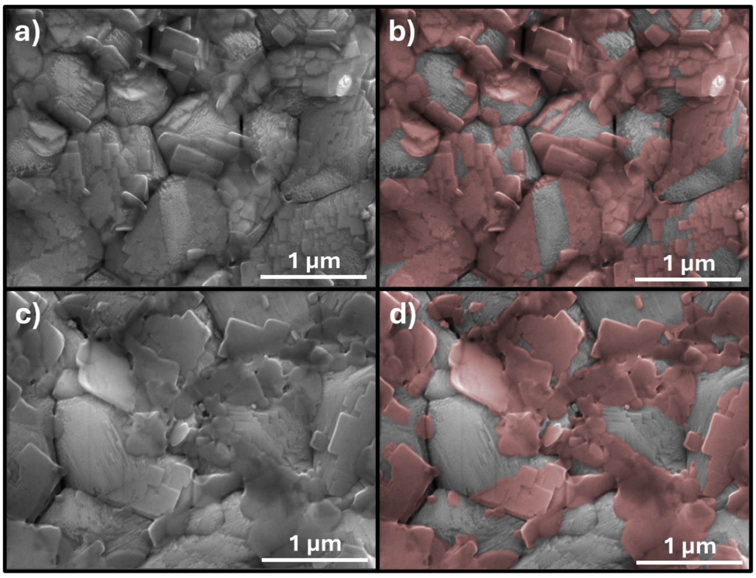

Figure 5.15: SEM images of perovskite-LPK heterojunctions after the 'HTM Wash', used for determining remaining surface coverage. a), b) Samples coated with 15 mM PEAI solution (annealed). c), d) Samples coated with 50 mM PEAI solution (no annealing). Original images in a), c). Red overlays in b) and d) highlight disconnected, recrystallized platelets. The relative pixel colour distribution was used to calculate % coverage with the use of open-source image editing software.[224] *Figure modified with permission from Ref. [217] under the terms of the CC BY 4.0 license.*

PEA.[222] The XRD and SEM data is included in Figs. 5.16 and 5.17 respectively. Here, the 'HTM Wash' has a far less pronounced impact. The diffractogram peaks show minimal changes, with only the co-crystallised F-PEA cation peaks disappearing. Similarly, the SEM images show far less pronounced changes to the surface morphology of the sample. For heterojunctions formed from a 15 mM solution, initially deposited regions of LPK appear to recrystallise into larger domains. In the 50 mM LPK sample, washing results in the appearance of 'gaps' in the deposited layer of material. This offers direct evidence that the F-PEA is still affected by the processing of the HTM solvent system on top, whilst undergoing less recrystallisation than their PEA counterparts.

The results presented above clearly demonstrate that conformally grown LPK layers are severely disrupted by the HTM solvent system. Recrystallisation is widespread, and whilst changes to processing conditions and A' cation chemistry can offer increased robustness, they do not prevent changes entirely. Crucially, even if a significant quantity of LPK is detectable in the XRD measurements, the morphology and coverage of the layer is significantly altered. This is of particular note as LPK layers are often discussed and illustrated in the literature as a distinct and uniform sheets of material.[80,98,225] The SEM images above demonstrate in many situations this may not be the case. As such, much of the understanding of their role in improving device performance may be based on an inaccurate picture of their state in a completed device.

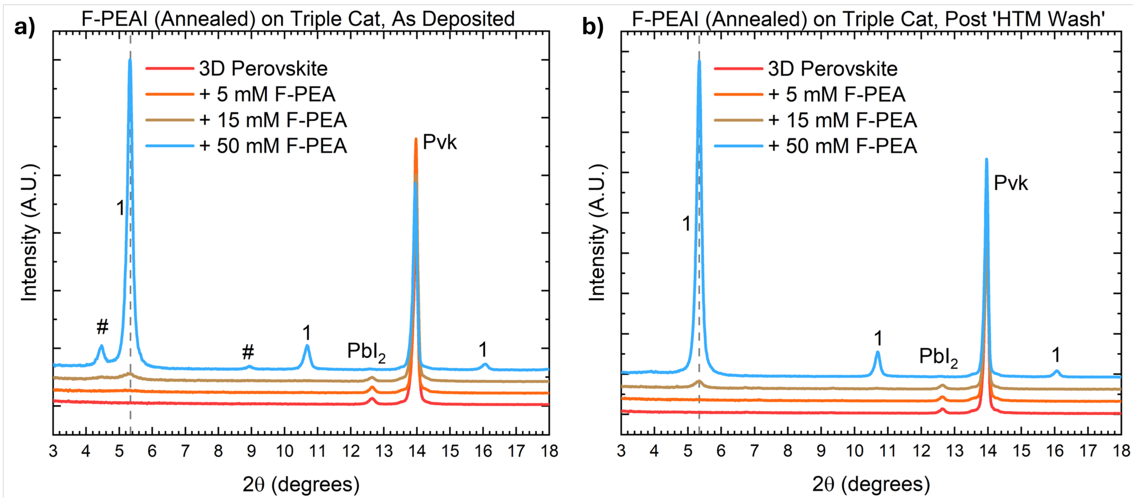

Figure 5.16: XRD Diffractograms of triple-cation perovskite films with increasing concentrations of F-PEA deposited with annealing. a) films after deposition, with no further processing. b) Films after the 'HTM Wash'. The peaks marked by the # symbol indicate unreacted F-PEA salt, with the numbers identifying the n-value of the LPK present. The vertical dashed line shows the position of the (002) LPK peak. *Figure modified with permission from Ref. [217] under the terms of the CC BY 4.0 license.*

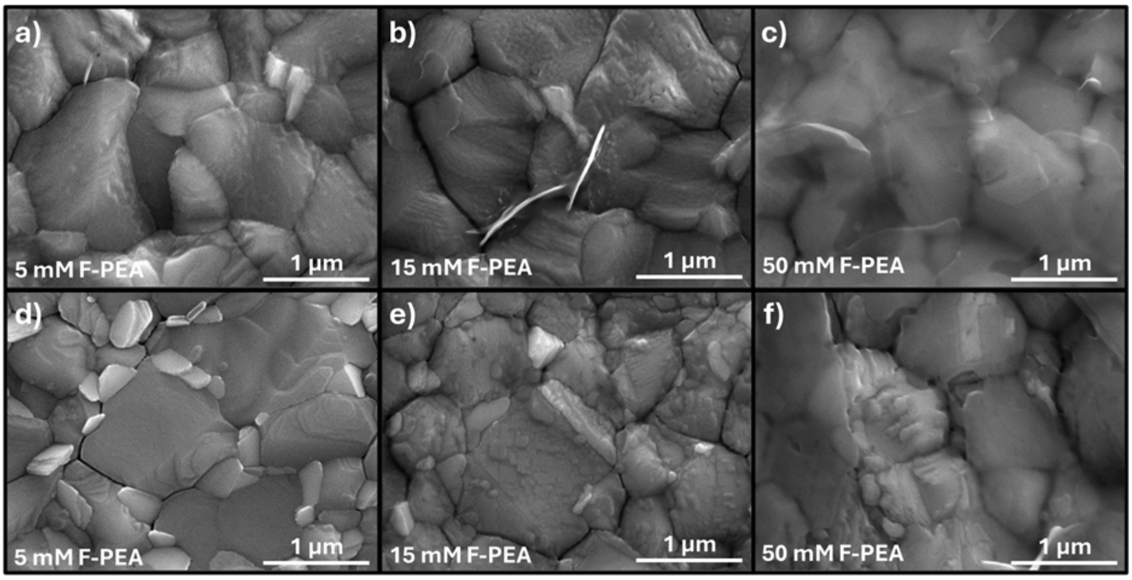

Figure 5.17: SEM images of annealed perovskite-LPK heterojunctions using F-PEA cation, before (a-c) and after (d-f) a 'HTM wash', as in Fig. 5.16. a), d) A triple cation perovskite film coated with 5 mM of F-PEAI solution. b), e) A triple cation perovskite film coated with 15 mM of F-PEAI solution. c), f) A triple cation perovskite film coated with 50mM of F-PEAI solution. *Figure reproduced with permission from Ref. [217] under the terms of the CC BY 4.0 license.*

5.2.3 Surface chemistry determination via XPS

Whilst the XRD and SEM studies above offer compelling evidence regarding the structural changes occurring at the perovskite-LPK interface, they do not confer any insights regarding the changes in the surface chemistry of the samples. XPS measurements which can identify differences between chemical species and bonding environments were therefore utilised to study the changes in the makeup of the first 9 nanometres the perovskite surface after HTM solution deposition. For these experiments, a set of four representative samples was selected, consisting of uncoated triple cation perovskite, and samples with PEA capping layers deposited from 2.5 mM, 15 mM and 50 mM of PEAI solution. These correspond to LPKs which did not have a detectable peak in the XRD diffractograms, ones with a clear peak which is severely disrupted after spincoating of the HTM, and samples with significant quantities of co-crystallised PEA salt. Here, all samples were annealed to ensure full formation of the LPK after deposition. Further details of the XPS data collection and analysis process are included in the methods, sections 2.6.7 and 2.8.6 respectively.

To facilitate reliable assignments of the XPS peaks to the species present within the perovskite heterojunctions, a set of initial measurements were collected for the constituent PEAI and FAI salt powders. The C 1s spectra for these samples are shown in Fig. 5.18. To account for the effects of sample charging, the binding energy values were referenced to the 284.8 eV value for a C-C bond.[226] The PEA sample contains the expected three chemical environments, with the peak at 284.8 eV assigned to C-C bonds, the peak at 285.9 eV assigned to the C-N environment of the ammonium group, and with the final broad peak at 291.9 eV assigned to the π-π* satellite peak of the aromatic ring. The FA powder sample contains two principal peaks - the reference C-C peak at 284.8 eV, and a peak at 287.8 eV assigned to the delocalised $C{=}NH_2$ environment of the amidinium moiety. The additional pair of peaks at 283.3 eV and 286.0 eV are evidence of sample oxidation or the presence of external contaminants, assigned to C=O double and C-O single bonding environments respectively. A full list of fitted peak positions, including the C 1s and N 1s regions, is included in Table 5.2, and the fitted peaks are included in the Appendix, section A.4.1.

The binding energy separation between matching N 1s and C 1s peaks was calculated next. The ammonium energy separation was determined to be 115.8 eV, and the amidinium separation was calculated as 112.3 eV. These values were used to confirm peak assignments in the perovskite-LPK heterojunction samples, which did not undergo any additional binding energy referencing or charge correction.

The C 1s regions for the triple cation and LPK-coated sample set are shown in Fig. 5.19, with full fitted peak positions included in Table 5.3 and plotted in the appendix, section A.4.2. These show clear evidence of an accumulation of the PEA cation as the LPK casting solution is increased. For the reference perovskite (a) and 2.5 mM LPK samples (b), the FAI peak at 288.8 eV is clearly visible. This peak has a significantly lower intensity in the 15 mM sample (c), and is fully gone at 50 mM (d). This occurs alongside the appearance of the C-N and π-π* satellite peaks associated with the PEA molecule at 286.7 eV and 292.2 eV respectively. This in-

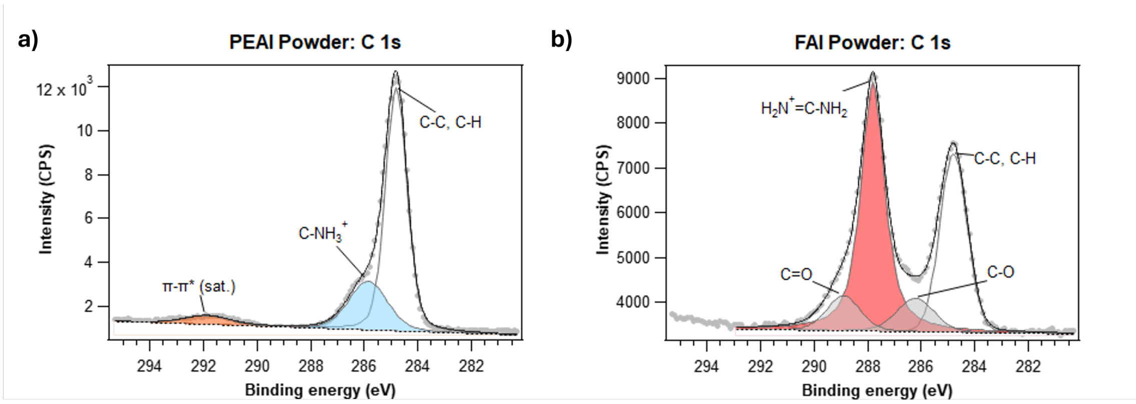

Figure 5.18: XPS Spectra showing the peak fitting of the C 1s region of reference A / A' cation powder precursors. a) PEAI powder sample data. b) FAI powder sample data. Peaks assigned to key chemical environments have been coloured for clarity. *Figure reproduced with permission from Ref. [217] under the terms of the CC BY 4.0 license.*

Table 5.2: Fitted peak positions (eV) for reference A / A' cation powders. C-O and C=O peaks are attributed to sample oxidation. Peak energies were referenced to the C-C peak at 284.8 eV. BE separation values indicate the difference between the C 1s and N 1s peaks for each functional group.

C 1s Peaks	C-C	C-NH$_3$	C=NH$_2$	π-π* Sat	C-O	C=O
PEAI	284.8	285.9		291.9		
FAI	284.8		287.8		286.2	288.9
N 1s Peaks		C-NH$_3$	C=NH$_2$	O1s	BE Separation	
PEAI		401.7		531.8 / 533.5	115.8	
FAI			400.1	532.0 / 533.4		112.3

dicates a build-up of the organic A' cation which eventually fully covers the surface and prevents probing of the underlying perovskite once a 50 mM LPK solution has been deposited. It is important to note that whilst the (a) and (b) samples do show a peak at the 286.7 eV region, there is no corresponding N 1s peak that can be used to assign these to a C-N bonding environment (shown in the appendix, Figs. A.14 b) and A.15 b)). Instead, these have been assigned to degradation of the carbon-containing sample moieties or oxidation and contamination that occurred during exposure of the sample to ambient atmospheres, with energies closely matched to C-O bonds. These samples also have significant C-O peaks in the O 1s spectra (shown in the appendix, Figs. A.14 - A.17, panel (f)), which reduce in intensity as the LPK solution concentration is increased. For the highest 50 mM sample, the only peak in the O 1s spectrum is attributed to C=O bonds, which are evidence of adsorbed CO$_2$ molecules. This suggests the LPK is at least partially limiting the extent of the degradation and contamination of the perovskite surface when exposed to ambient atmospheres. Additional evidence of the significant build-up of LPK material can be found in the Cs 3d region, shown in the appendix, Figs. A.14 - A.17, panel (d). The intensity of this peak decreases as the LPK concentration increases, until ultimately no peak is detected at 50 mM. This again indicates that the LPK layer is thicker than the probe depth of the XPS instrument.

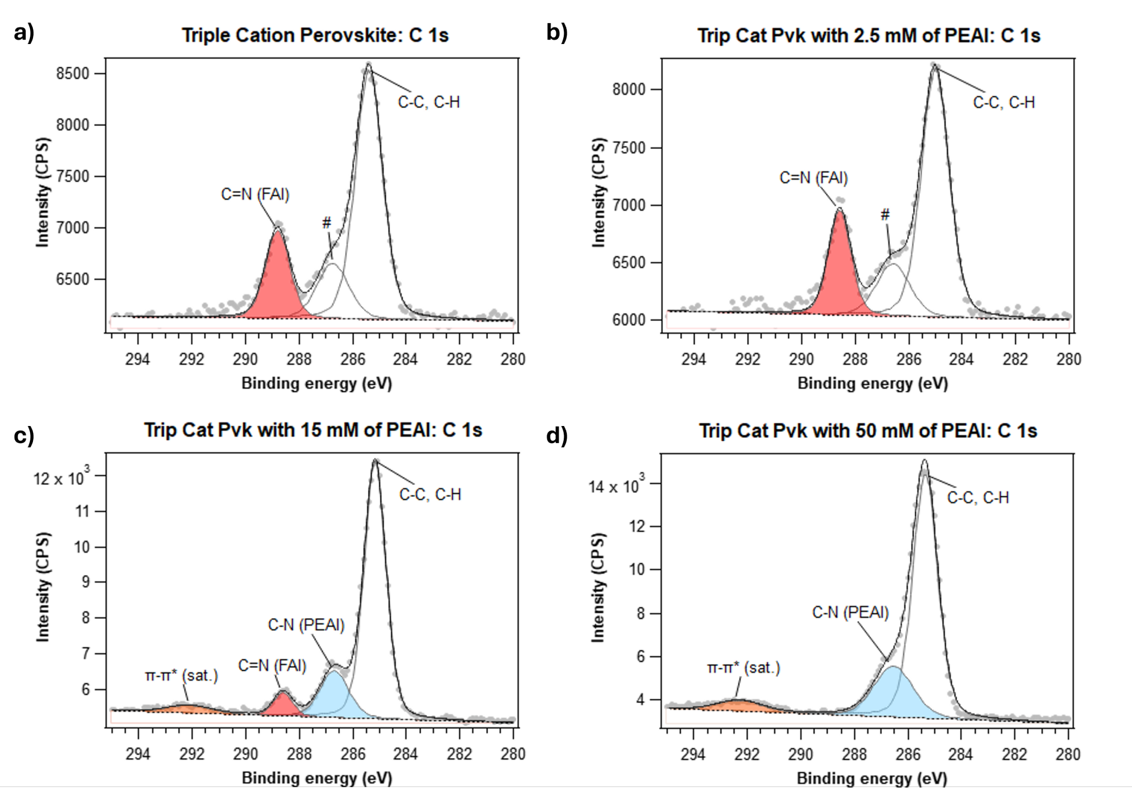

Figure 5.19: XPS Spectra showing the peak fitting of the C 1s regions of triple cation perovskite samples coated with increasing quantities of LPK. a) Reference triple cation film. b) Film with 2.5 mM LPK solution deposited. c) Film with 15 mM LPK solution deposited. d) Film with 50 mM LPK solution deposited. Peaks assigned to key chemical environments have been coloured for clarity. The C-C peak is attributed to both C-C bonds from within the PEA molecule (if present) and to surface contamination with carbon-containing compounds. The peak labelled with # is attributed to X-Ray induced degradation of the carbon-containing moieties or contamination / sample oxidation. *Figure reproduced with permission from Ref. [217] under the terms of the CC BY 4.0 license.*

Table 5.3: Peak positions (eV) for triple cation films coated with increasing quantities of LPK. C-O (Cont.) peak energies are attributed to sample contamination / oxidation from atmosphere exposure. The two peaks in the O1s region indicate contamination / oxidation and are assigned to C=O bonds and C-O / O-H bonds respectively. BE separation values indicate the difference between the C 1s and N 1s peaks for each functional group.

C 1s Peaks	C-C	C-NH_3	C=NH_2	π-π* Sat	C-O (Cont.)
Trip Cat	285.4		288.8		286.7
+ 2.5 mM	285.0		288.6		286.6
+ 15 mM	285.2	286.7	288.6	292.2	
+ 50 mM	285.4	286.5		292.3	
N 1s Peaks		**C-NH_3**	**C=NH_2**		**BE Separation**
Trip Cat			401.1		112.3
+ 2.5 mM			400.8		112.2
+ 15 mM		402.4	400.8		115.7 112.2
+ 50 mM		402.5			116.0
Other Peaks	**Pb $4f_{7/2}$**	**Pb $4f_{5/2}$**	**Cs $3d_{5/2}$**	**I $3d_{5/2}$**	**O 1s**
Trip Cat	139.0	143.9	725.4	619.7	532.4 / 533.8
+ 2.5 mM	138.7	143.5	725.2	619.5	532.2 / 533.5
+ 15 mM	138.7	143.6	725.2	619.6	532.3 / 533.8
+ 50 mM	138.7	143.6		619.6	532.8

XPS data for samples treated with the 'HTM Wash', included in Fig. 5.20, Table 5.4 and appendix section A.4.2, clearly indicate a significant disruption to the perovskite surface. All samples now feature a new peak in the C 1s spectrum around 293.4 eV as shown in Fig. 5.20, which is attributed to the CF_3 groups present within the LiTFSI and FK209 dopants.[227] Most importantly, the quantity of the PEA cation on the surface is severely diminished. The aromatic peaks at 292.3 eV are no longer distinguishable, and the main C-N peaks at 286.5 eV are gone in the 15 mM sample, and significantly diminished in intensity for the 50 mM sample. Additionally, the FA peak at 288.6 eV is now always visible, with essentially equivalent intensities in the uncoated, 2.5 mM and 15 mM samples, and only partial attenuation in the 50 mM sample. Similarly, the Cs 3d signal is now clearly distinguishable in all cases, as shown in Figs. A.18 - A.21, panel (d). These changes in the relative peak intensities demonstrate that the 'HTM Wash' results in a large scale disruption of the LPK deposited on the sample surface. The appearance of previously screened peaks indicates either a thinning of the material, or a non-uniform etching where parts of the LPK are removed to expose the triple cation perovskite underneath. This is consistent with both of the observed mechanisms of LPK loss, with mechanical ablation and platelet formation occurring in tandem.

The combined XRD, SEM and XPS studies into LPK passivation layers clearly prove that they are removed or recrystallised by the deposition of CTM on top. Despite the use of orthogonal solvents, the spincoating process results in a final structure which differs significantly from the initial deposited perovskite-LPK heterojunction. This raises important questions about their ultimate role in a solar cell, as they are highly unlikely to act as a 'uniform passivation layer', as they are commonly described.[147,228] For many of the conditions utilised within state-of-the-art solar cells,

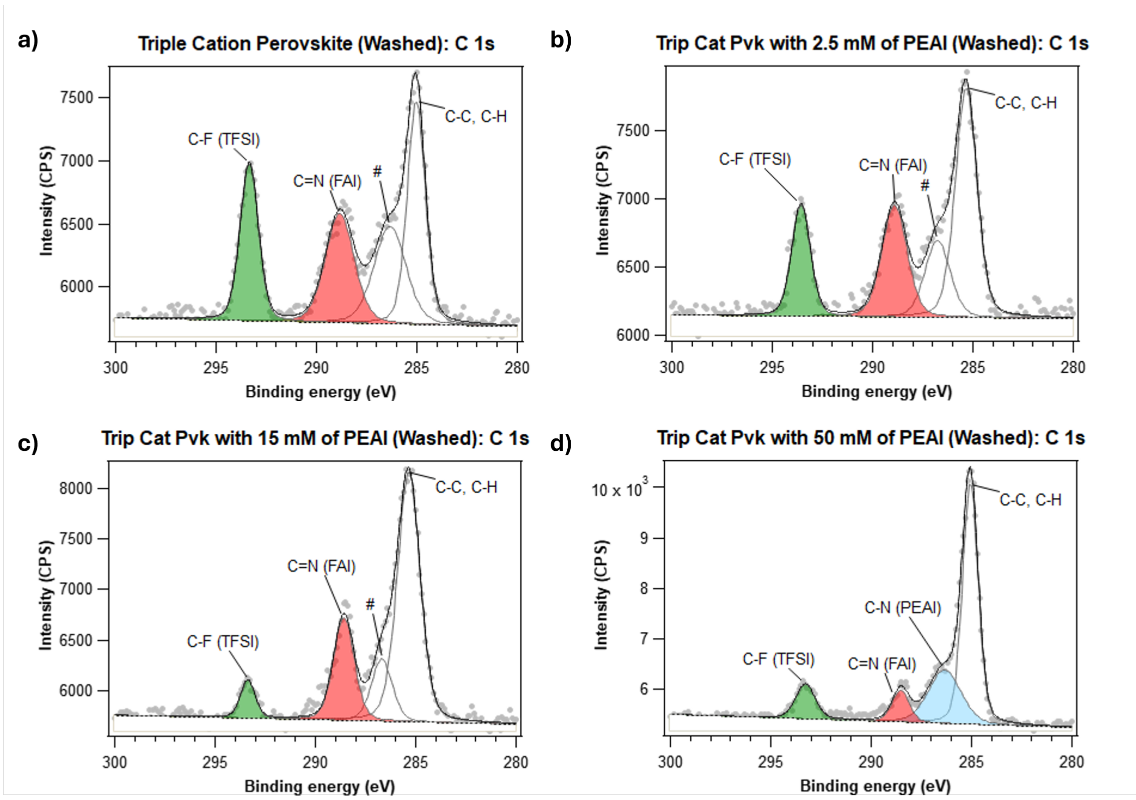

Figure 5.20: XPS spectra showing the peak fitting of the C 1s regions of triple cation perovskite samples coated with increasing quantities of LPK, after a 'HTM' washing step. a) Reference triple cation film. b) Film with 2.5 mM LPK solution deposited. c) Film with 15 mM LPK solution deposited. d) Film with 50 mM LPK solution deposited. Peaks assigned to key chemical environments have been coloured for clarity. The C-C peak is attributed to both C-C bonds from within the PEA molecule (if present) and to surface contamination with carbon-containing compounds. The peak labelled with # is attributed to X-Ray induced degradation of the carbon-containing moieties or contamination / sample oxidation. *Figure reproduced with permission from Ref. [217] under the terms of the CC BY 4.0 license.*

the remaining LPK material is all but undetectable on the sample surface. Given that devices which use LPK interlayers still see improved performance, the residual LPK material must still be able to passivate surface traps, or provide some other benefits. Here, it is most likely to be localised on grain boundaries and other defect-rich regions, without forming significant quantities of uniform, crystalline material. Studies by Cacovic *et al.* support this hypothesis, where very low concentrations of LPK solutions (0.5 mM), which do not form a distinct, observable LPK phase, are still able to reduce surface non-radiative recombination of the perovskite.[111] This observation highlights the need for studies which correlate the quantity of LPK within a device with their performance metrics.

Table 5.4: Peak positions (eV) for triple cation films coated with increasing quantities of LPK, after an 'HTM Wash'. C-O (Cont.) peak energies are attributed to sample contamination / oxidation from atmosphere exposure. The two peaks in the O1s region indicate contamination / oxidation, and the O=S bonds present within the TFSI molecule, respectively.

C 1s Peaks	C-C	C-NH_3	C=NH_2	π-π* Sat	C-O (Cont.)	C-F_3
Trip Cat	285.0		288.8		286.3	293.4
+ 2.5 mM	285.3		288.9		286.8	293.6
+ 15 mM	285.4		288.6		286.7	293.4
+ 50 mM	285.1	286.3	288.5			293.3
N 1s Peaks		C-NH_3	C=NH_2		BE Separation	
Trip Cat			400.9		112.1	
+ 2.5 mM			401.1		112.2	
+ 15 mM			400.9		112.3	
+ 50 mM		402.4	400.7		116.1 112.2	
Other Peaks	Pb $4f_{7/2}$	Pb $4f_{5/2}$	Cs $3d_{5/2}$	I $3d_{5/2}$	O 1s	F 1s
Trip Cat	138.7	143.6	725.2	619.5	531.6 / 533.2	689.3
+ 2.5 mM	139.8	144.7	725.3	619.6	531.8 / 533.2	689.3
+ 15 mM	138.6	143.5	725.2	619.5	531.8 / 533.1	689.3
+ 50 mM	138.5	143.4	725.1	619.4	533.1	689.2

5.3 Correlating Performance with LPK Quantity in Perovskite Solar Cells

The disruption of the LPK due to CTM formation raises questions regarding how the 'actual' LPK impacts device metrics. Here, using the findings of the structural studies to guide solar cell compositions, a range of solar cells were prepared where the LPK quantity was varied from well below the detection threshold of XRD measurements to ones with a significant quantity of recrystallised LPK. This allows a direct comparison between device performance and LPK quantity, and how it correlates to the optimal recipes in the literature. Both P-I-N and N-I-P architectures were studied, with the details of solar cell fabrication included in the methods, section 2.5. In brief, P-I-N devices used the architecture ITO / NiOx / Double Cat / LPK / PCBM / BCP / Ag, whilst N-I-P devices used the architecture FTO / SnOx / Triple Cat / LPK / Spiro-OMeTAD / Au. The concentration of the LPK was varied to match the concentration range used within the bilayer and mechanism studies above. The LPK was annealed for P-I-N cells, and left unannealed for N-I-P cells, following the approaches utilised in the literature for champion devices.[192,194] An additional set of annealed N-I-P devices was also prepared to further explore the impact of post-processing on LPK stability.

A set of representative champion devices is plotted in Fig. 5.21. The device parameters are listed in Table 5.5, with box plots containing the full dataset found in Figs. 5.23 and 5.24. In the case of the unannealed N-I-P devices, the optimal performance occurs with 15 mM of PEA passivation, whilst for P-I-N architectures the optimum occurs at 4 mM, reflecting the literature trends listed in Table. 5.1. In all cases, the deposition of increasing concentrations of PEAI solution leads to an increase in V_{OC}, rising from 1.09 ± 0.01 V to 1.12 ± 0.01 V with 15 mM of passivation. This indicates the deposition of PEA is successfully reducing interfacial recombination.[28] Crucially, in P-I-N devices, the rise in V_{OC} occurs alongside a sharp reduction in J_{SC} once the solution concentration is above 4 mM. This is clear evidence of a barrier to charge extraction present within the device, which correlates with an increased quantity of LPK within the film. The annealed set of N-I-P devices, shown in Figs. 5.22, 5.25 and Table 5.6 also shows a drop off in J_{SC} at PEA concentrations above 5 mM, with the optimal performance occurring at 2.5 mM. Here, the increased quantity of crystalline LPK formed by annealing leads to a more uniform passivation layer which is disrupted to a lesser degree after CTM deposition. In the case of P-I-N cells, the effect is compounded by the lower ability of the ETM solution to dissolve the surface material. These trends in device performance suggest, somewhat counter-intuitively, that moderately-thick LPK layers formed from solutions with concentrations above 10 mM actually act to hinder device performance.

The data collected for both of the P-I-N and N-I-P devices clearly recreate the divergence observed in the literature in optimal LPK recipes. In the collection of LPK deposition protocols listed in Table 5.1, the highest performance for N-I-P devices across a range of publications is found at A' cation solution concentrations of 15 mM - 20 mM, reflecting the observed behaviour for unannealed devices extremely closely. In the case of P-I-N devices, where the maximum PCE value occurs at 4 mM,

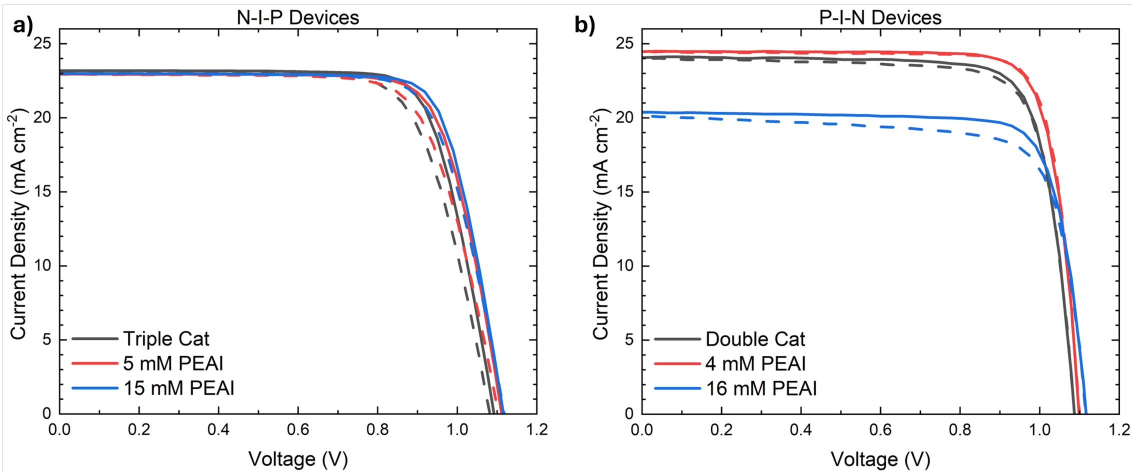

Figure 5.21: Solar cell data for a) N-I-P and b) P-I-N architecture cells, fabricated with increasing concentration of PEAI solution. Inset tables show reverse-scan parameters for each curve. *P-I-N Devices were fabricated and measured by Wai Kin Yiu. Figure modified with permission from Ref. [217] under the terms of the CC BY 4.0 license.*

Table 5.5: Champion solar cell reverse scan parameters for N-I-P and P-I-N devices.

Device	Composition	V_{OC} (V)	J_{SC} (mA cm^{-2})	PCE (%)	FF
N-I-P	Triple Cat	1.09 ± 0.01	23.2 ± 0.08	19.44 ± 0.01	0.77 ± 0.01
	5 mM	1.11 ± 0.01	22.9 ± 0.08	19.54 ± 0.01	0.77 ± 0.01
	15 mM	1.12 ± 0.01	23.0 ± 0.08	19.98 ± 0.01	0.78 ± 0.01
P-I-N	Double Cat	1.09 ± 0.01	24.1 ± 0.03	20.85 ± 0.01	0.80 ± 0.01
	4 mM	1.10 ± 0.01	24.5 ± 0.03	21.98 ± 0.01	0.82 ± 0.01
	16 mM	1.12 ± 0.01	20.4 ± 0.03	18.22 ± 0.01	0.80 ± 0.01

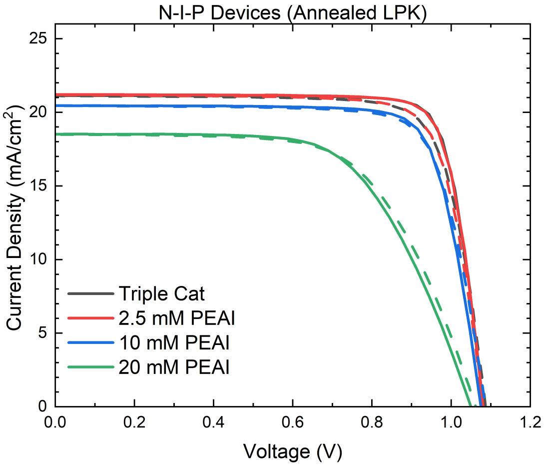

Figure 5.22: Champion N-I-P devices fabricated with increasing concentration of PEAI solution, with an annealing step after LPK formation. *Figure reproduced with permission from Ref. [217] under the terms of the CC BY 4.0 license.*

Table 5.6: Champion solar cell reverse scan parameters for annealed N-I-P devices.

Device	Composition	V_{OC} (V)	J_{SC} (mA cm^{-2})	PCE (%)	FF
N-I-P	Triple Cat	1.08 ± 0.01	21.1 ± 0.02	18.75 ± 0.01	0.82 ± 0.01
	2.5 mM	1.08 ± 0.01	21.2 ± 0.02	18.73 ± 0.01	0.82 ± 0.01
	10 mM	1.07 ± 0.01	20.5 ± 0.02	17.26 ± 0.01	0.79 ± 0.01
	20 mM	1.05 ± 0.01	18.5 ± 0.02	12.14 ± 0.01	0.63 ± 0.01

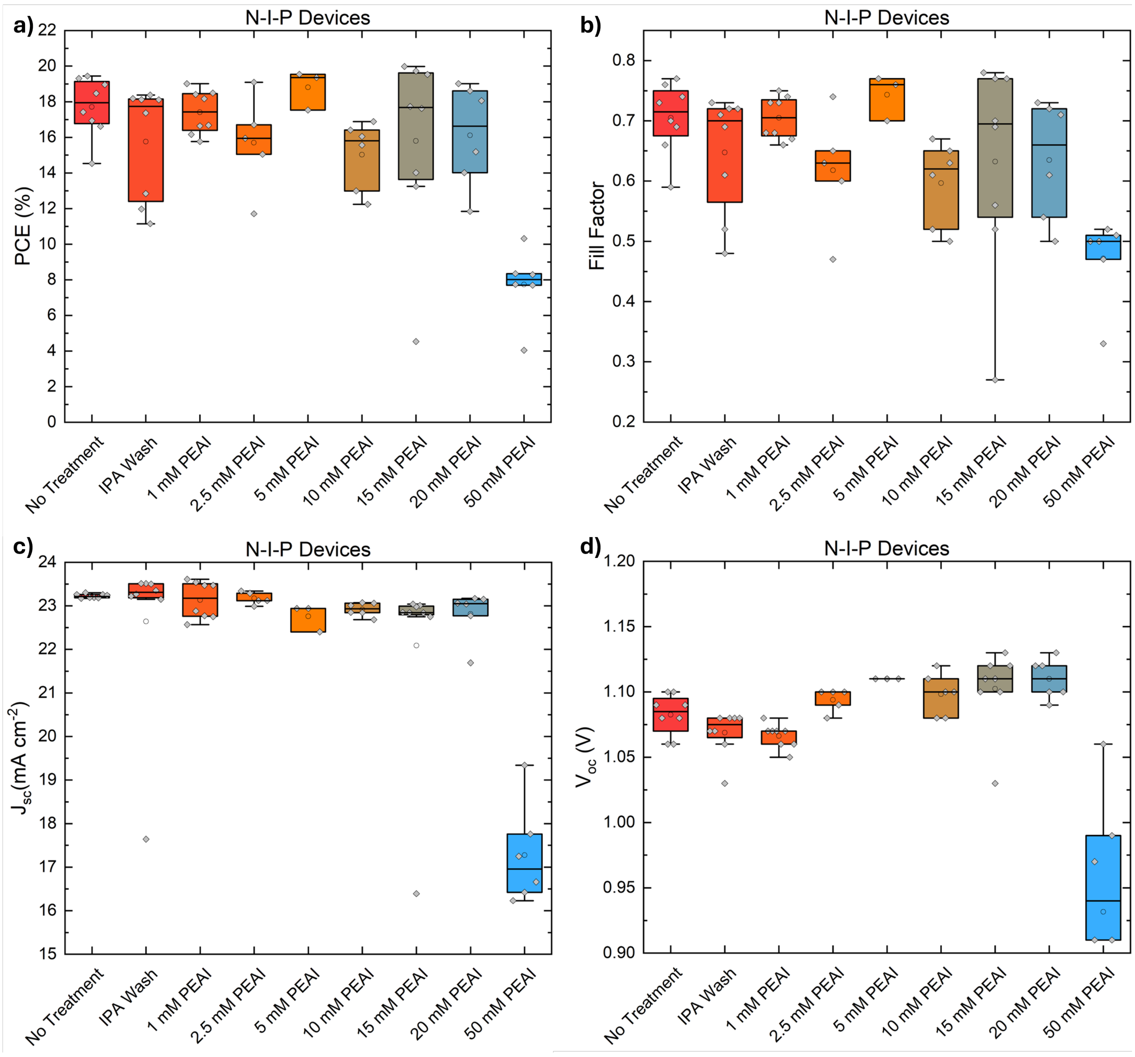

Figure 5.23: N-I-P device parameter statistical breakdowns. Each grey diamond represents a single solar cell. a) power conversion efficiency, b) fill factor, c) short-circuit current, d) open-circuit voltage. *Figure modified with permission from Ref. [217] under the terms of the CC BY 4.0 license.*

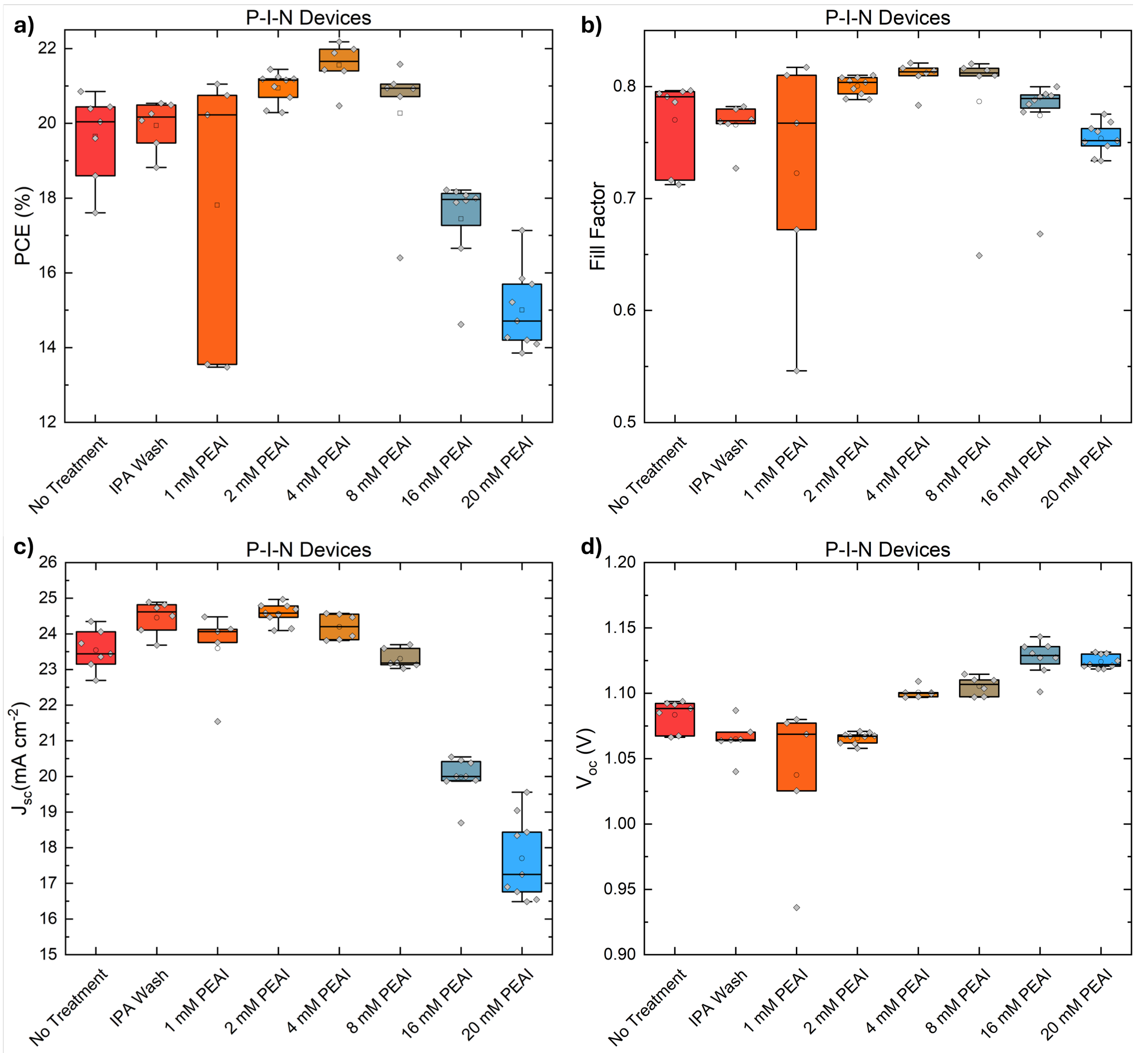

Figure 5.24: P-I-N device parameter statistical breakdowns. Each grey diamond represents a single solar cell. a) power conversion efficiency, b) fill factor, c) short-circuit current, d) open-circuit voltage. *P-I-N Device measurements were carried out by Wai Kin Yiu. Figure modified with permission from Ref. [217] under the terms of the CC BY 4.0 license.*

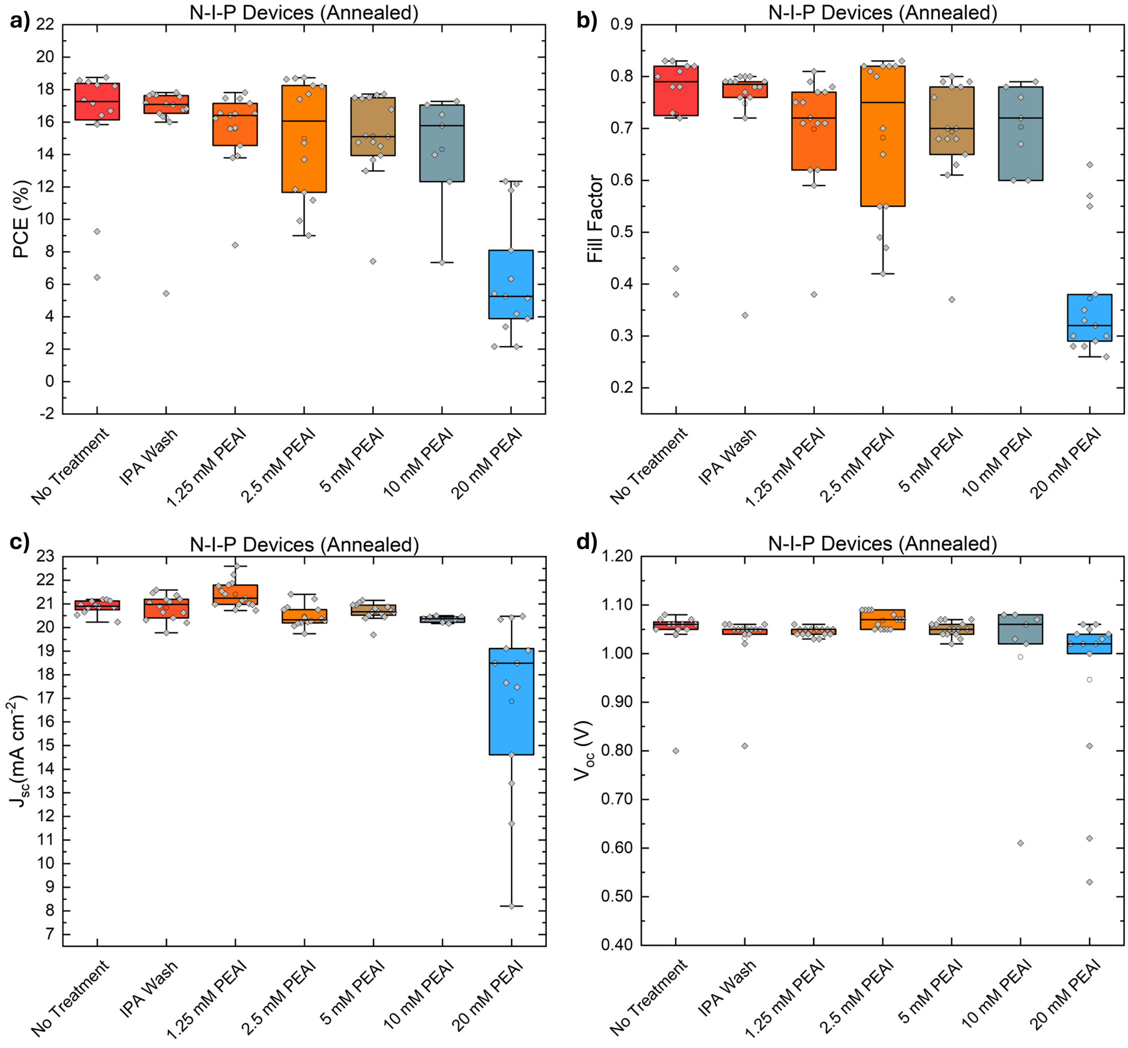

Figure 5.25: N-I-P devices parameter statistical breakdowns, with an annealing step after LPK deposition. Each grey diamond represents a single solar cell. a) power conversion efficiency, b) fill factor, c) short-circuit current, d) open-circuit voltage. *Figure modified with permission from Ref. [217] under the terms of the CC BY 4.0 license.*

the same matching trend is found, with low solution concentrations of 1.25 mM - 4 mM used in the literature. This occurs despite variations in A' cations, perovskite absorber compositions, CTM precursor solution recipes and deposition approaches between the literature dataset and the measurements employed here. To rationalise this trend, it is important to highlight that in both the N-I-P and P-I-N device sets studied, optimal performance occurs at a point where there is no crystalline LPK visible in diffractograms taken after CTM deposition. This is shown in Fig. 5.26, where samples representative of all three of the device fabrication approaches have no peaks in the low-angle regions which would indicate the presence of an LPK layer.

It is thus proposed that the order-of-magnitude variation in LPK recipes between the two device architectures is a direct consequence of the fabrication techniques and chemical compositions used for the CTM layers. Both approaches have settled on a final device with extremely small quantities of LPK on the sample surface, via a process of 'convergent optimisation'. N-I-P architectures find optimal performance with an initially higher concentration of LPK solution as they commonly avoid driving the crystallisation of the layer by not annealing after deposition. Additionally, they most commonly utilise HTM solutions with numerous polar additives which dissolve the excess A' cation and any LPK that does form.[192,222] Conversely, P-I-N cells anneal the deposited layer, and use small-molecule ETMs which do not require any polar additives and which can be deposited via evaporation processes.[51,219] This means the ETM deposition step disrupts the LPK far less, and thus the recipes find optimal performance with much lower LPK solution concentrations. Work by Chen *et al.* illustrates this point well, where both N-I-P and P-I-N cells were fabricated with a PEA LPK passivation layer.[194] The optimal performance for N-I-P cells occurs with 20 mM of PEA deposited, compared to the 4 mM for P-I-N cells. If both architectures use the same high concentration, the P-I-N cells see the same sharp loss of J_{SC} as observed here. The link between the capability of the CTM to chemically disrupt the LPK capping layer and the optimal deposition concentration is further corroborated by a report by Zhou et. al.[222] This is an outlier within the literature N-I-P dataset, where a 7.5 mM F-PEAI solution is used instead. This is in agreement with the observations that F-PEA is more resistant to disruption by HTM deposition. As it demonstrates greater stability, it follows that higher concentrations would lead to the efficiency losses observed for devices with 'excessive' concentrations of deposited LPK. Furthermore, work by Azmi et. al., which employs ETM layers deposited via evaporation, includes cross-sectional Scanning Transmission Electron Microscopy (STEM) images of clearly-distinguishable LPK layers.[112] This suggests that it is the spincoating step itself that is damaging to the LPK layer, supporting the proposed mechanism where small-molecule ETM layers disrupt the surface via physical ablation, rather than a chemical interaction.

It is important to note that the observation of no crystalline LPK peaks for optimal devices as shown in Fig. 5.26 does not necessarily mean there is no crystalline LPK present at all. The measurements were collected on a bench-top XRD instrument employing a fast scan speed, and thus evidence of crystalline material may have been hidden in the baseline signal. A series of calculations were carried out to model how the reduction of signal intensity and peak broadening for very thin samples would affect the LPK peak in this experiment. The details of this process

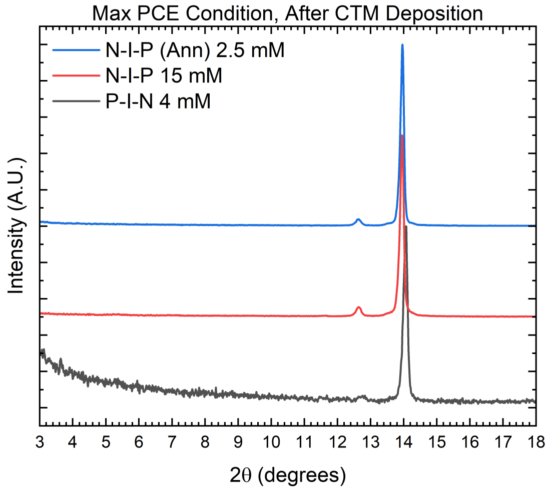

Figure 5.26: XRD diffractograms of A' cation concentrations giving maximum performance in P-I-N and N-I-P architectures. P-I-N data were taken during full device fabrication, as in Fig. 5.4. N-I-P data taken for bilayer samples treated with an 'HTM wash', as in Figs. 5.11 and 5.12. *Figure modified with permission from Ref. [217] under the terms of the CC BY 4.0 license.*

are discussed in the methods, section 2.8.7, which show that PEA LPK platelets past a lower bound of three layers of perovskite material would be undetectable by the measurements employed here.

Demonstrating that LPK passivation layers are highly unlikely to remain as an intact, continuous film within a completed device puts into question the mechanisms by which these materials improve stability and longevity of solar cells. These materials are often described as offering an improved barrier to moisture due to their increased hydrophobicity compared to a regular perovskite.[117] These effects are found to occur for an isolated perovskite-LPK bilayer, and thus are unlikely to play a part in the fully-assembled device. Nevertheless, many of the other processes by which LPKs have been reported to improve stability are not reliant on an intact layer of material. For example, even the largely disrupted residual LPK can act to passivate shallow trap states and surface defects.[229] It has been demonstrated that such defect states promote large scale degradation by reducing the energy barriers to ion migration and structural changes.[230] Furthermore, ionic vacancies have been identified as key sites in mediating light, oxygen and moisture induced degradation.[231] Thus, it follows that the presence of small quantities of residual LPK which can passivate grain boundaries and dangling bonds will increase the lifetime of a perovskite solar cell.[221,232] To gain a deeper understanding of the role of LPKs in devices, it is therefore crucial to measure *in-situ*, or with the use of systems which take the impact of post-processing into account. Alternatively, the use of more robust LPK passivation will help minimise the disconnect between devices and simple bilayer samples. The F-PEA cation was found to have far more resilience to dissolution by the HTM solvents. This highlights the potential of A' cations which will form stronger intermolecular interactions after deposition, such as hydrogen bonding or even photochemical cross-linking.[61,233] Another potential avenue for more robust surface passivation lies in A' cations which promote the form of quasi-LPK phases, such as 1D 'nanorods' or perovskitoids.[234,235]

5.4 Conclusions

The work presented in this chapter demonstrates the widespread and pronounced disruption of perovskite-LPK heterojunctions upon subsequent deposition of CTM layers. XRD and SEM studies show that the highly crystalline, conformally grown layers are thinned down, removed entirely or recrystallised into a residue of disconnected platelets. Investigations into the impact of the individual CTM components identified that the mechanism behind this process depends on the nature of the CTM utilised. Small-molecule ETMs most commonly used in P-I-N configurations directly damage the surface by a mechanical ablation process. In N-I-P cells, the LPK is also dissolved due to the addition of polar solvents and dopant salts in the HTM solution, leading to a far more pronounced loss of material. In both cases, the quantity, integrity and coverage of the LPK is significantly poorer than what was initially deposited.

Despite this disruption, the inclusion of LPK passivation still leads to improved device performance. Although it leads to relatively small improvements in V_{OC} and J_{SC} and FF, which in some cases differ by only the measurement error, the overall PCE for LPK-containing devices is 0.5 - 1% higher than in devices without an LPK layer. This is a significant increase for devices where the maximum efficiency was measured to be 22%. The residual LPK is found to be extremely thin in devices which have the highest efficiency, below a limit of around 5 nm for both P-I-N and N-I-P architectures. At this condition, it is uncertain whether the LPK is still located on the sample surface as a distinct layer, or is located largely at grain boundaries or defect sites. It is proposed that the variation in LPK deposition approaches in P-I-N and N-I-P devices stems from a ‘convergent optimisation’, where N-I-P cells compensate for the more significant disruption of the HTM deposition with higher concentrations of LPK solution, and vice-versa.

The key finding of this chapter is that there is a disconnect between an isolated bilayer of LPK deposited on a perovskite, and the material that is present within a complete device. Studies on control samples, which do not account for the impact of subsequent processing steps, may lead to an incomplete understanding of the perovskite / LPK / CTM system as a whole. An awareness of the impact the full fabrication process may have and *in-situ* measurements are thus key for gaining accurate insights into the role of the LPK and the further development of perovskite solar cell systems.

Chapter 6

Conclusion

In conclusion, this thesis explores a range of LPK materials both as standalone thin films or crystals, and as a heterojunction capping layers to tackle some of the fundamental questions underpinning their properties. By and large, these display a remarkable complexity, and it is found that many of the commonly-held assumptions about the properties of LPKs as a class of materials are only applicable to limited subsets of closely-related structures, or when they are present in high quantities as bulk layered materials such as single crystals.

Chapter 3 focuses on identifying how the A' cation selection impacts the structure and optoelectronic properties of the material as a whole. Here, very small changes to the A' cation size and chemistry can lead to significant variations in the optimal A' cation arrangements and the distortions of the perovskite sheets. Furthermore, it is difficult to draw clear links between the details of the layered structure and the bandgap energy or charge transport. This finding highlights that commonly-referenced links between parameters such as the perovskite bandgap and the Pb-I-Pb angle are not universally applicable within the subset of commonly utilised A' cations explored in this chapter.[168,182] This could indicate that the structural parameters which influence these properties have not been correctly identified, or that the values determined through single-crystal measurements do not reflect the 'real' structure of the perovskite with sufficient accuracy. Nonetheless, combining existing A' cations into mixed-cation structures is identified as a promising pathway for fine-tuning the properties of the LPK, as they allow the adjustment of PL energy or lattice spacing without the need for the synthesis of novel compounds.

Chapter 4 highlights how the impressive ambient stability of LPKs is largely due to a self-limiting degradation process, in which the top surface of the material is lost. The work builds on prior studies showing the degradation of LPK flakes under illumination.[203] Here, it is found that the build-up of degradation materials on the surface, largely consisting of PbI_2 species, acts to ultimately passivate the remaining perovskite below. Translating these findings to the more typical perovskite-LPK structures found in cutting-edge solar cells shows that the very thin layers of material used are, in fact, highly susceptible to degradation. Exposure to intense light, humidity, or solvents can all lead to the loss or recrystallisation of the LPK layer, highlighting the care that needs to be taken when discussing their role as an 'environmental passivation layer'. The change in observed behaviour is largely due to the much lower quantities of LPK present in a capping layer when compared to a bulk film, which means the buildup of degradation material which can then limit the process dues not occur.

Finally, Chapter 5 shows how this poor stability of thin layers of LPK means they are significantly disrupted during the solar cell fabrication process. Here, the deposition of small-molecule charge transport layers is sufficient to significantly reduce the integrity and crystallinity of the LPK layer, in some cases causing it to be effectively stripped off the top surface of the solar cell. Indeed, the best-performing solar cells across a range of architectures contain essentially no LPK interlayer after fabrication. This observation is at odds with literature reports which link improvements in stability, charge carrier extraction or improved band alignment to the presence of intact LPK interlayers.[148,219,220] Whilst it is clear that the inclusion of an LPK layer has a beneficial impact on a solar cell, this difference raises questions about the mechanism by which LPK layers improve performance and stability. As such, further studies are needed into the impact an LPK has on the properties of a perovskite solar cell which account for the effects of any subsequent fabrication steps, and accurately represent the state of the material as it appears in a completed device.

Overall, LPKs are a highly versatile class of materials, which have an important role to play in the future of perovskite solar cells. Further research will likely continue to improve their potential benefits with the development of novel A' cations and new approaches for their implementation. However, this thesis highlights that care should be taken when studying the properties of LPK materials. Essentially any aspect, from the distortions of the crystal lattice, bandgap position to stability can be unexpectedly changed by varying their chemistry or formation method. For an accurate understanding, it is important to fully characterise the material, and account for any changes that may be caused by further processing.

6.1 Future Work

For each of the chapters presented in this thesis, the most straightforward opportunity for further research is expanding the scope of the studies to cover a wider range of A' cations, conditions or materials tested. This is particularly applicable for Chapter 3, where expanding the synthetic space covered with new related cation families would increase the robustness of the trends already identified, and help identify new structure-property relations. The candidate new A' cations include chlorinated, brominated or fluorinated equivalents of the studied aromatic and aliphatic molecules, or compounds with even longer straight chain linkers joining the cation body to the ammonium head. This approach, combined with studying alternative perovskite compositions such as compounds containing tin B cations or bromide X anions would increase both the structural and optoelectronic variation within the sample set. Computational modelling is a key complimentary pathway to help achieve this, as it would be able to offer insights into both the structure and the energy level alignments of the studied compounds and highlight the most interesting candidate materials for synthesis.[83,236] This widened scope would greatly increase the likelihood of finding the key links between the cation chemistry, perovskite structure, and the overall material properties.

For the degradation studies shown in Chapter 4, exfoliated single crystals of other LPK materials would help demonstrate the applicability of the pinhole-mediated degradation mechanism to compounds templated by a greater variety of A' cations. However, *in-situ* measurements would offer the greatest benefits in understanding the mechanism of perovskite degradation. Studying the evolution of the PL response of freshly-exfoliated flakes over time would help quantify both the speed of degradation and the nature of the degradation products.[203] The observed rearrangement, degradation and dissolution of LPK capping layers could be studied in real-time with the use of *in-situ* beamline measurements, which would also be more sensitive to the changes occurring at the material surface.[95] This would help identify the nature of any intermediate species, the competing mechanism of higher-n LPK rearrangement and degradation, and the role any given A' cation has in mitigating the degradation process.

The mechanism of LPK disruption identified in Chapter 5 would be strengthened by studies into the effect of changing both the LPK capping layer, and the CTM deposited on top. The chemistry of the A' cation was found to play a role in the stability of the layer, as shown by the reduced disruption of the more robust F-PEA cation. As the variety of LPKs in use in the literature is very broad, it is important to demonstrate this effect on linear aliphatic chains, and other aromatic A' cations. Equally, studying how varying the CTM composition impacts the disruption process is key to understanding and mitigating its effects. Here, studies of other molecules such as Poly[bis(4-phenyl)(2,4,6-trimethylphenyl)amine (PTAA), and variation of the antisolvent system and deposition techniques to include toluene, DE and other popular approaches are key. Deposition of C_{60} or BCP via chemical vapour deposition approaches offers an opportunity to conclusively demonstrate behaviour suggested by literature reports, which show it is spincoating process and not the chemistry of the CTM itself that is the key factor leading to LPK disruption.[112]

Again, the use of *in situ* measurements would be highly beneficial in understanding the precise mechanism behind this interaction.

The next key research direction is understanding how some of the challenges identified in this work could be solved. The synthesis and implementation of A' cations with cross-linking functionality offers a pathway towards the formation of much more robust LPK materials.[61,62] An understanding of the structure-property relations would help inform which compounds would offer the best combination of the stability offered by cross-linking, and desirable properties such as good band alignment and high conductivity. This could be exploited to form materials which have greatly increased stability against environmental degradation, and the disruption that occurs during typical solar cell processing, which have minimal detrimental impact on the performance of the device they are implemented in. Given that existing LPK layers have been widely demonstrated to provide benefits to solar cell longevity and performance despite their instability, using robust, cross-linked cations would help determine whether some degree of LPK loss is in fact desirable. Studies of these compounds compared to non-cross linked analogues, combined with computational modelling, would facilitate a deeper understanding of how intact or disrupted LPK layers impact the band alignment, trap density, and environmental degradation processes. In this way, the development of novel A' cations for LPK systems will be rationally directed towards maximising the benefits they can provide in solar cells and other devices.

The studies of LPK behaviour within this work have the ultimate aim of supporting the fabrication of highly efficient and stable solar cells for large-scale industrial adoption. As such, long-term future experiments must be focused on translating the findings presented in this thesis to be applicable for large-scale fabrication. This would involve studies of perovskites formed by processes which can make solar cells at scale, such as roll-to-roll printing. Here, an in-depth understanding of A' cation chemistry and behaviour would facilitate the selection of the optimal LPK interlayer material. A knowledge of how these perovskite layers degrade is crucial to ensure they do not undergo any changes during the fabrication process itself, where they are likely to be exposed to solvent vapours for prolonged periods of time. Finally, insights into how the performance and stability improvements provided by the LPK layer are influenced by CTM deposition will inform the choice of material and deposition technique required to create the high-efficiency solar cells of the future.

Bibliography

(1) *CMA. 5: Outcome of the first global stocktake*; United Nations Framework Convention on Climate Change, 2024.

(2) Shih, C. F.; Zhang, T.; Li, J.; Bai, C. *Joule* **2018**, *2*, 1925–1949.

(3) *Energy Trends Section 1 : UK total energy*; Department for Energy Security & Net Zero, 2025.

(4) Graetzel, M.; Janssen, R. A.; Mitzi, D. B.; Sargent, E. H. *Nature* **2012**, *488*, 304–312.

(5) Polman, A.; Knight, M.; Garnett, E. C.; Ehrler, B.; Sinke, W. C. *Science* **2016**, *352*, aad4424.

(6) Battaglia, C.; Cuevas, A.; De Wolf, S. *Energy and Environmental Science* **2016**, *9*, 1552–1576.

(7) Chapin, D. M.; Fuller, C. S.; Pearson, G. L. *Journal of Applied Physics* **1954**, *25*, 676–677.

(8) Ranjan, S.; Balaji, S.; Panella, R. A.; Ydstie, B. E. *Computers and Chemical Engineering* **2011**, *35*, 1439–1453.

(9) Nikolaidou, K.; Sarang, S.; Ghosh, S. *Nano Futures* **2019**, *3*, 012002.

(10) Vigil-Galán, O.; Courel, M.; Andrade-Arvizu, J. A.; Sánchez, Y.; Espíndola-Rodríguez, M.; Saucedo, E.; Seuret-Jiménez, D.; Titsworth, M. *Journal of Materials Science: Materials in Electronics* **2015**, *26*, 5562–5573.

(11) O'Regan, B.; Gratzel, M. *Nature* **1991**, *353*, 737–740.

(12) Kahn, A. *Materials Horizons* **2016**, *3*, 7–10.

(13) Rühle, S. *Solar Energy* **2016**, *130*, 139–147.

(14) Warby, J.; Shah, S.; Thiesbrummel, J.; Gutierrez-Partida, E.; Lai, H.; Alebachew, B.; Grischek, M.; Yang, F.; Lang, F.; Albrecht, S.; Fu, F.; Neher, D.; Stolterfoht, M. *Advanced Energy Materials* **2023**, *13*, 2303135.

(15) Wang, D. et al. *Joule* **2025**, *9*, 101815.

(16) Hutter, E. M.; Gélvez-Rueda, M. C.; Osherov, A.; Bulović, V.; Grozema, F. C.; Stranks, S. D.; Savenije, T. J. *Nature Materials* **2017**, *16*, 115–120.

(17) Wang, T.; Daiber, B.; Frost, J. M.; Mann, S. A.; Garnett, E. C.; Walsh, A.; Ehrler, B. *Energy and Environmental Science* **2017**, *10*, 509–515.

(18) Wolff, C. M.; Caprioglio, P.; Stolterfoht, M.; Neher, D. *Advanced Materials* **2019**, *31*, 1902762.

(19) Manser, J. S.; Kamat, P. V. *Nature Photonics* **2014**, *8*, 737–743.

(20) Wehrenfennig, C.; Eperon, G. E.; Johnston, M. B.; Snaith, H. J.; Herz, L. M. *Advanced Materials* **2014**, *26*, 1584–1589.

(21) Milot, R. L.; Sutton, R. J.; Eperon, G. E.; Haghighirad, A. A.; Martinez Hardigree, J.; Miranda, L.; Snaith, H. J.; Johnston, M. B.; Herz, L. M. *Nano Letters* **2016**, *16*, 7001–7007.

(22) Shockley, W.; Queisser, H. *Journal of Applied Physics* **1961**, *32*, 510–519.

(23) De Vos, A. *Journal of Physics D: Applied Physics* **1980**, *13*, 839–846.

(24) Shockley, W.; Read, W. T. *Physical Review* **1952**, *87*, 835–842.

(25) Chen, J.; Park, N. G. *Advanced Materials* **2019**, *31*, 1803019.

(26) Choi, H.; Ke, J. C. R.; Skalsky, S.; Castle, C. A.; Li, K.; Moore, K. L.; Flavell, W. R.; Parkinson, P. *Journal of Materials Chemistry C* **2020**, *8*, 7509–7518.

(27) Richheimer, F.; Toth, D.; Hailegnaw, B.; Baker, M. A.; Dorey, R. A.; Kienberger, F.; Castro, F. A.; Kaltenbrunner, M.; Scharber, M. C.; Gramse, G.; Wood, S. *Nanoscale* **2022**, *14*, 2605–2616.

(28) Hart, L. J.; Angus, F. J.; Li, Y.; Khaleed, A.; Calado, P.; Durrant, J. R.; Djurišić, A. B.; Docampo, P.; Barnes, P. R. *Energy and Environmental Science* **2024**, *17*, 7107–7118.

(29) McAllister, A.; Bayerl, D.; Kioupakis, E. *Applied Physics Letters* **2018**, *112*, 251108.

(30) Qi, B.; Wang, J. *Physical Chemistry Chemical Physics* **2013**, *15*, 8972–8982.

(31) Green, M. A.; Dunlop, E. D.; Yoshita, M.; Kopidakis, N.; Bothe, K.; Siefer, G.; Hao, X.; Jiang, J. Y. *Progress in Photovoltaics: Research and Applications* **2025**, *33*, 795–810.

(32) Goldschmidt, V. M. *Naturwissenschaften* **1926**, *14*, 477–485.

(33) Bartel, C. J.; Sutton, C.; Goldsmith, B. R.; Ouyang, R.; Musgrave, C. B.; Ghiringhelli, L. M.; Scheffler, M. *Science Advances* **2019**, *5*, eaav0693.

(34) Krishnamoorthy, T.; Ding, H.; Yan, C.; Leong, W. L.; Baikie, T.; Zhang, Z.; Sherburne, M.; Li, S.; Asta, M.; Mathews, N.; Mhaisalkar, S. G. *Journal of Materials Chemistry A* **2015**, *3*, 23829–23832.

(35) Noel, N. K.; Stranks, S. D.; Abate, A.; Wehrenfennig, C.; Guarnera, S.; Haghighirad, A. A.; Sadhanala, A.; Eperon, G. E.; Pathak, S. K.; Johnston, M. B.; Petrozza, A.; Herz, L. M.; Snaith, H. J. *Energy and Environmental Science* **2014**, *7*, 3061–3068.

(36) Saparov, B.; Hong, F.; Sun, J. P.; Duan, H. S.; Meng, W.; Cameron, S.; Hill, I. G.; Yan, Y.; Mitzi, D. B. *Chemistry of Materials* **2015**, *27*, 5622–5632.

(37) Park, B. W.; Philippe, B.; Zhang, X.; Rensmo, H.; Boschloo, G.; Johansson, E. M. *Advanced Materials* **2015**, *27*, 6806–6813.

(38) Jeon, N. J.; Noh, J. H.; Kim, Y. C.; Yang, W. S.; Ryu, S.; Seok, S. I. *Nature Materials* **2014**, *13*, 897–903.

(39) Fakharuddin, A.; Gangishetty, M. K.; Abdi-Jalebi, M.; Chin, S. H.; bin Mohd Yusoff, A. R.; Congreve, D. N.; Tress, W.; Deschler, F.; Vasilopoulou, M.; Bolink, H. J. *Nature Electronics* **2022**, *5*, 203–216.

(40) Kim, J. Y.; Lee, J. W.; Jung, H. S.; Shin, H.; Park, N. G. *Chemical Reviews* **2020**, *120*, 7867–7918.

(41) Knutson, J. L.; Martin, J. D.; Mitzi, D. B. *Inorganic Chemistry* **2005**, *44*, 4699–4705.

(42) Caputo, M. et al. *Scientific Reports* **2019**, *9*, 15159.

(43) Stoumpos, C. C.; Malliakas, C. D.; Kanatzidis, M. G. *Inorganic Chemistry* **2013**, *52*, 9019–9038.

(44) Hautzinger, M. P.; Mihalyi-Koch, W.; Jin, S. *Chemistry of Materials* **2024**, *36*, 10408–10420.

(45) Amat, A.; Mosconi, E.; Ronca, E.; Quarti, C.; Umari, P.; Nazeeruddin, M. K.; Grätzel, M.; De Angelis, F. *Nano Letters* **2014**, *14*, 3608–3616.

(46) Lee, J.-H.; Bristowe, N. C.; Lee, J. H.; Lee, S.-H.; Bristowe, P. D.; Cheetham, A. K.; Jang, H. M. *Chemistry of Materials* **2016**, *28*, 4259–4266.

(47) Meier, F.; Schumann, S. N.; Streiter, M.; Deibel, C. *The Journal of Physical Chemistry C* **2021**, *125*, 17411–17417.

(48) Nedelcu, G.; Protesescu, L.; Yakunin, S.; Bodnarchuk, M. I.; Grotevent, M. J.; Kovalenko, M. V. *Nano Letters* **2015**, *15*, 5635–5640.

(49) Lee, M. M.; Teuscher, J.; Miyasaka, T.; Murakami, T. N.; Snaith, H. J. *Science* **2012**, *338*, 643–647.

(50) Kim, H. S.; Lee, C. R.; Im, J. H.; Lee, K. B.; Moehl, T.; Marchioro, A.; Moon, S. J.; Humphry-Baker, R.; Yum, J. H.; Moser, J. E.; Grätzel, M.; Park, N. G. *Scientific Reports* **2012**, *2*, 591.

(51) Zhao, K. et al. *Nature* **2024**, *632*, 301–306.

(52) Shen, L.; Song, P.; Jiang, K.; Zheng, L.; Qiu, J.; Li, F.; Huang, Y.; Yang, J.; Tian, C.; Jen, A. K.; Xie, L.; Wei, Z. *Nature Communications* **2024**, *15*, 10908.

(53) Liu, J. et al. *Nature* **2024**, *635*, 596–603.

(54) Azarhoosh, P.; McKechnie, S.; Frost, J. M.; Walsh, A.; Van Schilfgaarde, M. *APL Materials* **2016**, *4*, 091501.

(55) Li, X.; Hoffman, J. M.; Kanatzidis, M. G. *Chemical Reviews* **2021**, *121*, 2230–2291.

(56) Kagan, C. R.; Mitzi, D. B.; Dimitrakopoulos, C. D. *Science* **1999**, *286*, 945–947.

(57) Ruddlesden, S. N.; Popper, P. *Acta Crystallographica* **1958**, *11*, 54–55.

(58) Lemmerer, A.; Billing, D. G. *CrystEngComm* **2010**, *12*, 1290–1301.

(59) Kikuchi, K.; Takeoka, Y.; Rikukawa, M.; Sanui, K. *Current Applied Physics* **2004**, *4*, 599–602.

(60) Luo, B.; Guo, Y.; Xiao, Y.; Lian, X.; Tan, T.; Liang, D.; Li, X.; Huang, X. *Journal of Physical Chemistry Letters* **2019**, *10*, 5271–5276.

(61) Proppe, A. H.; Wei, M.; Chen, B.; Quintero-Bermudez, R.; Kelley, S. O.; Sargent, E. H. *Journal of the American Chemical Society* **2019**, *141*, 14180–14189.

(62) Ortiz-Cervantes, C.; Román-Román, P. I.; Vazquez-Chavez, J.; Hernández-Rodríguez, M.; Solis-Ibarra, D. *Angewandte Chemie - International Edition* **2018**, *57*, 13882–13886.

(63) Dion, M.; Ganne, M.; Tournoux, M. *Materials Research Bulletin* **1981**, *16*, 1429–1435.

(64) Mao, L.; Ke, W.; Pedesseau, L.; Wu, Y.; Katan, C.; Even, J.; Wasielewski, M. R.; Stoumpos, C. C.; Kanatzidis, M. G. *Journal of the American Chemical Society* **2018**, *140*, 3775–3783.

(65) Ortiz-Cervantes, C.; Carmona-Monroy, P.; Solis-Ibarra, D. *ChemSusChem* **2019**, *12*, 1560–1575.

(66) Billing, D. G.; Lemmerer, A. *New Journal of Chemistry* **2008**, *32*, 1736–1746.

(67) Passarelli, J. V.; Fairfield, D. J.; Sather, N. A.; Hendricks, M. P.; Sai, H.; Stern, C. L.; Stupp, S. I. *Journal of the American Chemical Society* **2018**, *140*, 7313–7323.

(68) Gao, Y. et al. *Nature Chemistry* **2019**, *11*, 1151–1157.

(69) Dunlap-Shohl, W. A.; Barraza, E. T.; Barrette, A.; Dovletgeldi, S.; Findik, G.; Dirkes, D. J.; Liu, C.; Jana, M. K.; Blum, V.; You, W.; Gundogdu, K.; Stiff-Roberts, A. D.; Mitzi, D. B. *Materials Horizons* **2019**, *6*, 1707–1716.

(70) Billing, D. G.; Lemmerer, A. *CrystEngComm* **2007**, *9*, 236–244.

(71) Gilley, I. W.; Wiggins, T. E.; Sargent, E. H.; Kanatzidis, M. G. *Accounts of Chemical Research* **2025**, *58*, 2243–2254.

(72) Cao, D. H.; Stoumpos, C. C.; Farha, O. K.; Hupp, J. T.; Kanatzidis, M. G. *Journal of the American Chemical Society* **2015**, *137*, 7843–7850.

(73) Mitzi, D. B. *Journal of Materials Chemistry* **2004**, *14*, 2355–2365.

(74) Dahlman, C. J.; Decrescent, R. A.; Venkatesan, N. R.; Kennard, R. M.; Wu, G.; Everest, M. A.; Schuller, J. A.; Chabinyc, M. L. *Chemistry of Materials* **2019**, *31*, 5832–5844.

(75) Dong, J.; Shao, S.; Kahmann, S.; Rommens, A. J.; Hermida-Merino, D.; ten Brink, G. H.; Loi, M. A.; Portale, G. *Advanced Functional Materials* **2020**, *30*, 2001294.

(76) Li, Y.; Milić, J. V.; Ummadisingu, A.; Seo, J. Y.; Im, J. H.; Kim, H. S.; Liu, Y.; Dar, M. I.; Zakeeruddin, S. M.; Wang, P.; Hagfeldt, A.; Grätzel, M. *Nano Letters* **2019**, *19*, 150–157.

(77) Zhao, W.; Dong, Q.; Zhang, J.; Wang, S.; Chen, M.; Zhao, C.; Hu, M.; Jin, S.; Padture, N. P.; Shi, Y. *Journal of Materials Chemistry A* **2020**, *8*, 9919–9926.

(78) Sheikh, M. A. K.; Kowal, D.; Mahyuddin, M. H.; Cala', R.; Auffray, E.; Witkowski, M. E.; Makowski, M.; Drozdowski, W.; Wang, H.; Dujardin, C.; Cortecchia, D.; Birowosuto, M. D. *Journal of Physical Chemistry C* **2023**, *127*, 10737–10747.

(79) Straus, D. B.; Kagan, C. R. *Journal of Physical Chemistry Letters* **2018**, *9*, 1434–1447.

(80) Sirbu, D.; Balogun, F. H.; Milot, R. L.; Docampo, P. *Advanced Energy Materials* **2021**, *11*, 2003877.

(81) Hong, X.; Ishihara, T.; Nurmikko, A. V. *Physical Review B* **1992**, *45*, 6961–6964.

(82) Miyata, A.; Mitioglu, A.; Plochocka, P.; Portugall, O.; Wang, J. T. W.; Stranks, S. D.; Snaith, H. J.; Nicholas, R. J. *Nature Physics* **2015**, *11*, 582–587.

(83) Traore, B.; Pedesseau, L.; Assam, L.; Che, X.; Blancon, J. C.; Tsai, H.; Nie, W.; Stoumpos, C. C.; Kanatzidis, M. G.; Tretiak, S.; Mohite, A. D.; Even, J.; Kepenekian, M.; Katan, C. *ACS Nano* **2018**, *12*, 3321–3332.

(84) Cheng, L.; Jiang, T.; Cao, Y.; Yi, C.; Wang, N.; Huang, W.; Wang, J. *Advanced Materials* **2020**, *32*, 1904163.

(85) Li, W.; Feng, X.; Guo, K.; Pan, W.; Li, M.; Liu, L.; Song, J.; He, Y.; Wei, H. *Advanced Materials* **2023**, *35*, 2211808.

(86) Cheng, B.; Li, T. Y.; Wei, P. C.; Yin, J.; Ho, K. T.; Retamal, J. R. D.; Mohammed, O. F.; He, J. H. *Nature Communications* **2018**, *9*, 5196.

(87) Zhang, Y.; Sun, M.; Zhou, N.; Huang, B.; Zhou, H. *Journal of Physical Chemistry Letters* **2020**, *11*, 7610–7616.

(88) Liu, Y.; Ye, H.; Zhang, Y.; Zhao, K.; Yang, Z.; Yuan, Y.; Wu, H.; Zhao, G.; Yang, Z.; Tang, J.; Xu, Z.; Liu, S. *Matter* **2019**, *1*, 465–480.

(89) Gélvez-Rueda, M. C.; Hutter, E. M.; Cao, D. H.; Renaud, N.; Stoumpos, C. C.; Hupp, J. T.; Savenije, T. J.; Kanatzidis, M. G.; Grozema, F. C. *Journal of Physical Chemistry C* **2017**, *121*, 26566–26574.

(90) Zhang, Y.; Liu, Y.; Xu, Z.; Yang, Z.; Liu, S. *Small* **2020**, *16*, 2003145.

(91) Blancon, J. C. et al. *Science* **2017**, *355*, 1288–1292.

(92) Chen, A. Z.; Shiu, M.; Ma, J. H.; Alpert, M. R.; Zhang, D.; Foley, B. J.; Smilgies, D. M.; Lee, S. H.; Choi, J. J. *Nature Communications* **2018**, *9*, 1336.

(93) Proppe, A. H.; Quintero-Bermudez, R.; Tan, H.; Voznyy, O.; Kelley, S. O.; Sargent, E. H. *Journal of the American Chemical Society* **2018**, *140*, 2890–2896.

(94) Hu, Y.; Spies, L. M.; Alonso-Álvarez, D.; Mocherla, P.; Jones, H.; Hanisch, J.; Bein, T.; Barnes, P. R.; Docampo, P. *Journal of Materials Chemistry A* **2018**, *6*, 22215–22225.

(95) Proppe, A. H.; Johnston, A.; Teale, S.; Mahata, A.; Quintero-Bermudez, R.; Jung, E. H.; Grater, L.; Cui, T.; Filleter, T.; Kim, C. Y.; Kelley, S. O.; De Angelis, F.; Sargent, E. H. *Nature Communications* **2021**, *12*, 3472.

(96) Hu, Y.; Schlipf, J.; Wussler, M.; Petrus, M. L.; Jaegermann, W.; Bein, T.; Müller-Buschbaum, P.; Docampo, P. *ACS Nano* **2016**, *10*, 5999–6007.

(97) Liu, Y.; Akin, S.; Pan, L.; Uchida, R.; Arora, N.; Milić, J. V.; Hinderhofer, A.; Schreiber, F.; Uhl, A. R.; Zakeeruddin, S. M.; Hagfeldt, A.; Dar, M. I.; Grätzel, M. *Science Advances* **2019**, *5*, eaaw2543.

(98) Chen, P.; Bai, Y.; Wang, S.; Lyu, M.; Yun, J. H.; Wang, L. *Advanced Functional Materials* **2018**, *28*, 1706923.

(99) Roose, B.; Dey, K.; Chiang, Y. H.; Friend, R. H.; Stranks, S. D. *Journal of Physical Chemistry Letters* **2020**, *11*, 6505–6512.

(100) Jiang, X.; Zhang, J.; Ahmad, S.; Tu, D.; Liu, X.; Jia, G.; Guo, X.; Li, C. *Nano Energy* **2020**, *75*, 104892.

(101) Jackson, P.; Hariskos, D.; Wuerz, R.; Kiowski, O.; Bauer, A.; Friedlmeier, T. M.; Powalla, M. *Physica Status Solidi - Rapid Research Letters* **2015**, *9*, 28–31.

(102) Weerasinghe, H. C. et al. *Nature Communications* **2024**, *15*, 1656.

(103) Blackburn, D. et al. *ACS Applied Energy Materials* **2025**, *8*, 2219–2228.

(104) Yang, W. S.; Noh, J. H.; Jeon, N. J.; Kim, Y. C.; Ryu, S.; Seo, J.; Seok, S. I. *Science* **2015**, *348*, 1234–1237.

(105) Pratap, S.; Babbe, F.; Barchi, N. S.; Yuan, Z.; Luong, T.; Haber, Z.; Song, T. B.; Slack, J. L.; Stan, C. V.; Tamura, N.; Sutter-Fella, C. M.; Müller-Buschbaum, P. *Nature Communications* **2021**, *12*, 5264–5273.

(106) Glück, N.; Hill, N. S.; Giza, M.; Hutter, E.; Grill, I.; Schlipf, J.; Bach, U.; Müller-Buschbaum, P.; Hartschuh, A.; Bein, T.; Savenije, T.; Docampo, P. *J. Mater. Chem. A* **2024**, *12*, 11635–11643.

(107) Giesbrecht, N.; Schlipf, J.; Grill, I.; Rieder, P.; Dyakonov, V.; Bein, T.; Hartschuh, A.; Müller-Buschbaum, P.; Docampo, P. *J. Mater. Chem. A* **2018**, *6*, 4822–4828.

(108) Liu, X.; Guo, Y.; Cheng, Y.; Lu, S.; Li, R.; Chen, J. *Chem. Commun.* **2023**, *59*, 13394–13405.

(109) Shen, X. et al. *Advanced Materials* **2023**, *35*, 2211742.

(110) Chen, P.; Xiao, Y.; Li, S.; Jia, X.; Luo, D.; Zhang, W.; Snaith, H. J.; Gong, Q.; Zhu, R. *Chemical Reviews* **2024**, *124*, 10623–10700.

(111) Cacovich, S.; Vidon, G.; Degani, M.; Legrand, M.; Gouda, L.; Puel, J. B.; Vaynzof, Y.; Guillemoles, J. F.; Ory, D.; Grancini, G. *Nature Communications* **2022**, *13*, 2868.

(112) Azmi, R. et al. *Science* **2022**, *376*, 73–77.

(113) Yoo, J. J.; Seo, G.; Chua, M. R.; Park, T. G.; Lu, Y.; Rotermund, F.; Kim, Y. K.; Moon, C. S.; Jeon, N. J.; Correa-Baena, J. P.; Bulović, V.; Shin, S. S.; Bawendi, M. G.; Seo, J. *Nature* **2021**, *590*, 587–593.

(114) Giordano, F.; Abate, A.; Correa Baena, J. P.; Saliba, M.; Matsui, T.; Im, S. H.; Zakeeruddin, S. M.; Nazeeruddin, M. K.; Hagfeldt, A.; Graetzel, M. *Nature Communications* **2016**, *7*, 10379.

(115) Salim, K. M. M.; Masi, S.; Gualdrón-Reyes, A. F.; Sánchez, R. S.; Barea, E. M.; Krecĉmarová, M.; Sánchez-Royo, J. F.; Mora-Seró, I. *ACS Energy Letters* **2021**, *6*, 3511–3521.

(116) Kim, G.; Min, H.; Lee, K. S.; Lee, D. Y.; Yoon, S. M.; Seok, S. I. *Science* **2020**, *370*, 108–112.

(117) Chen, R.; Wang, J.; Liu, Z.; Ren, F.; Liu, S.; Zhou, J.; Wang, H.; Meng, X.; Zhang, Z.; Guan, X.; Liang, W.; Troshin, P. A.; Qi, Y.; Han, L.; Chen, W. *Nature Energy* **2023**, *8*, 839–849.

(118) Hoke, E. T.; Slotcavage, D. J.; Dohner, E. R.; Bowring, A. R.; Karunadasa, H. I.; McGehee, M. D. *Chemical Science* **2015**, *6*, 613–617.

(119) Muscarella, L. A.; Ehrler, B. *Joule* **2022**, *6*, 2016–2031.

(120) Xue, D. J.; Hou, Y.; Liu, S. C.; Wei, M.; Chen, B.; Huang, Z.; Li, Z.; Sun, B.; Proppe, A. H.; Dong, Y.; Saidaminov, M. I.; Kelley, S. O.; Hu, J. S.; Sargent, E. H. *Nature Communications* **2020**, *11*, 1514.

(121) Zheng, X.; Wu, C.; Jha, S. K.; Li, Z.; Zhu, K.; Priya, S. *ACS Energy Letters* **2016**, *1*, 1014–1020.

(122) Tong, C. J.; Geng, W.; Tang, Z. K.; Yam, C. Y.; Fan, X. L.; Liu, J.; Lau, W. M.; Liu, L. M. *Journal of Physical Chemistry Letters* **2015**, *6*, 3289–3295.

(123) Yun, J. S.; Kim, J.; Young, T.; Patterson, R. J.; Kim, D.; Seidel, J.; Lim, S.; Green, M. A.; Huang, S.; Ho-Baillie, A. *Advanced Functional Materials* **2018**, *28*, 1705363.

(124) Müller, C.; Glaser, T.; Plogmeyer, M.; Sendner, M.; Döring, S.; Bakulin, A. A.; Brzuska, C.; Scheer, R.; Pshenichnikov, M. S.; Kowalsky, W.; Pucci, A.; Lovrinčić, R. *Chemistry of Materials* **2015**, *27*, 7835–7841.

(125) Schlipf, J.; Bießmann, L.; Oesinghaus, L.; Berger, E.; Metwalli, E.; Lercher, J. A.; Porcar, L.; Müller-Buschbaum, P. *Journal of Physical Chemistry Letters* **2018**, *9*, 2015–2021.

(126) Frost, J. M.; Butler, K. T.; Brivio, F.; Hendon, C. H.; Van Schilfgaarde, M.; Walsh, A. *Nano Letters* **2014**, *14*, 2584–2590.

(127) Schlipf, J.; Hu, Y.; Pratap, S.; Bießmann, L.; Hohn, N.; Porcar, L.; Bein, T.; Docampo, P.; Müller-Buschbaum, P. *ACS Applied Energy Materials* **2019**, *2*, 1011–1018.

(128) Aristidou, N.; Sanchez-Molina, I.; Chotchuangchutchaval, T.; Brown, M.; Martinez, L.; Rath, T.; Haque, S. A. *Angewandte Chemie - International Edition* **2015**, *54*, 8208–8212.

(129) Aristidou, N.; Eames, C.; Islam, M. S.; Haque, S. A. *Journal of Materials Chemistry A* **2017**, *5*, 25469–25475.

(130) Ma, S.; Yuan, G.; Zhang, Y.; Yang, N.; Li, Y.; Chen, Q. *Energy and Environmental Science* **2022**, *15*, 13–55.

(131) Aristidou, N.; Eames, C.; Sanchez-Molina, I.; Bu, X.; Kosco, J.; Saiful Islam, M.; Haque, S. A. *Nature Communications* **2017**, *8*, 15218.

(132) Li, Z.; Yang, M.; Park, J. S.; Wei, S. H.; Berry, J. J.; Zhu, K. *Chemistry of Materials* **2016**, *28*, 284–292.

(133) Smith, I. C.; Hoke, E. T.; Solis-Ibarra, D.; McGehee, M. D.; Karunadasa, H. I. *Angewandte Chemie - International Edition* **2014**, *53*, 11232–11235.

(134) Li, X.; Hoffman, J.; Ke, W.; Chen, M.; Tsai, H.; Nie, W.; Mohite, A. D.; Kepenekian, M.; Katan, C.; Even, J.; Wasielewski, M. R.; Stoumpos, C. C.; Kanatzidis, M. G. *Journal of the American Chemical Society* **2018**, *140*, 12226–12238.

(135) Eames, C.; Frost, J. M.; Barnes, P. R.; O'Regan, B. C.; Walsh, A.; Islam, M. S. *Nature Communications* **2015**, *6*, 7497.

(136) Lin, Y.; Bai, Y.; Fang, Y.; Wang, Q.; Deng, Y.; Huang, J. *ACS Energy Letters* **2017**, *2*, 1571–1572.

(137) Li, H.; Song, J.; Pan, W.; Xu, D.; Zhu, W.-a.; Wei, H.; Yang, B. *Advanced Materials* **2020**, *32*, 2003790.

(138) Tang, J.; Tian, W.; Zhao, C.; Sun, Q.; Zhang, C.; Cheng, H.; Shi, Y.; Jin, S. *ACS Omega* **2022**, *7*, 10365–10371.

(139) Safdari, M.; Svensson, P. H.; Hoang, M. T.; Oh, I.; Kloo, L.; Gardner, J. M. *Journal of Materials Chemistry A* **2016**, *4*, 15638–15646.

(140) Tsai, H. et al. *Nature* **2016**, *536*, 312–317.

(141) Lai, H.; Lu, D.; Xu, Z.; Zheng, N.; Xie, Z.; Liu, Y. *Advanced Materials* **2020**, *32*, 2001470.

(142) Wang, Z.; Lin, Q.; Chmiel, F. P.; Sakai, N.; Herz, L. M.; Snaith, H. J. *Nature Energy* **2017**, *2*, 17135.

(143) Quan, L. N.; Yuan, M.; Comin, R.; Voznyy, O.; Beauregard, E. M.; Hoogland, S.; Buin, A.; Kirmani, A. R.; Zhao, K.; Amassian, A.; Kim, D. H.; Sargent, E. H. *Journal of the American Chemical Society* **2016**, *138*, 2649–2655.

(144) Mahmud, M. A.; Duong, T.; Yin, Y.; Pham, H. T.; Walter, D.; Peng, J.; Wu, Y.; Li, L.; Shen, H.; Wu, N.; Mozaffari, N.; Andersson, G.; Catchpole, K. R.; Weber, K. J.; White, T. P. *Advanced Functional Materials* **2020**, *30*, 1907962.

(145) Lv, Y.; Song, X.; Yin, Y.; Feng, Y.; Ma, H.; Hao, C.; Jin, S.; Shi, Y. *ACS Applied Materials and Interfaces* **2020**, *12*, 698–705.

(146) Mozaffari, N. et al. *Solar RRL* **2022**, *6*, 2200355.

(147) Teale, S.; Degani, M.; Chen, B.; Sargent, E. H.; Grancini, G. *Nature Energy* **2024**, *9*, 779–792.

(148) Li, J.; Jin, C.; Jiang, R.; Su, J.; Tian, T.; Yin, C.; Meng, J.; Kou, Z.; Bai, S.; Müller-Buschbaum, P.; Huang, F.; Mai, L.; Cheng, Y. B.; Bu, T. *Nature Energy* **2024**, *9*, 1540–1550.

(149) Du, S.; Huang, H.; Lan, Z.; Cui, P.; Li, L.; Wang, M.; Qu, S.; Yan, L.; Sun, C.; Yang, Y.; Wang, X.; Li, M. *Nature Communications* **2024**, *15*, 5223.

(150) Vella, B.; Fsadni, M. H.; Pope, T.; Giza, M.; Angus, F. J.; Shmarov, I.; Lalaguna, P. L.; Cariello, M.; Wilson, C.; Kadodwala, M.; Penfold, T. J.; Docampo, P.; Cooke, G. *Journal of Materials Chemistry A* **2024**, *12*, 22844–22858.

(151) Mccusker, L. B.; Von Dreele, R. B.; Cox, D. E.; Louër, D.; Scardi, P. *Journal of Applied Crystallography* **1999**, *32*, 36–50.

(152) Koo, B. R.; Oh, D. H.; Riu, D. H.; Ahn, H. J. *ACS Applied Materials and Interfaces* **2017**, *9*, 44584–44592.

(153) Kulkarni, A. K.; Schulz, K. H.; Lim, T. S.; Khan, M. *Thin Solid Films* **1999**, *345*, 273–277.

(154) Giza, M.; Kozikov, A.; Lalaguna, P. L.; Hutchinson, J. D.; Verma, V.; Vella, B.; Kumar, R.; Hill, N.; Sirbu, D.; Arca, E.; Healy, N.; Milot, R. L.; Kadodwala, M.; Docampo, P. *Small Structures* **2024**, *5*, 2400234.

(155) Nečas, D.; Klapetek, P. *Central European Journal of Physics* **2012**, *10*, 181–188.

(156) Bragg, W. H.; Bragg, W. L. *Proceedings of the Royal Society of London. Series A, Containing Papers of a Mathematical and Physical Character* **1913**, *88*, 428–438.

(157) Kelly, A.; Knowles, K. M. In *Crystallography and Crystal Defects*; John Wiley & Sons, Ltd: 2012; Chapter Ap. 3, pp 469–472.

(158) Momma, K.; Izumi, F. *Journal of Applied Crystallography* **2011**, *44*, 1272–1276.

(159) Schmid, M.; Steinrück, H.-P.; Gottfried, J. M. *Surface and Interface Analysis* **2014**, *46*, 505–511.

(160) Major, G. H.; Fairley, N.; Sherwood, P. M. A.; Linford, M. R.; Terry, J.; Fernandez, V.; Artyushkova, K. *Journal of Vacuum Science & Technology A* **2020**, *38*, 061203.

(161) Moulder, J. F.; Stickle, W. F.; Sobol, P. E.; Bomben, K. D. In *Handbook of X-ray photoelectron spectroscopy*; Perkin-Elmer Corporation: 1992, p 189.

(162) Stokes, A. R.; Wilson, A. J. *Mathematical Proceedings of the Cambridge Philosophical Society* **1942**, *38*, 313–322.

(163) De Keijser, T. H.; Langford, J. I.; Mittemeijer, E. J.; Vogels, A. B. P. *Journal of Applied Crystallography* **1982**, *15*, 308–314.

(164) Balzar, D. *International Union of Crystallography Monographs on Crystallography* **1999**, *10*, 94–126.

(165) Halder, N. C.; Wagner, C. N. J. *Acta Crystallographica* **1966**, *20*, 312–313.

(166) Liu, C.; Fang, Z.; Sun, J.; Shang, M.; Zheng, K.; Yang, W.; Ge, Z. *Nano Energy* **2022**, *93*, 106800.

(167) Mosconi, E.; Alothman, A. A.; Long, R.; Kaiser, W.; De Angelis, F. *ACS Energy Letters* **2023**, *8*, 748–752.

(168) Wang, P. X.; Najarian, A. M.; Hao, Z.; Johnston, A.; Voznyy, O.; Hoogland, S.; Sargent, E. H. *Journal of Physical Chemistry Letters* **2020**, *11*, 10144–10149.

(169) Smith, M. D.; Connor, B. A.; Karunadasa, H. I. *Chemical Reviews* **2019**, *119*, 3104–3139.

(170) Du, K. Z.; Tu, Q.; Zhang, X.; Han, Q.; Liu, J.; Zauscher, S.; Mitzi, D. B. *Inorganic Chemistry* **2017**, *56*, 9291–9302.

(171) Dohner, E. R.; Jaffe, A.; Bradshaw, L. R.; Karunadasa, H. I. *Journal of the American Chemical Society* **2014**, *136*, 13154–13157.

(172) Liu, Z.; Meng, K.; Wang, X.; Qiao, Z.; Xu, Q.; Li, S.; Cheng, L.; Li, Z.; Chen, G. *Nano Letters* **2020**, *20*, 1296–1304.

(173) Billing, D. G.; Lemmerer, A. *Acta Crystallographica Section B: Structural Science* **2007**, *63*, 735–747.

(174) Lemmerer, A.; Billing, D. G. *Dalton Transactions* **2012**, *41*, 1146–1157.

(175) Zhao, R.; Sabatini, R. P.; Zhu, T.; Wang, S.; Morteza Najjarian, A.; Johnston, A.; Lough, A. J.; Hoogland, S.; Sargent, E. H.; Seferos, D. S. *Journal of the American Chemical Society* **2021**, *143*, 19901–19908.

(176) Ahmad, S.; Fu, P.; Yu, S.; Yang, Q.; Liu, X.; Wang, X.; Wang, X.; Guo, X.; Li, C. *Joule* **2019**, *3*, 794–806.

(177) Chen, Z.; Guo, Y.; Wertz, E.; Shi, J. *Advanced Materials* **2019**, *31*, 1803514.

(178) Passarelli, J. V.; Mauck, C. M.; Winslow, S. W.; Perkinson, C. F.; Bard, J. C.; Sai, H.; Williams, K. W.; Narayanan, A.; Fairfield, D. J.; Hendricks, M. P.; Tisdale, W. A.; Stupp, S. I. *Nature Chemistry* **2020**, *12*, 672–682.

(179) Choghaei, M.; Schiffer, M.; Tyagi, V.; Righetto, M.; Du, J.; Buchmüller, M.; Brinkmann, K. O.; Brocks, G.; Görrn, P.; Herz, L. M.; Tao, S.; Riedl, T.; Olthof, S. *Journal of Materials Chemistry A* **2025**, *13*, 18935–18947.

(180) Baur, W. H. *Acta Crystallographica Section B Structural Crystallography and Crystal Chemistry* **1974**, *30*, 1195–1215.

(181) Robinson, K.; Gibbs, G. V.; Ribbe, P. H. *Science* **1971**, *172*, 567–570.

(182) Sichert, J. A.; Hemmerling, A.; Cardenas-Daw, C.; Urban, A. S.; Feldmann, J. *APL Materials* **2019**, *7*, 041116.

(183) Prasanna, R.; Gold-Parker, A.; Leijtens, T.; Conings, B.; Babayigit, A.; Boyen, H. G.; Toney, M. F.; McGehee, M. D. *Journal of the American Chemical Society* **2017**, *139*, 11117–11124.

(184) Wiktor, J.; Fransson, E.; Kubicki, D.; Erhart, P. *Chemistry of Materials* **2023**, *35*, 6737–6744.

(185) Cannelli, O.; Wiktor, J.; Colonna, N.; Leroy, L.; Puppin, M.; Bacellar, C.; Sadykov, I.; Krieg, F.; Smolentsev, G.; Kovalenko, M. V.; Pasquarello, A.; Chergui, M.; Mancini, G. F. *The Journal of Physical Chemistry Letters* **2022**, *13*, 3382–3391.

(186) Yazdani, N. et al. *Nature Physics* **2024**, *20*, 47–53.

(187) Zhang, H. et al. *Nature Physics* **2023**, *19*, 545–550.

(188) Wu, X. et al. *Science Advances* **2017**, *3*, e1602388.

(189) Datta, K.; van Gorkom, B. T.; Chen, Z.; Dyson, M. J.; van der Pol, T. P.; Meskers, S. C.; Tao, S.; Bobbert, P. A.; Wienk, M. M.; Janssen, R. A. *ACS Applied Energy Materials* **2021**, *4*, 6650–6658.

(190) Bai, Y.; Xiao, S.; Hu, C.; Zhang, T.; Meng, X.; Lin, H.; Yang, Y.; Yang, S. *Advanced Energy Materials* **2017**, *7*, 1701038.

(191) DeQuilettes, D. W.; Zhang, W.; Burlakov, V. M.; Graham, D. J.; Leijtens, T.; Osherov, A.; Bulović, V.; Snaith, H. J.; Ginger, D. S.; Stranks, S. D. *Nature Communications* **2016**, *7*, 11683.

(192) Petrulevicius, J.; Yang, Y.; Liu, C.; Steponaitis, M.; Kamarauskas, E.; Daskeviciene, M.; Bati, A. S.; Malinauskas, T.; Jankauskas, V.; Rakstys, K.; Kanatzidis, M. G.; Sargent, E. H.; Getautis, V. *ACS Applied Materials and Interfaces* **2024**, *16*, 7310–7316.

(193) Wygant, B. R.; Ye, A. Z.; Dolocan, A.; Vu, Q.; Abbot, D. M.; Mullins, C. B. *Journal of the American Chemical Society* **2019**, *141*, 18170–18181.

(194) Chen, H. et al. *Nature Photonics* **2022**, *16*, 352–358.

(195) Zibouche, N.; Islam, M. S. *ACS Applied Materials and Interfaces* **2020**, *12*, 15328–15337.

(196) Liu, F. *Progress in Surface Science* **2021**, *96*, 100626.

(197) Puebla, S.; Li, H.; Zhang, H.; Castellanos-Gomez, A. *Advanced Photonics Research* **2022**, *3*, 2100221.

(198) Reese, M. O. et al. *Solar Energy Materials and Solar Cells* **2011**, *95*, 1253–1267.

(199) Fang, H. H.; Yang, J.; Adjokatse, S.; Tekelenburg, E.; Kamminga, M. E.; Duim, H.; Ye, J.; Blake, G. R.; Even, J.; Loi, M. A. *Advanced Functional Materials* **2020**, *30*, 1907979.

(200) Sheikh, T.; Nawale, V.; Pathoor, N.; Phadnis, C.; Chowdhury, A.; Nag, A. *Angewandte Chemie - International Edition* **2020**, *59*, 11653–11659.

(201) Levine, I.; Menzel, D.; Musiienko, A.; MacQueen, R.; Romano, N.; Vasquez-Montoya, M.; Unger, E.; Mora Perez, C.; Forde, A.; Neukirch, A. J.; Korte, L.; Dittrich, T. *Journal of the American Chemical Society* **2024**, *146*, 23437–23448.

(202) Lin, W. C.; Lo, W. C.; Li, J. X.; Wang, Y. K.; Tang, J. F.; Fong, Z. Y. *npj Materials Degradation* **2021**, *5*, 13.

(203) Fang, H.-H. H.; Yang, J.; Tao, S.; Adjokatse, S.; Kamminga, M. E.; Ye, J.; Blake, G. R.; Even, J.; Loi, M. A. *Advanced Functional Materials* **2018**, *28*, 1800305.

(204) Ederer, J.; Janoš, P.; Ecorchard, P.; Tolasz, J.; Štengl, V.; Beneš, H.; Perchacz, M.; Pop-Georgievski, O. *RSC Advances* **2017**, *7*, 12464–12473.

(205) Zhao, J.; Deng, Y.; Wei, H.; Zheng, X.; Yu, Z.; Shao, Y.; Shield, J. E.; Huang, J. *Science Advances* **2017**, *3*, eaao5616.

(206) Dučinskas, A.; Kim, G. Y.; Moia, D.; Senocrate, A.; Wang, Y. R.; Hope, M. A.; Mishra, A.; Kubicki, D. J.; Siczek, M.; Bury, W.; Schneeberger, T.; Emsley, L.; Milić, J. V.; Maier, J.; Grätzel, M. *ACS Energy Letters* **2021**, *6*, 337–344.

(207) Kim, K.; Park, C.; Cha, E.; Kang, D.; Park, J.; Cho, S.; Yi, Y.; Park, S. *Journal of Physics: Energy* **2023**, *5*, 024011.

(208) Han, Y.; Yue, S.; Cui, B.-B. *Advanced Science* **2021**, *8*, 2004805.

(209) Oesinghaus, L.; Schlipf, J.; Giesbrecht, N.; Song, L.; Hu, Y.; Bein, T.; Docampo, P.; Müller-Buschbaum, P. *Advanced Materials Interfaces* **2016**, *3*, 1600403.

(210) Kavadiya, S.; Strzalka, J.; Niedzwiedzki, D. M.; Biswas, P. *Journal of Materials Chemistry A* **2019**, *7*, 12790–12799.

(211) Phillips, L. J.; Rashed, A. M.; Treharne, R. E.; Kay, J.; Yates, P.; Mitrovic, I. Z.; Weerakkody, A.; Hall, S.; Durose, K. *Solar Energy Materials and Solar Cells* **2016**, *147*, 327–333.

(212) Zhou, Y.; You, L.; Wang, S.; Ku, Z.; Fan, H.; Schmidt, D.; Rusydi, A.; Chang, L.; Wang, L.; Ren, P.; Chen, L.; Yuan, G.; Chen, L.; Wang, J. *Nature Communications* **2016**, *7*, 11193.

(213) Smecca, E.; Numata, Y.; Deretzis, I.; Pellegrino, G.; Boninelli, S.; Miyasaka, T.; La Magna, A.; Alberti, A. *Physical Chemistry Chemical Physics* **2016**, *18*, 13413–13422.

(214) Yuan, H.; Debroye, E.; Janssen, K.; Naiki, H.; Steuwe, C.; Lu, G.; Moris, M.; Orgiu, E.; Uji-I, H.; De Schryver, F.; Samorì, P.; Hofkens, J.; Roeffaers, M. *Journal of Physical Chemistry Letters* **2016**, *7*, 561–566.

(215) Leguy, A. M.; Hu, Y.; Campoy-Quiles, M.; Alonso, M. I.; Weber, O. J.; Azarhoosh, P.; Van Schilfgaarde, M.; Weller, M. T.; Bein, T.; Nelson, J.; Docampo, P.; Barnes, P. R. *Chemistry of Materials* **2015**, *27*, 3397–3407.

(216) Hutchinson, J. D.; Ruggeri, E.; Woolley, J. M.; Delport, G. G. G. G. G.; Stranks, S. D.; Milot, R. L. *Advanced Functional Materials* **2023**, *33*, 2305736.

(217) Giza, M.; Angus, F. J.; Yiu, W. K.; McRoberts, M.; Vella, B.; Wang, J.; Djurišić, A. B.; Cooke, G.; Arca, E.; Docampo, P. *Cell Reports Physical Science* **2025**, *6*, 102890.

(218) Grancini, G.; Roldán-Carmona, C.; Zimmermann, I.; Mosconi, E.; Lee, X.; Martineau, D.; Narbey, S.; Oswald, F.; De Angelis, F.; Graetzel, M.; Nazeeruddin, M. K. *Nature Communications* **2017**, *8*, 15684.

(219) Xiong, S. et al. *Nature Communications* **2024**, *15*, 5607.

(220) Sidhik, S. et al. *Science* **2022**, *377*, 1425–1430.

(221) Jiang, Q.; Zhao, Y.; Zhang, X.; Yang, X.; Chen, Y.; Chu, Z.; Ye, Q.; Li, X.; Yin, Z.; You, J. *Nature Photonics* **2019**, *13*, 460–466.

(222) Zhou, Q.; Liang, L.; Hu, J.; Cao, B.; Yang, L.; Wu, T.; Li, X.; Zhang, B.; Gao, P. *Advanced Energy Materials* **2019**, *9*, 1802595.

(223) Zhou, H.; Cai, K.; Yu, S.; Wang, Z.; Xiong, Z.; Chu, Z.; Chu, X.; Jiang, Q.; You, J. *Nature Communications* **2024**, *15*, 6679.

(224) The GIMP Development Team GNU Image Manipulation Program (GIMP), Version 3.0.4. Community, Free Software (license GPLv3), 2025.

(225) Wu, G.; Liang, R.; Ge, M.; Sun, G.; Zhang, Y.; Xing, G. *Advanced Materials* **2022**, *34*, 2105635.

(226) Grey, L. H.; Nie, H. Y.; Biesinger, M. C. *Applied Surface Science* **2024**, *653*, 159319.

(227) Forster-Tonigold, K.; Buchner, F.; Bansmann, J.; Behm, R. J.; Groß, A. *Batteries and Supercaps* **2022**, *5*, e202200307.

(228) Zhang, Z.; Qiao, L.; Meng, K.; Long, R.; Chen, G.; Gao, P. *Chemical Society Reviews* **2022**, *52*, 163–195.

(229) Oner, S. M.; Sezen, E.; Yordanli, M. S.; Karakoc, E.; Deger, C.; Yavuz, I. *Journal of Physical Chemistry Letters* **2022**, *13*, 324–330.

(230) Tan, S.; Yavuz, I.; Weber, M. H.; Huang, T.; Chen, C. H.; Wang, R.; Wang, H. C.; Ko, J. H.; Nuryyeva, S.; Xue, J.; Zhao, Y.; Wei, K. H.; Lee, J. W.; Yang, Y. *Joule* **2020**, *4*, 2426–2442.

(231) Lanzetta, L.; Aristidou, N.; Haque, S. A. *Journal of Physical Chemistry Letters* **2020**, *11*, 574–585.

(232) Isikgor, F. H. et al. *Joule* **2021**, *5*, 1566–1586.

(233) Yang, K.; Shao, B.; Guo, A.; Cui, F.; Yang, X. *New Journal of Chemistry* **2023**, *47*, 9594–9600.

(234) Wang, J.; Liu, L.; Chen, S.; Qi, L.; Zhao, M.; Zhao, C.; Tang, J.; Cai, X.; Lu, F.; Jiu, T. *Small* **2022**, *18*, 2104100.

(235) Chen, J.; Yang, Y.; Dong, H.; Li, J.; Zhu, X.; Xu, J.; Pan, F.; Yuan, F.; Dai, J.; Jiao, B.; Hou, X.; Jen, A. K.; Wu, Z. *Science Advances* **2022**, *8*, eabk2722.

(236) Fridriksson, M. B.; Maheshwari, S.; Grozema, F. C. *Journal of Physical Chemistry C* **2020**, *124*, 22096–22104.

Appendix A

Supporting Figures and Tables

A.1 A’ Cation Salt NMR Spectra

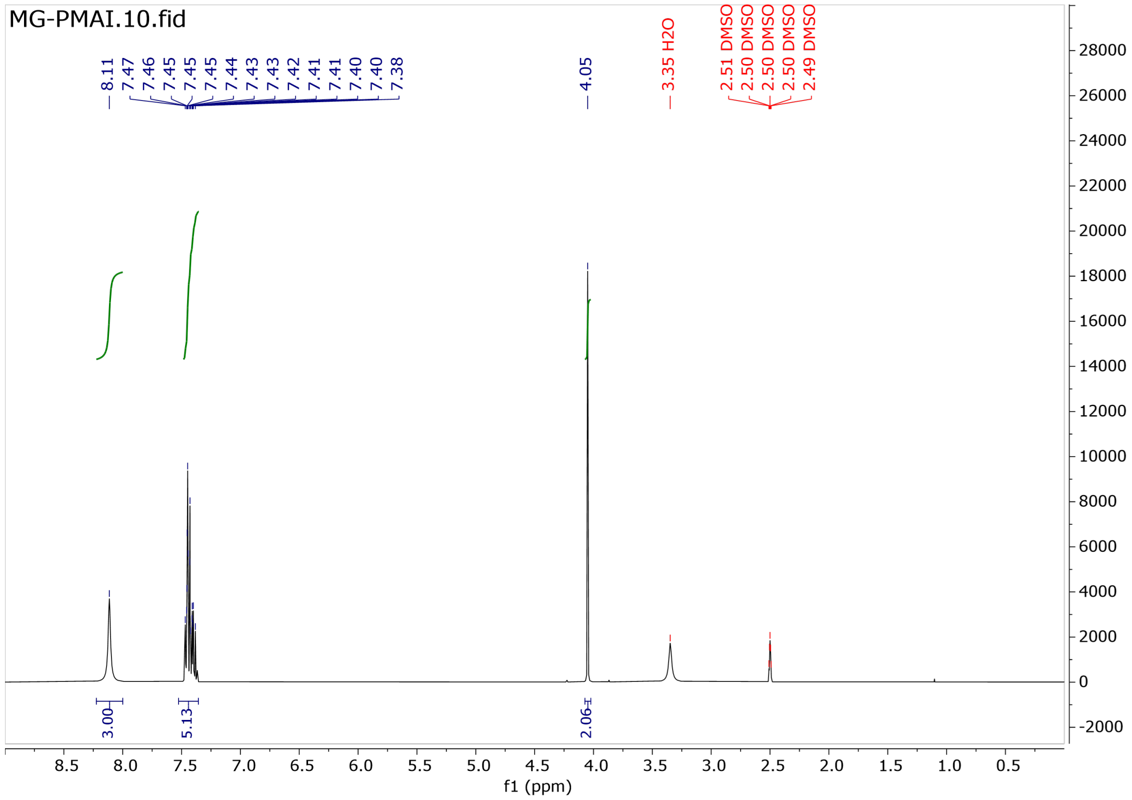

Figure A.1: ^{1}H NMR spectrum of PMAI, taken in DMSO-D6.

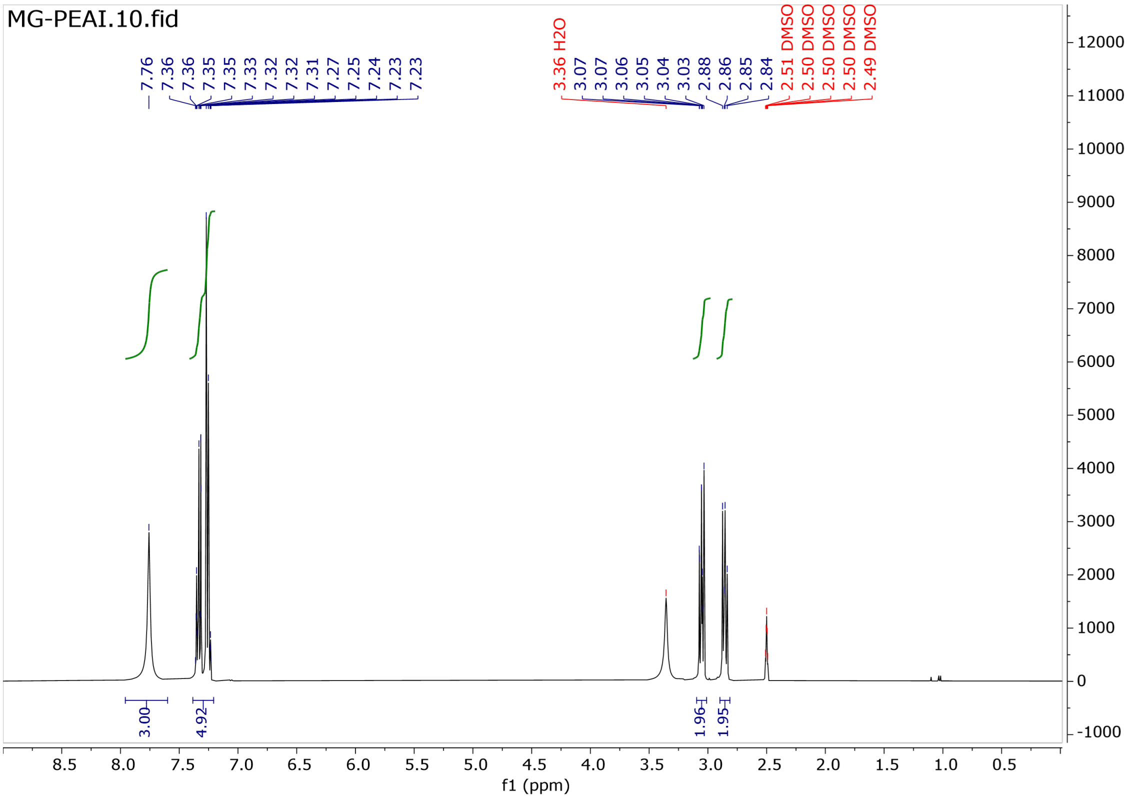

Figure A.2: ^{1}H NMR spectrum of PEAI, taken in DMSO-D6.

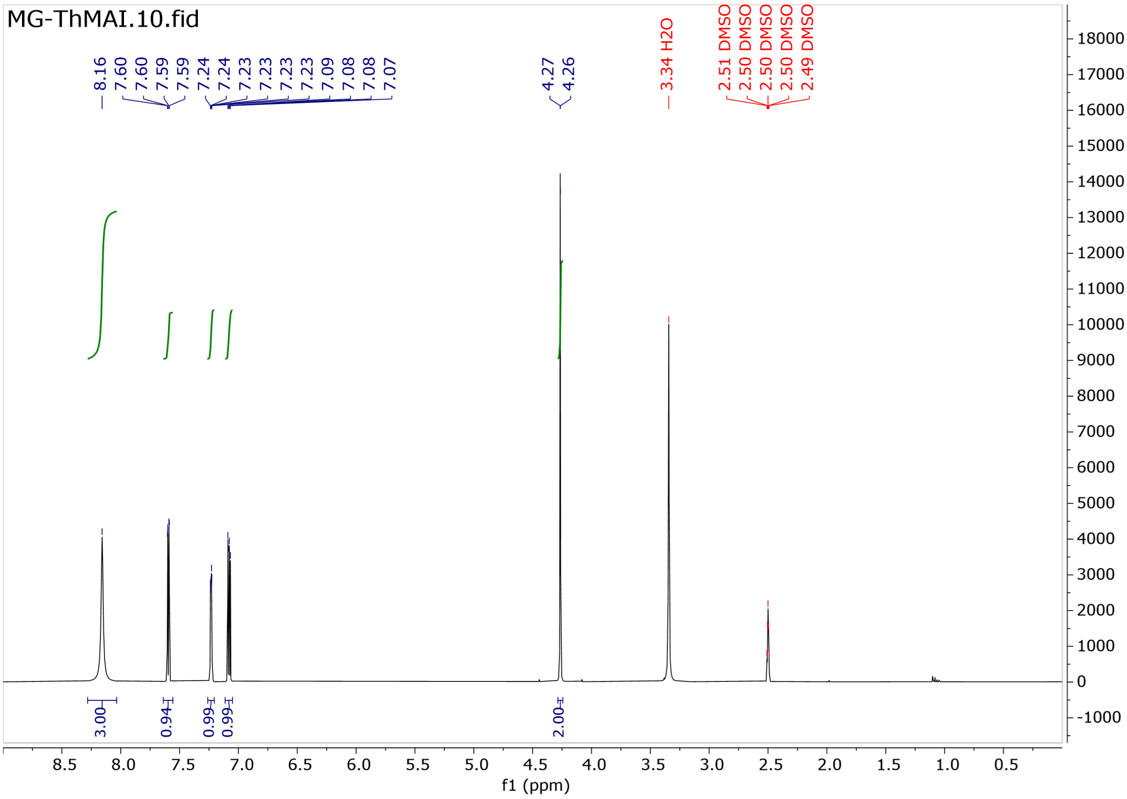

Figure A.3: ^{1}H NMR spectrum of ThMAI, taken in DMSO-D6.

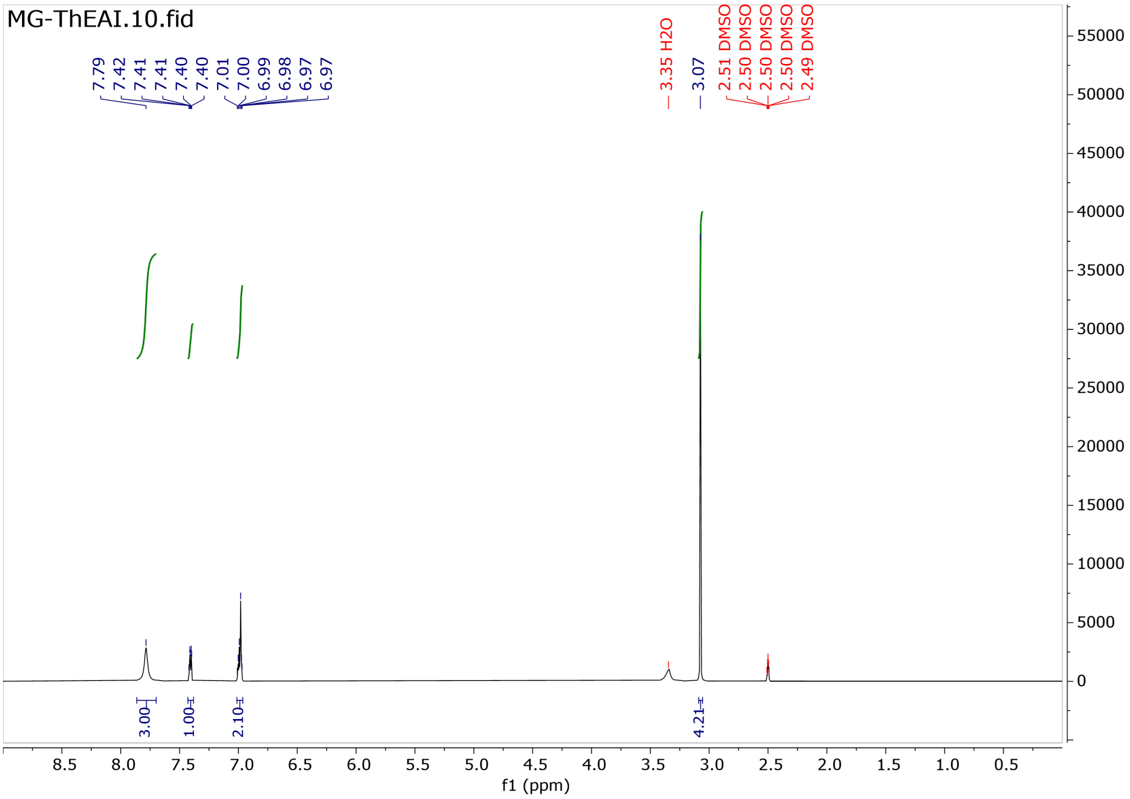

Figure A.4: ^{1}H NMR spectrum of ThEAI, taken in DMSO-D6.

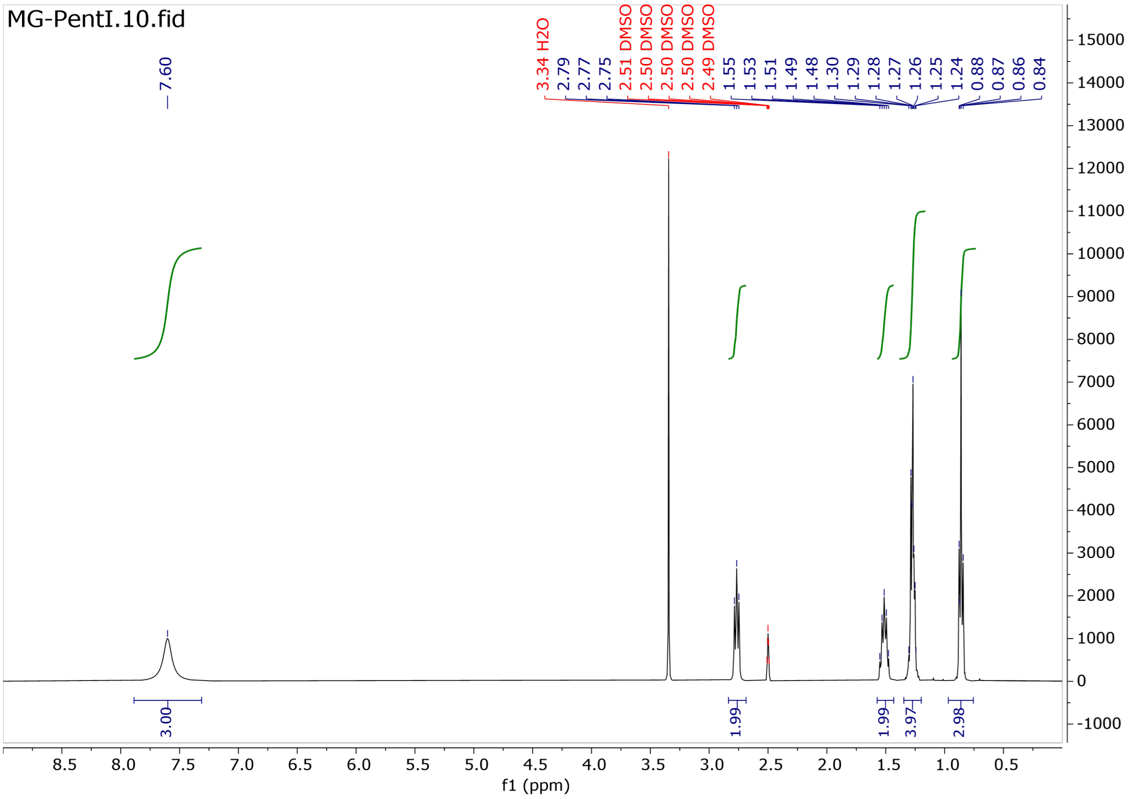

Figure A.5: ^{1}H NMR spectrum of PentAI, taken in DMSO-D6.

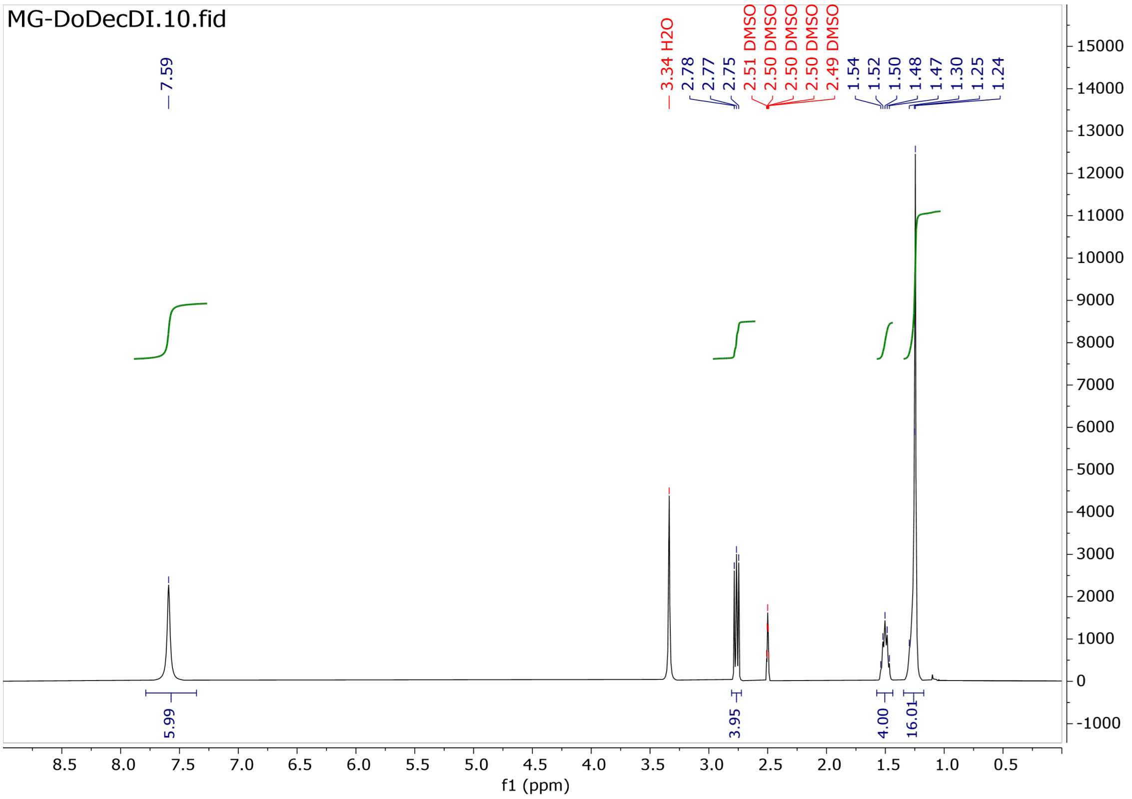

Figure A.6: ^{1}H NMR spectrum of 1-12 DodecAI, taken in DMSO-D6.

A.2 Chapter 3 Crystal Data

Table A.1: Crystal Data for LPKs Templated by Aromatic A' Cations, taken from .cif files.

	PMA	PEA	ThMA	ThEA
CCDC Ref.	N/A	1542461	N/A	1043214
Formula	$(C_7H_{10}N)_2PbI_4$	$(C_8H_{12}N)_2PbI_4$	$(C_5H_8NS)_2PbI_4$	$(C_6H_{10}NS)_2PbI_4$
M_r (Da)	931.11	959.17	943.16	1942.44
T (K)	298(2)	296(2)	295(2)	296(2)
Crystal Size (mm)	0.2×0.15×0.02	0.344×0.217×0.03	0.07×0.06×0.01	Unknown
Crystal System	Orthorhombic	Triclinic	Orthorhombic	Monoclinic
Space group (no.)	*Pbca* (61)	*P-1* (2)	*Pbca* (61)	*Cc* (9)
a (Å)	9.1552(11)	8.7389(2)	8.819(10)	12.2840(8)
b (Å)	8.6944(10)	8.7403(2)	8.545(11)	12.3250(9)
c (Å)	28.759(4)	32.9952(6)	28.78(4)	31.381(3)
α(°)	90	84.646(1)	90	90
β(°)	90	84.657(1)	90	90.972(5)
γ(°)	90	89.643(1)	90	90
V (Å^3)	2289.2(5)	2498.29(9)	2169(5)	4750.4(6)
Z	4	4	4	4
D_c (Mg m^{-3})	2.702	2.550	2.889	2.716
μ Mo-Kα(mm^{-1})	12.761	11.697	13.658	12.474
θ range (°)	2.638 - 28.287	3.29 - 30.08	2.831 - 25.306	1.30 - 33.97
Reflections used	9904	9937	1936	9538
F(000)	1648	1712.0	1664	3456
R Factor (all)	0.0355	0.0743	0.1024	0.0959

Table A.2: Crystal Data for LPKs Templated by Aliphatic A' Cations, taken from .cif files.

	ButA	PentA	HexA	OctA
CCDC Ref.	665690	665692	665695	805431
Formula	$(C_4H_{12}N)_2PbI_4$	$(C_5H_{14}N)_2PbI_4$	$(C_6H_{16}N)_2PbI_4$	$(C_8H_{20}N)_2PbI_4$
M_r (Da)	863.08	891.13	919.19	975.29
T (K)	293(2)	293(2)	293(2)	293(2)
Crystal Size (mm)	0.15×0.14×0.08	0.5×0.46×0.14	0.46×0.28×0.05	0.55×0.2×0.02
Crystal System	Orthorhombic	Monoclinic	Orthorhombic	Orthorhombic
Space group (no.)	*Pbca* (61)	$P2_1/a$ (14)	*Pbca* (61)	*Pbca* (61)
a (Å)	8.87640(10)	8.6716(7)	8.9413(2)	8.9817(4)
b (Å)	8.69250(10)	8.9297(6)	8.6874(2)	8.6886(3)
c (Å)	27.6014(5)	14.8805(13)	32.7027(10)	37.4821(18)
α(°)	90	90	90	90
β(°)	90	100.212(2)	90	90
γ(°)	90	90	90	90
V (Å^3)	2129.67(5)	1134.01(15)	2540.24(11)	2925.0(2)
Z	4	2	4	4
D_c (Mg m^{-3})	2.692	2.61	2.403	2.215
μ Mo-Kα(mm^{-1})	13.705	12.873	11.498	9.992
θ range (°)	2.73 - 27.98	2.54 - 30.76	2.6 - 29.94	2.51 - 27.99
Reflections used	4303	4406	5270	3892
F(000)	1520	792	1648	1776
R Factor (all)	0.0534	0.0562	0.0958	0.0821

Table A.3: Crystal Data for LPKs Templated by mixed A' Cations, taken from .cif files.

	PMA + ButA
CCDC Ref.	N/A
Formula	$(C_4H_{12}N),(C_7H_{10}N)PbI_4$
M_r (Da)	897.09
T (K)	295(2)
Crystal Size (mm)	0.54×0.40×0.01
Crystal System	Monoclinic
Space group (no.)	$P2_1/c$ (14)
a (Å)	14.859(3)
b (Å)	8.8655(14)
c (Å)	8.7030(14)
α(°)	90
β(°)	103.855(7)
γ(°)	90
V (Å^3)	1113.1(3)
Z	2
D_c (Mg m^{-3})	2.676
μ Mo-Kα(mm^{-1})	13.116
θ range (°)	2.696 - 28.222
Reflections used	6724
F(000)	792
R Factor (all)	0.0574

A.3 Chapter 3 Thin Film Diffractograms

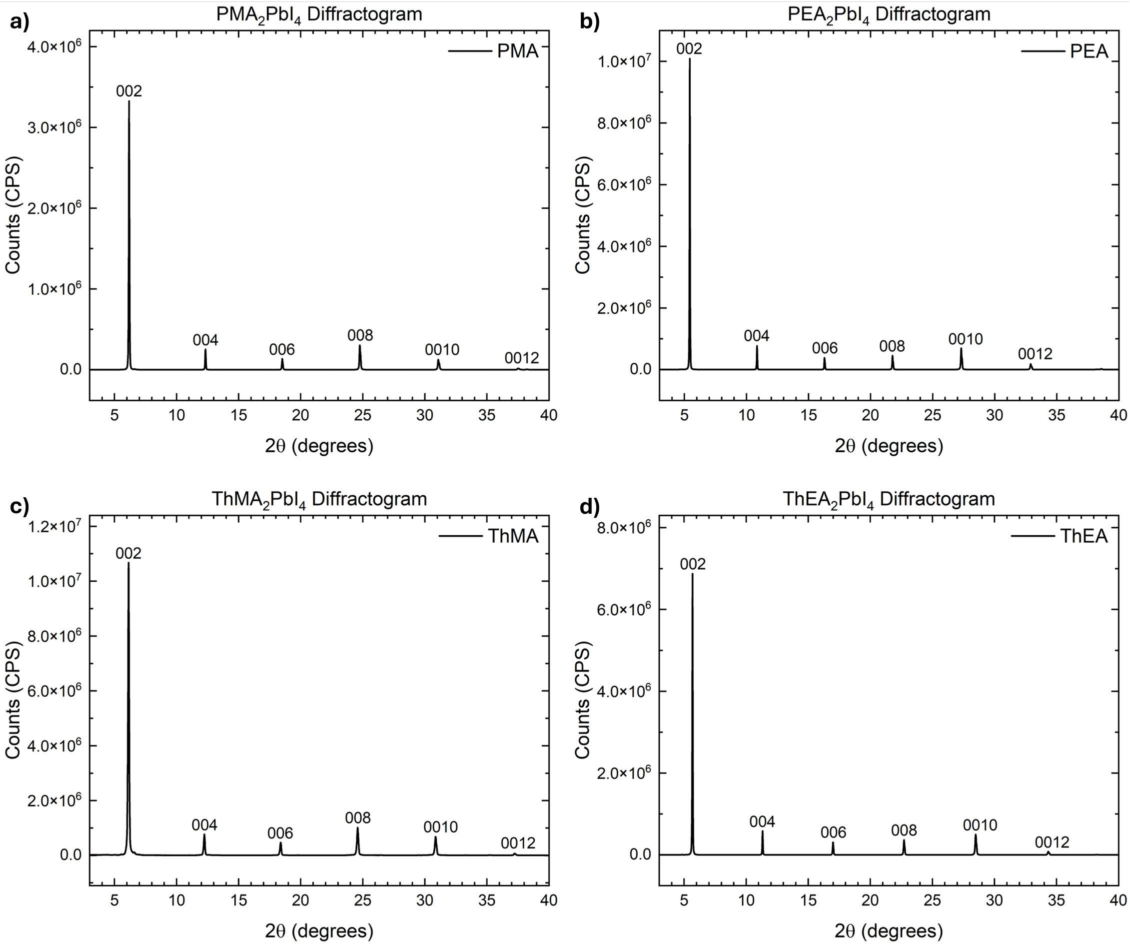

Figure A.7: Aromatic A' cation-templated perovskite thin-film diffractograms. a) PMA$_2$PbI$_4$, b) PEA$_2$PbI$_4$, c) ThMA$_2$PbI$_4$, d) ThEA$_2$PbI$_4$. Peaks are labelled with the respective hkl values.

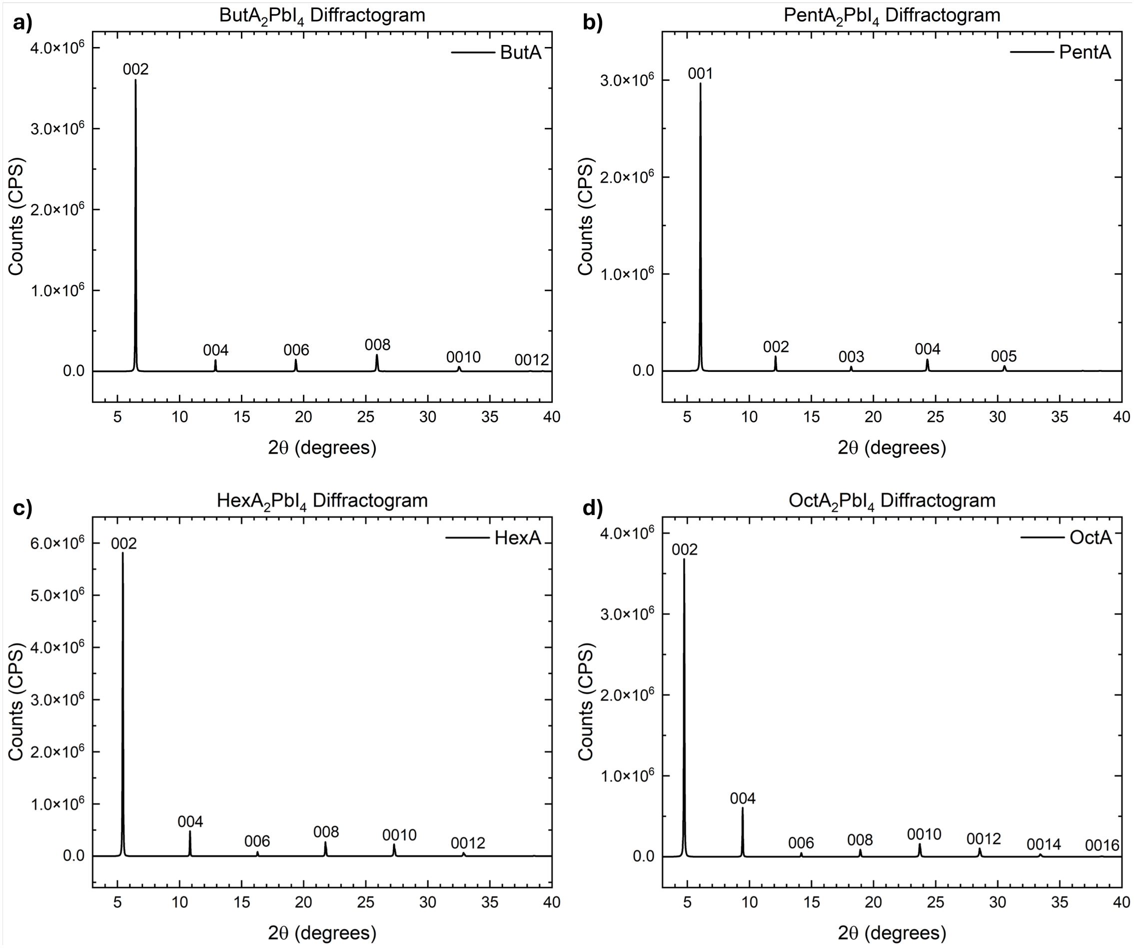

Figure A.8: Aliphatic A' cation-templated perovskite thin-film diffractograms. a) ButA$_2$PbI$_4$, b) PentA$_2$PbI$_4$, c) HexA$_2$PbI$_4$, d) OctA$_2$PbI$_4$. Peaks are labelled with the respective hkl values.

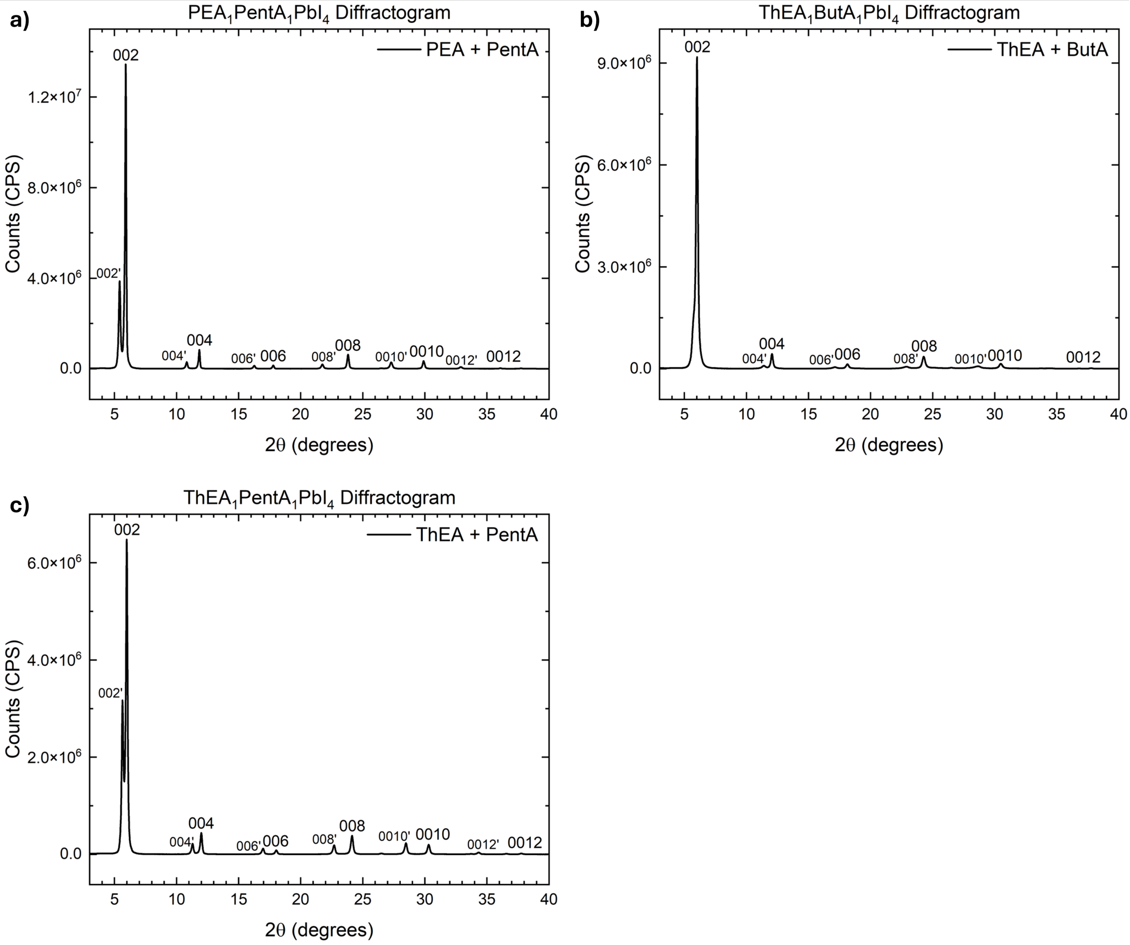

Figure A.9: Mixed A’ cation-templated perovskite thin-film diffractograms (Type 1). a) $\mathrm{PEA_1PentA_1PbI_4}$, b) $\mathrm{ThEA_1ButA_1PbI_4}$, c) $\mathrm{ThEA_1PentA_1PbI_4}$. Peaks are labelled with the respective hkl values. Peaks attributed to a second LPK phase in the film have labels containing a ’ symbol.

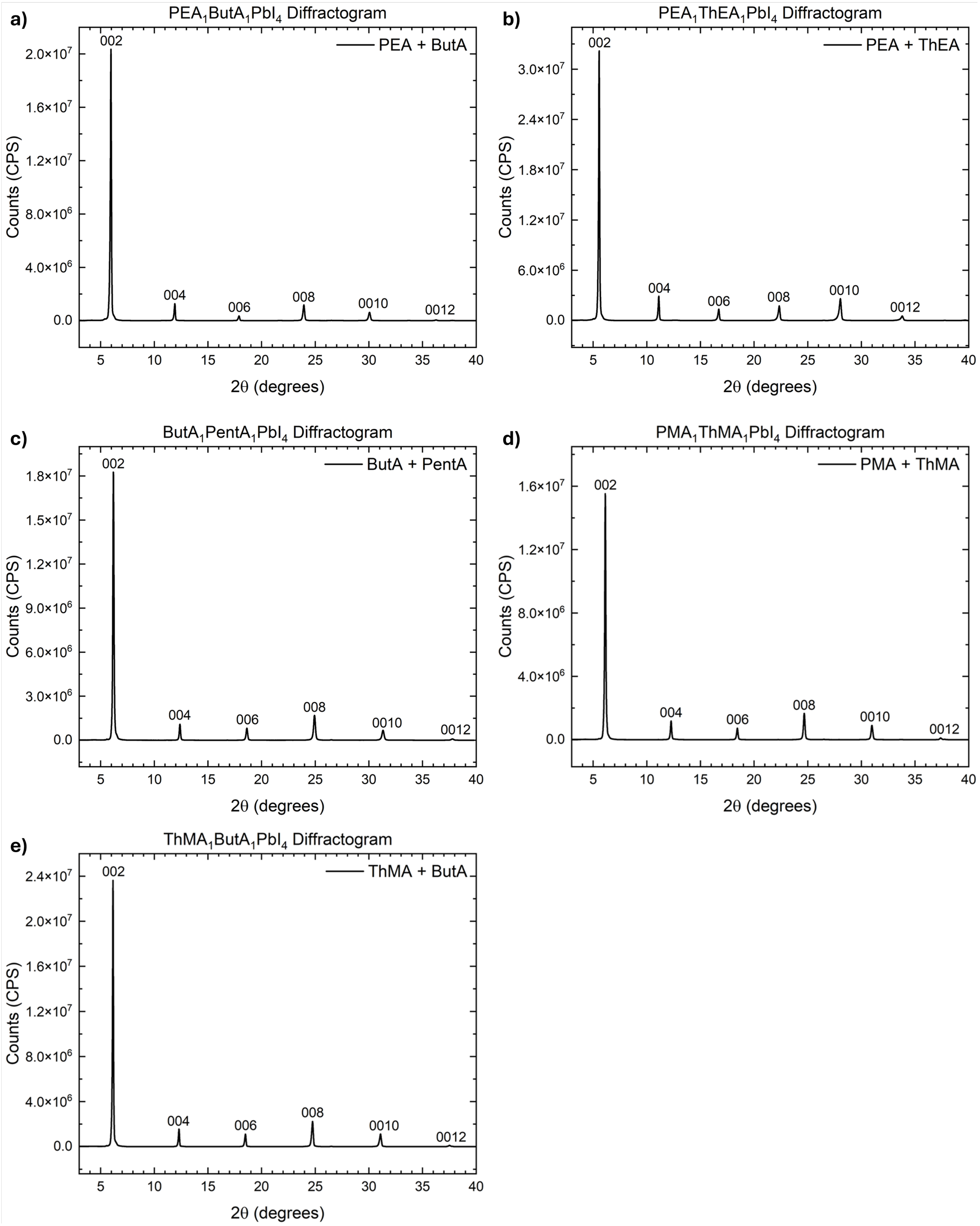

Figure A.10: Mixed A' cation-templated perovskite thin-film diffractograms (Type 2). a) PEA$_1$ButA$_1$PbI$_4$, b) PEA$_1$ThEA$_1$PbI$_4$, c) ButA$_1$PentA$_1$PbI$_4$. d) PMA$_1$ThMA$_1$PbI$_4$. e) ThMA$_1$ButA$_1$PbI$_4$. Peaks are labelled with the respective hkl values.

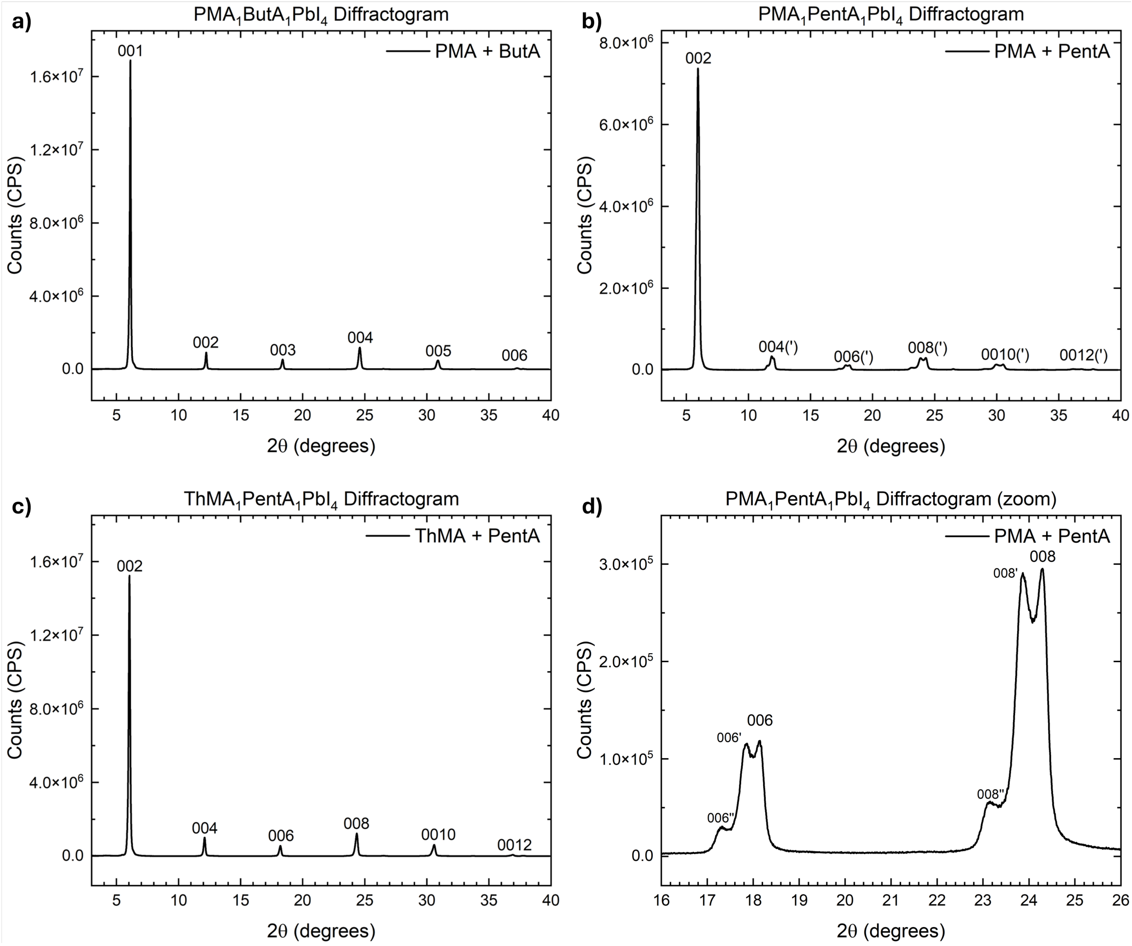

Figure A.11: Mixed A' cation-templated perovskite thin-film diffractograms (Type 3). a) $PMA_1ButA_1PbI_4$, b) $PMA_1PentA_1PbI_4$, c) $ThMA_1PentA_1PbI_4$. d) Zoomed in region of the $PMA_1PentA_1PbI_4$ shown in (b). Peaks are labelled with the respective hkl values. Peaks attributed to additional LPK phases in the film have labels containing a ' or " symbol.

A.4 Chapter 5 Fitted XPS Peaks

A.4.1 Reference Powder Data

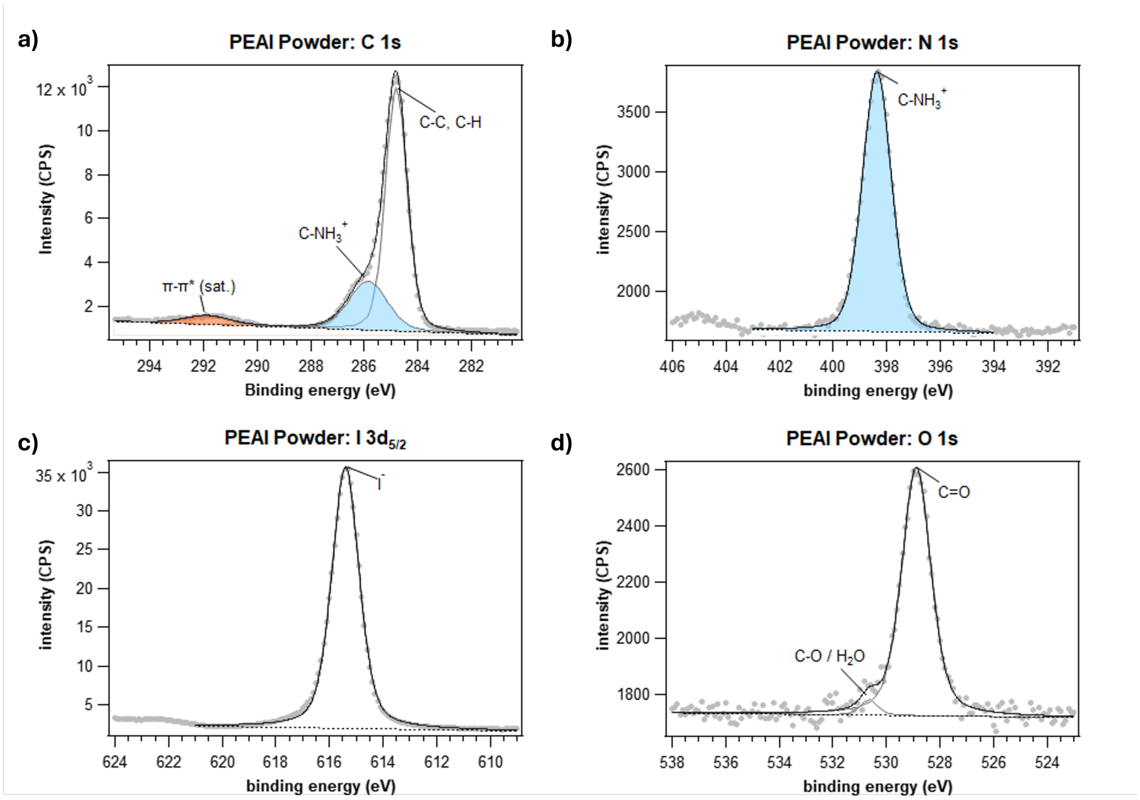

Figure A.12: Fitted XPS peak data for a PEAI powder sample. a) C 1s region. b) N 1s region. c) I 3d region. d) O 1s region. Peaks assigned to key chemical environments have been coloured for clarity across matching regions.

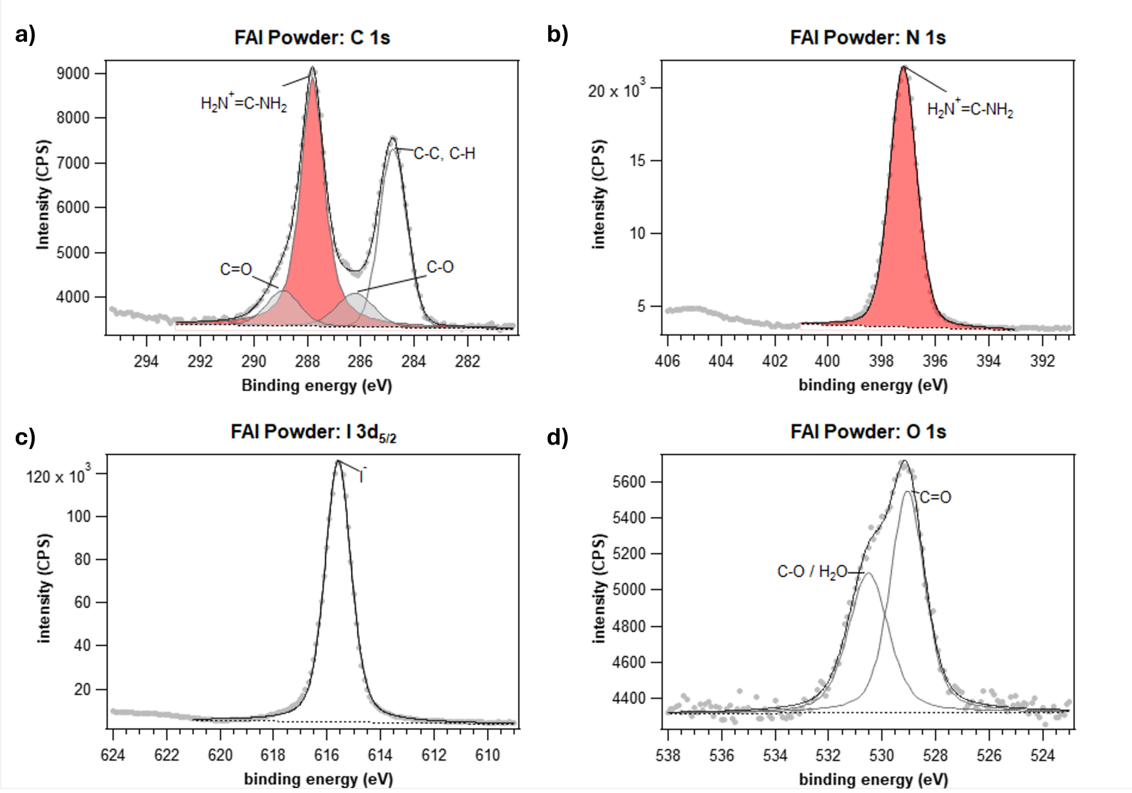

Figure A.13: Fitted XPS peak data for a FAI powder sample. a) C 1s region. b) N 1s region. c) I 3d region. d) O 1s region. Peaks assigned to key chemical environments have been coloured for clarity across matching regions.

A.4.2 Thin Film Data

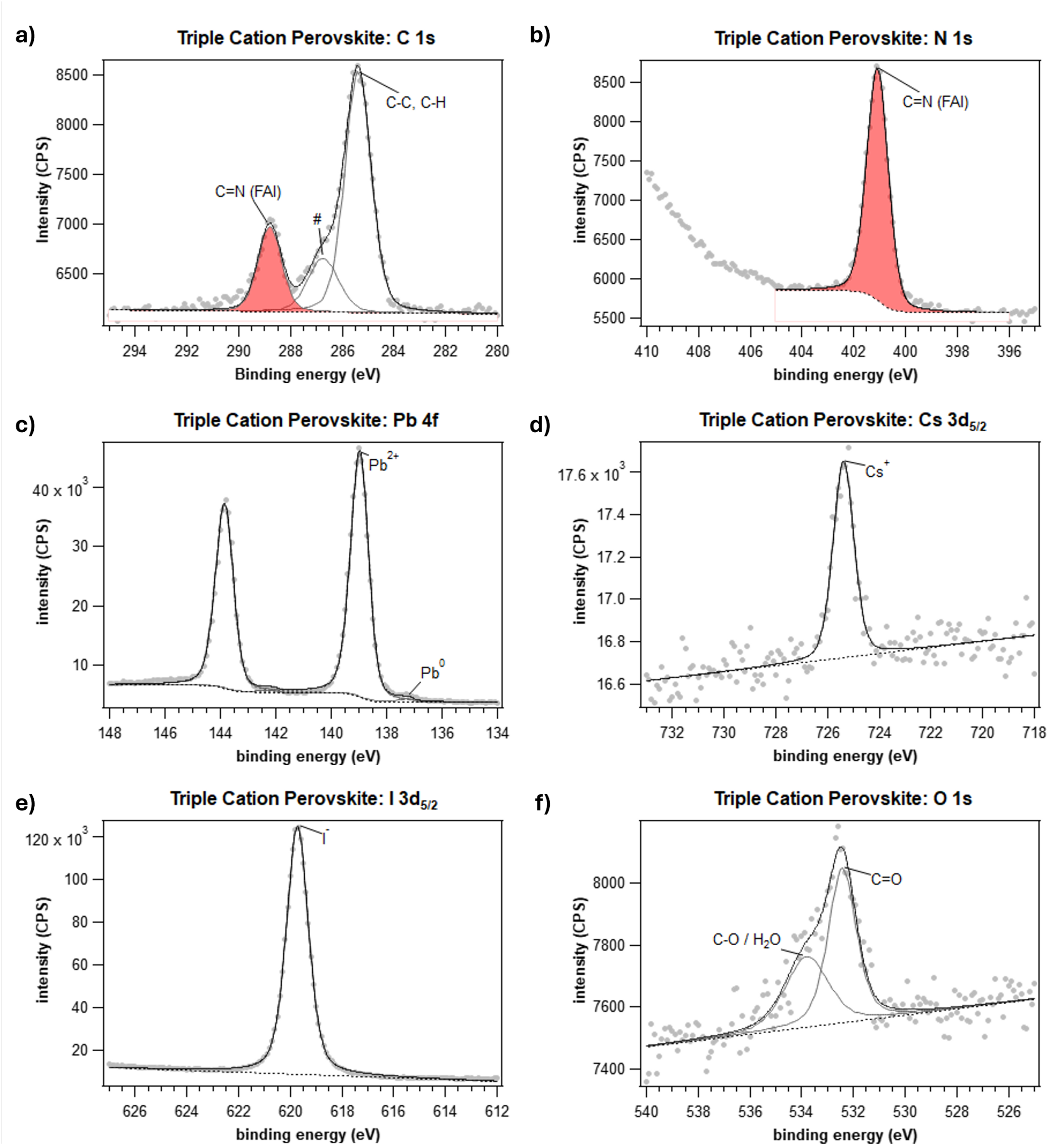

Figure A.14: Fitted XPS peak data for a triple cation sample. a) C 1s region. b) N 1s region. c) Pb 4f region. d) Cs 3d region. e) I 3d region. f) O 1s region. Peaks assigned to key chemical environments have been coloured for clarity across matching regions.

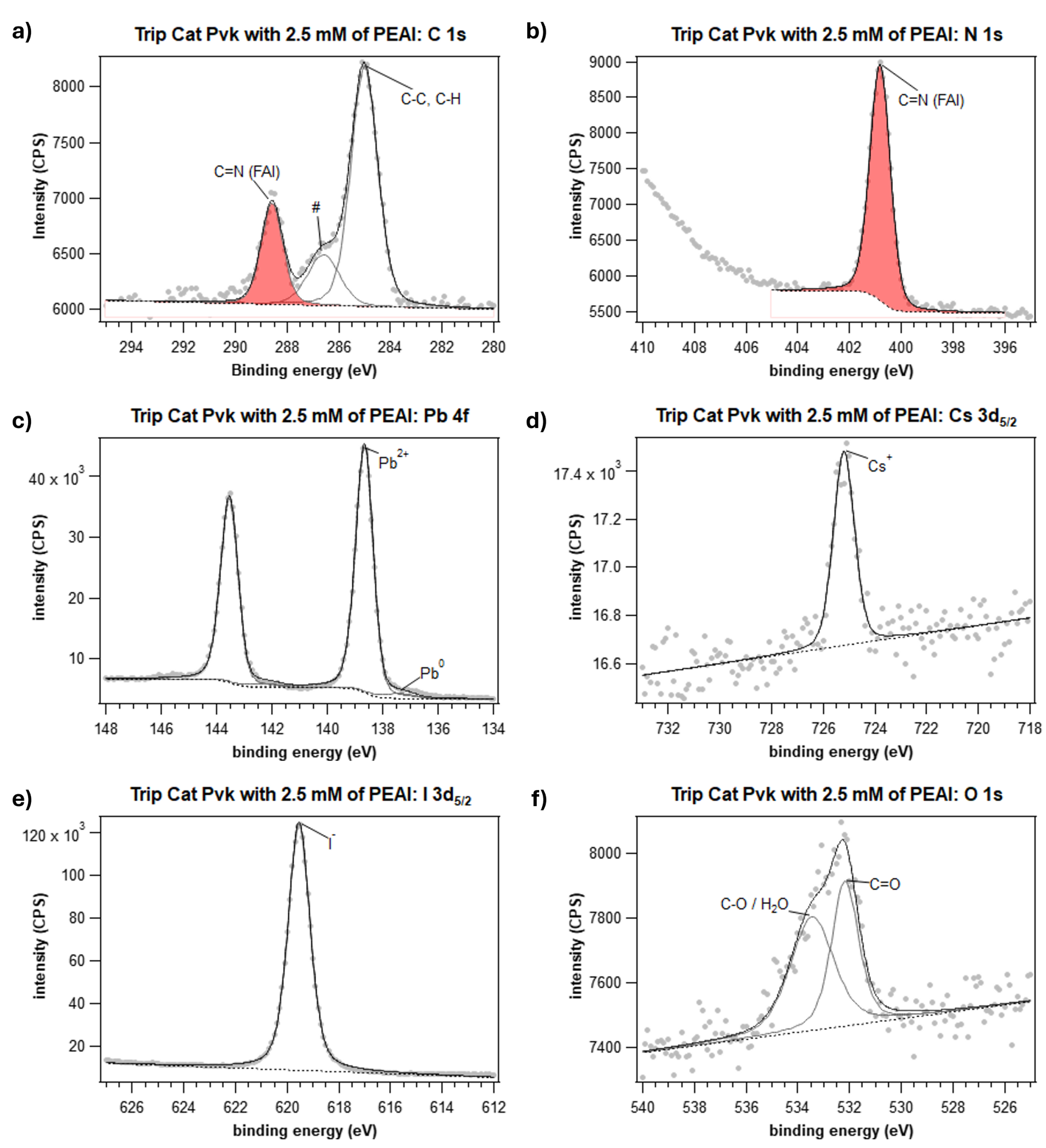

Figure A.15: Fitted XPS peak data for a triple cation sample with 2.5 mM of PEAI. a) C 1s region. b) N 1s region. c) Pb 4f region. d) Cs 3d region. e) I 3d region. f) O 1s region. Peaks assigned to key chemical environments have been coloured for clarity across matching regions.

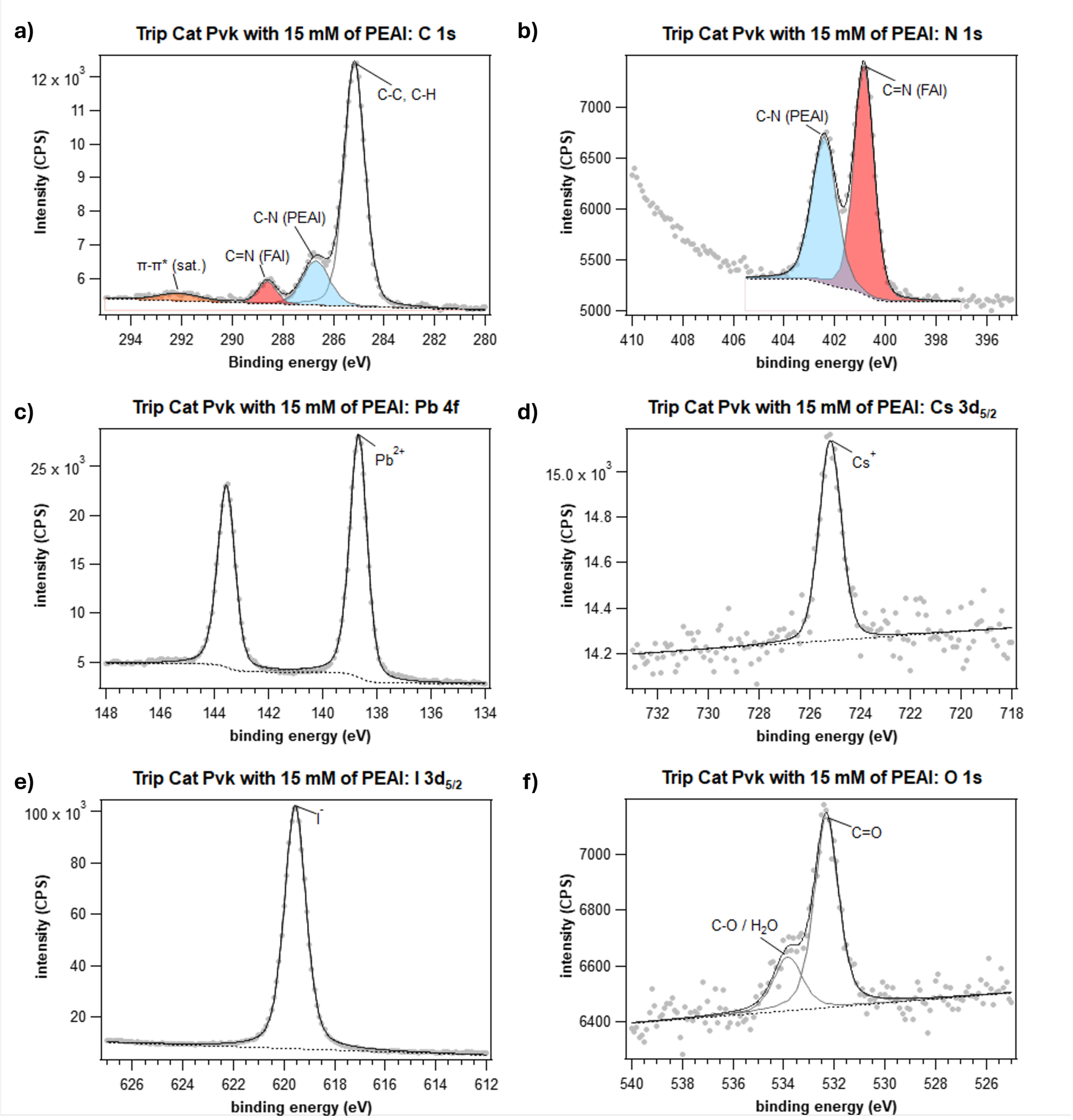

Figure A.16: Fitted XPS peak data for a triple cation sample with 15 mM of PEAI. a) C 1s region. b) N 1s region. c) Pb 4f region. d) Cs 3d region. e) I 3d region. f) O 1s region. Peaks assigned to key chemical environments have been coloured for clarity across matching regions.

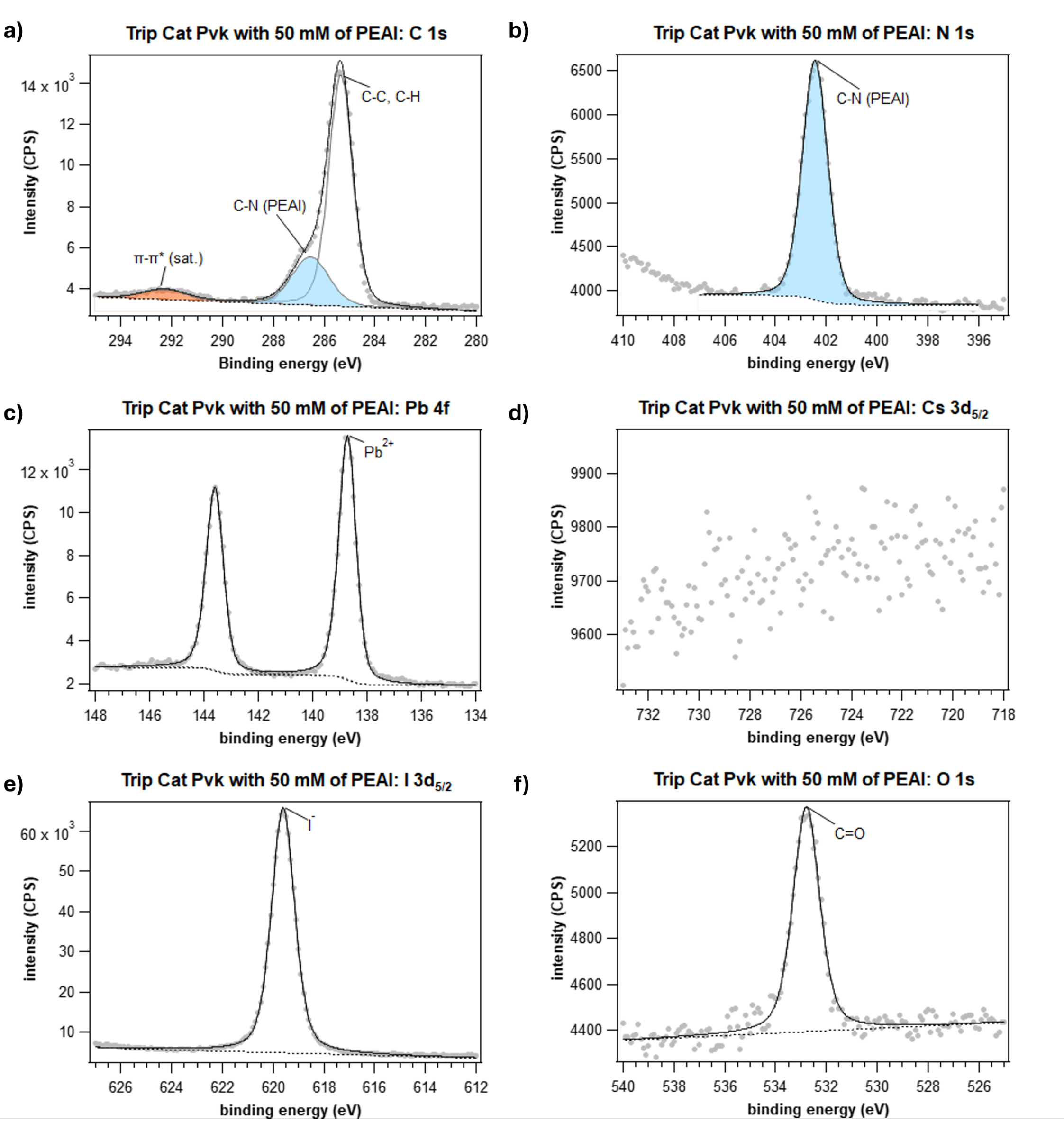

Figure A.17: Fitted XPS peak data for a triple cation sample with 50 mM of PEAI. a) C 1s region. b) N 1s region. c) Pb 4f region. d) Cs 3d region. e) I 3d region. f) O 1s region. Peaks assigned to key chemical environments have been coloured for clarity across matching regions.

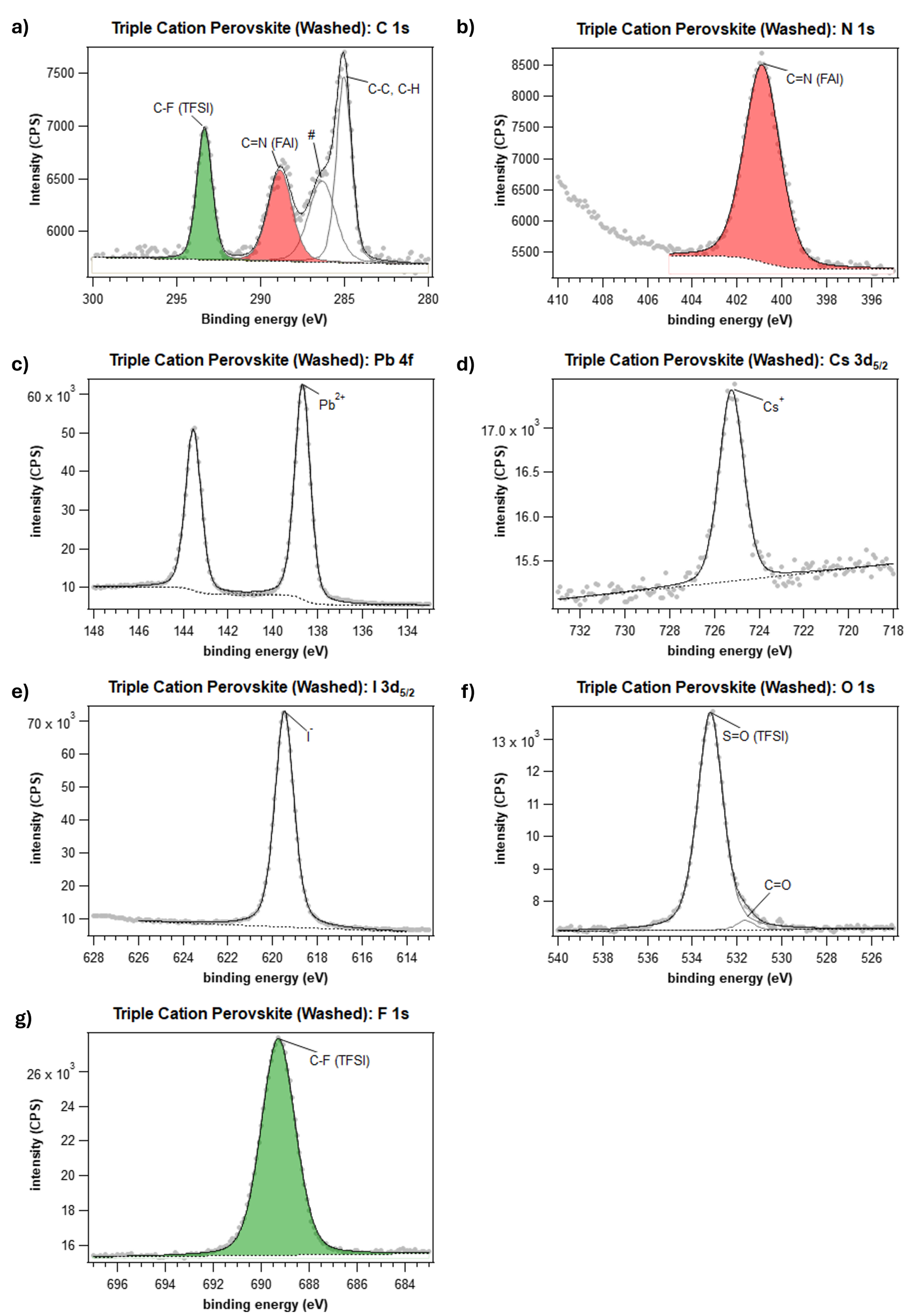

Figure A.18: Fitted XPS peak data for a washed triple cation sample. a) C 1s region. b) N 1s region. c) Pb 4f region. d) Cs 3d region. e) I 3d region. f) O 1s region. g) F 1s region. Peaks assigned to key chemical environments have been coloured for clarity across matching regions.

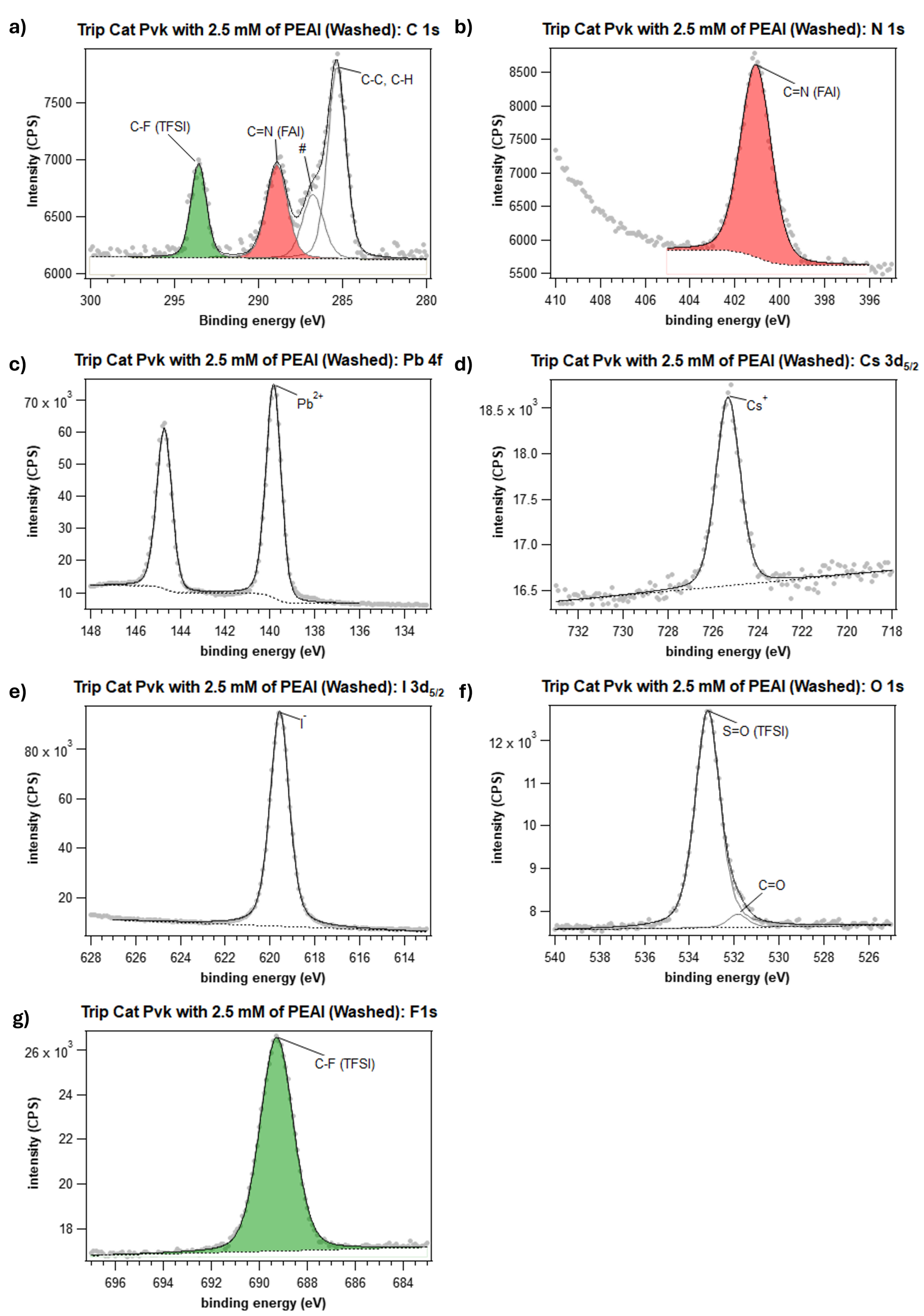

Figure A.19: Fitted XPS peak data for a washed triple cation sample with 2.5 mM of PEAI. a) C 1s region. b) N 1s region. c) Pb 4f region. d) Cs 3d region. e) I 3d region. f) O 1s region. g) F 1s region. Peaks assigned to key chemical environments have been coloured for clarity across matching regions.

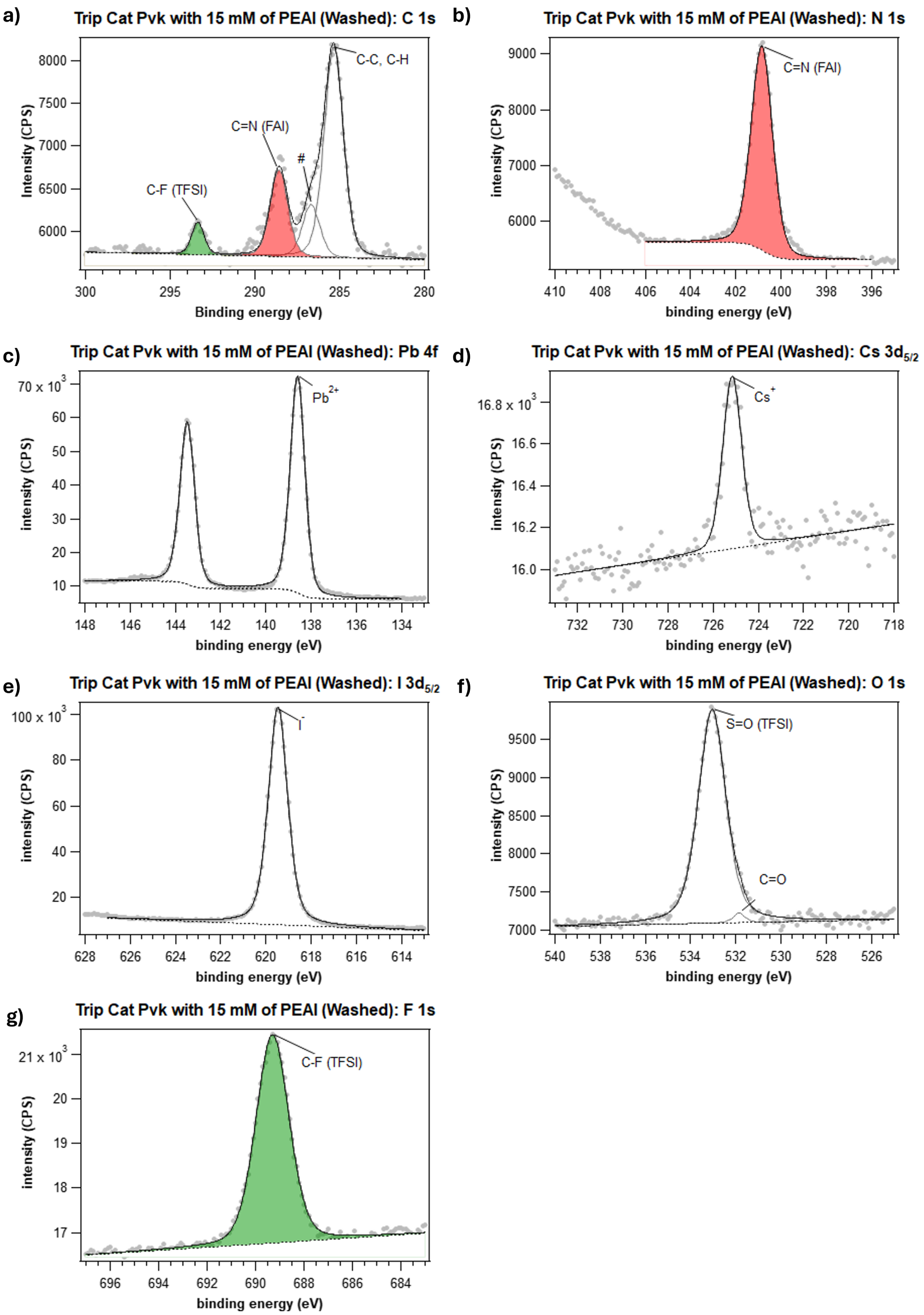

Figure A.20: Fitted XPS peak data for a washed triple cation sample with 15 mM of PEAI. a) C 1s region. b) N 1s region. c) Pb 4f region. d) Cs 3d region. e) I 3d region. f) O 1s region. g) F 1s region. Peaks assigned to key chemical environments have been coloured for clarity across matching regions.

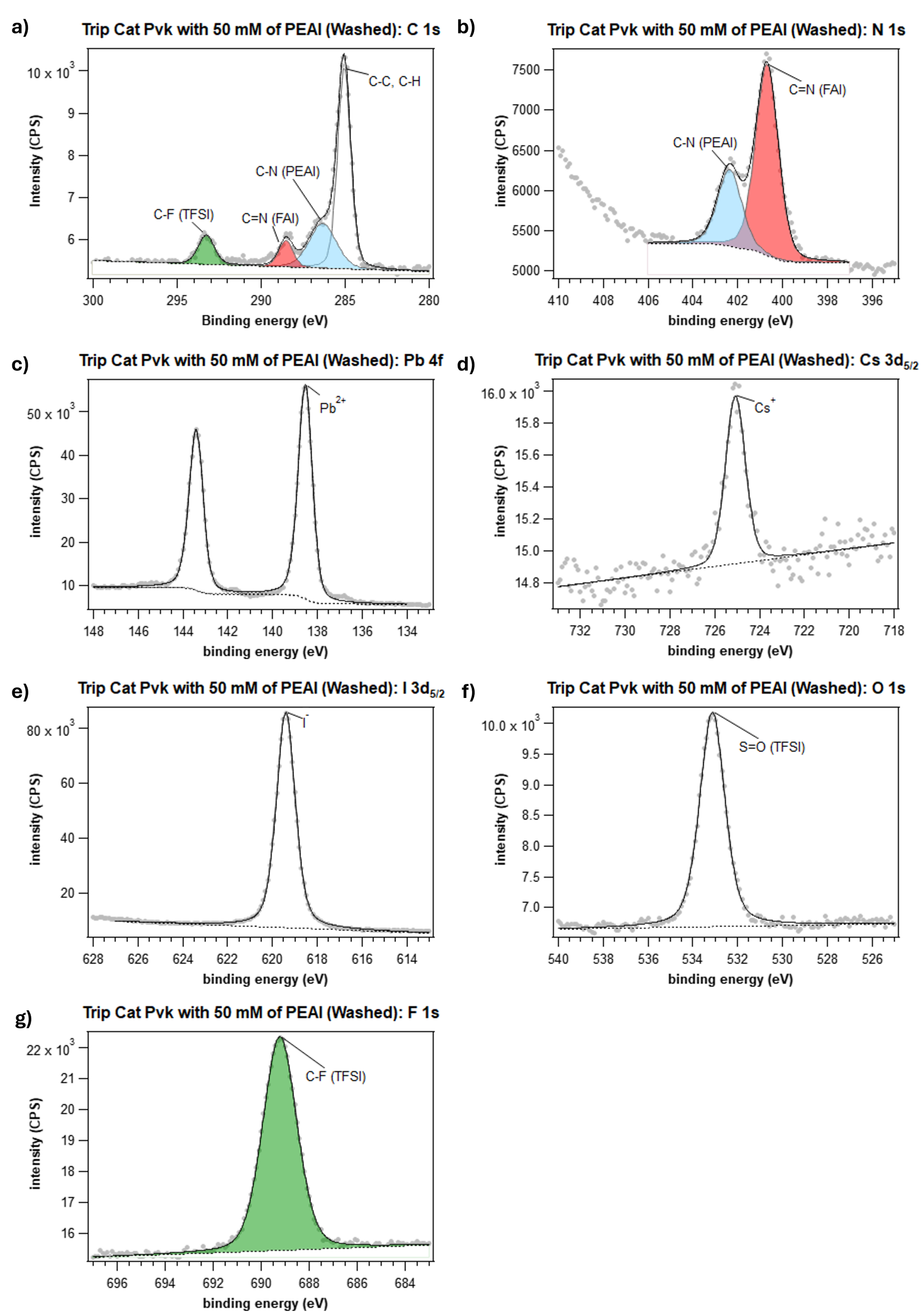

Figure A.21: Fitted XPS peak data for a washed triple cation sample with 50 mM of PEAI. a) C 1s region. b) N 1s region. c) Pb 4f region. d) Cs 3d region. e) I 3d region. f) O 1s region. g) F 1s region. Peaks assigned to key chemical environments have been coloured for clarity across matching regions.